Stable p-i-n solar cells using metal halide perovskites

Yuze Li

THÈSE

Pour obtenir le grade de

DOCTEUR DE L'UNIVERSITÉ GRENOBLE ALPES

Spécialité : Chimie inorganique et bio-inorganique

Arrêté ministériel : 25 mai 2016

Présentée par

Yuze LI

Thèse dirigée par **Peter REISS**, CEA Grenoble et codirigée par **Elisabeth DJURADO**, Grenoble INP

préparée au sein du **Laboratoire Systèmes Moléculaires et Nano Matériaux pour l'Énergie et la Santé**
dans **l'École Doctorale Chimie et Sciences du Vivant**

Cellules solaires p-i-n à base de pérovskites halogénées

Stable p-i-n solar cells using metal halide perovskites

Thèse soutenue publiquement le **9 février 2022**,
devant le jury composé de :

Madame Zhuoying CHEN
CHARGEE DE RECHERCHE, CNRS, Rapporteur
Monsieur Olivier MARGEAT
MAITRE DE CONFERENCE, Université Aix Marseille, Rapporteur
Monsieur Daniel BELLET
PROFESSEUR DES UNIVERSITES, Grenoble INP, Président
Monsieur Alain IBANEZ
DIRECTEUR DE RECHERCHE, CNRS, Examinateur
Monsieur Philippe LANG
DIRECTEUR DE RECHERCHE, CNRS, Examinateur
Monsieur Peter REISS
DIRECTEUR DE RECHERCHE, CEA Grenoble, Directeur de thèse
Madame Elisabeth Djurado
PROFESSEURE, Grenoble INP, invitée
Madame Stéphanie Pouget
INGENIEUR DE RECHERCHE, CEA Grenoble, invitée

Overall

Le sujet principal de cette thèse est le développement de la couche de transport des charges positives (trous) utilisée dans des cellules solaires à base de pérovskites halogénées. Le matériau étudié pour cette application est l'oxyde de nickel (NiO) et trois voies différentes ont été explorées dans le but d'optimiser la cristallinité, la morphologie et les propriétés de transport des couches minces de NiO. Dans tous les cas l'influence sur les performances des cellules solaires pérovskite a été étudiée.

Le chapitre 1 présente brièvement le contexte et l'état de la recherche photovoltaïque actuelle, et clarifie l'objectif de ce travail. Ensuite, les principes de base des cellules photovoltaïques sont présentés. Les caractéristiques des matériaux hybrides de pérovskite à base d'halogénures de plomb ainsi que des matériaux de transport de charge sont également discutées. Comme toile de fond des chapitres suivants, ce chapitre présente brièvement les problèmes d'architecture, de stabilité et d'hystérésis des cellules solaires pérovskite.

Le chapitre 2 présente les techniques de dépôt des couches minces utilisées pour la fabrication des cellules solaires pérovskite et les techniques de caractérisation pour la couche de pérovskite et les couches de transport de charge. La caractérisation des cellules solaires pérovskite repose principalement sur des mesures de la densité du courant en fonction de la tension appliquée J(V) décrites dans le chapitre 1. L'utilisation combinée de ces mesures J(V), de la microscopie électronique à balayage (MEB) et de diverses méthodes spectroscopiques donne des pistes pour optimiser les cellules solaires à pérovskite.

Le chapitre 3 concerne tout d'abord l'optimisation de la composition de la couche pérovskite en introduisant du PbI2 et de MACl afin de maximiser les performances en cellule solaire. Par la suite, nous nous sommes intéressés à la passivation de la couche de transport de trous (NiO) pour améliorer l'interface et la cristallinité de la couche de pérovskite. L'introduction d'une couche de passivation à base de la 4-diméthylaminopyridine n'a non seulement amélioré fortement le facteur de remplissage (fill factor) de la cellule solaire et par conséquent son rendement, mais également la stabilité sous atmosphère humide.

Dans le chapitre 4 une nouvelle méthode de dépôt pour la couche conducteur de trous NiO est présentée par pulvérisation électrostatique (electrospray deposition, ESD). Cette méthode apporte une meilleure morphologie de surface et des couches NiO plus denses que la méthode conventionnelle de dépôt par enduction centrifuge (spin-coating). De plus, l'ESD permet d'introduire une quantité précise de dopants dans le NiO, comme par exemple le cuivre ou le lithium. En faisant varier les paramètres tels que la température et le temps de dépôt, nous avons obtenu des films minces de Cu:NiO denses et uniformes. Leur utilisation dans

des cellules solaires pérovskite a permis d'améliorer efficacement les performances, notamment le fill factor. La préparation de la couche de transport de trous dans les chapitres 3 et 4 nécessite un traitement à haute température, ce qui peut limiter son application par exemple dans des cellules solaires souples ou tandem. Dans le chapitre 5 nous développons une nouvelle méthode de synthèse de nanoparticules de NiO. Ces particules d'une taille <10 nm sont synthétisées par voie chimique en solvant organique en présence de molécules stabilisantes appropriées. L'optimisation de la synthèse a permis de contrôler précisément la taille et la phase cristalline des nanoparticules. Nous démontrons également que les nanoparticules de NiO présentent un potentiel pour des cellules solaires pérovskite entièrement inorganique, en utilisant comme couche de transport d'électrons le SnO2.

Les principaux résultats ainsi que les perspectives ouvertes par ce travail de thèse sont résumés dans le chapitre 6.

Chapter 1 briefly introduces the background and status of current photovoltaic research, and clarifies the purpose of this work. Then the basic principles of photovoltaics are introduced in detail. The characteristics of organic and inorganic lead halide perovskite materials and charge transport materials that constitute perovskite solar cells are also discussed. As the background of the subsequent chapters, this chapter briefly introduces the structure, stability and hysteresis problems of perovskite solar cells.

Chapter 2 introduces the new thin film deposition technology (under the background of manufacturing perovskite solar cells) and the characterization technology applied to perovskite active materials and charge transport layers. The work in the remaining chapters mainly relies on the J-V scanning of perovskite solar cells, which will be described in Chapter 1. The combined use of J-V scanning and microscope, and spectroscopy provides guidance for optimizing perovskite solar cells.

Chapter 3 discusses the use of composition optimization engineering to introduce excess PbI2 and MACl (to be presented in Chapter 1) in the perovskite precursors to maximize the performance of perovskite solar cells. Subsequently, we developed a simple hole transport layer passivation material to fix the contact problem at the interface and to increase the crystallinity of the perovskite crystals. The introduction of passivation layer not only improved the FF of the solar cell to a great extent, but also effectively improved the stability of the perovskite solar cell under humid atmosphere.

Chapter 4, a novel thin film deposition method, Electrostatic Spray Deposition (ESD), is presented to prepare charge transport layers. This method brings better surface morphology and denser Cu:NiO films than the conventional spin-coating method. By varying the parameters such as temperature and deposition time, we obtained uniform dense Cu:NiO thin films. The application of this film to perovskite solar cells can effectively improve the performance of solar cells with favorable FF. In addition, this approach allows the use of different ions for the doping of NiO, such as Li.

Chapter 5 describes a method for the synthesis of NiO nanoparticles. The preparation of the hole transport layer in Chapter 3 and 4 requires high temperature processing, which can limit the application of this NiO hole transport layer. In this chapter, ultra-small NiO nanoparticles are synthesized by trying different synthetic routes. The size of the nanoparticles is well controlled and has an excellent particle size distribution. The NiO nanoparticles show potential for application in all-inorganic charge transport layer perovskite solar cell devices.

Acknowledgements

First and foremost, I would like to thank my supervisor Prof. Peter Reiss and co-supervisor Prof. Elisabeth Djurado for their professional guidance, constant support and patience. Without their full discussion, enthusiasm and encouragement, this thesis would have been difficult to complete.

I have also had the luxury of having many great colleagues and friends here in the DRF/IRIG/DIESE/SYMMES/STEP group. Thank you for the times when you have helped me with understanding experiments and interpreting results and thank you for your friendship.

I am indebted to Dr.Jiajiu Ye who have contributed a lot to my research life. I am deeply grateful Prof. Dmitry Aldakov for his valuable help with XPS and UPS characterization. Besides, I would like to thank Benjamin Grevin for his AFM help. I acknowledge Dr. MEDJAHED Aicha asma and Prof Stéphanie Pouget for their technical support and discussion about XRD characterization. I benefited a lot from the discussions with you.

I thank my family for fostering my curiosity while I was growing up. Thank you for everything you have given me, I could not have come close to writing a paper without all the things you have taught me.

Lastly, and most importantly, I am very grateful to my fiancée; for all the love and support I received during my doctoral studies. She gave me the strength to pursue my PhD while she endured the cold and rainy months and stood by me patiently when I was stupid, stressed and frustrated with my work.

Abbreviations

AFM	Atomic Force Microscopy
AM 1.5G	Air Mass 1.5 Global
Ag	Silver
Au	Gold
CB	Conduction band
CB	Chlorobenzene
Cu:NiO	Cu doped NiO
DMF	Dimethylformamide
DMSO	Dimethyl sulfoxide
Eg	Bandgap
FTO	Fluorine-doped Tin Oxide
FF	Fill factor
FA	Formamidinium
GIXRD	Grazing incidence X-Ray diffraction
HOMO	Highest occupied molecular orbital
HTM	Hole transporting materials
ITO	Tin-doped indium oxide
IPA	Isopropyl alcohol
J-V	Current density-voltage
Jsc	Short current density
LUMO	Lowest unoccupied molecular orbital
mpp	Maximum power point
MA	Methylammonium
NiO	Nickel Oxides
Nps	nanoparticles
[60]PCBM	[6,6]-Phenyl-C61-Butyric-acid-Methyl ester
PCE	Power conversion efficiency

Abbreviations

PL	Photoluminescence
PV	Photovoltaic
PVK	perovskite
PSC	Perovskite solar cell
RMS	Root mean square
SEM	Scanning electron microscope
spiro-MeOTAD	2,2',7,7'-Tetrakis-(N,N-di-4-methoxyphenylamino)-9,9'-spirobifluorene
SnO_2	Tin oxide
TEM	Transmission electron microscopy
TUNA	Tunneling AFM
UPS	Ultraviolet photoelectron spectroscopy
VB	Valence band
Voc	Open-circuit voltage
WF	Work function
XPS	X-ray photoelectron spectroscopy
XRD	X-ray diffraction

Content

Chapter I Introduction

Context

One of the most pressing issues confronting humanity in the 21st century is energy production. Due to economic and population expansion, the world's energy consumption is continually growing. To fulfill these requirements, demand for all fuels continues to rise; fossil fuels continue to account for approximately 80% of worldwide energy consumption, including 65% of global electricity generation[1]. As a result, worldwide CO_2 emissions are rising, and fossil resources are running out. To lessen the impact of growing energy demand on increasing carbon emissions, there is growing interest in renewable energies, especially for power generation. They mainly include hydroelectricity, wind power, solar power, geothermal power and renewable fuel energies. Figure 1.1 shows the evolution of the respective shares of solar, wind and geothermal / biomass in electricity production. In 2018, solar energy production grew very rapidly, and is expected to increase further in the years to come. Converting solar energy into electricity is a clean and sustainable way to solve the problems of the energy crisis and global warming.

Figure 1.1 Distribution of share of renewable energy in electricity production by source. Adapted from Ref 2.

There has already been a political and societal change away from fossil fuels and toward carbon-neutral energy generation. The quest for clean energy to meet the Paris Agreement's objectives has fueled a surge in large-scale photovoltaic (PV) installations on rooftops and solar farms during the last ten years (which now lacks

US backing). The total quantity of PV installed throughout the world had topped 100 GWp by the end of 2012. (Giga-watt peak)[3].PV is expected to account for about a third of all newly installed electricity generating by 2030. Renewables are expected to account for 72 % of power production capacity investments between now and 2040, with solar power coming in second only to wind power.

Thin-film PV light-absorbing semiconductors are the focus of a long-standing scientific community, with the goal of developing a semiconducting material that can compete with common solar module materials such as crystalline (c-Si) and amorphous silicon (a-Si). The common inorganic thin-film solar cells include cadmium telluride (CdTe), copper indium gallium selenide (CIGS), and copper zinc tin sulfide (CZTS). However, the efficiency of commercial inorganic thin-film solar cells is usually restricted, although they are still competitive due to the use of less bulk material and less expensive manufacturing processes. Solar cells made on CdTe have managed to grab a small portion of the PV market. However, due to the shortage of tellurium as a rare earth metal and the toxicity of cadmium, CdTe solar cells are still not widely applied. CIGS PVs that employ indium and gallium rare earth elements have similar commercial challenges. CZTS, which mainly employs earth-abundant materials, is maybe the only potential emerging inorganic PV technology. CZTS solar cells, on the other hand, have a power conversion efficiency (PCE) of about 10%, which is substantially lower than silicon-based PV[4].

The earliest alternatives to inorganic thin-film photovoltaics include organic solar cells made of semiconducting organic polymers or fullerenes, and dye-sensitized solar panels are made up of small molecules of photosensitive dye. These organic films can be deposited onto flexible substrates utilizing roll-to-roll methods since they are generally produced at low temperatures (<150 °C) and in solution (such as slot-die coating, spray coating, or screen printing). Although the photovoltaic efficiency is still not as good as that of silicon-based solar cells, the above-mentioned points are still what make them competitive. With the development of lead halide perovskite solar cells, another candidate has emerged in the photovoltaic field. Perovskites were first discovered by a German mineralogist, Gustav Rose, in the Russian Ural Mountains in 1839 and named after the Russian mineralogist Lev Perovski[5]. In solar cells, typical organic-inorganic lead halide perovskite structure compounds are AMX_3. A was initially methylammonium (CH_3NH_3, MA), but meanwhile formamidinium ($NH_2CH{=}NH_2^+$, FA) and mixtures of both and with cesium have been reported to improve stability and solar cell performance[6]; M is mainly Pb^{2+}, but also Sn ions can be incorporated in small quantities[7]; X is mainly I^-, eventually in coexistence with other halogens. Research on perovskite photovoltaics has exploded in the last decade. They are considered as one of the most promising emerging photovoltaic technologies because the power conversion efficiency (PCE) increased from 9% to over 25% in last decade[8,9]. I will discuss their unique structural and optoelectronic features leading to these spectacular performances

later in this chapter. Figure 1.2 depicts the increase in world record performance of all solar cell technologies as measured by the National Renewable Energy Laboratory[10].

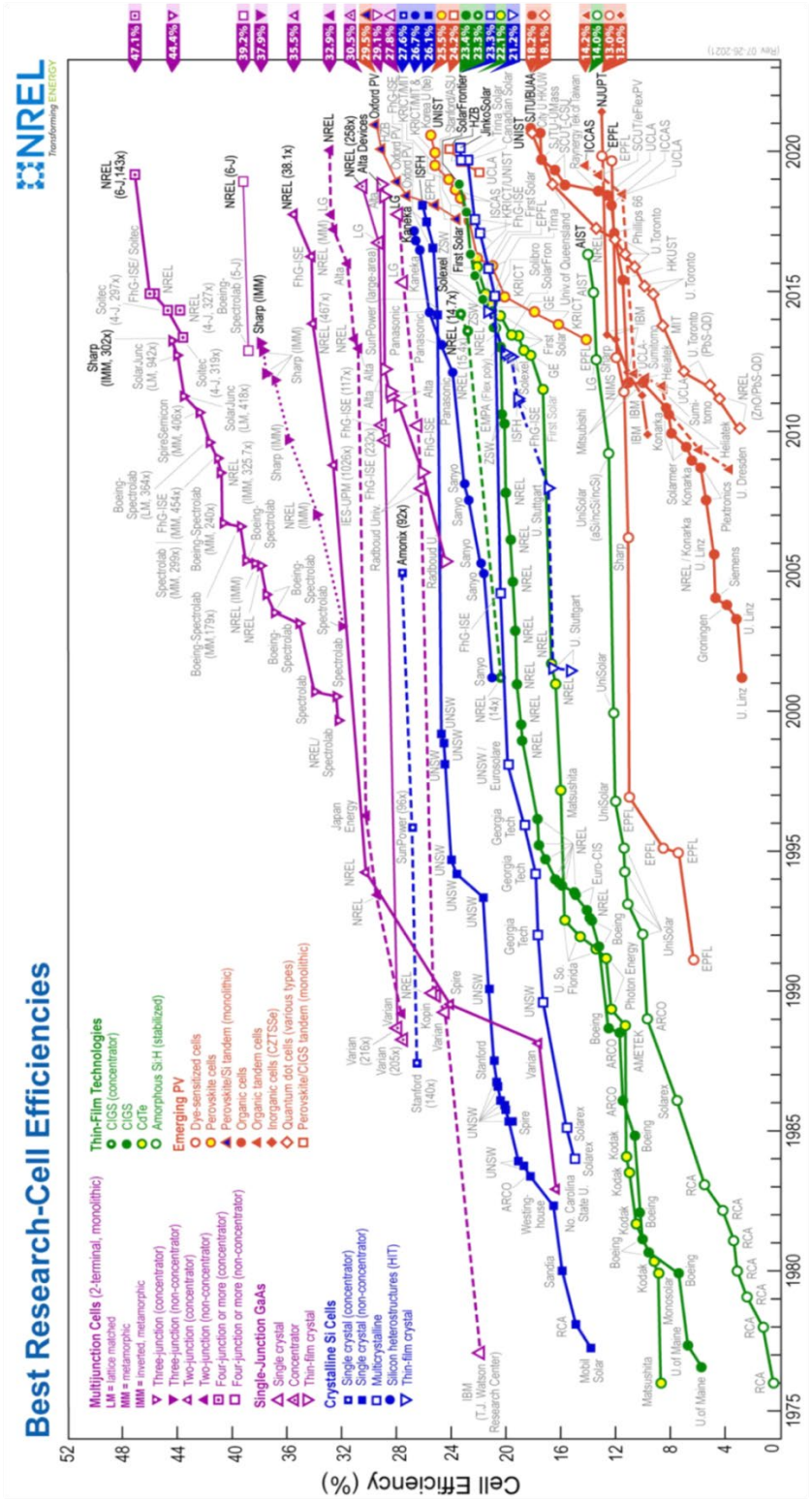

Figure 1.2: Record solar cell power conversion efficiences, certified by the National Renewable Energy Laboratory (NREL)

Organic-inorganic lead halide perovskite solar cells demonstrate impressive photovoltaic conversion performance due to their nearly ideal photovoltaic properties. The band gap of perovskite can be adjusted by

changing the chemical composition and stoichiometry of perovskite crystals. By changing the ratios of methylammonium (MA or CH_3NH_3), formamidinium (FA or $CH(NH_2)_2$), iodine (I), bromide (Br), and chloride (Cl) in the composition of perovskite crystals, different band gaps of perovskite crystals were produced. MAPI($CH_3NH_3PbI_3$), a typical organic-inorganic lead halide perovskite material, with a band gap of 1.57 eV[11]. Because of its high extinction coefficient and suitable bandgap, these perovskite materials need only 400 nm to absorb all photons in the UV-NIR range and make the perovskite a high light-absorbing material[12]. The common apex structure of perovskite results in a larger unit cell volume than the common edge and coplanar structures, allowing the filling of large-sized ions. Even if a large number of crystal defects are generated, or the composition and geometry of the ion components are different, the structure is still stable, which facilitates the diffusion and migration of the defects. This special structure makes the diffusion length of carriers longer than 1 μm[13].

Despite the advantages of perovskite absorbers described above, any discussion of perovskite-based photovoltaics' commercial viability must address one issue: perovskite stability. Some people are curious as to how long the claimed high-efficiency perovskite solar cells will function reliably. This suspicion is not unreasonable since perovskite solar cells need to be exposed to sunlight to work. Indeed the active layer and charge transport layers of perovskite solar cells, exposed to sunshine, are sensitive to UV damage, especially when organic charge transport layers are employed[14]. Perovskite crystals are also extremely sensitive to water. Water normally causes irreversible decomposition of perovskite crystals, resulting in the inability of the solar cell to efficiently generate photocurrent in the presence of water[15]. In addition, the tetragonal-cubic phase transition of methylammonium lead iodide perovskite crystal phase transition temperature occurred at 330K. The change of crystal structure due to the increase of temperature will affect the optical and electrical properties of perovskite crystals, further affecting the performance of PSCs[16,17]. As the study of perovskite progressed, more stable cationic FA, and the mixing of organic-inorganic cations with I,Br,Cl gradually improved the stability of perovskite. The use of new UV-insensitive inorganic carrier transport layers such as SnO_2, NiO has also become a hot topic.

Thesis Motivation

The photovoltaic conversion efficiency and stability of perovskite solar cells need to be guaranteed before they can be commercialized. Furthermore, raw materials and processes should be inexpensive and suitable for high-volume manufacturing. As a result, this thesis focuses on these requirements and is dedicated to improving the photovoltaic conversion efficiency and stability of perovskite solar cells as much as possible. Furthermore, in order to reduce the cost of raw materials, we have turned our attention to an inorganic stable

material for use as the hole-transport layer: NiO. We developed solar cell manufacturing recipes for various device architectures based on previous research to produce reference devices with high conversion efficiency. Then we created a simple passivation material to modify the interfaces and successfully improve the efficiency and stability of perovskite solar cells. After that, we looked into a new method of preparing the charge transport layer, Electrostatic Spray Deposition (ESD). Because this method is simple and repeatable, it has a wide range of applications. Finally, in order to adapt to potential large-scale industrial production, we developed NiO nanoparticles that are suitable for low-temperature processing and can be used in a simpler and less expensive manner.

Thesis Overview

Chapter 1 briefly introduces the background and status of current photovoltaic research, and clarifies the purpose of this work. Then the basic principles of photovoltaics are introduced in detail. The characteristics of organic and inorganic lead halide perovskite materials and charge transport materials that constitute perovskite solar cells are also discussed. As the background of the subsequent chapters, this chapter briefly introduces the structure, stability and hysteresis problems of perovskite solar cells.

Chapter 2 introduces the new thin film deposition technology (under the background of manufacturing perovskite solar cells) and the characterization technology applied to perovskite active materials and charge transport layers. The work in the remaining chapters mainly relies on the J-V scanning of perovskite solar cells, which will be described in Chapter 1. The combined use of J-V scanning and microscope, and spectroscopy provides guidance for optimizing perovskite solar cells.

Chapter 3 discusses the use of composition optimization engineering to introduce excess PbI_2 and MACl (to be presented in Chapter 1) in the perovskite precursors to maximize the performance of perovskite solar cells. Subsequently, we developed a simple hole transport layer passivation material to fix the contact problem at the interface and to increase the crystallinity of the perovskite crystals. The introduction of passivation layer not only improved the FF of the solar cell to a great extent, but also effectively improved the stability of the perovskite solar cell under humid atmosphere.

Chapter 4, a novel thin film deposition method, Electrostatic Spray Deposition (ESD), is presented to prepare charge transport layers. This method brings better surface morphology and denser Cu:NiO films than the conventional spin-coating method. By varying the parameters such as temperature and deposition time, we obtained uniform dense Cu:NiO thin films. The application of this film to perovskite solar cells can effectively

improve the performance of solar cells with favorable FF. In addition, this approach allows the use of different ions for the doping of NiO, such as Li.

Chapter 5 describes a method for the synthesis of NiO nanoparticles. The preparation of the hole transport layer in Chapter 3 and 4 requires high temperature processing, which can limit the application of this NiO hole transport layer. In this chapter, ultra-small NiO nanoparticles are synthesized by trying different synthetic routes. The size of the nanoparticles is well controlled and has an excellent particle size distribution. The NiO nanoparticles show potential for application in all-inorganic charge transport layer perovskite solar cell devices.

1.1. The photovoltaic effect

Before going into the details of the structural and electronic properties of metal halides perovskites, we first recall some basic knowledge about photovoltaics. Photovoltaics (PV) is the field of science dealing with solar cells. These devices are capable of directly converting light into electricity, as was first demonstrated by Edmond Becquerel in 1839. The photovoltaic effect is the generation of photogenerated electric potential and photogenerated current by a semiconductor under light conditions. It is necessary to establish certain basic physics concepts to comprehend the photovoltaic effect, some of which will be discussed in this section.

The photovoltaic effect is a physical effect in which electrons are emitted when a light beam strikes a semiconductor. The emitted electrons are called "photoelectrons". In the photovoltaic effect, photoelectron emission occurs only when a photon with energy (Eg=hv) greater than the work function of object is irradiated on the object. Unlike conductors, which have free electrons, or insulators, which have very few free electrons, the outermost electrons of a semiconductor are not as easily bound by the nucleus as in the case of conductors, nor are they as tightly bound by the nucleus as in the case of insulators, so the conductive properties of semiconductors lie somewhere in between.

According to the solid energy band theory, the Pauli exclusion principle dictates that when two identical atoms unite to create a diatomic molecule, each atomic orbital divides into two molecular orbitals with differing energies, allowing the electrons in the original atomic orbital to inhabit the new orbital structure. When a large number of identical atoms are gathered into a solid, the atomic orbitals overlap each other and the energy levels with similar energies are considered as a continuum, i.e. energy bands. Electrons first occupy energy bands of low energy and gradually occupy energy bands of higher energy levels. Depending on the electron filling, the energy bands are divided into conduction bands (CB) and valence bands (VB). Energy gap between CB and VB is called the forbidden band (bang gap having the energy Eg). In the forbidden band, there are no

electrons allowed to exist. The forbidden band separates the conduction band from the valence band. For a semiconductor, most of its electrons are in the valence band and cannot move freely. However, under the action of external factors such as heat and light, a small number of electrons in the valence band can cross the forbidden band and leap to the conduction band to become carriers. Electrons can be excited into or above the CB by incident photons with energy equal to or greater than Eg. Excess thermal energy exists in electrons excited above the CB, which can be used to relax back down to the CB edge by thermalization[18]. The conduction band and valence band are used to describe inorganic semiconductors, in which the band structure is composed of the interacting orbitals of the atoms forming the inorganic semiconductor crystal[19]. In the case of organic semiconductors, the energy bands are determined by the order in which the electrons are arranged as the atoms combine to form molecules, where the highest occupied molecular orbital (HOMO) and the lowest unoccupied molecular orbital (LUMO) levels are similar to the valence and conduction bands of inorganic substances[20], respectively, as shown in Figure 1.3.

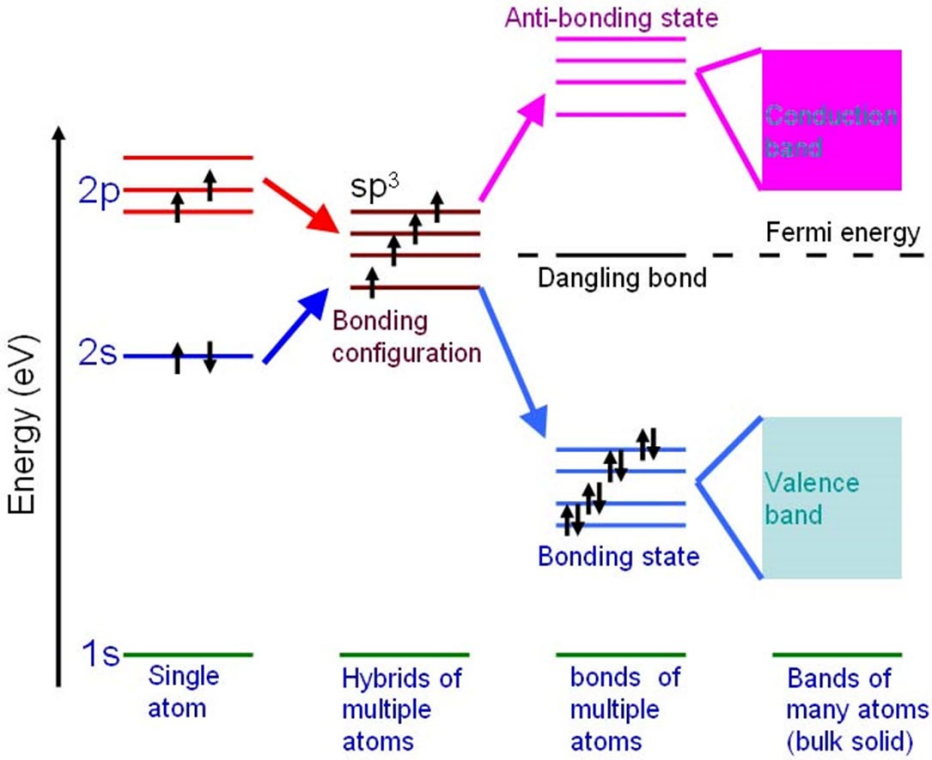

Figure 1.3 A) Relative s and p states of a four-valent atom. B) During covalent bonding between these atoms, relative amounts of p and s bonding and antibonding. C) In a crystalline material made up of numerous atoms, the formation of conduction and valence bands. D) A photon excites a valence electron to the conduction band, where E > Eg. Adapted from Ref 21[21].

The Fermi energy level is defined as the highest energy level in the energy band of a solid filled with electrons at a temperature of absolute zero. Commonly expressed as E_F. The physical meaning of the Fermi energy level is that the probability that a state on that energy level is occupied by an electron is 1/2. In semiconductor

physics, the Fermi energy level is a very important physical parameter, and once its value is known, the statistical distribution of electrons on each quantum state at a certain temperature is completely determined. It is related to the temperature, the type of conductivity of the semiconductor material, the content of impurities and the selection of the energy zero point. n-type semiconductor (being beneficial for giving electrons) Fermi energy level is close to the conduction band edge. P-type semiconductor (being favorable for receiving electrons) Fermi energy level is close to the valence band edge.

When p-type and n-type semiconductors are in contact with each other, the Fermi energy levels of the two semiconductors align because of thermal equilibrium effects. Because of the concentration difference, free electrons (from the n-side) and holes (from the p-side) start to diffuse into the p and n regions, respectively. The recombination of free charges occurs at the interface. As this process continues, a region of intrinsic carrier depletion called the depletion region is formed. Any free charge moving towards the depletion region will experience a positive charge (due to the presence of the donor levels) in the n region and a negative charge (due to the presence of the acceptor levels) in the p type region. The free charges are then driven away from the junction; the depletion zone is then kept free of charge. The change in energy across the junction is qV_{bi} (V_{bi}=built-in potential), which represents an energy barrier to further charge transport, under equilibrium conditions. The Fermi level across the junction is constant to allow the valence band and conduction band to be continuous. With the application of a forward bias ($V> 0$), the energy barrier height decreases, as well as the electric field. A net current is produced because the drift current will not be sufficient anymore to cancel out all the diffusion current. The net current flow results from a net majority carrier diffusion current. With the application of a reverse bias ($V<0$), the energy barrier height increases, as well as the electric field. The increase in energy barrier will cause drift current to effectively oppose the diffusion current. However, there will be a remaining current due to thermally generated minority carriers. The net current flow will be dominated by thermally generated minority carrier drift current.

In all cases the photoexcitation process can be described as an electron absorbing the excitation light energy is excited across the band gap and leaves a hole behind. The electron-hole pair is called an exciton. The excitons either diffuse in any directions in the material and eventually separate into free electrons and holes or they recombine[22]. If the diffusion takes place toward the junction, then the charges will experience the electric field at the depletion region. Separation of charges (holes will be accelerated toward the p-type semiconductor and electrons toward the n-type semiconductor) will occur because they will be swept across the built-in electric field, through the junction. When the free electrons and holes are collected at appropriate electrodes, a photogenerated current and a photogenerated electric potential are generated. As a result, whether the photoelectric process can create a photovoltaic potential and photocurrent is determined by the effective

separation of the electron-hole pair upon photoexcitation of the active layer and by the transport of the charge carriers to the electrodes. Two processes will impact the free charge: charge diffusion and charge drift. The photoelectric phenomenon and PV p-n junction is depicted schematically in Figure 1.4.

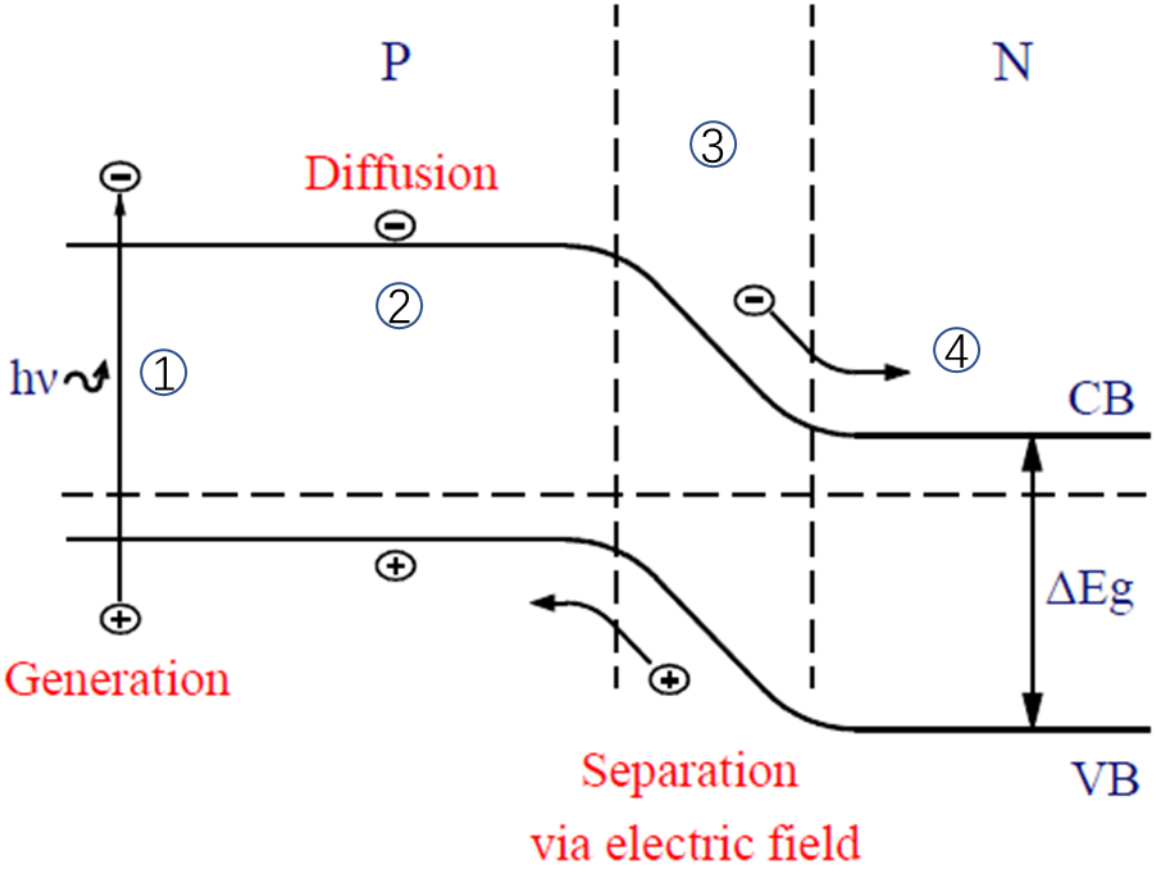

Figure 1.4: A schematic image of a PV p-n junction and photovoltaic phenomenon, in which 1) photons with hv≥ Eg are absorbed and an electron-hole pair is formed (the electron is promoted to the conduction band); 2-3) If the pair is formed near the junction, the electron and the hole will experience a strong electric field and be separated; otherwise, the exciton will reach the junction by diffusion and then be swept through the electric field, electrons move towards the n-type region and holes to the p-type region; 4) charge carriers collected by the electrode and current generation.

We barely scratched the surface of the photovoltaic effect here. It is worth noting that in perovskite solar cells, the p-i-n or n-i-p model is commonly used (discussed later), where a thick undoped intrinsic semiconductor (perovskite) exists between the p-type semiconductor and the n-type semiconductor as a large depletion region, forming a 'sandwich structure'. In a perovskite solar cell, the perovskite layer acts as the light absorbing layer and absorbs photons to excite electrons in the valence band. Charge separation occurs spontaneously due to the very low exciton binding energy. Perovskites are ambipolar and exhibit good mobilities for both electrons and holes. Therefore, a large number of free carriers are generated in the perovskite layer under light conditions,

and the efficient extraction of carriers is highly dependent on the selection of the charge transport layer.

Under light conditions (E>Eg), the populations of electrons in the conduction band and valence band are altered. Since the complex rate (the rate of equilibrium between bands) tends to be much slower than the energy relaxation rate within each band, the conduction band and valence band can each have individual populations in internal equilibrium, even if these bands are not in equilibrium for electron exchange. The shifts in equilibrium make the carrier population no longer describable in terms of individual Fermi energy levels, but can be described using the concept of individual quasi-Fermi energy levels for each band.

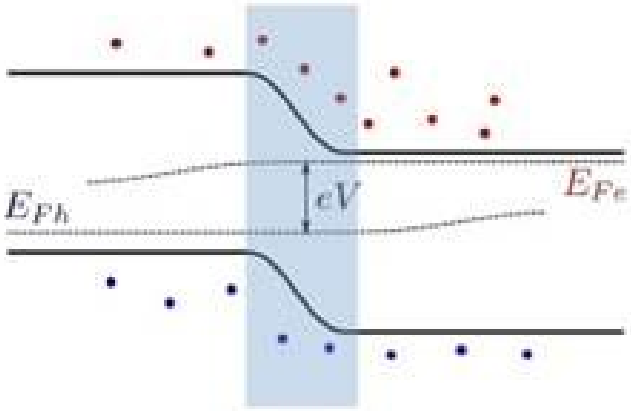

Figure 1.5: Energy-band diagram of a p-n junction including quasi-Fermi levels. Adapted from Ref 23.

The quasi-Fermi levels $E_{F,e}$ and $E_{F,h}$ indicate the density of free photogenerated electrons (holes) in the conduction (valence) band. The quasi-Fermi level splitting (QFLS) is the difference between $E_{F,e}$ and $E_{F,h}$, as shown in Figure 1.5.

1.2. Characterization of Solar Cells

1.2.1. Solar Irradiance Spectrum

The band gap of a semiconductor is the key to absorbing light, and only a few semiconductors with the proper band gap have the potential for PV applications. Atmospheric mass (air mass, often abbreviated AM) is used to describe the extent to which the atmosphere affects the reception of sunlight at the Earth's surface. The sun can be regarded as a black body with 5800K, so the spectrum outside the atmosphere is referred to as "AM0", meaning "zero atmospheres". Because of the effect of the atmosphere, the solar irradiance at the Earth's surface is not uniform. A sun zenith angle of z = 48.2° corresponds to "AM1.5," 1.5 atmospheric thicknesses. Despite the fact that the AM number at midday in the summer is less than 1.5 at mid-latitudes, greater values are utilized in the morning and evening, as well as during other times of the year. As a result, at mid-latitudes,

AM1.5 can be used to represent the total yearly average. Figure 1.5 shows Solar irradiance spectrum above the atmosphere and at the surface. The AM1.5 global is the best estimate of the spectrum of light that flat solar cells will receive while they are in operation. Suns are the units of measurement for the standard intensity of sunlight on a solar cell, with 1 sun equaling 1000 Wm^{-2} of AM1.5 illumination[24].

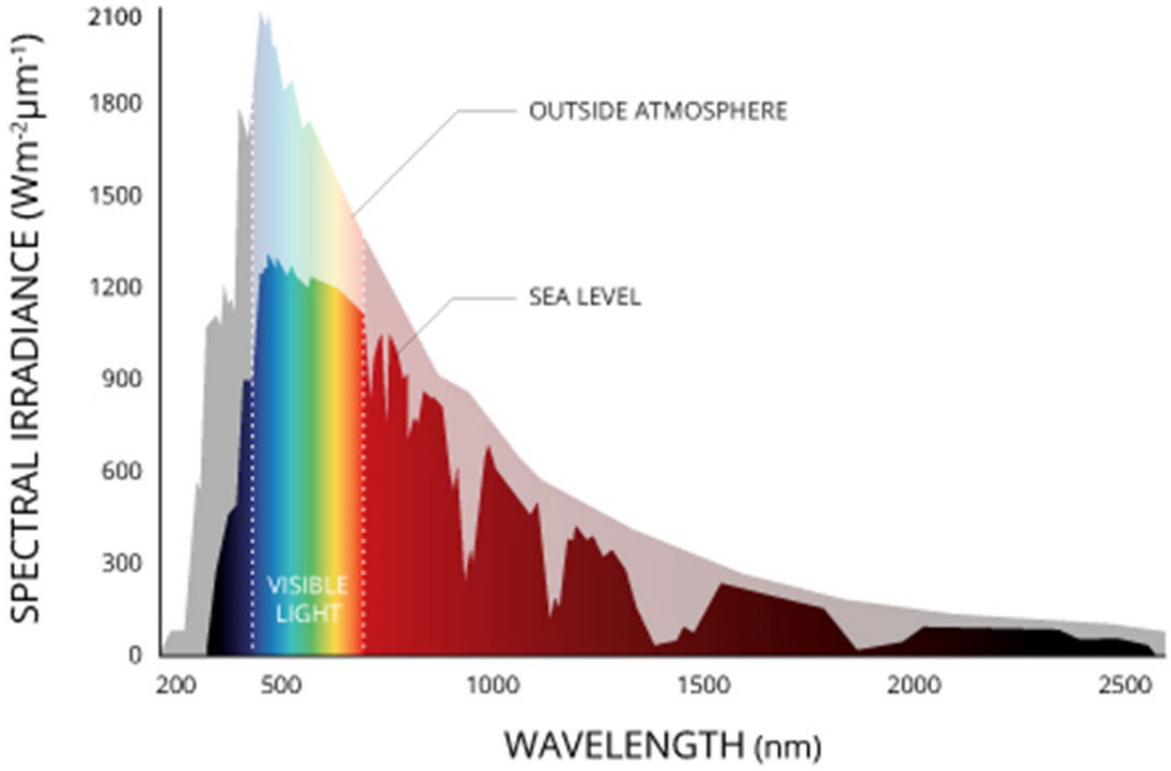

Figure 1.6: Solar irradiance spectrum above the atmosphere and at the surface. AM0 is the spectral irradiance received outside the Earth's atmosphere and AM1.5 is defined as light irradiating at a zenith angle of 48.2° and passing through 1.5 atmosphere thickness on the Earth's surface at mid-latitudes. This model, which represents the Earth as a plane with a horizontally inclined steradian field of view, is used in most flat solar cells.

The lower the band gap in the AM1.5 spectrum, the more photons the semiconductor can absorb, whereas a semiconductor with a large band gap can only absorb some of the shorter wavelengths i.e., higher energy photons. A band gap that is too narrow, on the other hand, is also unsuitable. Because photons with energies above the band gap do not excite more free electrons, they instead excite the same number of electrons to higher energy levels. The extra energy is lost as heat as electrons at higher energy levels thermalize back to the edge of the conduction band. The PCE of a solar cell is determined by a balance between photon energy loss as heat and absorbing as much spectrum irradiance as possible. The maximum theoretical efficiency of this solar cell, is known as the Shockley-Queisser limit, assuming that a single p-n junction is used to collect

power from the cell and that the only loss mechanism is radiative recombination in the solar cell. Figure 1.7 shows the bandgap versus theoretical PCE. It can be calculated that for a semiconductor with an ideal band gap value of 1.34 eV, the maximum efficiency is close to 33.7%.[25] Perovskite cells have an efficiency limit of around 31% (without the angular restriction), which is similar to the Shockley-Queisser limit achieved by gallium arsenide (GaAs) cells (33%). Furthermore, by combining a wavelength-dependent angular-restriction design with a textured light-trapping structure, the Shockley-Queisser limit could be attained using a 200 nm-thick perovskite solar cell[26].

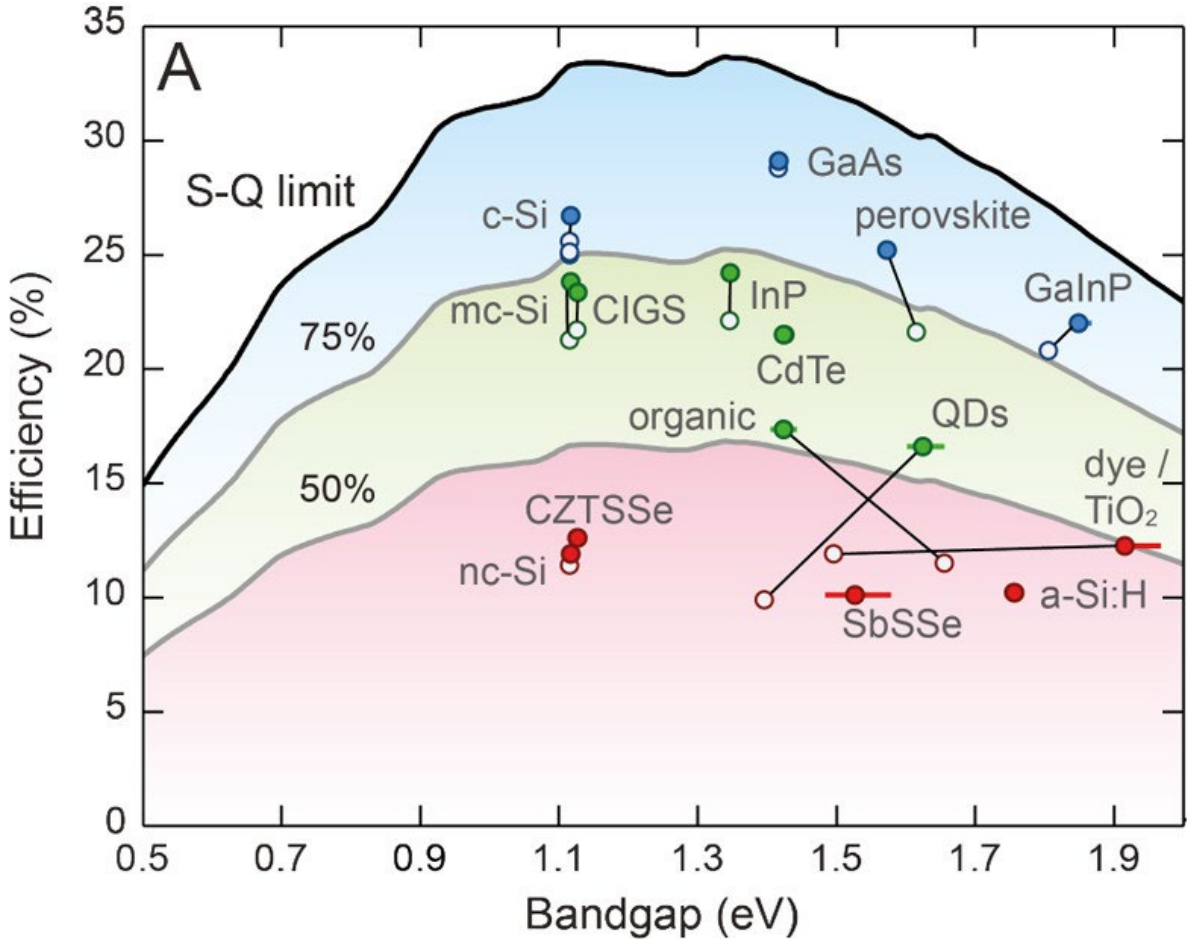

Figure 1.7 Record efficiency of solar cells of different materials against their bandgap, in comparison to the SQ limit (top solid line). Adapted from Ref 27.

1.2.2. Equivalent Circuit Model

The Shockley ideal photodiode equation describes the characteristics of a basic PV device (Equation 2). The photocurrent produced by the absorbing layer is I_{ph}, the diode current (also known as dark diode current) is I_D, and I_0 is the reverse saturation current of the diode. k_B is the Boltzmann constant and T is the temperature (in Kelvin). The diode current (which opposes the photocurrent) grows exponentially as the applied voltage (V)

rises.

$$I(V) = I_{ph} - I_D = I_{ph} - I_0\left(e^{\frac{qV}{k_BT}} - 1\right) \qquad Eq(2)$$

However, the actual situation goes on to consider the loss of solar cells and the non-ideal diode case, and the model is transformed into Equation 3. Rs is Series resistance, including semiconductor resistance, contact resistance, metallization resistance. Rsh is the Shunt resistance (in parallel) describing the imperfections in the production process. k_B is the Boltzmann constant and T is the temperature (in Kelvin). The ideal factor n is mainly used to measure the type of compounding that occurs in a solar cell. In an ideal diode with n=1, all compounding must take place beyond the photosensitive absorber layer's depletion zone. For absorbers with charge recombination or diodes with large energy barriers, the ideal factor can reach n = 2.

$$I(V) = I_{ph} - I_0\left(e^{\frac{q(V+I\times R_S)}{nk_BT}} - 1\right) - \frac{V + I \times R_s}{R_{sh}} \qquad Eq(3)$$

The major solar cell parameters that contribute to solar cell power conversion efficiency (PCE) are discussed in the following section.

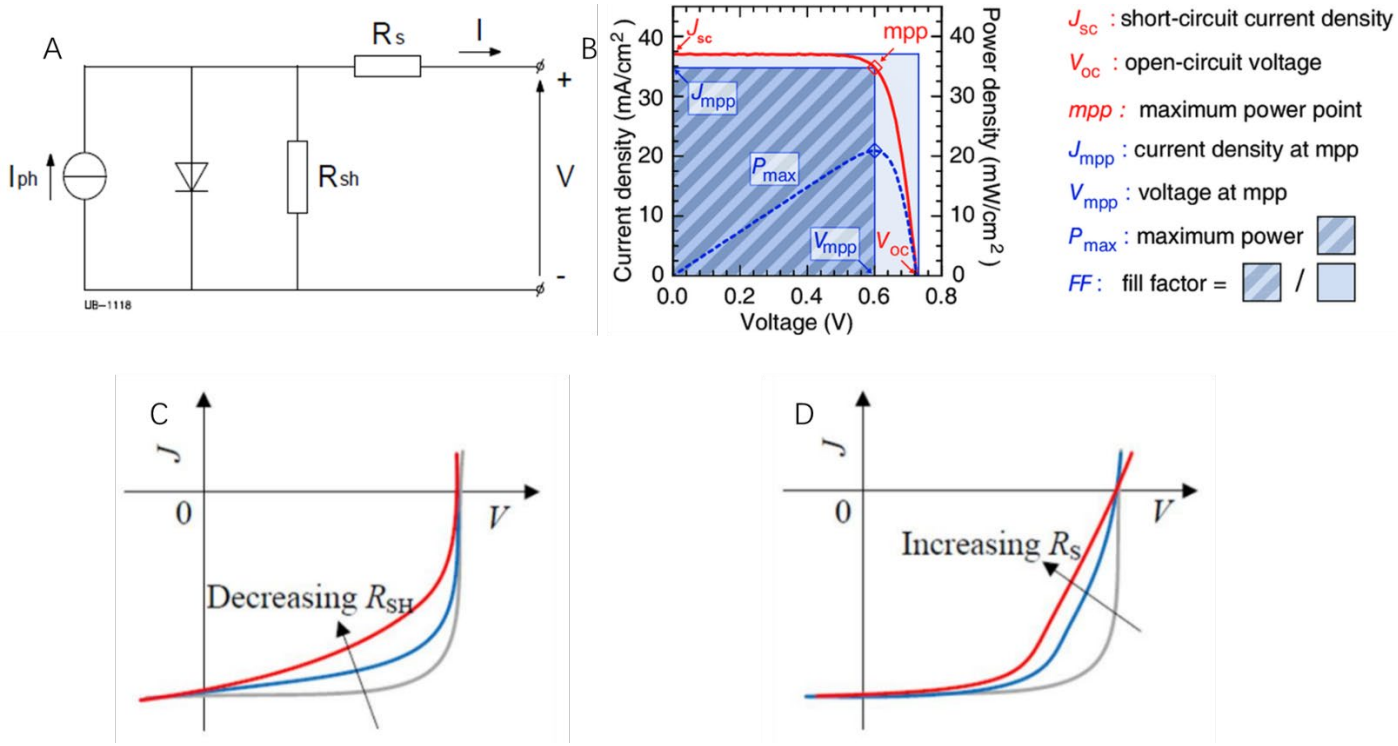

Figure 1.8 A) Solar cell diode circuit generating photovoltage V with I_{ph} photocurrent density, R_{sh} shunt resistance, and R_s series resistance; B) J-V characteristic curve of a solar cell. Adapted from Ref 28[28]; C-D) R_{sh} effects and R_s effects on the J-V curve performance. Adapted from Ref 29[29].

Current-voltage scan results are an important indicator used to judge the performance of solar cells. A solar cell with a known active area is connected to the test equipment and the current output is recorded at different bias voltages. Figure 1.8B shows a typical J-V characteristic curve of a solar cell. The key metrics are

discussed in detail later.

For perovskite solar cells, an illumination mask to accurately measure the effective area of the solar cell is required. Another point of interest is the scan speed as well as the scan direction. The history of the solar cell, including the illumination and bias voltage, is crucial for characterizing the performance of a perovskite solar cell. This is known as the hysteresis effect. This means that the forward and backward sweep of the solar cell may not give the same results. The hysteresis phenomenon is one of the most important indicators for judging perovskite solar cells, which will discussed in detail later.

Several significant evaluations of checklists for accurate and dependable solar cell testing have been conducted in PV research. Authors are now required to submit a checklist form with their submissions to the Nature family journals[30]. The following is an explanation of these criteria[31–34].

• To provide simulated AM1.5 lighting, the right filters and diffusion optics should be employed. It should be indicated if light emitting diodes are utilized or if there is a substantial spectrum mismatch.

• Illumination sources should be calibrated regularly, and spectral mismatches in calibration reference cells should be reported. The source optics should be adjusted and cleaned regularly.

• Always utilize and declare an illumination mask with a defined region.

• If more than one active region is lit on a single substrate, the device must be checked for cross-talk between those areas to ensure that photocurrent is not generated by more than one active area.

• Divergent and diffuse light should be avoided as much as possible since light can be dispersed in via the borders of gadgets. This should be minimized in both the device layout and the testing configuration.

• Current-voltage sweeps should be constant across devices being compared, conducted at varied scan speeds (where possible), and cycled many times to evaluate the influence of repeated sweeps.

• Any preconditioning based on voltage or light and storage must be stated, as well as the speeds and directions of the sweeps. PSCs have been shown to improve when stored or exposed to light.

• A stable current and power output measurement or a maximum power tracking measurement are required for confirmed PCE and *Jsc*.

• When possible, double-check the *Jsc* using integrated internal or external quantum efficiency measurements.

Short Circuit Current density (*Jsc*)

For perovskite solar cells, it is crucial to specify the area of the active region. Therefore, the current density, i.e., the current divided by the active area, is used to judge the performance of a perovskite solar cell.

When the solar cell is placed under the illumination of a standard light source and the output of the solar cell

module is short-circuited, the current flowing through both ends of the solar cell is the short-circuit current of the cell module. The short-circuit current is equal to the photogenerated current. It is proportional to the number of photons absorbed by the active layer. Once the narrower the band gap of the semiconductor, the more photons absorbed, the larger the photocurrent obtained.

In the process of photogenerated carrier transport, any unnecessary recombination, carrier transfer in active layer, charge transport layer, etc. will affect the value of *Jsc*. In order to maximize the *Jsc*, the most direct way is to increase the thickness of the active layer to absorb as many photons as possible. For perovskite solar cells, the active layer thickness can reach the micron level because of the remarkable charge mobilities of perovskite. In addition, it has been reported that the photon recycling mechanism in the perovskite layer, which is called long-lived free charge in the perovskite, can recombine with other free charges to re-generate photons to excite the perovskite[35]. This property makes it possible that even a large perovskite layer thickness does not significantly reduce the *Jsc* value. For perovskite solar cells, the size of *Jsc* is mainly influenced by the quality of the perovskite crystal (e.g., grain size and defect density), which is mainly affected by the fabrication process.

Open circuit voltage (*Voc*)

Under the illumination of the light source, the output voltage value of the solar cell is the open circuit voltage when the two ends are open circuit (the positive and negative terminals of the solar cell module are not connected to the load). In a classical single-junction solar cell, when the applied bias voltage is equal to *Voc*, the built-in potential of the device is canceled and the generated photoelectrons cannot be swept out of the active layer.

For perovskite solar cells, the band gap of perovskite mainly affects the *Voc* of the device, but is not the only factor. The choice of the charge transport layer in 'sandwich' perovskite solar cells is also critical. Theoretically, the quasi-Fermi level splitting (QFLS) of perovskite should be aligned with the charge transport layer (as shown in Figure 1.9A). In Shockley-Queisser theory, the QFLS is considered to be equivalent to the *Voc*. In addition, the charge transport layer should be selective for a charge. Take the hole transport layer as an example (HTL). A schematic representation of the recombination process that may lead to *Voc* reduction, as shown in Figure 1.9B, indicates that: 1) electrons can reach the HTL by additional high-energy interfacial states or by the lack of HTL selectivity at some points of the substrate. Thus, electrons on the HTL can recombine with holes in the HTL (2), or they can reach the contacts where they are trying to reach the external circuit (3) with the holes are compounded. Finally, the thickness of these charge transport layers was the focus of attention. These layers must be thick enough to completely cover the substrate for efficient charge selection, but they

should not be so thick as to cause a loss of extraction due to charge recombination in them.

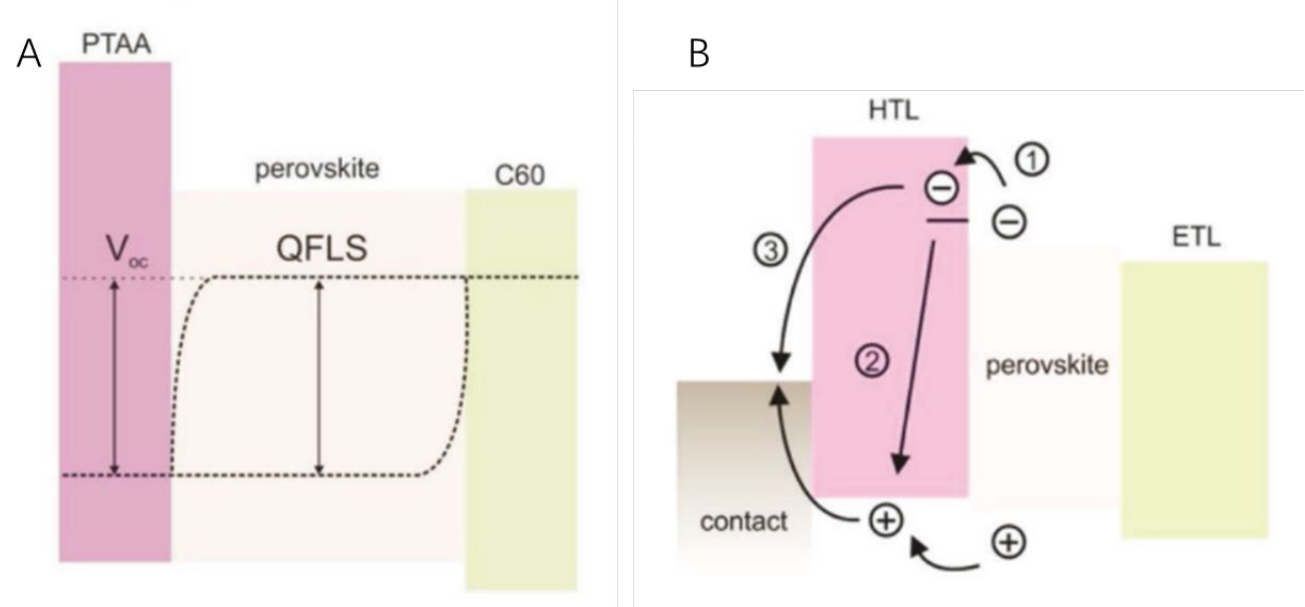

Figure 1.9 A) Schematic diagram of the relationship between QFLS and *Voc* in a perovskite solar cell. The dashed lines indicate the E_{Fe} and E_{Fh} that define the QFLS; B) The recombination process that may lead to Voc reduction. Adapted from Ref 36.

Fill Factor (*FF*)

As illustrated in Figure 1.8B, the fill factor is a percentage. The product of J_{SC} and V_{OC} is represented in one area, while the maximum power point (P_{MPP}), where the product of voltage and current is at its maximum, is represented in the other. Equation 4 shows how to calculate the FF using the symbols for maximum power point voltage (V_{MPP}) and current (J_{MPP}).

$$FF = \frac{V_{MPP} \times J_{MPP}}{V_{oc} \times J_{sc}} \qquad Eq(4)$$

A high FF indicates a good solar cell, and it is a performance parameter that should always be optimized during manufacturing optimization. Low fill factor can be caused by high series resistance, low shunt resistance and high reverse saturation current (discussed later). Physically low shunt resistance is caused by partial shorting the solar cell. High series resistance is because of the transport layer resistances and the metal semiconductor contacts. High reverse saturation current is because of high recombination in the active region. In addition, poor metal-to-semiconductor contact can substantially reduce the fill factor. Good FFs for perovskite solar cell are generally about 80%.

Power Conversion Efficiency (PCE)

The power conversion efficiency of a solar cell is a proportion of the power it can create compared to the

power incident on it. PCE is determined from a power ratio in which the incident light power is P_{IN} and the P_{MPP} is calculated from the product of the V_{MPP} and current J_{MPP}. This is the same as computing the P_{MPP} by multiplying *Voc, Jsc*, and *FF* together, as shown by Equation 5 illustrates.

$$PCE = \frac{P_{MPP}}{P_{IN}} = \frac{V_{oc} \times J_{sc} \times FF}{P_{IN}} \qquad Eq(5)$$

Table 1.1 Demonstrates the highest efficiency solar cell based on different technologies recorded in the laboratory where the perovskite solar cell is based on the n-i-p configuration on SnO_2[37].

	Perovskite solar cell	Crystalline Silicon Heterojunction Solar Cell
Voc (V)	1.194	0.74
Jsc (mA/cm^2)	25.09	41.8
FF (%)	84.7	82.7
PCE (%)	25.4	25.6

Table 1.1 The highest efficiency solar cell based on different technologies recorded in the laboratory. Adapted from Ref 37 and Ref 38.

Series Resistance (R_s)

The series resistance of a solar cell reflects the processes that hinder the transport of photogenerated carriers. These include charge recombination during power generation, and resistance in charge transfer and transport from the solar cell. If the carrier mobility of the active material is low or the active layer is too thick, the carriers have to travel a long way before they are trapped or recombined, and these can cause an increase in the series resistance. In addition, if the interface between the active layer and the carrier transport layer is poor (high defect density), it will also affect the collection of photogenerated carriers. Finally, the poor conductivity of the carrier transport layer will also significantly increase the series resistance. Figure 1.8C shows the effect of increasing series resistance on the JV characteristics of the solar cell. Note that a larger Rs also results in a loss of *Voc*.

Shunt Resistance (R_{sh})

The process of current bypassing the p-n junction structure of a solar cell is represented by the shunt resistance, also known as leakage resistance. The active layer homogeneity is important in perovskite thin film solar cells. Pinholes, for example, can be produced by the roughness of the substrate or during the production process. The impact of lowering shunt resistance on the solar cell's J-V characteristics is seen in Figure 1.8D.

1.3. Perovskite Crystal

Hybrid organic-inorganic metal halide perovskites (metal halide perovskites) represent a class of materials with the stoichiometry ABX_3, whereas A, B and X denote an organic cation with the charge +1, for example, $CH_3NH_3^+$ (methylamine), an inorganic cation with the charge +2, for example, Pb^{2+}, and a halide ion with the charge -1, i.e. I^-, Br^- or Cl^-, respectively. Metal halide perovskites are semiconductors with a wide variety of band gaps that could be modified by changing stoichiometry. States in the BX_6 octahedra that share the X^- - corners with neighboring octahedra in perovskite crystals generate the valence and conduction bands of metal halide perovskites[39], as shown in Figure 1.10. The structure of the perovskite crystal and the charge are balanced by the organic cations. In order to improve the performance of perovskite solar cells, a mixture of various cations and anions is often used. Perovskite mixtures leading to high efficiency devices include $MAPbI_{3-x}Cl_x$[40], $MAPb(I_{1-x}Br_x)_3$[41], $FAPbI_xBr_{3-x}$[42], $FA_{0.2}MA_{0.8}PbI_{3-x}Cl_x$[43], $(FAPbI3)_{0.85}(MAPbBr3)_{0.15}$[44]. Recent high PCE PSCs have used a triple cation composition $CsI_{0.025}((FAPbI_3)_{0.83}(MAPbBr_3)_{0.17})_{0.975}$[45].

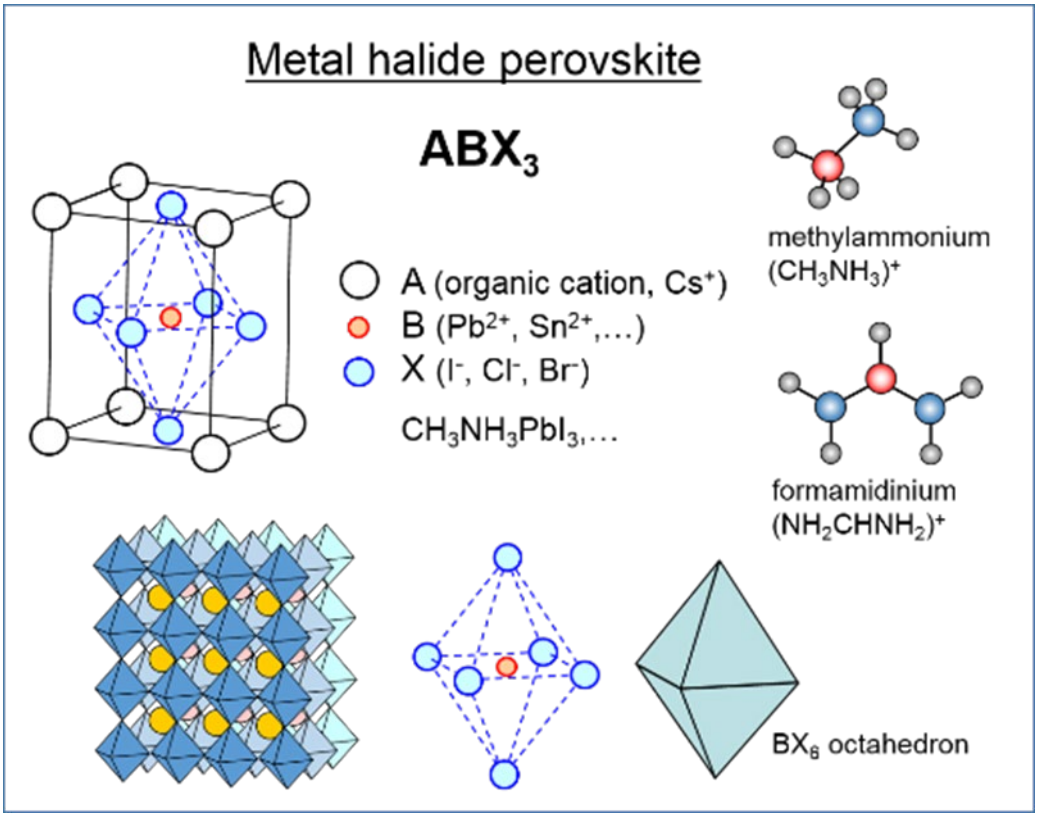

Figure 1.10: The crystal structure of a perovskite phase in a cubic symmetry (α). The positions and chemical structures of common materials for the organic cations A, metal cations B, and halide anions X are shown. BX_6 octahedra share the X^- - corners with neighbored octahedra in perovskite crystals. Adapted from Ref 46[46].

1.3.1. Perovskite crystal structure

The perovskite unit cell can be seen as an organic A cation cage encircling an octahedral structure of halide anions X, with the metal cation B in the center. The extended perovskite crystal structure contains numerous phases with different unit cells. Temperature, pressure, and the composition of the perovskite can influence phase changes. The crystallographic stability and probable structure can be deduced by considering a Goldschmidt tolerance factor t and an octahedral factor μ[47]. Here, t is defined as the ratio of the distance A-X to the distance B-X. In an ideal sphere model, we find:

$$t = \frac{r_A + r_B}{\sqrt{2(r_B + r_X)}} \quad and \quad \mu = \frac{r_B}{r_X}$$

Where r_A, r_B and r_X are the ionic radii of elements A, B and X respectively.

In general, perovskite structures are stable when t is ranging between 0.8 and 1.0 and μ between 0.442 and 0.895[48]. Therefore, any combination of compatible ions can form a perovskite crystal[49]. The organic cation A acts as a charge neutralizer in the ABX_3 network[50]. However, because of its size, it has the potential to cause the entire network to expand or shrink, resulting in changes in the length of the B - X bond. The 3D perovskite structure will be unstable if cation A is too big. The network produced will be too constrained if this cation is too small[51]. The most common divalent heavy metal cation B having an oxidation state (+ II) for photovoltaic applications is Pb^{2+}. It is possible to substitute it with another element of the same group, such as Sn or Ge. The replacement of Pb aroused the interest of researchers to overcome the problem of toxicity. Nevertheless, Pb remains the most stable in the oxidation state (+ II), unlike Sn and Ge, which changes from the oxidation state (+ II) to the oxidation state (+ IV) easily, which justifies that perovskite-based cells containing Pb are the most stable and the best performing. The X^- ion is a halide (Cl^-, Br^- or I^-) and its variation causes a modification of the band gap energy of the perovskite, as explained later. The perovskite in the case of $MAPbI_3$ composition presents an orthorhombic symmetry up to 162 K, and above it turns to tetragonal phase. At ambient temperature, it remains tetragonal, and only becomes a cubic phase state at temperatures exceeding 330 K[52]. It is worth noting that the predicted phase transition from tetragonal to cubic happens within the range of a solar cell expected working temperature (up to 350 K). The use of various cations or cation mixtures, as well as halides or halide blends, results in varied perovskite phase structures around room temperature, as well as variable phase transition temperatures. Each phase has different electrical and optical characteristics[53]. Table 1.2 is a summary table with information on the phases at room temperature, band gaps, conduction band minima (CBM), and valence band minima (VBM) for different perovskite films.

Composition	Bandgap (eV)	Structure at room temperature	Carrier diffusion length(µm)	CBM(eV)	VBM(eV)
$CH_3NH_3PbI_3$	1.5-1.61	Tetragonal	0.4	-3.93	-5.3
$CH_3NH_3PbBr_3$	2.32	Cubic	0.5	-3.36	-5.58
$CH_3NH_3PbCl_3$	3.1	Cubic	…		
$CH_3HN_3PbI_{3-x}Cl_x$	1.55-1.64	Tetragonal	1	-3.75	-5.43
$CH_3HN_3PbI_{3-x}Br_x$	1.5-2.32	Tetragonal/cubic turn x>0.2	…	…	…
$HC(NH_2)_2PbI_3$	1.47	Tetragonal	6.6	-4.2	-5.7
$HC(NH_2)_2PbBr_3$	2.23	Cubic	19	…	…

Table 1.2: Perovskite band gap energies (eV), structure at room temperature, carrier diffusion lengths, and conduction band minima (CBM) and valence band maxima (VBM) are summarized. Iodide (I), bromide (Br), chloride (Cl), methylammonium (MA, CH_3NH_3), and formamidinium (FA, $HC(NH_2)_2$) are some of the typical compounds utilized in the perovskite active layer.

1.3.2. Multi-ion hybrid perovskite

In order to improve the photovoltaic properties of the hybrid perovskites and their stability, the study focused on the partial mixture of the organic cation MA with FA to obtain $MA_{1-x}FA_xPbI3$ type compounds to enhance the carrier diffusion length. The FA cation has a larger ionic radius (2.8 Å) compared to MA, leading to a Goldschmidt tolerance factor t=1.01 for FAPI ($FAPbI_3$). In addition, the carrier diffusion length was increased significantly from 0.4 µm to 6.6 µm[13,54]. However, at room temperature (RT), FAPI is either in the yellow δ-$FAPbI_3$ non-perovskite polymorph phase (non-photoactive) or in the cubic perovskite phase (photoactive). Theoretically, the yellow δ-$FAPbI_3$ non-perovskite polymorph phase can be transformed to photoactive black α-$FAPbI_3$ by annealing at high temperature (>140°C). However, the black phase could degenerate to stable yellow δ-$FAPbI_3$ non-perovskite polymorph phase at room temperature for pure FA[55,56]. It has been shown that the partial substitution of FA by MA stabilizes the photoactive cubic perovskite phase[57]. Also, the substitution of cations reduces the band gap of perovskite to 1.43 eV[58], which is closer to the optimum value specified by the Shockley-Quesser limit (~1.34 eV). Because of the decrease in band gap the absorption coefficient α of $FAPbI_3$ is slightly lower than that of $MAPbI_3$. Therefore, the perovskite layer based on FA is thicker than the perovskite based on MA[59].

In order to improve the crystallinity of $MAFAPbI_3$ mixed perovskite, recent research has focused on adding a small amount of cesium (Cs) to the MA / FA mixture. This cation has an ionic radius of 1.81 Å, which is

considerably smaller than MA (2.70 Å) or FA (2.79 Å), and allows stabilization of the black phase of $FAPbI_3$ and removal of crystallization defects[60,61].

The electronic band structure of perovskite materials is also known to be affected by X halides. The effect of modifying the perovskite composition on phase states is widely studied as a function of mixed halide concentration. Simple words, by substituting bromide and chloride for iodide, the band gap of $MAPbI_3$ may be lowered by 50 and 150 meV, respectively. The introduction of such halides causes the PbI_6 octahedra to shrink, reducing the unit cell size and causing strain in the crystal lattice, which moves the absorption range blue[62].

1.3.3. Trap-assisted recombination

Generally, the trap-assisted recombination in PSCs is very low[63]. However, charge recombination is an important factor affecting device performance. The bandgap is produced between bonding and antibonding orbitals in typical semiconductors like GaAs. Within the bandgap, point defects or dangling bonds manifest as weak bonding or non-bonding states. The bandgap in perovskites is produced by two antibonding orbitals. As a result, defects states will only form shallow traps or will be confined in the conduction or valance band, having little impact on radiative recombination and other optical characteristics, as Figure 1.11 shown[64]. The recombination caused by traps in the band gap is called nonradiative Shockley-Reed-Hall recombination. It has been reported that iodine species produce the majority of intra band gap traps in perovskite photoactive absorbing layers due to their low activation energy[65]. The latest findings show that in perovskite crystals, the accumulated negative iodine vacancies near the grain boundaries are filled with photogenerated carriers to become neutral. These filled defects impede the movement of the vacancies[66]. Therefore, it is beneficial to control the trap concentration by making large crystals with lower grain boundary density. In PSC devices, trap sites are found as long as they are at the interface between the perovskite and the carrier transport layer[66]. If the extraction of carriers for charge transport layers is poor, it will lead to carrier accumulation at the interface. This kind of accumulation is also regarded as the reason for hysteresis in perovskite solar cell. Therefore, the selection of the carrier transport layer and the modification of the interface are crucial. By examining the link between *Voc* and light intensity, we were able to learn more about the device's charge carrier recombination mechanism. If recombination of free electrons and holes in the active layer dominates, the slope of *Voc* against light intensity is often larger than kT/q, and *Voc* is significantly dependent on light intensity, where q is the electronic charge, k is the Boltzmann constant, and T is the Kelvin temperature[67].

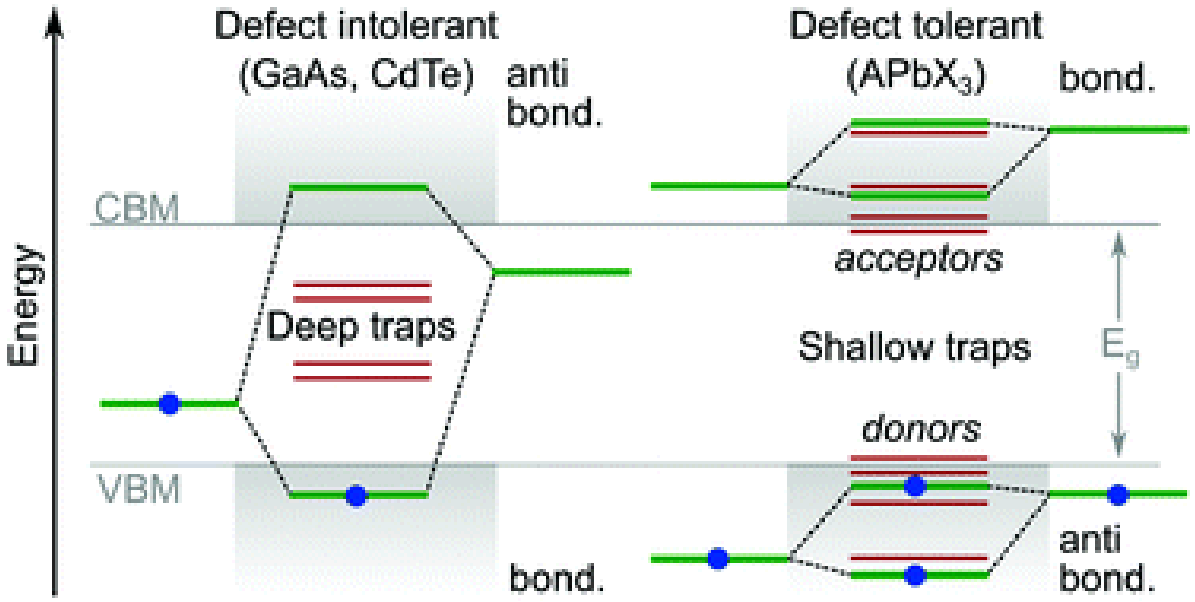

Figure 1.11: Schematic representation of electronic band structure of typical defect-intolerant semiconductors and perovskites. Adapted from Ref 64.

1.4. Perovskite solar cell working principle

1.4.1. Presentation of the different structures of Perovskite solar cells

The first Perovskite-based solar cell, reported by Miyasaka's group, adopted the same structure as dye cells, and used a liquid electrolyte[68]. This liquid electrolyte has since been replaced by the use of a layer of mesoporous metal oxide (TiO_2 and Al_2O_3) as a support for the deposition of Perovskite. This mesoporous configuration, shown in Figure 1.12(a), resulted in the first high yield cells. The morphology of the perovskite in this case is mainly controlled by the underlying mesoporous scaffolding, which makes perovskite deposition easy and reproducible. The main disadvantages of this structure are the low *Voc* and the low light absorption for wavelengths greater than 700 nm[14]. In addition, the deposition of the mesoporous layer generally requires a high temperature annealing process, which is impractical for fabricating large area devices on flexible substrates. Therefore, by optimizing the interfaces and controlling the growth of perovskite, it has been possible to overcome the mesoporous layer while achieving high yields.

Planar structures, inspired by organic photovoltaics, have been developed in which the perovskite is deposited between two semiconductor layers, one of type n called electron transport layer (ETL), and another of type p called hole transport layer (HTL). These planar structures can be classified into two categories: direct n-i-p or inverse p-i-n, depending on which transport layer meets light first. Due to the differences in processing, the

architecture of the devices determines the choice of charge transport (ETL and HTL) and collection (cathode and anode) materials, the corresponding material preparation methods and, therefore, the performance of the solar cells. In this thesis work, we focused on the study of planar architecture of the p-i-n type.

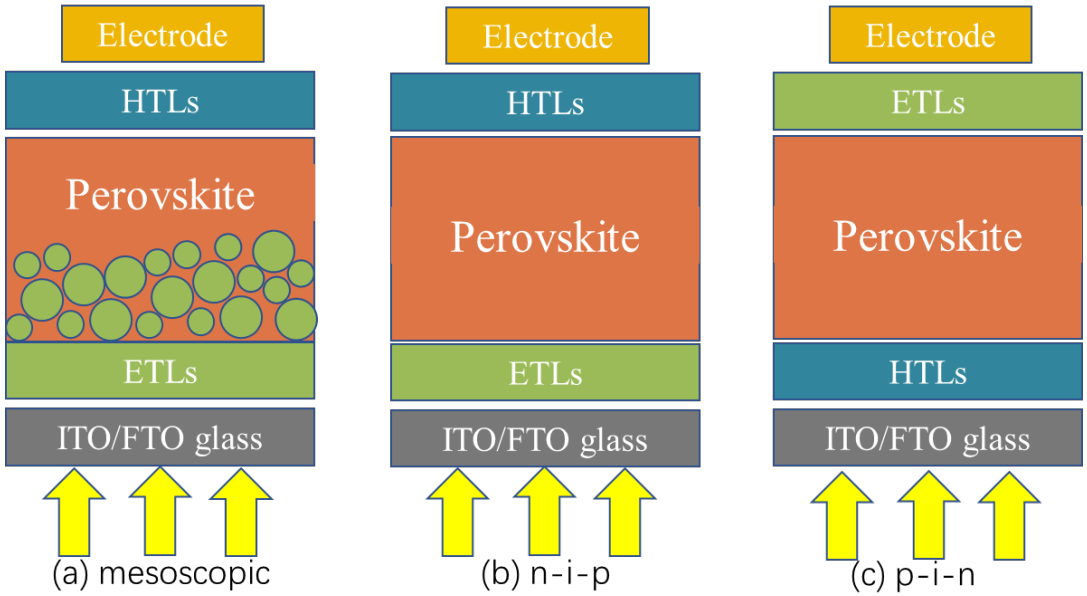

Figure 1.12: Structure of the different architectures of Perovskite solar cells: (a) mesoporous structure, (b) n-i-p planar structure, (c) p-i-n planar structure.

In the p-i-n structure, the P (HTL) layer is deposited first on the glass / ITO (FTO) substrate. The thin layer of perovskite is then deposited on the HTL layer and the device is completed by depositing the N layer (ETL) on top of the perovskite. This layer, generally speaking, is an organic layer, typically the thick [60]PCBM and a metal (Al / Ag) cathode. Recently, the efficiencies of the device having a planar p-i-n architecture have increased significantly through the use of more advanced preparation methods and the development of this structure which has used inorganic layers such as Nickel (NiO) and Zinc (Oxides) ZnO), which made it possible to widen the choice of HTL layers. The selection of the charge transport layer is discussed in the next section.

1.4.2. Charge transport in the perovskite active layer

When a semiconductor is irradiated by a photon, the electron in the valence band of the semiconductor is excited to the conduction band and leaves a hole in the valence band. This electron-hole pair is called an exciton. Excitons can be divided into tightly bound Frenkel excitons and weakly bound Wannier-Mott excitons because of their binding strength. The binding energy of Frenkel excitons is typically 0.1 to 1 eV, while the binding energy of Wannier-Mott excitons is about 10 meV. The exciton binding energy is inversely

proportional to the Coulombic charge shielding within the material, defined as the dielectric constant εr of semiconductor. Temperature plays an important role in the separation of excitons. The higher the temperature, the more likely it is that the excitons will separate.

For lead halide perovskites, most of the excitons produced are weakly bound Wannier-Mott excitons, thus generating a large amount of free charge in the perovskite. It has been reported that the exciton binding energy in MAPI perovskite is only 12 meV[69], which is much smaller than the available thermal energy (26 meV) at room temperature. Table 1.3 lists the exciton binding energy of several perovskites.

2 K, orthorhombic phase

Compound	E_g (meV)	R^* (meV)	μ (m_e)	ε_{eff}	g_{eff}
$FAPbI_3$	1501	14	0.09	9.35	2.3
$MAPbI_{3-x}Cl_x$	1596	14	0.10	9.85	2.3
$MAPbI_3$	1652	16	0.104	9.4	
$FAPbBr_3$	2233	22	0.115	8.42	
$MAPbBr_3$[a]	2292	25	0.117	7.5	

[a] The data for the $MAPbBr_3$ do not show a detectable 2s state and therefore have a significant errors of ±10% for μ and ±20% for R^*.

High temperature tetragonal phase

Compound	E_g (meV)	R^* (meV)	μ (m_e)	ε_{eff}	Temperature (K)
$FAPbI_3$	1521	10	0.095	11.4	140–160
$MAPbI_{3-x}Cl_x$	1600	10	0.105	11.9	190–200
$MAPbI_3$	1608	12	0.104	10.9	155–190
$FAPbBr_3$	2294	24	0.13	8.6	160–170

Table 1.3: The parameters of the fit full Landau fan chart for four different compounds in the low temperature, orthorhombic and the higher temperature, tetragonal phases. Adapted from Ref 70.

It is generally believed that the low exciton binding energy exhibited by MAPI perovskite films at room temperature (tetragonal phase) is due to the dielectric shielding of MA cations. Cationic mixing of perovskite has been found to reduce the exciton binding energy due to MA cations[71,72]. Due to the low exciton binding energy at room temperature, the electron-hole pairs dissociate rapidly and form free charges. For the classical depletion layer model, i.e., the charge needs to be swept out of the active layer by the built-in potential, there is still a debate whether to use perovskite solar cells. Some argue that since charge diffusion is very efficient in perovskite, the built-in potential is not the main reason for carrier transport. This view is that the photogenerated charge depends entirely on the charge transport layer's ability to select the charge. It's probable that the light-generated charge is well protected from the external electric field, given the evidence for a significant number of free ions in perovskites[73]. It has been argued that the built-in electric field at the interface

between the charge transport layer and the perovskite layer significantly affects the carrier extraction[74].

The charge mobility in perovskite is impressive. In the case of MAPI perovskite film, for example, although many reported values fluctuate within an acceptable range, the carrier mobility is about 20-40$cm^2V^{-1}s^{-1}$ [75]. For mixed cation CsFAMA perovskite, the reported carrier mobility is greater than 20 $cm^2V^{-1}s^{-1}$[76]. The diffusion of carriers in this perovskite length is also striking. For MAPI perovskite film, the reported carrier diffusion length exceeds 100 nm[77]. When Cl^- is introduced, the carrier diffusion length increases to a staggering 1000 nm[78]. As previously described, there is a photon recycling mechanism in perovskite. The free carriers in the active layer of perovskite can recombine and release photons to activate the perovskite to generate new free carriers. Eventually the carriers reach the charge transport interface and thus contribute to the enhancement of photocurrent.

The success of organic-inorganic lead halide perovskite solar cells is due to their photovoltaic properties. The high absorption coefficient of perovskite allows efficient absorption of photons, in fact the thickness of the perovskite layer is only a few hundred nanometers. For most perovskites, the carrier diffusion length is greater than the film thickness. With the introduction of FA,Cl, the carrier diffusion length of hybrid perovskite exceeds 1000 nm, which is much larger than the thickness of the perovskite layer. Taken together, the high carrier mobility, amazing carrier lifetime and photon recycling mechanism make perovskite solar cells a candidate to be comparable to crystalline silicon-based solar cells.

1.4.3. Perovskite solar cell Optimization Engineering

Compositional engineering, such as partially replacing I with a tiny halide of Br or Cl, has been discovered to considerably aid the creation of high-quality perovskites. Cl doping, in particular, can alter crystallization dynamics by boosting rapid nucleation and lengthening the crystal growth process, allowing for perovskite development with larger grain sizes and preferred crystal orientation[79]. Because of the insertion of Pb-Br bonds in the lattice, which improved the crystal stability by increasing the binding energy of each unit, the mobility of excess Cl^- was effectively avoided by binary halide (Br/Cl) doping. PVK-BrCl, binary halide-doped perovskites with significantly reduced nonradiative recombination centers, produced a champion PCE in the associated cells, resulting in improved storage stability[79]. Excess PbI_2 has been shown to stay in the perovskite layer, providing a moisture barrier at grain boundaries and interfaces, reducing the density of charge trap states in the immediate region[80,81]. Furthermore, the inclusion of inorganic cations such as Cs aids in the passivation of defect sites (at grain boundaries and interfaces), as well as the slowing of halide migration and phase separation[82]. All experiments conducted in this report used excessive amounts of PbI_2 multi-cation perovskite

CsFAMA. As a result, carefully engineering the perovskite composition is an effective technique to improve the crystal quality of perovskite solar cells, resulting in high efficiency and stability.

1.4.4. Charge transport layer

As mentioned above, the charge carrier mobility in perovskite is impressive. A large amount of free charge in the active layer of perovskite can spread in any direction. The charge transport layer is essential for charge selectivity. For electron transport materials, the CB (inorganic semiconductor) or LUMO (organic semiconductor) should be aligned with the CB of the perovskite to transport as many electrons as possible. Also the VB (inorganic semiconductor) or HOMO (organic semiconductor) of the electron transport material should be as low as possible below the VB of the perovskite to block hole leakage from the electron transport layer. Similarly, the hole transport layer is selected based on the VB or HOMO aligned with the perovskite valence band and the higher CB or LUMO. As a result, the hole transport layer transports photo-generated holes successfully while effectively limiting photo-generated electron leakage. Figure 1.13 shows a schematic diagram of the carrier transport layer energy bands.

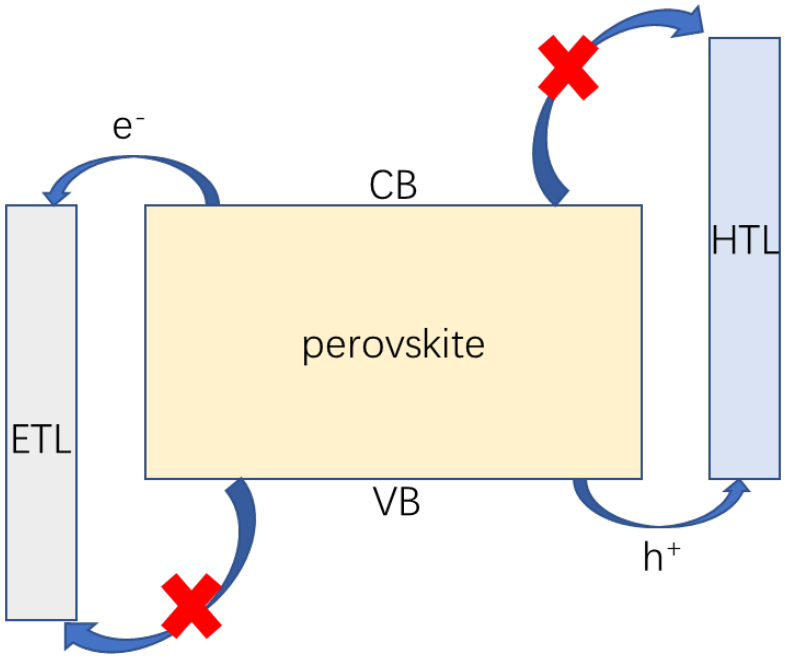

Figure 1.13: Schematic diagram of the carrier transport layer energy bands.

Figure 1.14 lists the common charge transport layers[83]. This thesis focuses on the study of the properties of HTLs, and here we list several essential elements for the selection of HTLs. HTMs should have (i) high hole mobility to decrease losses during hole transport, (ii) compatible valence band maximum with perovskite material, (iii) high moisture and heat stability for long-term operation, and (iv) cheap cost material and processing for PSC devices to work efficiently. Hole mobility of HTLs has a considerable influence on PSC

PCEs. Using HTMs with low hole mobilities causes significant ohmic losses across the HTM, resulting in a poor fill factor[84].

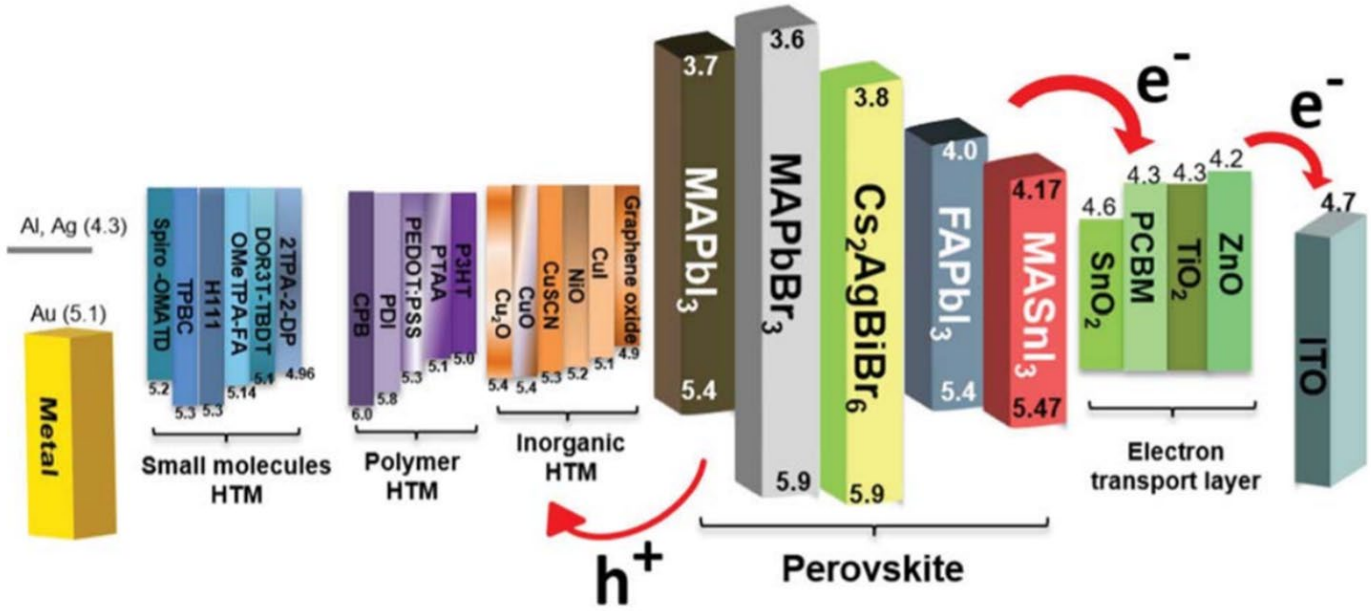

Figure 1.14 List of common charge transport layers. Adopted from Ref 83.

NiOx inorganic hole transport layer

At present, the most common hole transport materials used for p-i-n perovskite solar cell are poly(3,4-ethylenedioxythiophene) polystyrene sulfonate (PEDOT:PSS) and Poly[bis(4-phenyl)(2,4,6-trimethylphenyl)amine] (PTAA) [85–87]. However, electrode corrosion due to the acidity of PEDOT:PSS leads to a decrease in stability. Furthermore, due to the high synthesis costs of these organic polymers, the interest in this kind of hole transporting materials for high-performance PSC is limited. Recently, nickel oxide, a p-type semiconductor, has attracted interest. NiO_x has a suitable bandgap (>3.5eV), and a deep VBM (~5.2eV) [88,89]. These characteristics are beneficial for a suitable band alignment with the perovskite. In addition, the inexpensive and simple preparation process brings NiO_x-based hole transport layer excellent stability and possibility of industrial production. So far, a large number of approaches for fabricating NiO_x layers has been reported, such as solution process,[90] pulsed laser deposition[91] and others. Jen's group first get an efficiency of about 15% with a Cu-doped NiO layer using solution-based method[92]. Soon after, Seok and his group further pushed the efficiency to over 17% with a very high fill factor (FF=0.813) by applying a pulsed laser deposited NiO_x hole transport layer[91]. Li and co-workers developed a new Mg-doped NiO layer with enhanced conductivity and were able to increase efficiency to 18.2% for small area device and 15.3% for 1 cm^2 devices[93].

Nickel oxide, being a well-known metal deficient p-type semiconductor, is likely to produce defects under an

excess oxygen environment, as shown by the equations below[94]:

$$2Ni^{2+} + \frac{1}{2}O_2(g) \rightarrow O^{2-} + V_{Ni}^{0} + 2Ni^{3+}$$

$$V_{Ni}^{0} \rightarrow V_{Ni}' + h^{\cdot}$$

$$V_{Ni}' \rightarrow V_{Ni}'' + h^{\cdot}$$

To maintain charge neutrality in the crystal, Ni^{3+} is created by Ni^{2+}, and the amount of Ni^{3+} is associated with the annealing process, which regulates the oxygen doping concentration. Furthermore, ionized defects (V′ N and V''_{Ni}) linked with hole formation might arise from neutral Ni vacancies (V^{0}_{Ni}) formed in conjunction with Ni^{3+}. It's worth noting that V''_{Ni} is one of the most important flaws that affects the NiO film's electrical performance. It also has the lowest formation energy, making it the most stable defect in the band gap. Under the assumption that oxygen vacancies are minimal in comparison to Ni vacancies, a suggested defect equilibrium may be described as follows when divalent Cu dopants are added into NiO_x.

$$2NiO \xrightarrow{CuO} Cu_{Ni}^{x} + V_{Ni}'' + 2h^{\cdot} + 3O_{O}^{x} + 2Ni_{surface}^{x}$$

This suggests that when the Cu concentration rises, the amount of Ni vacancies rises as well. Monovalent alkali metals, such as lithium (Li^{+}) ion, can also be utilized for doping to boost the electrical conductivity of NiO_x films, in addition to Cu metal ions. Li^{+} (0.76Å) has a comparable ionic radius to Ni^{2+} (0.69Å), therefore it can be doped into the NiO_x lattice easily. Its introduction causes a rise in Ni^{3+} ion concentration and, as a result, a decrease in NiO_x film resistivity. The most intriguing property of monovalent alkali metal doping, in contrast to p-type dopants, is that it can boost conductivity while having no effect on the light-transmitting ability of NiO_x HTLs[94].

1.4.5. Charge transport to the electrode

When the carrier successfully crosses the charge transport layer and before it is collected by the electrode, there are two types of contact because of the energy barrier between the metal electrons and the semiconductor charge transport layer. Because of the energy barrier $E_b = E_c - E_F$; electrons can flow from the semiconductor to the metal, but not from the metal to the semiconductor.

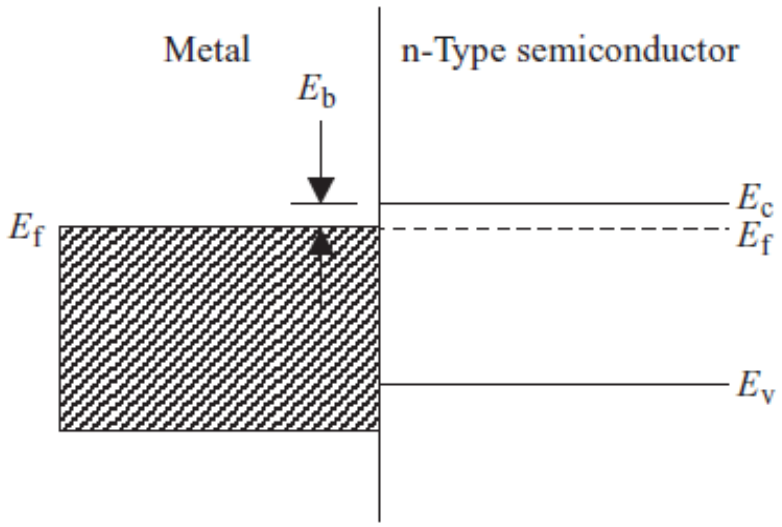

Figure 1.15: Schematic diagram of metal electrode and n-type semiconductor energy band.

Band-bending happens to the charge transport through the junction. The type of bending depends on the kind of charges present at the interface of the junction. In the Figure 1.16 case (a), E_F shifts towards the CB near the interface because the positive charges will attract the electrons present in the CB. E_F "enters" the energy band of the metal, which is called ohmic contact. In this case, the electrons are more easily collected by the electrodes, and minimize voltage losses at junctions present in the solar cell. In the Figure 1.16 case (b), the negative trapped charge will result in a large energy barrier E_b, impeding electrons to flow. This is known as Schottky contact. A typical Schottky barrier occurs between [6,6]-Phenyl C61 butyric acid methyl ester ([60]PCBM) and the metal electrode[94]. This causes a significant performance loss. To avoid the Schottky barrier, LiF for Al and Bathocuproine (BCP) for Ag are usually applied to fix the work function.

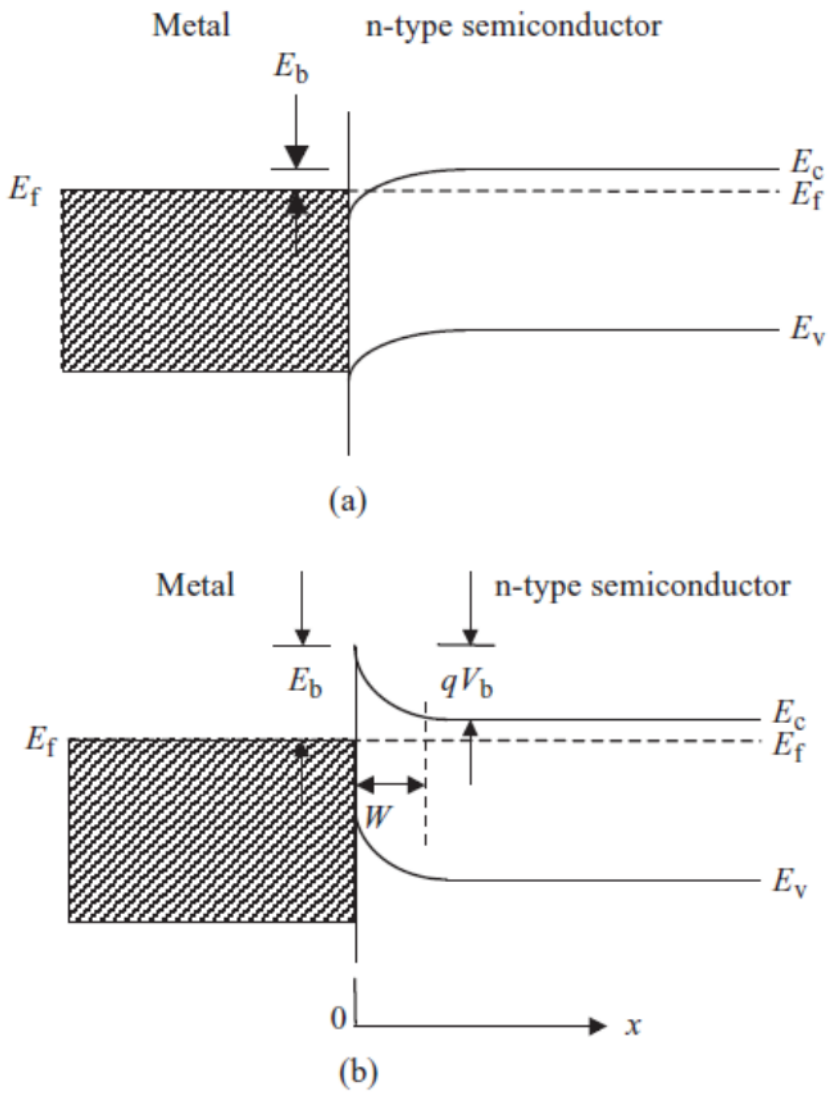

Figure 1.16: Schematic diagram of ohmic contact and Schottky barrier.

1.5. Perovskite solar cell stability

It is difficult to test the long-term stability of solar devices under realistic conditions in a short period. To withstand constant AM1.5 light exposure, a typical PV module (with encapsulation) should strive to keep 80% of its initial PCE after 25 years (including the UV portion of the spectrum). It should be able to endure operating temperatures of up to 350K in the summer, as well as precipitation and water vapor (up to 80% relative humidity). Perovskite devices are notorious for their volatility. Perovskite typically decompose to hydrates or their original components PbX_2 and MAX or FAX (X = I, Cl, Br) under these environments[95,96].

1.5.1. Water induced degradation of perovskites

Water is fatal to unencapsulated perovskite solar cells and causes irreversible decomposition of perovskite.

Liquid water rapidly decomposes the perovskite crystal structure along the grain boundaries and the brownish-black peroviskite layer is visually seen to turn yellow[97]. The degradation routes that $MAPbI_3$ films undergo are as follows:

$$4CH_3NH_3PbI_3 + 8H_2O \rightarrow (CH_3NH_3)_4PbI_6 \cdot 2H_2O + 3(OH)_2 + HI\uparrow$$

$$(CH_3NH_3)_4PbI_6 \cdot 2H_2O \rightarrow (CH_3NH_3)_xPbI_{2+x} + (4-x)CH_3NH_2\uparrow + (4-x)HI + 2H_2O$$

$$2(CH_3NH_3)_xPbI_{2+x} + 2CO_2 + O_2 \rightarrow 2PbCO_3 + 2I_2\uparrow + 2xCH_3NH_2\uparrow + 2xHI\uparrow$$

$$(CH_3NH_3)_xPbI_{2+x} + H_2O + \frac{1}{2}O_2 \rightarrow Pb(OH)_2 + I_2\uparrow + xHI\uparrow + xCH_3NH_2\uparrow$$

$$Pb(OH)_2 \rightarrow PbO + H_2O$$

Figure 1.17: Degradation routes of $MAPbI_3$ induced by water. Adopted from Ref 97.

The above reaction is only possible when a large amount of decomposition products is washed away, for example, by immersing perovskite in water. For encapsulated perovskite solar cells, direct flushing of water is not possible. Perovskite solar cells employ organic cations that are extremely hygroscopic. It has been proposed that water molecules establish weak hydrogen bonds with the cations, compromising the crystal structural stability[98]. A hydrated perovskite phase can emerge as a result of this. This transformation is reversible under anealing[99]. However, it has been suggested that with enough moisture penetration, the perovskite crystal decomposes. Shown below is a chain of reactions that could be responsible for non-reversible degradation in $MAPbI_3$ perovskites.

$$CH_3NH_3PbI_{3\ (S)} + H_2O_{(g)} \rightleftharpoons CH_3NH_3PbI_3.H_2O_{\ (S)}$$

$$4CH_3NH_3PbI_3.H_2O_{\ (s)} \rightleftharpoons (CH_3NH_3)_4PbI_6.2H_2O_{\ (s)} + 3PbI_{2\ (s)} + 2H_2O_{\ (g)}$$

$$(CH_3NH_3)_4PbI_6.2H_2O_{\ (s)} \rightarrow 4CH_3NH_{2\ (g)} + 4HI_{\ (g)} + PbI_{2\ (s)} + 2H_2O_{\ (g)}$$

Then,

$$4CH_3NH_{2\ (g)} + 4HI_{\ (g)} \rightarrow 4\ CH_3NH_3I_{\ (s)}$$

$$4\ CH_3NH_3I_{\ (s)} \xrightarrow{H_2O} 4CH_3NH_3^+{}_{(aq)} + 4I^-{}_{(aq)}$$

Figure 1.18: Chain of reactions from MAPbI perovskites, catalyzed by moisture. Adapted from Ref 100.

This illustrates the conversion of $MAPbI_3$ to an aqueous form of methylammonium lead iodide (MAI) and lead iodide (PbI_2). From this, hydroiodic acid (HI) and methylamine are produced, as shown in Figure 1.18. More water is created in the presence of oxygen. This starts a cyclic process that leads to even more moisture loss. The development of the perovskite active layer can also be influenced by the presence of excess PbI_2. This is to increase the strength of the bonds between the organic component and the metal halides to reduce this impact. It is critical that active layers are deposited in a humidified environment. Hydrophobic interlayers can also be used to shield the perovskite from moisture in the environment.

1.5.2. Temperature induced degradation of perovskites

A PSC is supposed to function at a maximum operating temperature of around 350 K. $MAPbI_3$ crystals are reported to start decomposing in an inert atmosphere and emit I_2 gas at temperatures above 350 K, which coincides with the solar cell operating temperature. Photodecomposition and thermal decomposition in methylammonium halide lead perovskites and inferred design principles to increase photovoltaic device stability[95]. In addition, MAPI crystals are subject to a phase transition at 330 K, changing from a tetragonal to a cubic phase[101]. The introduction of FA was reported to be effective in improving the thermal stability of perovskite crystals[102]. Degradation or discoloration does not occur even when exposed to temperatures up to 420 K for more than 1 h. At temperatures up to 430K, $FAPbI_3$ possesses an excellent tetragonal black phase, although this black phase is vulnerable to humid surroundings. The black phase is no longer stable in a humid atmosphere, and it has been demonstrated to change to a yellow hexagonal structured perovskite. The optimal

FA black phase could well be regained by re-annealing a perovskite film, indicating that this FA phase transition is reversible. This undesirable hexagonal phase has straight PbI_6 chains, a wide optical band gap, and poor charge separation and transfer characteristics[103].

1.6. Hysteresis Effect

The hysteresis is a J-V hysteresis where when measuring the J-V characteristics by scanning the voltage on its terminals, the forward scanning J-V curve is different from the reverse scanning, as shown in Figure 1.19. The voltage scan direction/rate/range, history of voltage conditioning, and device configuration all impact J-V performance.

The new study suggests that the hysteresis effect in perovskite solar cells may be due to the following four mechanisms: (a) slow transient capacitive current; (b) dynamic trapping and detrapping processes of charge carriers; (c) band bending due to ion migration, and (d) band bending due to ferroelectric polarization[104]. The larger interfacial polarization and the corresponding dielectric constant induce an enhanced capacitive effect in the PSC. The slow decay of the capacitive current leads to residual nonstationary photocurrents that lead to increased photoresponse under fast reverse scanning, resulting in J-V hysteresis. Reducing the charge traps at the perovskite grain boundaries and crystal surfaces helps to mitigate the hysteresis effect, suggesting that carrier extraction affects J-V hysteresis. In addition, the free ions in perovskite migrate under the electric field and accumulate at the perovskite/charge transport layer interface, causing band bending. Bind bending affects the steady-state photocurrent and thus changes the J-V characteristics. The slow ion relaxation and redistribution cause the hysteresis in the J-V characteristic.

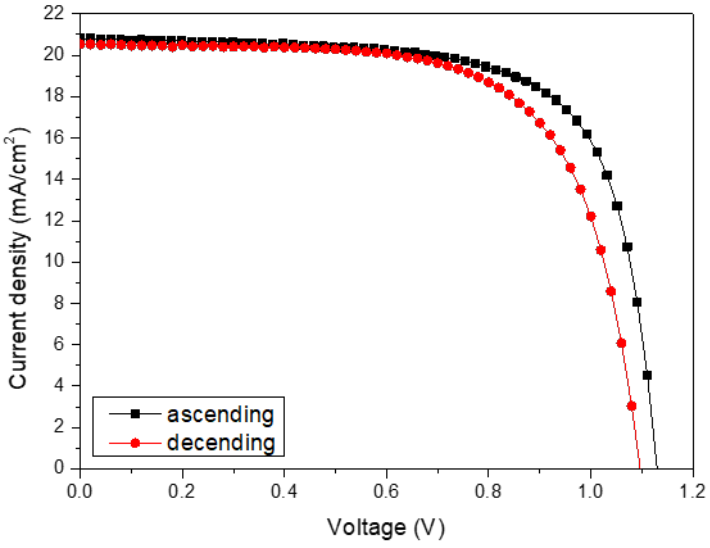

Figure 1.19: Representative J–V curves of reverse and forward scans for a PSC exhibiting hysteresis.

References

1. EIA. Key World Energy Statistics 2020. *Int. Energy Agency* 33, 4649 (2020).
2. Looney, B. Statistical Review of World Energy globally consistent data on world energy markets . and authoritative publications in the field of energy. *Rev. World Energy data* 70, 8–20 (2021).
3. Hodes, G. Perovskite-Based Solar Cells. 342, 317–319 (2013).
4. Rao, S., Morankar, A., Verma, H. & Goswami, P. Emerging Photovoltaics: Organic, Copper Zinc Tin Sulphide, and Perovskite-Based Solar Cells. *J. Appl. Chem.* 2016, 1–12 (2016).
5. Online, V. A., Gao, P. & Nazeeruddin, M. K. Environmental Science Organohalide lead perovskites for photovoltaic applications. *Energy Environ. Sci.* 1, 2448–2463 (2014).
6. Yang, W. S. *et al.* Iodide management in formamidinium-lead-halide-based perovskite layers for efficient solar cells. *Science (80-.).* 356, 1376–1379 (2017).
7. Herz, L. M. Charge-Carrier Dynamics in Organic-Inorganic Metal Halide Perovskites. *Annu. Rev. Phys. Chem.* 67, 65–89 (2016).
8. Kim, H. S. *et al.* Lead iodide perovskite sensitized all-solid-state submicron thin film mesoscopic solar cell with efficiency exceeding 9%. *Sci. Rep.* 2, 1–7 (2012).
9. Jeong, M. *et al.* Stable perovskite solar cells with efficiency exceeding 24.8% and 0.3-V voltage loss. *Science (80-.).* 369, 1615–1620 (2020).
10. Best-Research-Cell-Efficiencies-Rev210726.Pdf. https://www.nrel.gov/pv/assets/pdfs/best-research-cell-efficiencies-rev210726.pdf.
11. Amnuyswat, K. & Thanomngam, P. Improvement of energy gap prediction for hybrid perovskite materials by first-principle calculation. *AIP Conf. Proc.* 2010, (2018).
12. De Wolf, S. *et al.* Organometallic halide perovskites: Sharp optical absorption edge and its relation to photovoltaic performance. *J. Phys. Chem. Lett.* 5, 1035–1039 (2014).
13. Adhyaksa, G. W. P. *et al.* Carrier Diffusion Lengths in Hybrid Perovskites: Processing, Composition, Aging, and Surface Passivation Effects. *Chem. Mater.* 28, 5259–5263 (2016).
14. Leijtens, T. *et al.* Overcoming ultraviolet light instability of sensitized TiO2 with meso-superstructured organometal tri-halide perovskite solar cells. *Nat. Commun.* 4, 1–8 (2013).
15. Snaith, H. J. Perovskites: The emergence of a new era for low-cost, high-efficiency solar cells. *J. Phys. Chem. Lett.* 4, 3623–3630 (2013).
16. Wu, K. *et al.* Temperature-dependent excitonic photoluminescence of hybrid organometal halide perovskite films. *Phys. Chem. Chem. Phys.* 16, 22476–22481 (2014).
17. Yu, Y. *et al.* Gate-tunable phase transitions in thin flakes of 1T-TaS2. *Nat. Nanotechnol.* 10, 270–276 (2015).

18. Woolley, J. C. *Introduction to solid state physics*. *Journal of the Mechanics and Physics of Solids* vol. 6 (1957).
19. Eisberg, R M; Resnick, R. *Quantum physics of atoms, molecules, solids, nuclei and particles. Fizik-e Koantomy atomha, molekolha, jamedat, hasteh-ha va zarat-e bonyady*.
20. Clayden, J. *et al. pdf Organic Chemistry Description :* (2001).
21. Yougui Liao. *Practical Electron Microscopy and Database*. (2006).
22. Cölle, M. & Brütting, W. Thermal and Structural Properties of the Organic Semiconductor Alq3 and Characterization of Its Excited Electronic Triplet State. *Phys. Org. Semicond.* 95–128 (2006).
23. Martí, A. Fundamentals of solar cells (advanced topics). https://www.cheetah-exchange.eu/webinars.asp?i=51 (2017).
24. NREL. Solar Spectra. https://www.nrel.gov/grid/solar-resource/spectra.html.
25. Rühle, S. Tabulated values of the Shockley-Queisser limit for single junction solar cells. *Sol. Energy* 130, 139–147 (2016).
26. Sha, W. E. I., Ren, X., Chen, L. & Choy, W. C. H. The efficiency limit of CH3NH3PbI3 perovskite solar cells. *Appl. Phys. Lett.* 106, 1–14 (2015).
27. Ehrler, B. *et al.* Photovoltaics reaching for the shockley-queisser limit. *ACS Energy Lett.* 5, 3029–3033 (2020).
28. Uddin, M. G. *Development of Simplified In Situ Processing Routes for Rear-Side Patterning of Silicon Heterojunction Interdigitated Back Contact (SHJ-IBC) Solar Cells*. https://erepo.uef.fi/handle/123456789/20514 (2018).
29. Komilian, S. Investigation into Device Optimisation of Organic Solar Cells Using Narrow Bandgap Polymer and the Role of Acceptor Material. (2019).
30. A checklist for photovoltaic research. *Nat. Mater.* 14, 1073 (2015).
31. Yalçin, L. & Öztürk, R. Performance comparison of c-Si, mc-Si and a-Si thin film PV by PVsyst simulation. *J. Optoelectron. Adv. Mater.* 15, 326–334 (2013).
32. Christians, J. A., Manser, J. S. & Kamat, P. V. Best practices in perovskite solar cell efficiency measurements. Avoiding the error of Making Bad Cells Look Good. *J. Phys. Chem. Lett.* 6, 852–857 (2015).
33. Snaith, H. J. The perils of solar cell efficiency measurements. *Nat. Photonics* 6, 337–340 (2012).
34. Snaith, H. J. How should you measure your excitonic solar cells? *Energy Environ. Sci.* 5, 6513–6520 (2012).
35. Pazos-Outón, L. M. *et al.* Photon recycling in lead iodide perovskite solar cells. *Science (80-.).* 351, 1430–1433 (2016).
36. Caprioglio, P. *et al.* On the Relation between the Open-Circuit Voltage and Quasi-Fermi Level

Splitting in Efficient Perovskite Solar Cells. *Adv. Energy Mater.* 9, 1–10 (2019).

37. Yoo, J. J. *et al.* Efficient perovskite solar cells via improved carrier management. *Nature* 590, 587–593 (2021).
38. Masuko, K. *et al.* Achievement of more than 25% conversion efficiency with crystalline silicon heterojunction solar cell. *IEEE J. Photovoltaics* 4, 1433–1435 (2014).
39. Filip, M. R., Eperon, G. E., Snaith, H. J. & Giustino, F. Steric engineering of metal-halide perovskites with tunable optical band gaps. *Nat. Commun.* 5, (2014).
40. Bai, Y. *et al.* Effects of a Molecular Monolayer Modification of NiO Nanocrystal Layer Surfaces on Perovskite Crystallization and Interface Contact toward Faster Hole Extraction and Higher Photovoltaic Performance. *Adv. Funct. Mater.* 26, 2950–2958 (2016).
41. Zong, B. *et al.* Highly stable hole-conductor-free CH3NH3Pb(I1-xBrx)3 perovskite solar cells with carbon counter electrode. *J. Alloys Compd.* 748, 1006–1012 (2018).
42. Suo, J. *et al.* Surface Reconstruction Engineering with Synergistic Effect of Mixed-Salt Passivation Treatment toward Efficient and Stable Perovskite Solar Cells. *Adv. Funct. Mater.* 31, (2021).
43. Feng, M. *et al.* High-Efficiency and Stable Inverted Planar Perovskite Solar Cells with Pulsed Laser Deposited Cu-Doped NiOxHole-Transport Layers. *ACS Appl. Mater. Interfaces* 12, 50684–50691 (2020).
44. Reyna, Y. *et al.* Performance and stability of mixed FAPbI3(0.85)MAPbBr3(0.15) halide perovskite solar cells under outdoor conditions and the effect of low light irradiation. *Nano Energy* 30, 570–579 (2016).
45. Ye, J. *et al.* Doped Bilayer Tin(IV) Oxide Electron Transport Layer for High Open-Circuit Voltage Planar Perovskite Solar Cells with Reduced Hysteresis. *Small* 17, 1–9 (2021).
46. Norbert Nickel. Metal halide perovskites for solar cells. https://www.helmholtz-berlin.de/forschung/oe/se/silizium-photovoltaik/arbeitsgebiete/perowskite/index_en.html.
47. Li, C. *et al.* Formability of ABX 3 (X = F, Cl, Br, I) halide perovskites. *Acta Crystallogr. Sect. B Struct. Sci.* 64, 702–707 (2008).
48. Yi, Z. *et al.* Will organic-inorganic hybrid halide lead perovskites be eliminated from optoelectronic applications? *Nanoscale Adv.* 1, 1276–1289 (2019).
49. Ball, J. M. & Petrozza, A. Defects in perovskite-halides and their effects in solar cells. *Nat. Energy* 1, (2016).
50. Borriello, I., Cantele, G. & Ninno, D. Ab initio investigation of hybrid organic-inorganic perovskites based on tin halides. *Phys. Rev. B - Condens. Matter Mater. Phys.* 77, 1–9 (2008).
51. Mitzi, D. B., Prikas, M. T. & Chondroudis, K. Thin film deposition of organic-inorganic hybrid materials using a single source thermal ablation technique. *Chem. Mater.* 11, 542–544 (1999).

52. Whitfield, P. S. *et al.* Structures, Phase Transitions and Tricritical Behavior of the Hybrid Perovskite Methyl Ammonium Lead Iodide. *Sci. Rep.* 6, 1–16 (2016).
53. Palazon, F. *et al.* Room-Temperature Cubic Phase Crystallization and High Stability of Vacuum-Deposited Methylammonium Lead Triiodide Thin Films for High-Efficiency Solar Cells. *Adv. Mater.* 31, 1–6 (2019).
54. Zhumekenov, A. A. *et al.* Formamidinium Lead Halide Perovskite Crystals with Unprecedented Long Carrier Dynamics and Diffusion Length. *ACS Energy Lett.* 1, 32–37 (2016).
55. Slimi, B. *et al.* Perovskite FA1-xMAxPbI3 for Solar Cells: Films Formation and Properties. *Energy Procedia* 102, 87–95 (2016).
56. Jiang, S. *et al.* Phase Transitions of Formamidinium Lead Iodide Perovskite under Pressure. *J. Am. Chem. Soc.* 140, 13952–13957 (2018).
57. Medjahed, A. A. Structure-properties correlation in hybrid perovskite for photovoltaics. (2021).
58. Targhi, F. F., Jalili, Y. S. & Kanjouri, F. MAPbI3 and FAPbI3 perovskites as solar cells: Case study on structural, electrical and optical properties. *Results Phys.* 10, 616–627 (2018).
59. Yang, W. S. *et al.* High-performance photovoltaic perovskite layers fabricated through intramolecular exchange. *Science (80-.).* 348, 1234–1237 (2015).
60. Lee, J. W., Seol, D. J., Cho, A. N. & Park, N. G. High-efficiency perovskite solar cells based on the black polymorph of HC(NH2)2PbI3. *Adv. Mater.* 26, 4991–4998 (2014).
61. Stoumpos, C. C., Malliakas, C. D. & Kanatzidis, M. G. Semiconducting tin and lead iodide perovskites with organic cations: Phase transitions, high mobilities, and near-infrared photoluminescent properties. *Inorg. Chem.* 52, 9019–9038 (2013).
62. Yin, W. J., Yan, Y. & Wei, S. H. Anomalous alloy properties in mixed halide perovskites. *J. Phys. Chem. Lett.* 5, 3625–3631 (2014).
63. Hamatani, T., Shirahata, Y., Ohishi, Y., Fukaya, M. & Oku, T. Arsenic and Chlorine Co-Doping to CH3NH3PbI3 Perovskite Solar Cells. *Adv. Mater. Phys. Chem.* 07, 1–10 (2017).
64. Jin, H. *et al.* It's a trap! on the nature of localised states and charge trapping in lead halide perovskites. *Materials Horizons* vol. 7 397–410 (2020).
65. Sum, T. C. & Mathews, N. Advancements in perovskite solar cells: Photophysics behind the photovoltaics. *Energy Environ. Sci.* 7, 2518–2534 (2014).
66. Sherkar, T. S. *et al.* Recombination in Perovskite Solar Cells: Significance of Grain Boundaries, Interface Traps, and Defect Ions. *ACS Energy Lett.* 2, 1214–1222 (2017).
67. Kuik, M., Koster, L. J. A., Wetzelaer, G. A. H. & Blom, P. W. M. Trap-assisted recombination in disordered organic semiconductors. *Phys. Rev. Lett.* 107, 1–5 (2011).
68. Lee, M. M., Teuscher, J., Miyasaka, T., Murakami, T. N. & Snaith, H. J. Efficient hybrid solar cells

based on meso-superstructured organometal halide perovskites. *Science (80-.).* 338, 643–647 (2012).

69. Chen, X., Lu, H., Yang, Y. & Beard, M. C. Excitonic Effects in Methylammonium Lead Halide Perovskites. *J. Phys. Chem. Lett.* 9, 2595–2603 (2018).
70. Galkowski, K. *et al.* Determination of the exciton binding energy and effective masses for methylammonium and formamidinium lead tri-halide perovskite semiconductors. *Energy Environ. Sci.* 9, 962–970 (2016).
71. Even, J., Pedesseau, L. & Katan, C. Analysis of multivalley and multibandgap absorption and enhancement of free carriers related to exciton screening in hybrid perovskites. *J. Phys. Chem. C* 118, 11566–11572 (2014).
72. Miyata, A. *et al.* Direct measurement of the exciton binding energy and effective masses for charge carriers in organic-inorganic tri-halide perovskites. *Nat. Phys.* 11, 582–587 (2015).
73. Mora-Seró, I. How Do Perovskite Solar Cells Work? *Joule* 2, 585–587 (2018).
74. Yang, G. *et al.* Interface engineering in planar perovskite solar cells: Energy level alignment, perovskite morphology control and high performance achievement. *J. Mater. Chem. A* 5, 1658–1666 (2017).
75. Herz, L. M. Charge-Carrier Mobilities in Metal Halide Perovskites: Fundamental Mechanisms and Limits. *ACS Energy Lett.* 2, 1539–1548 (2017).
76. McMeekin, D. P. *et al.* Crystallization Kinetics and Morphology Control of Formamidinium–Cesium Mixed-Cation Lead Mixed-Halide Perovskite via Tunability of the Colloidal Precursor Solution. *Adv. Mater.* 29, (2017).
77. Zhao, Y., Nardes, A. M. & Zhu, K. Solid-state mesostructured perovskite CH3NH3PbI 3 solar cells: Charge transport, recombination, and diffusion length. *J. Phys. Chem. Lett.* 5, 490–494 (2014).
78. Stranks, S. D. *et al.* Electron-hole diffusion lengths exceeding 1 micrometer in an organometal trihalide perovskite absorber. *Science (80-.).* 342, 341–344 (2013).
79. Zhang, H. *et al.* Influence of Cl Incorporation in Perovskite Precursor on the Crystal Growth and Storage Stability of Perovskite Solar Cells. *ACS Appl. Mater. Interfaces* 11, 6022–6030 (2019).
80. Wang, L., Mccleese, C., Kovalsky, A., Zhao, Y. & Burda, C. Femtosecond Time-Resolved Transient Absorption Spectroscopy of CH3NH3PbI3 Perovskite Films: Evidence for Passivation Effect of PbI2. *J. Am. Chem. Soc.* 136, 12205–12208 (2014).
81. Du, T. *et al.* Formation, location and beneficial role of PbI2 in lead halide perovskite solar cells. *Sustain. Energy Fuels* 1, 119–126 (2017).
82. Serhan, M. *et al.* Cs0.15FA0.85PbI3 perovskite solar cells for concentrator photovoltaic applications. *AIChE Annu. Meet. Conf. Proc.* 0–6 (2019).
83. Bakr, Z. H. *et al.* Advances in hole transport materials engineering for stable and efficient perovskite

solar cells. *Nano Energy* 34, 271–305 (2017).

84. Alnuaimi, A., Almansouri, I. & Nayfeh, A. Effect of mobility and band structure of hole transport layer in planar heterojunction perovskite solar cells using 2D TCAD simulation. *J. Comput. Electron.* 15, 1110–1118 (2016).
85. Bi, C. *et al.* Non-wetting surface-driven high-aspect-ratio crystalline grain growth for efficient hybrid perovskite solar cells. *Nat. Commun.* 6, 1–7 (2015).
86. Luo, D. *et al.* Enhanced photovoltage for inverted planar heterojunction perovskite solar cells. *Science (80-.).* 360, 1442–1446 (2018).
87. Teddy Salim, Shuangyong Sun, Yuichiro Abe, Anurag Krishna, A. C. G. and Y. M. L. Perovskite-Based Solar Cells: Impact of Morphology and Device Architecture on Device Performance. *J. Mater. Chem. A* (2015).
88. Wang, K. C. *et al.* P-type mesoscopic nickel oxide/organometallic perovskite heterojunction solar cells. *Sci. Rep.* 4, 1–8 (2014).
89. Chan, I. M., Hsu, T. Y. & Hong, F. C. Enhanced hole injections in organic light-emitting devices by depositing nickel oxide on indium tin oxide anode. *Appl. Phys. Lett.* 81, 1899–1901 (2002).
90. Manders, J. R. *et al.* Solution-Processed Nickel Oxide Hole Transport Layers in High Effi ciency Polymer Photovoltaic Cells. *Adv. Funct. Mater.* 23, 2993–3001 (2013).
91. Park, J. H. *et al.* Efficient CH3NH3PbI3 Perovskite Solar Cells Employing Nanostructured p-Type NiO Electrode Formed by a Pulsed Laser Deposition. *Adv. Mater.* 27, 4013–4019 (2015).
92. Kim, J. H. *et al.* High-performance and environmentally stable planar heterojunction perovskite solar cells based on a solution-processed copper-doped nickel oxide hole-transporting layer. *Adv. Mater.* 27, 695–701 (2015).
93. Li, G. *et al.* Overcoming the Limitations of Sputtered Nickel Oxide for High-Efficiency and Large-Area Perovskite Solar Cells. *Adv. Sci.* 4, 1–8 (2017).
94. Troughton, J. *et al.* A universal solution processed interfacial bilayer enabling ohmic contact in organic and hybrid optoelectronic devices. *Energy Environ. Sci.* 13, 268–276 (2020).
95. Juarez-Perez, E. J. *et al.* Photodecomposition and thermal decomposition in methylammonium halide lead perovskites and inferred design principles to increase photovoltaic device stability. *J. Mater. Chem. A* 6, 9604–9612 (2018).
96. Guo, R. *et al.* Degradation mechanisms of perovskite solar cells under vacuum and one atmosphere of nitrogen. *Nat. Energy* 6, (2021).
97. Huang, J., Tan, S., Lund, P. D. & Zhou, H. Impact of H2O on organic-inorganic hybrid perovskite solar cells. *Energy Environ. Sci.* 10, 2284–2311 (2017).
98. Rajagopal, A., Yao, K. & Jen, A. K. Y. Toward Perovskite Solar Cell Commercialization: A

Perspective and Research Roadmap Based on Interfacial Engineering. *Adv. Mater.* 30, 1–45 (2018).

99. Eperon, G. E. *et al.* The Importance of Moisture in Hybrid Lead Halide Perovskite Thin Film Fabrication. *ACS Nano* 9, 9380–9393 (2015).
100. Tolueinia, P. *et al.* Moisture-Induced Structural Degradation in Methylammonium Lead Iodide Perovskite Thin Films. *ACS Appl. Energy Mater.* 3, 8240–8248 (2020).
101. Kim, J. *et al.* Size-dependent phase transition in methylammonium lead iodide perovskite microplate crystals. *Polym. J.* 48, 829–834 (2016).
102. Leijtens, T. *et al.* Towards enabling stable lead halide perovskite solar cells; Interplay between structural, environmental, and thermal stability. *J. Mater. Chem. A* 5, 11483–11500 (2017).
103. Binek, A., Hanusch, F. C., Docampo, P. & Bein, T. Stabilization of the trigonal high-temperature phase of formamidinium lead iodide. *J. Phys. Chem. Lett.* 6, 1249–1253 (2015).
104. Chen, B., Yang, M., Priya, S. & Zhu, K. Origin of J-V Hysteresis in Perovskite Solar Cells. *J. Phys. Chem. Lett.* 7, 905–917 (2016).

Chapter II Experimental Method

This chapter describes the methods used to fabricate and characterize charge transport and perovskite materials. The preparation of perovskite solar cells is described in detail in Chapter 3.

2.1. Deposition Techniques

2.1.1. Thermal evaporation of top electrode

In the thermal evaporation process, the solid material is heated above the vaporization temperature. The whole evaporation process needs to be carried out under a high vacuum (<$1*10^{-6}$ mbar). The high vacuum allows the vaporized material to pass through the vacuum chamber without colliding with other gas molecules and eventually nucleating on the target surface. In thermal evaporation, a high current is passed through the wire ringing the crucible to heat the source material until it evaporates. A crystal of quartz vibrating at a specific frequency is calibrated and used to monitor the evaporation rate. When the evaporation temperature is stabilized, the substrate is rotated to obtain a uniform and dense film. High vacuum thermal evaporation allows precise control of the film thickness, with tolerances of less than 1 nm.

Figure 2.1 shows the thermal evaporation instrument we used to evaporate the Ag electrode. 200 nm Ag is evaporated at the rate of 2Å/s. In addition, because of the presence of the Schottky barrier between [60]PCBM and Ag electrode, an ultra-thin buffer layer of Bathocuproine (BCP) was deposited on the surface of [60]PCBM by thermal vapor deposition. The 4 nm BCP layer was precisely deposited at a rate of 1Å/s.

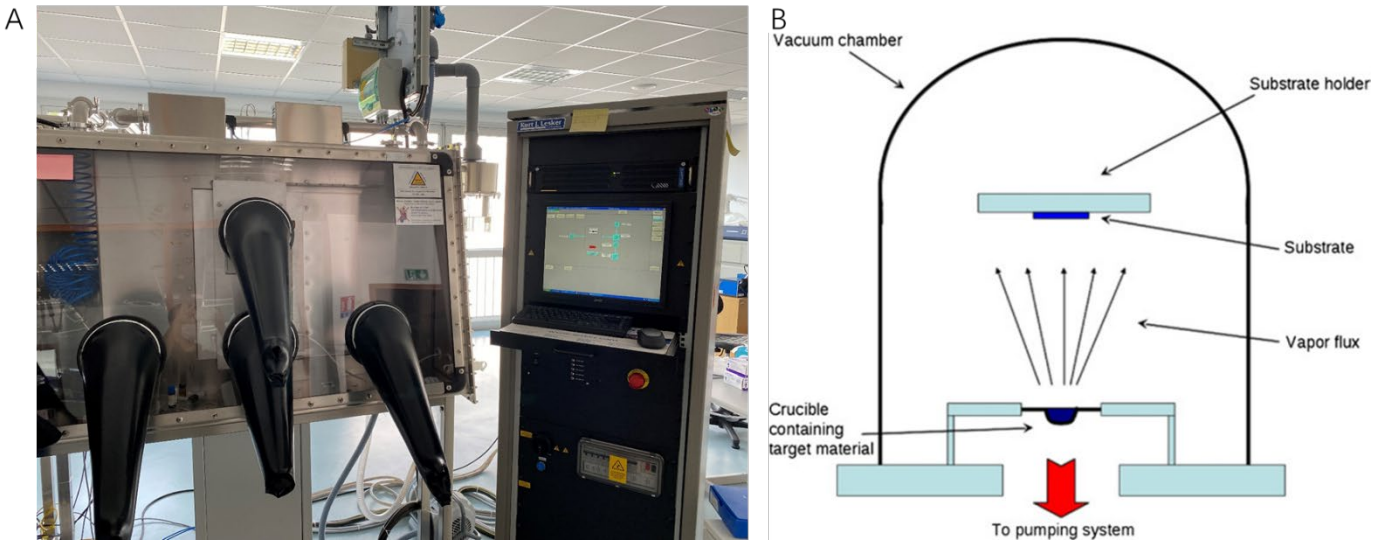

Figure 2.1 A) Image of thermal evaporation instrument; B) sketch of thermal evaporation instrument.

2.1.2. Electrostatic spray deposition (ESD)

2.1.2.1 ESD principle

Electrostatic spray deposition (ESD) is a deposition process based on electrohydrodynamic atomization laws of liquids. In ESD a precursor solution is pumped through a metallic nozzle at a controlled flow rate. The solution is then atomized at the nozzle tip into an aerosol by applying an electrical field between the nozzle and the heated substrate. The electrical field generates the aerosol and directs it towards the substrate where the droplets spread, dry, and decompose to form the film. A schematic drawing of the vertical ESD system is presented in Figure 2.2. The vertical orientation of the technique prevents droplets and solutions from dripping on the substrate.

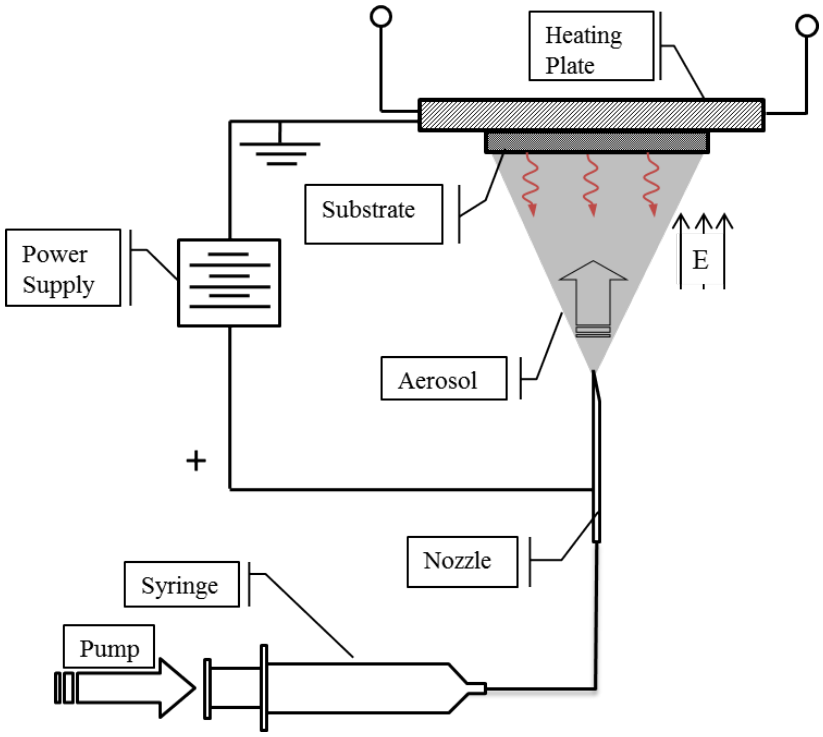

Figure 2.2 Schematic drawing of a vertical electrostatic spray deposition (ESD) device[1].

2.1.2.2 Different ESD deposition stages

The ESD deposition process can be divided into five stages, illustrated in Figure 2.3. The aerosol is formed when the liquid precursor is pumped through a metal nozzle where a very high positive DC voltage (about 10 kV) is applied between the nozzle and the grounded substrate. A tangential electrical force accelerates the positive electrical charges at the surface upwards deforming the meniscus into a cone-like shape, named cone-jet spraying mode. The repulsive forces between the surface charges counteract the surface tension of the liquid, causing the droplet to elongate (Figure 2.4). A stable conical shape (called Taylor cone) is formed characterized by mono-sized spherical droplets in the micrometers range (Figure 2.5). Hydrodynamic

instabilities break the surface tension of the cone and form charged droplets with micrometric sizes. The self-repulsion force between the droplets avoids agglomeration and creates the aerosol, thus completing stage 1. During stage 2, the charged droplets are directed towards the grounded substrate by the Coulombic forces (Figure 2.6). The droplets will undergo a decrease in size during flight time. Solvent losses are determined by the substrate temperature, the nozzle-to-substrate distance, and the volatility of the solutions. Stage 3 corresponds to the impact of droplets onto the substrate where they spread and dry (stage 4) as the film begins to form (Figure 2.7). The substrate temperature is usually chosen to cause complete solvent evaporation, and may even be enough to decompose and promote partial (or complete) chemical reaction between the precursor salts, during stage 5 of the deposition.

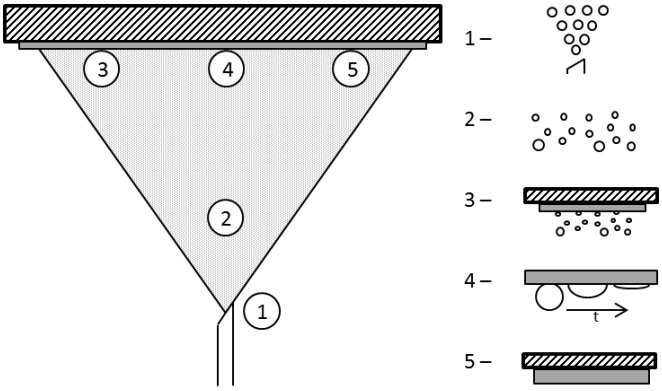

Figure 2.3 Sequential ESD stages 1 – aerosol formation; 2 – droplet transport; 3 – droplet impact; 4 – spreading and drying; 5 – decomposition and reaction. Adapted from Ref 2[2].

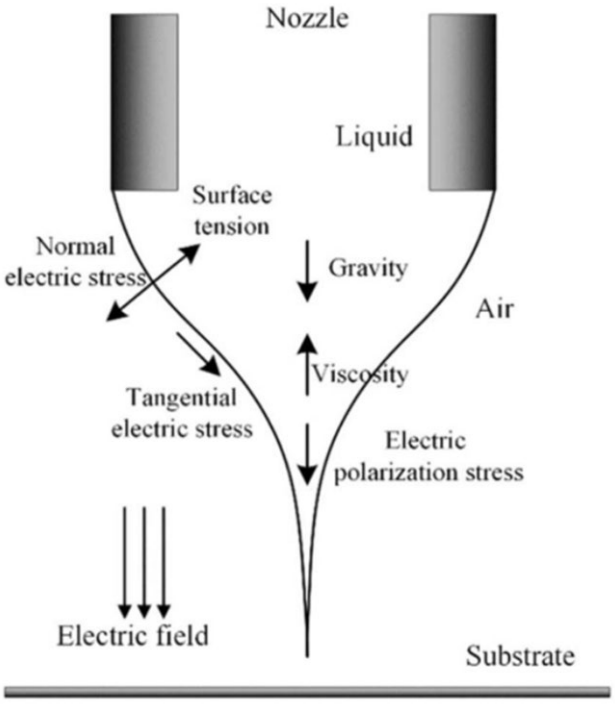

Figure 2.4 Coupling distribution map of various forces of cone jet ejection based on the dielectric model. Adapted from Ref 3[3].

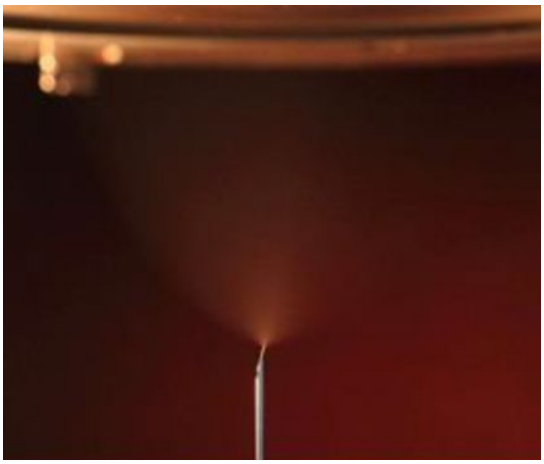

Figure 2.5 Image of the cone-jet mode.

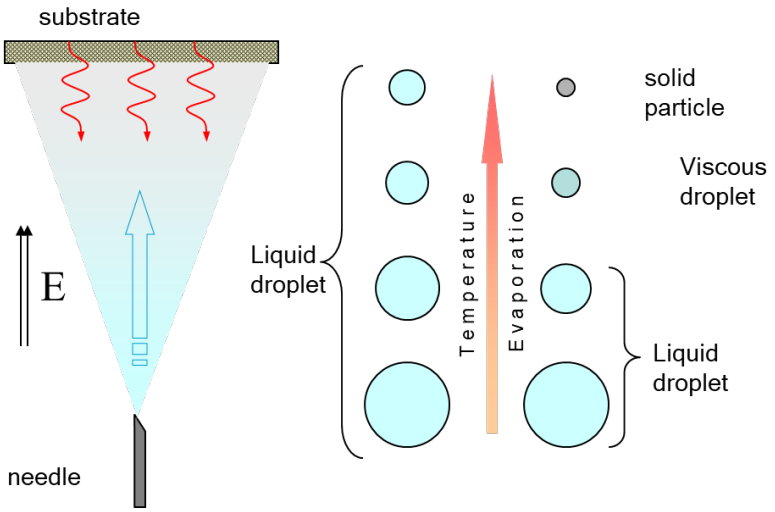

Figure 2.6 Aerosol transport through ESD process with a decrease of droplet size during the flight time.

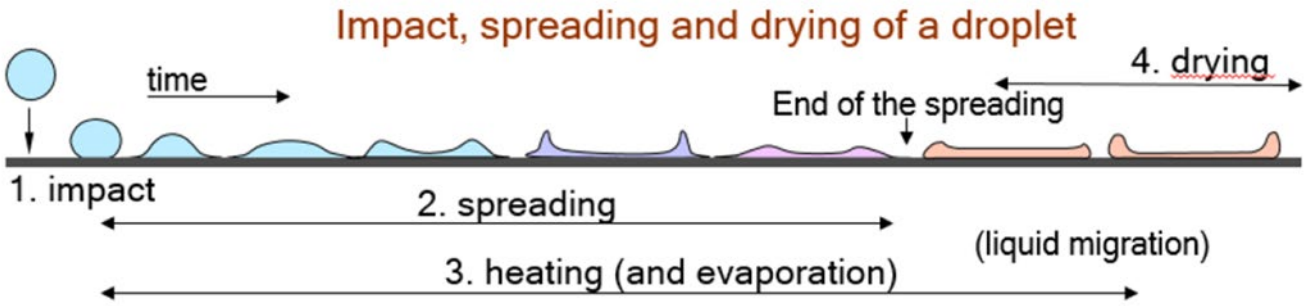

Figure 2.7 Impacting droplet on the hot substrate surface: spreading and drying.

2.1.2.3 Microstructural control in ESD coating

The microstructure of the deposited layer is a consequence of the physicochemical properties of the precursor solution combined with the deposition conditions such as solution flow rate, the nozzle-to-substrate distance or/and substrate temperature. The mechanism of film formation and the resulting microstructure depends mainly on the size of the droplets impacting the substrate. Droplet size in the aerosol can vary from ~10 nm to 100 µm[4] depending on the experimental setup. Several studies have modeled how the solution properties and the deposition parameters determine droplet size formed at the nozzle[5,6]. Gañan-Calvo's relationship[6] specified in Equation 1 below shows that the droplet size d varies mainly according to the flow rate Q, and less strongly with the electrical conductivity of the solution *K*, and surface tension of the solution γ. The density is ρ, and vacuum permeability is ε_0. The relationship is valid under the conditions of the cone-jet spraying mode.

$$d \sim \left(\frac{\rho \varepsilon_0 Q^a}{\gamma K} \right)^{1/6} \qquad \text{Equation 1}$$

As expressed by Equation 1, the increasing flow rate will generate larger droplets, with marked effects on

the film microstructure.

Ultimately, it is the size of the droplet impacting the hot substrate and the combined effects of relative spreading and drying rates that determine film morphology. Two general cases may be distinguished: the droplets retain enough liquid so that it undergoes simultaneous spreading and drying on the surface of the substrate leading to dense, reticulated, or cracked coatings (Figure 2.8A); the droplets completely dry during flight forming solid particles that impact and accumulate on the substrate, forming a porous microstructure (Figure 2.8B).

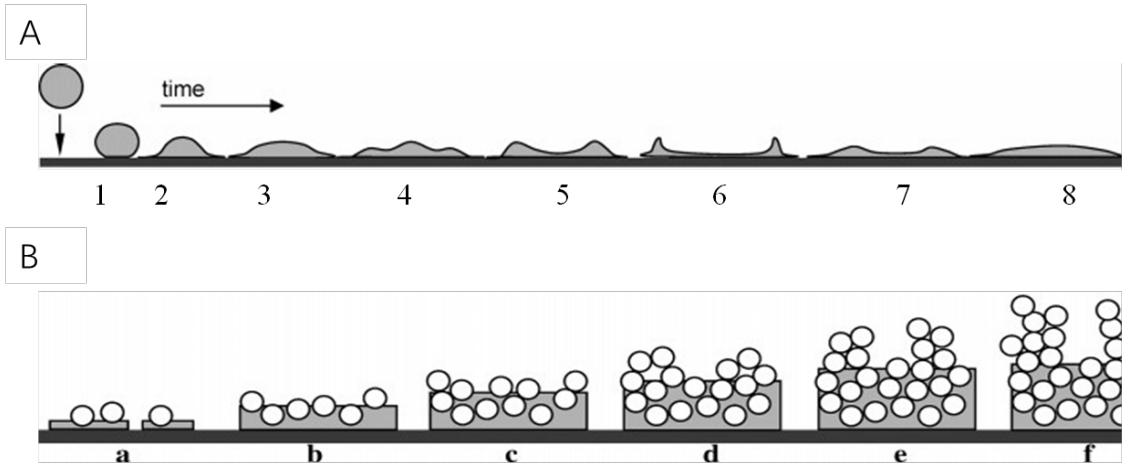

Figure 2.8 A) Spreading of a liquid droplet on a smooth surface; B) film growth using solid particles. Adapted from 7[7]

The particular case of reticulation occurs whenever the simultaneous spreading and drying solidify the droplet at the moment it reaches maximum spreading. Dense films required adequate amounts of liquid in the droplets to avoid cracking due to stresses generated during drying.

After droplets of a given size are generated at the nozzle, other effects come into play causing droplets to undergo dynamic changes in size due to solvent evaporation occurring during the flight between the nozzle and the heated substrate. In this regard, the effect of parameters such as solution boiling point, nozzle-to-substrate distance, and substrate temperature must be taken into account when considering the desired morphology.

As aforementioned, the increase in flow rate leads to the generation of larger droplets, with the microstructure evolving from practically dense to reticular morphology. As expected, increasing nozzle-to-substrate distance has the opposite effect, and thus compensates for the increase in initial droplet size obtained at larger flow rates by allowing more time for solvent evaporation to occur. The combination of both allows fine-tuning of the dense-type morphology and may create conditions for the appearance of different ones. Different morphologies are obtained if complete solvent evaporation occurs during flight (Figure 2.8B), in which case

the solute particles precipitate into solid particles. Because the surface of these particles is charged, they are electrostatically attracted towards points in the substrate with higher curvatures[2]. This effect is termed preferential landing (Figure 2.9) and leads to the formation of branched structures resembling corals.

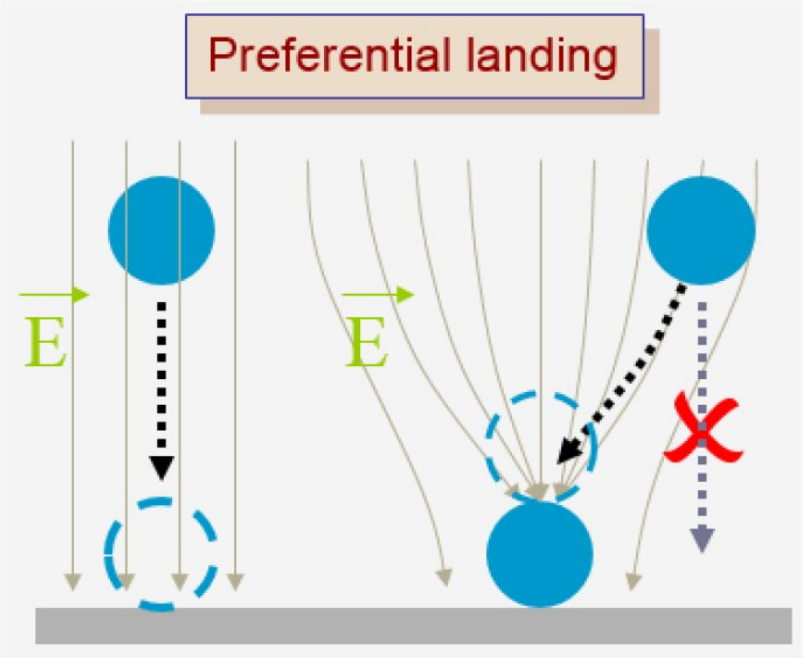

Figure 2.9 Preferential landing of charged particles on the hot substrate surface

2.1.2.4 Forming NiO dense film

The film morphology is influenced by of many additional elements, including the relative rate of spreading, precipitation, and decomposition. If the spreading is slow but the precipitation and decomposition are quick, a grainy structure will form. The optimum circumstances for forming a dense layer are (i) wet particles impacting the heated substrate, (ii) large solubilities of the solute in the solvent, and (iii) fast spreading of the solution droplets. There are a few key elements to consider while making a dense NiO film, as listed below.

1. Solution of precursors: the relatively low surface tension and viscosity are required and conductivity values of the solution may vary between 10^{-8} and 10^{-1} $S.cm^{-1}$ to get a jet cone mode. One fundamental characteristic is the boiling point which limits the possible film morphologies[8]. Butyl carbitol with a high boiling point of 231 °C was selected in this study to favor the formation of large liquid droplets impacting the substrate. Surface tension must not be too high; otherwise, corona discharges would occur, preventing atomization. This is also why the precursor solution is seldom an aqueous solution.
2. The precursors selected in this study are Nickel(II) nitrate hexahydrate ($Ni(NO_3)_2 \cdot 6\ H_2O$), Copper(II) nitrate trihydrate ($Cu(NO_3)_2 \cdot 3\ H_2O$), and Butyl carbitol. All chemicals were purchased from Sigma Aldrich and used without further purification. The precursor solution preparation depends on the coated material and, for clarity, details of the working solutions are provided in the following chapters.
3. Substrate temperature: When the deposition temperature is too low, the solvent does not evaporate during

the flight. A dense film with cracks is expected caused by a lot of thermal stresses due to the excess of the solvent when drying. Because there is a large quantity of liquid in the deposited layer owing to the low evaporation rate, when the spraying stops, the temperature of the large volume of liquid rises quickly, resulting in fast solvent evaporation. This causes a significant volume shift and tensions in the deposited layer. Furthermore, due to adhesion to the substrate, the deposited layer is unable to shrink freely. On the contrary, when the deposition temperature is too high, the dried droplets impact the substrate and cannot spread, resulting in a porous coating. It is, therefore, necessary to respect a certain quantity of liquid to promote the spreading of the droplets on the heated substrate but to avoid an excess that would lead to a cracked coating.

4. Flow rate: The precursor solution flow rate regulates the amount of liquid that reaches the substrate while also regulating the size of the droplets in the spray according to Gañan-Calvo's relationship[6]. To get dense films, it is required to select large flow rates to obtain enough liquid to favor the droplet spreading on the substrate. But at the same time, we must be careful not to produce droplets that are too liquid which, once spread on the hot substrate, would lead to large thermal pressures, which eventually give cracked films.
5. Nozzle-to-substrate distance: Adjusting the nozzle-to-substrate distance simply changes the size of the droplets during the flight and finally impacts the substrate. It is important to choose an appropriate distance so that the right amount of solvent evaporates during the transport of the droplets from the nozzle to the substrate. This will prevent large amounts of solution from reaching the substrate, which can lead to cracks, or overly dry solid particles reaching the substrate to form a granular film.

Deposition time: It is very important to choose the deposition time according to the desired thickness. As the deposition time increases, the thickness of the film layer can be varied. However, if the deposition time is large, the preferential landing of the droplets will result in a porous film structure. If the deposition time is too low, the final film will not cover the substrate uniformly.

The main process parameters in ESD are substrate temperature, concentration, and deposition time for a given solution of precursors. After studying the evolution of the coating microstructure as a function of each process parameter separately[9], a coherent picture of the process comes up with the temperature correlation with the nozzle-to-substrate distance and the precursor solution flow rate to deposit a dense and continuous doped-zirconia layer using one solution of precursors. The first three of them are directly correlated because they all influence the equilibrium between the flux of the incoming solution and the solvent evaporation at the surface of the substrate. We have demonstrated[9] that a careful correlation of these parameters allows the deposition of dense and continuous doped-zirconia coatings over a large range of process parameters. A three-dimensional domain rather than a point or a range of values of these parameters describes the optimal conditions. The most suitable conditions for the synthesis of good quality coatings are rather low flow rates and long distances. The substrate temperature has to be chosen accordingly.

2.1.2.5 Advantages of ESD process

The ESD method can offer several advantages over conventional coating techniques. ESD is a low-cost chemical method since it does not require expensive equipment or vacuum generation. Furthermore, it leads to coatings with a high coverage rate, allowing the use of small amounts of precursors. ESD is an innovative technique that enables the deposition of films with a large variety of original morphologies by a nano-texturing approach. It has been reported to be used in depositing a lot of oxide materials at a low deposition temperature while ensuring strong adhesion to the substrate. $LiMn_2O_4$[10], Y_2O_3-doped $BaZrO_3$[11], Ta_2O_5[12], ZnO[13], Al_2O_3[13], ZrO_2[14], , Y_2O_3-doped ZrO_2[15], $La_{2-x}Pr_xNiO_4$[16], Pr_6O_{11}[17], $Ca_3Co_4O_9$[18], $La_{1-x}Sr_xCoFeO_3$[19,20] were successfully deposited by ESD. Additionally, it has been used in depositing thin-film $CuInSe_2$ for solar cells, biopolymers, Co_3O_4 for lithium-ion batteries[21,22]. Templates have been used to obtain gradient porosity levels in TiO_2 films with very interesting results[23]. Moreover, this technique allows for excellent control over the stoichiometry and the thickness of the films. Indeed, the thickness of ESD-derived coatings can be controlled easily from several nanometers up to some tenths of micrometers[24].

2.2. Device Characterizations

Typical perovskite solar cells are characterized using the following techniques.

2.2.1. Current-Voltage Measurements

Current-voltage measurements of the devices were performed with a Keithley 2400 Source meter under AM 1.5G illumination with a xenon-lamp-based calibrated solar simulator (Newport, AAA). An NREL-certified silicon reference cell was used to calibrate the intensity to 1000 mW cm^{-2} before the experiments. The cells were measured with a mask (0.09 cm^2). Typically, the applied bias was swept from -0.1 V to +1.2 V and back again at a scan rate of 20 mV s^{-1} for both forward and reverse scans. Usually, we use box plots to count the different parameters of the solar cell. In Figure 2.10B, the meaning of the different parts of the box plot is shown, where the area of the rectangle can reflect the distribution of the data

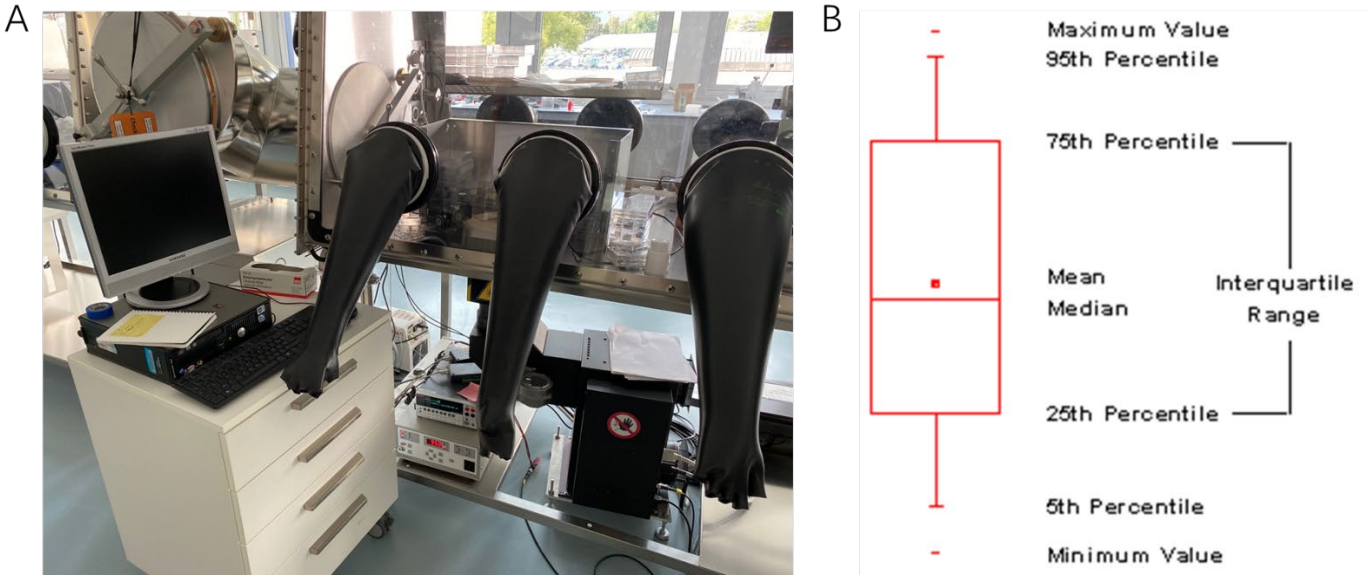

Figure 2.10 A) Image of Current-Voltage Measurements setup; B) The meaning of the different parts of the box plot

2.2.2. Scanning Electron Microscopy (SEM)

A scanning electron microscope (SEM) is a type of electron microscope that uses a high-energy concentrated beam of electrons to scan across material and take pictures of it. Secondary electrons, back-scattered electrons, and characteristic X-rays are produced when electrons interact with electrons in the sample and carry out information about the sample surface topography and composition. In most cases, the electron beam is scanned in a raster scan pattern, and the position of the beam is coupled with the received signal to create a picture. Samples must be electrically conductive to avoid charge accumulation on the surface; nonconducting samples are commonly covered with an ultrathin metal layer. Samples must be photographed under vacuum in traditional SEM. A ZEISS-ultra 55 scanning electron microscope (SEM) with a 7 kV accelerating voltage was used to examine the surface morphology of the films.

2.2.3. Atomic Force Microscopy (AFM)

AFM is a technique for imaging that employs a cantilever beam with an extremely sharp tip at the end. Si or Silicon Nitride is commonly used for the cantilever. Hooke's Law states that when the tip is brought close to the specimen, the contact between the specimen surfaces deflects the cantilever. The 3D picture of the sample surface can be created with suitable data computation and processing, and therefore the surface topography can be determined. AFM produces three-dimensional surface profiles and does not require any extra preparation of the sample. There is no need for a vacuum. It may be used in the open air or even within a liquid. When done inside UHV, high resolution can reach real atomic size. AFM images were carried out with a Bruker Dimension Icon atomic force microscope

2.2.4. Tunneling AFM (TUNA)

Tunneling AFM (TUNA), like Conductive AFM (C-AFM), can be used to locate electrical defects in semiconductor and data storage devices, as well as to investigate conductive polymers, organics, and other materials.

TUNA functions in the same way as C-AFM, but with higher current sensitivity. The lateral resolution is determined by the tip geometry, which is generally equal to the end radius of the tip. A configurable bias voltage is provided between the conductive tip and the sample with the tip at virtual ground (see Figure 2.11). A linear amplifier with a range of 80 fA to 120 pA measures the current going through the sample while scanning in Contact Mode. Simultaneous topographic and current pictures are obtained by maintaining a constant tension between tip and sample, allowing for the direct connection of local topography with electrical parameters.

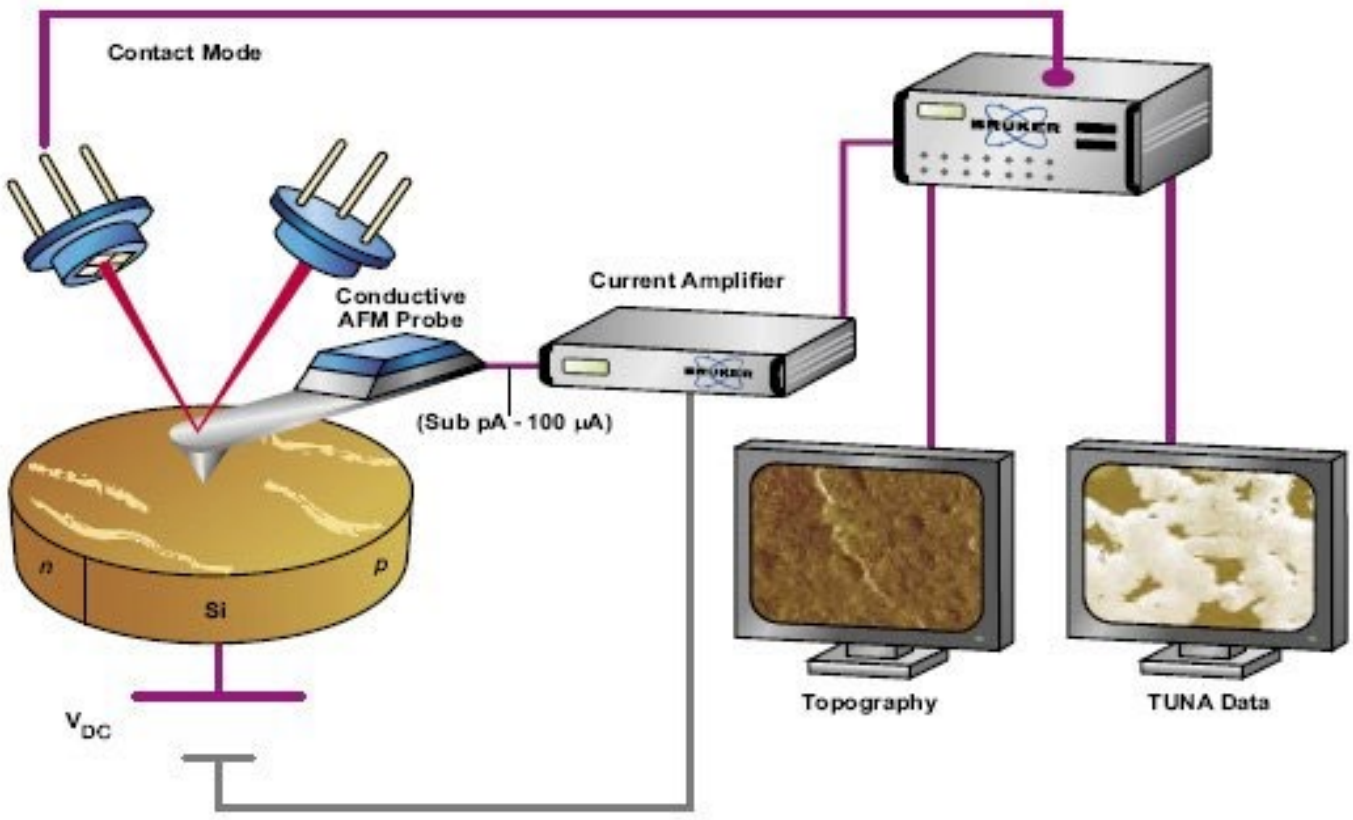

Figure 2.11 Tunneling AFM Block Diagram. Adopted from Bruker[25].

2.2.5. Absorption: UV-vis spectroscopy

Both UV absorption spectra and visible absorption spectra belong to molecular spectra, and they are both generated due to the leap of valence electrons. The UV-visible spectra and the degree of absorption produced by the absorption of UV and visible light by molecules or ions of a substance can be used to analyze, determine, and infer the composition, content, and structure of a substance.

2.2.6. Steady State Photoluminescence

A laser is focused onto a sample's surface. As the sample absorbs the incident light, it will get photoexcited if the bandgap has an energy less than or equal to the energy of the incoming laser. The sample exhibits photoluminescence at a wavelength equal to the sample's bandgap after radiative recombination of excited states. PL spectra were recorded using a FLUOROLOG fluorescence spectrophotometer (Jobin-Yvon).

2.2.7. UV photoelectron spectroscopy (UPS) and X-ray photoelectron spectroscopy (XPS)

A sample is illuminated by a beam of photons with varied known energy. Electrons are ejected from the material, each with kinetic energy determined by the electron orbital from which it originated and the energy of the photon that pushed it out of its nucleus. Typically, an electron can be freed from within a material to a depth of 5 nm and still escape from that sample. The top surface of thin films is only examined. UPS uses UV photons, while XPS uses X-rays with energies greater than 1.5 keV.

2.2.8. X-ray Diffraction (XRD)

The structural characterizations of the perovskite material were carried out on the perovskite thin layers, just after manufacture and after different types of aging to determine the defects created following these aging.

A crystalline material can be defined as a repetition of a pattern in the 3 dimensions of space according to a network defined by 3 base vectors $\vec{a}, \vec{b}$ and $\vec{c}$.The diagram of Figure 2.12 represents X-ray reflection by parallel and equidistant reticular planes, identified by the Miller indices h, k, and l and spaced by the interreticular distance d_{hkl}.

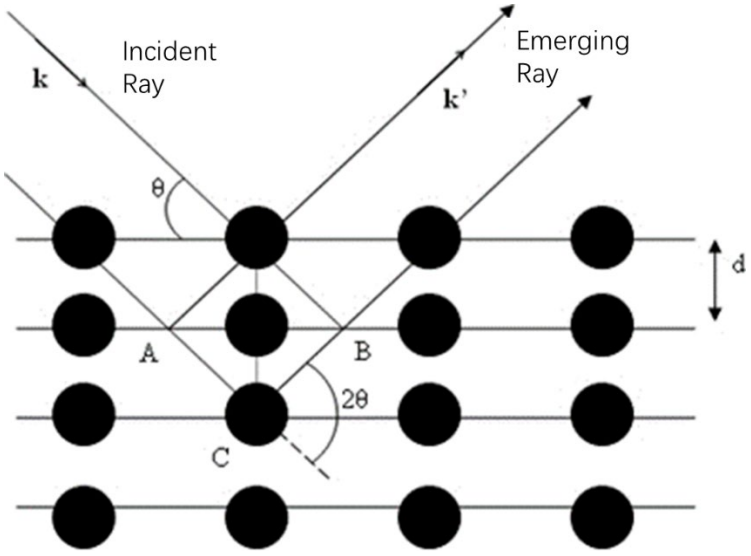

Figure 2.12 X-ray reflection by a family of reticular planes spaced at a distance d_{hkl}.

The incident X-rays are scattered coherently by the electrons of the material atoms, resulting in diffraction by the crystalline material. The criteria of constructive interference are reflected in Bragg's law.

$$\lambda = 2d_{hkl} \sin \theta_{hkl} \quad \text{Bragg's law}$$

where 2θ is the scattering angle (Bragg angle), d_{hkl} the inter-reticular distance of the (*hkl*) planes and λ the wavelength. The values of the scattering angle for the different Bragg peaks can be used to determine the unit cell parameters according to the crystal symmetry. Indeed, the inter-reticular distance d_{hkl} of a family of planes (*hkl*) is expressed as a function of the cell parameters of the material and the *hkl* indices. The simplest example is that of the cubic structure (α = β = γ = 90 ° and a = b = c), in which the inter-reticular distance is given by:

$$d_{hkl} = \frac{a}{\sqrt{(h^2 + k^2 + l^2}}$$

X-ray diffraction is still one of the most used methods for determining a material crystal structure and microstructure (grain size, strain). This non-destructive technique can be done in an inert environment or the open air. Depending on the nature of the materials (monocrystalline, polycrystalline, textured, oriented), different measurement configurations can be used.

2.2.8.1. Classical measurement type "θ / 2θ".

The most traditional measurement is "θ / 2θ" where the angle of incidence on the sample as well as the angle 2θ are changed for this measurement. Only families of planes parallel to the sample's surface are probed in this type of measurement. An important quantity is the scattering vector $\vec{Q}$ with $\vec{Q} = \vec{K}d - \vec{K}i$ (Figure 2.13). In a scattering experiment, periodicity or more generally correlations in atomic positions are probed along the direction of $\vec{Q}$only. Qualitatively to any periodicity d probed along the direction of $\vec{Q}$, a diffraction peak will be associated with an angle 2θ linked to d by Bragg's law. And therefore, during a θ / 2θ measurement for

which $\vec{Q}$ is kept perpendicular to the surface of the sample, the diffraction peaks are associated with families of planes parallel to this surface. The information that can be drawn from these measurements is first of all the positions of the peaks, which provide information on the inter-reticular distances from which the cell parameters can be deduced. The relative intensities are related tothe nature and positions of the atoms in the cell through the structure factor. However in our case they will give us information on the existence of eventual preferential orientation in the perovskite layer. Finally, the shape of the peaks gives us some indication of the defects that exist in the atomic stack (deformations, size of crystallites, etc.). XRD measurements were performed on a Panalytical Empyrean diffractometer equipped with a cobalt anode beam tube (Co λKα1 = 1.7890 Å, Co λKα2 = 1.7929 Å), a Göbel mirror, and a 1D Pixel detector.

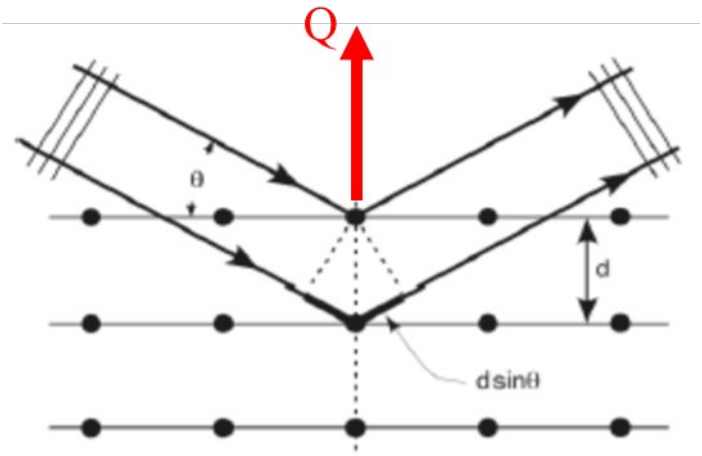

Figure 2.13 traditional measurement mode "θ / 2θ". The diffusion vector is perpendicular to the surface.

2.2.8.2. Grazing incidence X-ray diffraction (GIXD)

Grazing incidence X-ray diffraction (GIXD) is a technique in which the incident angle of the X-ray beam on the sample surface is kept constant at a value usually slightly above the critical angle (below which there is total reflection). This has the benefit of limiting the penetration depth of the X-rays into the sample, resulting in reduced background scattering from the substrate, which is especially significant for thin films. In a 2θ scan, the direction of the scattering vector is therefore changing. The penetration depth of the X-ray beam depends on the wavelength and on the density of the layer; it can be changed by changing the incidence angle from a few nanometers to several hundred nanometers.

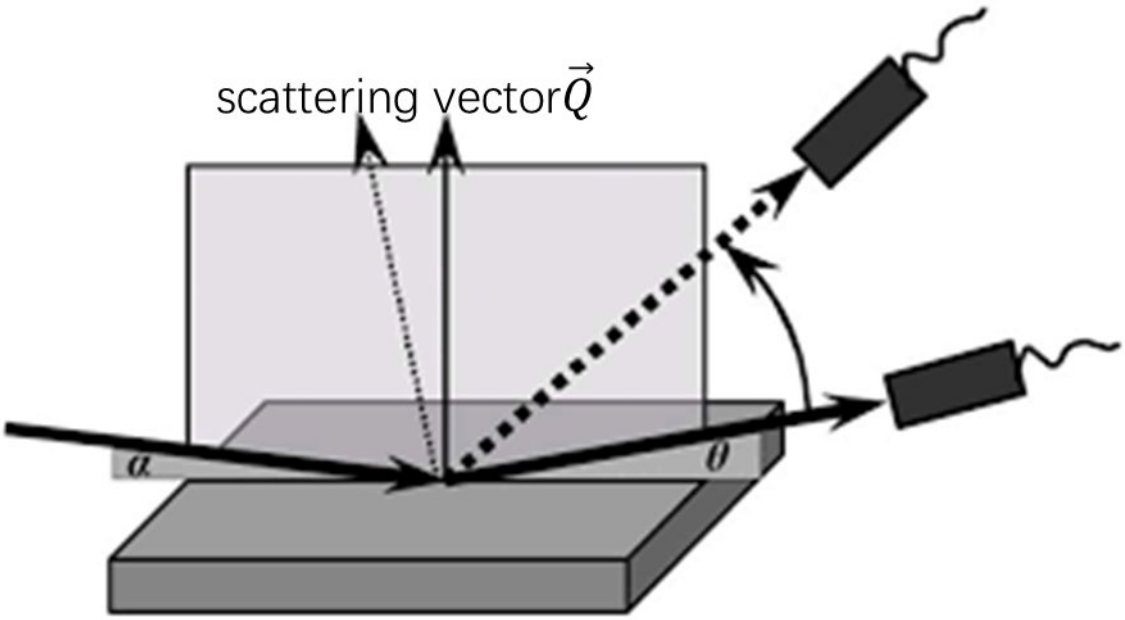

Figure 2.14 Grazing incidence diffraction geometry. The angle of incidence, α, is close to the critical angle for the sample. The beam is diffracted in the plane of the surface of the sample by the angle 2θ. Adapted from 26[26]

References

1. Leeuwenburgh, S., Wolke, J., Schoonman, J. & Jansen, J. Electrostatic spray deposition (ESD) of calcium phosphate coatings. *J. Biomed. Mater. Res. - Part A* 66, 330–334 (2003).
2. Chen, C. H., Kelder, E. M., Jak, M. J. G. & Schoonman, J. Electrostatic spray deposition of thin layers of cathode materials for lithium battery. *Solid State Ionics* 86–88, 1301–1306 (1996).
3. Cai, S. *et al.* Mechanisms, influencing factors, and applications of electrohydrodynamic jet printing. *Nanotechnol. Rev.* 10, 1046–1078 (2021).
4. Jaworek, A. & Sobczyk, A. T. Electrospraying route to nanotechnology: An overview. *J. Electrostat.* 66, 197–219 (2008).
5. Wilhelm, O., Mädler, L. & Pratsinis, S. E. Electrospray evaporation and deposition. *J. Aerosol Sci.* 34, 815–836 (2003).
6. Gañán-Calvo, A. M., Dávila, J. & Barrero, A. Current and droplet size in the electrospraying of liquids. Scaling laws. *J. Aerosol Sci.* 28, 249–275 (1997).
7. Neagu, R., Perednis, D., Princivalle, A. & Djurado, E. Initial stages in zirconia coatings using ESD. *Chem. Mater.* 17, 902–910 (2005).
8. Chen, C. H., Kelder, E. M. & Schoonman, J. Unique porous LiCoO2 thin layers prepared by electrostatic spray deposition. *J. Mater. Sci.* 31, 5437–5442 (1996).
9. Neagu, R., Perednis, D., Princivalle, A. & Djurado, E. Zirconia coatings deposited by electrostatic spray deposition. Influence of the process parameters. *Surf. Coatings Technol.* 200, 6815–6820 (2006).
10. Shu, D., Chung, K. Y., Cho, W. Il & Kim, K. B. Electrochemical investigations on electrostatic spray deposited LiMn2O4 films. *J. Power Sources* 114, 253–263 (2003).
11. Somroop, K., Pornprasertsuk, R. & Jinawath, S. Fabrication of Y2O3-doped BaZrO3 thin films by electrostatic spray deposition. *Thin Solid Films* 519, 6408–6412 (2011).
12. Salaün, A. L., Mantoux, A., Blanquet, E. & Djurado, E. ESD and ALD Depositions of Ta[sub 2]O[sub 5] Thin Films Investigated as Barriers to Copper Diffusion for Advanced Metallization. *J. Electrochem. Soc.* 156, H311 (2009).
13. Jaworek, A., Sobczyk, A. T., Krupa, A., Lackowski, M. & Czech, T. Electrostatic deposition of nanothin films on metal substrate. *Bull. Polish Acad. Sci. Tech. Sci.* 57, 63–70 (2009).
14. *Surface and Interface Research and Engineering Delft University of Technology A Collection of Mini Posters*. (1997).
15. Nguyen, T. & Djurado, E. Deposition and characterization of nanocrystalline tetragonal zirconia films using electrostatic spray deposition. *Solid State Ionics* 138, 191–197 (2001).
16. Sharma, R. K. *et al.* Electrochemical Performance and Chemical Stability of Architecturally Designed

La2-XPrxNiO4+ IT-SOFC Cathodes. *ECS Trans.* 72, 1–8 (2016).

17. Sharma, R. K. & Djurado, E. An efficient hierarchical nanostructured Pr6O11 electrode for solid oxide fuel cells. *J. Mater. Chem. A* 6, 10787–10802 (2018).
18. Djurado, E. *et al.* Electrostatic spray deposition of Ca3Co4O9 + δ layers to be used as cathode materials for IT-SOFC. *Solid State Ionics* 286, 102–110 (2016).
19. Marinha, D., Dessemond, L. & Djurado, E. Comprehensive Review of Current Developments in IT-SOFCs. *Curr. Inorg. Chem.* 3, 2–22 (2013).
20. Hsu, C.-S. & Hwang, B.-H. Microstructure and Properties of the La[sub 0.6]Sr[sub 0.4]Co[sub 0.2]Fe[sub 0.8]O[sub 3] Cathodes Prepared by Electrostatic-Assisted Ultrasonic Spray Pyrolysis Method. *J. Electrochem. Soc.* 153, A1478 (2006).
21. Abbas, M. *et al.* Control of structural, electronic, and optical properties of eumelanin films by electrospray deposition. *J. Phys. Chem. B* 115, 11199–11207 (2011).
22. Sun, Y., Feng, X. Y. & Chen, C. H. Hollow Co3O4 thin films as high performance anodes for lithium-ion batteries. *J. Power Sources* 196, 784–787 (2011).
23. Sokolov, S., Paul, B., Ortel, E., Fischer, A. & Kraehnert, R. Template-assisted electrostatic spray deposition as a new route to mesoporous, macroporous, and hierarchically porous oxide films. *Langmuir* 27, 1972–1977 (2011).
24. Chen, C. H., Emond, M. H. J., Kelder, E. M., Meester, B. & Schoonman, J. Electrostatic sol-spray deposition of nanostructured ceramic thin films. *J. Aerosol Sci.* 30, 959–967 (1999).
25. Bruker. TUNA & Conductive AFM. https://blog.brukerafmprobes.com/guide-to-spm-and-afm-modes/tuna-conductive-afm/.
26. Bouroushian, M. & Kosanovic, T. Characterization of Thin Films by Low Incidence X-Ray Diffraction. *Cryst. Struct. Theory Appl.* 01, 35–39 (2012).

Chapter III. Optimisation of triple cation perovskite absorber layer and engineering of the absorber-hole transport layer interface

As mentioned above, at room temperature (RT), FAPI is either in the yellow δ-$FAPbI_3$ non-perovskite polymorph phase or in the cubic perovskite phase. Theoretically, the yellow δ-$FAPbI_3$ non-perovskite polymorph phase can be transformed to photoactive black α-$FAPbI_3$ by annealing at high temperature (>140°C). However, the black phase could degenerate to stable yellow δ-$FAPbI_3$ non-perovskite polymorph phase at room temperature for pure FA[1]. However, it has been shown that the substitution of at least 15-20% of FA by MA stabilizes the cubic perovskite phase[2]. The introduction of a trace amount of Cesium (Cs) into the basic FAMA perovskite to form triple cationic perovskites can effectively reduce the defects in the perovskite crystal and adjust the bandwidth of perovskite[3,4]. The introduction of Br^- further increases the band gap of triple cationic perovskite, which increases the open-circuit voltage of perovskite solar cells. In this chapter, the role of Cl^- will be discussed. By introducing different amounts of methylammonium chloride (MACl) compared to the standard CsFAMA triple cationic perovskite, the effect of Cl^- on the lattice of the perovskite is investigated using X-ray diffraction and the effect on the final device is studied to determine the appropriate amount of Cl^-.

The research was done in collaboration with Jiajiu Ye, a CEA postdoctoral followed working on the optimization of hybrid perovskite materials for n-i-p structured perovskite solar cells with tin oxide as the electron transport layer. The results have been published in the journal *Small* 2021*, 17,* 2005671: 'Doped Bilayer Tin(IV) Oxide (SnO_2) Electron Transport Layer (ETL) for High Open-Circuit Voltage Planar Perovskite Solar Cells with Reduced Hysteresis'.

The second part of the chapter focuses on the introduction of a completely new passivation material for application on the hole transport layer (HTL). A cheap, simple and large-scale solution processing sequential deposition technique was studied to produce a highly efficient organic-inorganic hybrid perovskite solar cell. As outlined before, in this work, the p-i-n perovskite solar cells (PSC), (inverted planar) will be discussed. In addition, surface modifications in the PSC are also reported. As mentioned above, there is a large energy level offset at the interface between the NiO_x layer and the perovskite layer. NiO_x is one of the most investigated hole-transporting layers (HTLs) due to its large bandgap with high transmittance in the visible range, deep valence band edge, and intrinsic p-type conductivity. However, when low-temperature processes are used, its crystalline quality can be deteriorated with the formation of more defects such as interstitial vacancies and defects in NiO_x. Such punctual defects lead to hole accumulation near the perovskite interface with the trap-assisted non-radiative recombination losses, consequently decreasing the device performances. Moreover, rough contact with the perovskite layer can be a consequence of these defects, degrading the crystalline quality and morphology of the perovskite layer with lower light absorption. So, it is of great importance to control the interface between NiO_x and perovskite photoactive layer to improve the overall performance and stability of

the PSCs proposing an alternative low-temperature-processed NiO_x. In addition to the use of p-type dopants, another approach is the surface modification by thin organic layers as a passivation layer to adjust work function and also the surface energy[5–7]. Here we explore dimethylamino(4-)pyridine (DMAP) for this purpose. This chapter introduces the process for preparing perovskite cells by using solution processing sequential deposition techniques and various characterization methods in detail.

3.1. Perovskite-based photovoltaic device

3.1.1. P-I-N structure

The photovoltaic device studied in this work is made using the so-called direct p-i-n structure. The structure of the solar cell is as follows: glass/ Fluorine-doped Tin Oxide (FTO) / Hole Transport Layer (HTL) / active layer (perovskite) / Electron Transport Layer (ETL)/ metal electrode. The structure of the solar cell is shown in Figure 3.1, and a photo of the test device on a 17 x 25 mm substrate.

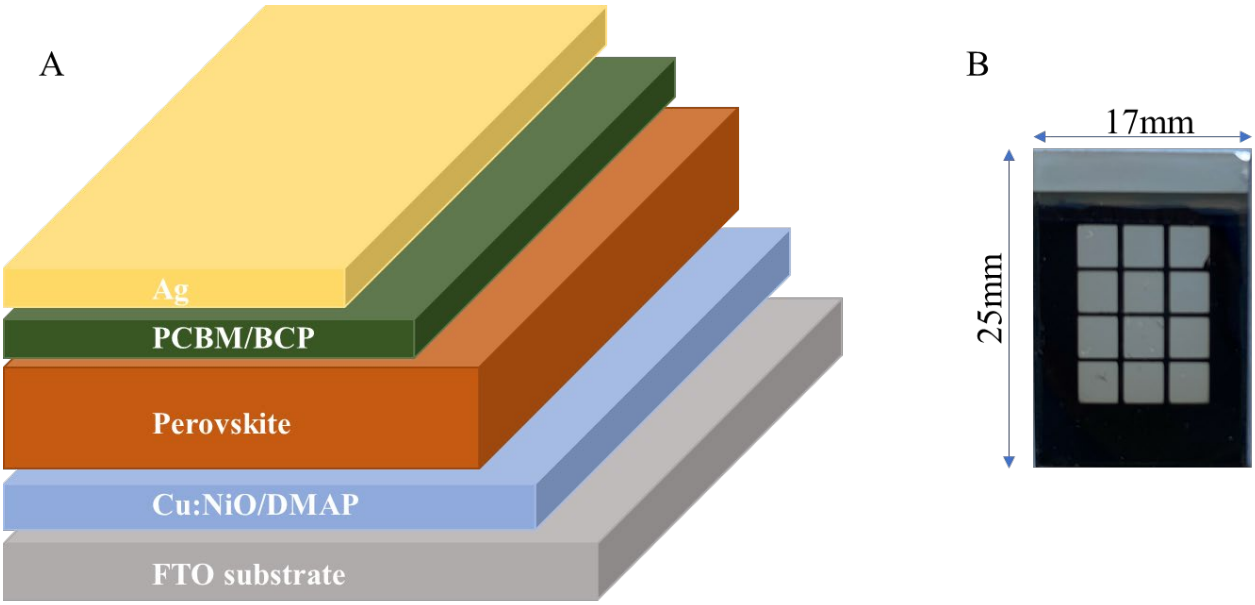

Figure 3.1 A) The structure of perovskite solar cell with p-i-n stacking. B) A photo of a substrate with twelve cells prepared in the laboratory.

3.1.2. Cell fabrication: materials and preparation processes

This section will describe the materials used to fabricate the films, the solution preparation and the methods used to deposit the different layers.

Formamidinium iodide (FAI), methylammonium bromide (MABr), and methylammonium chloride (MACl) were procured from GreatCell Solar. PbI2 were purchased from Xi'an Polymer Light Technology Corp. Lead (II) bromide ($PbBr_2$, 99%), [6,6]-Phenyl C61 butyric acid methyl ester ([60]PCBM, 99%), Bathocuproine (BCP, 99%), chlorobenzene (anhydrous, 99.8%), dimethylsulfoxide (DMSO, anhydrous, ≥99.9%), N,Ndimethylformamide (DMF, anhydrous, 99.8%), monoethanolamine ($NH_2CH_2CH_2OH$, MEA), 4-Dimethylaminopyridine (DMAP, 99%) and isopropyl alcohol (IPA, anhydrous, 99.5%) were purchased from Sigma Aldrich. Nickel acetate tetrahydrate ($Ni(CH_3COO)_2{\cdot}4H_2O$), Copper(II) acetate monohydrate ($Cu(CH_3COO)_2{\cdot}H_2O$) were acquired from Alfa Aesar. All the chemicals used in this study were used without

further purification.

3.1.2.1. Substrate glass/FTO

The FTO glass substrates for solar cell manufacturing is supported by Youxuan Technology Company (China). These 25mm x 17mm substrates are fully coated with ITO and have a square resistance of 8 Ω/sq. The transmittance of these FTO substrates in the visible light region can reach 85%. Their total thickness is 2000 μm, of which 250 nm is FTO. In order to remove contaminants on the transparent conductive glass, these substrates were first immersed in an acetone washing solution for an ultrasonic bath for 30 minutes. Then use a cleaning agent to clean the substrate and soak in deionized water for 10 minutes in an ultrasonic bath. Finally, the conductive glasses were immersed in isopropanol for ultrasonic cleaning for 30 minutes. After washing, the substrates were dried in a clean oven at 70°C and ambient humidity for at least 30 minutes. The dried substrates should be stored in a dry and clean environment. The roughness of FTO used here is around 50nm.

3.1.2.2. Hole transport layer (HTL)

As mentioned above, the hole transport material in this work was selected as Cu doped NiO. All the hole transport layers discussed in this section use a widely accepted method[8,9]. The Cu:NiO precursor was made as following process: Nickel acetate tetrahydrate ($Ni(CH3COO)_2 \cdot 4H_2O$) and Copper(II) acetate monohydrate ($Cu(CH3COO)_2 \cdot H_2O$) (mole radio Cu/Ni = 5%) were dissolved in ethanol with monoethanolamide ($NH_2CH_2CH_2OH$). The mole ratio of metal ions: MEA was maintained at 1:1 in solution. Dissolution took place while stirring in a sealed glass vial under air at 40 ° C for 1 h. The solution appeared homogeneous and deep green after approximately 40 min. Before spin-coating, the FTO substrates were exposed to UV–ozone for 45 min to remove residual organic pollutants. After UV-ozone treatment, the top of the FTO glass needs to be covered with a high temperature resistant tape to ensure that the back electrode part will not be covered by the hole transport layer, as shown in Figure 3.2A. The Cu:NiO precursor was deposited by spin-coating onto the FTO substrates. Unless otherwise specified, all hole transport layers were prepared by using an SCS P6700 spin coater (Putten, The Netherlands) in an atmospheric environment. All depositions by spin coating are performed using the same spin coater. Before annealing, the tape must be removed. Unless otherwise stated, the Cu:NiO precursor films were heated to 275 ° C for 45 min in air then raised up to 500° C for 60 min in air. To optimize the quality of the hole transport layer, different conditions for spin-coating are summarized in Table 3.1. The prepared Cu:NiO hole transport layer needs to undergo a secondary UV-Ozone treatment (45min) before it can be used in the preparation of subsequent depositions.

Concentration	Solvent	Filter	Deposition condition: Speed (rpm)/ Acceleration (rpm^{-1})/ Time (sec)	secondary UV-Ozone treatment
0.2M	EtOH	PTFE 0.2µm	3000/3000/30	45min
0.2M	EtOH	PTFE 0.2µm	5000/5000/30	45min
0.6M	EtOH	PTFE 0.2µm	3000/3000/30	45min

Table 3.1 The different concentration of HTL precursor used for the development of cells

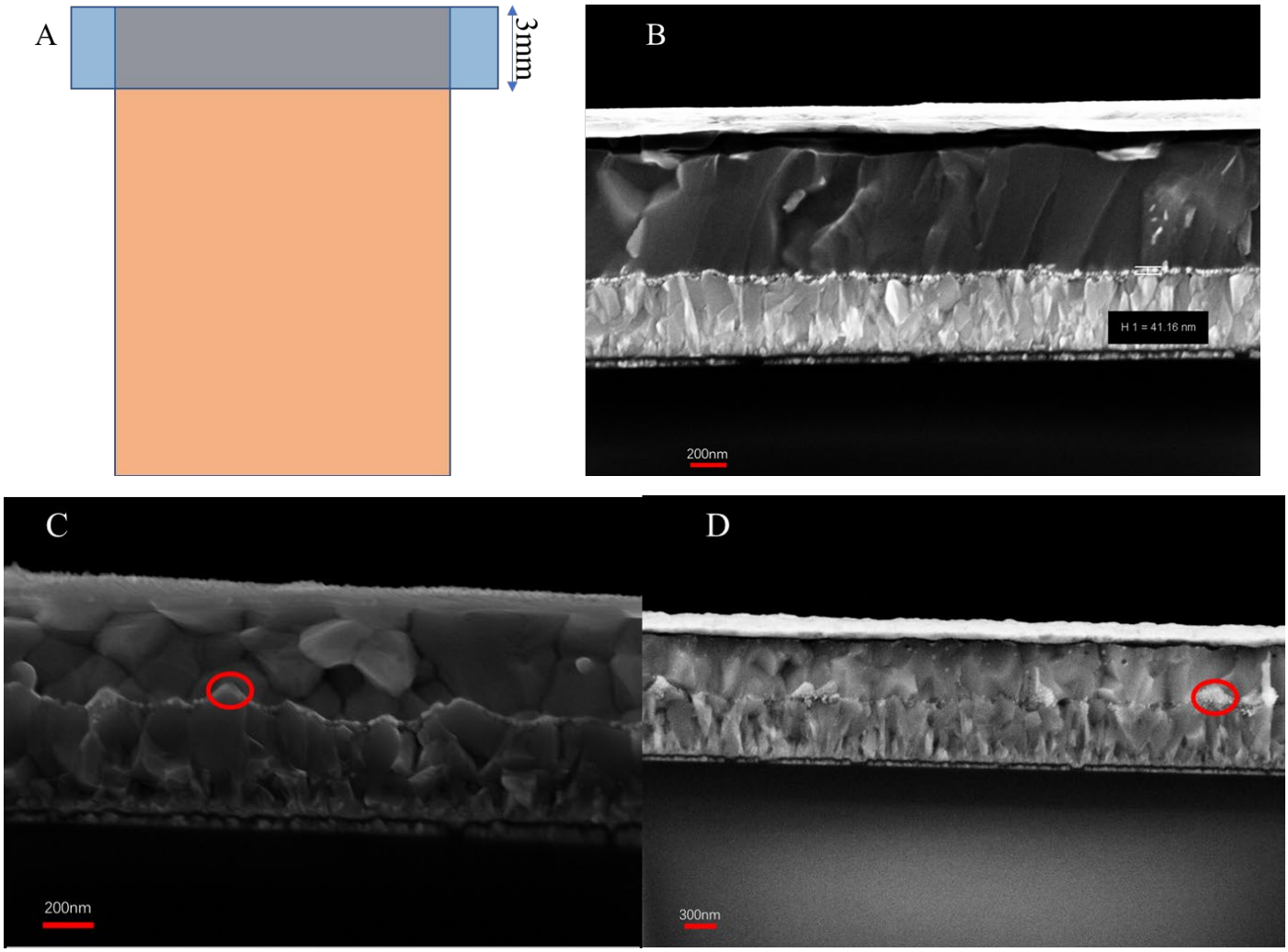

Figure 3.2 A) Schematic diagram of using tape to protect the back electrode; B) Cross-section SEM of device based on Cu:NiO made by 0.2M, 3000rpm; C) Cross-section SEM of device based on Cu:NiO made by 0.2M, 5000rpm; D) Cross-section SEM of device based on Cu:NiO made by 0.6M, 3000rpm

Figure 3.2B-D shows the thickness of the Cu:NiO layer prepared by applying different spin coating conditions.

The cross-section SEM shows that when the precursor concentration is 0.2 M and the rotational speed is 3000 rpm, the thickness of the hole transport layer is about 50 nm, which can just cover the FTO glass surface completely. When increasing the rotational speed to 5000 rpm, the thickness of Cu:NiO decreases to 20 nm. Considering the high roughness of the FTO surface (40~50 nm), the too thin hole transport layer may not cover the FTO surface completely. As shown in the red circle of Figure 3.2C, the FTO surface that is not covered by Cu:NiO appears. When the precursor concentration was increased to 0.6 M, the thickness of the hole transport layer was slightly increased. However, because of the high precursor concentration, the Cu:NiO surface appears inhomogeneous, as shown in Figure 3.2D. This may be due to the Marengoni effect caused by the inhomogeneity of the precursors with too high concentration when drying on the FTO surface[10]. Table 3.2 shows the best performance of perovskite solar cell based on different Cu:NiO. Notice that all these cells are fabricate with C_{60} as electron transport layer, which present relatively low *Voc* and *Jsc*.

	Voc (V)	Jsc (mA/cm^2)	FF	PCE (%)
0.2M 3000rpm	0.84	14.22	0.61	7.29
0.2M 5000prm	0.75	13.96	0.62	7.09
0.6M 3000rpm	0.51	4.22	0.53	1.14

Table 3.2 Best performance of perovskite solar cell based on different Cu:NiO

3.1.2.3.Perovskite active layer CsFAMA

3.1.2.3.1. Formula

In most of this work, the active layer used to fabricate batteries and various characterizations is triple cation perovskite $Cs_{0.02}FA_{0.83}MA_{0.15}Pb(I_{0.85}Br_{0.15})_3$, called CsFAMA. The preparation of the perovskite precursor solution and the deposition of the absorber layer are carried out in an argon-filled glove box. A perovskite precursor solution was typically made by combining PbI_2 (1M), FAI (1.15M), $PbBr_2$ (0.21M) and MABr (0.21 M) in 1 mL of a DMF/DMSO (4:1 v/v) mixed solvent. Then, to create a triple cation CsMAFA perovskite, 17.5 μL of CsI solution (2 M in DMSO) was added. For the perovskite solar cell with MACl modification, different amount PbI_2 and MACl were added into precursor. Details will be discussed later. The prepared precursor is bright yellow.

3.1.2.3.2. Deposition and annealing

The CsFAMA precursor solution was stirred for 1 hour at room temperature in the glove box. The resultant solution must be filtered using a PTFE filter with a pore size of 0.45 m. The resulting solution was then spin-coated onto the hole transport layer (Cu:NiO) substrates that has been cleaned and treated with UV-Ozone, as

illustrated in Figure 3.3. The spin-coating process is divided into two stages: a 10-second start at 1000 rpm, followed by a 25-second rise to 4000 rpm. During the second spin-coating operation, 150 µL of chlorobenzene were poured over the substrate after 15 seconds. The substrate was then heated for 50 minutes at 100°C on a hotplate. The absorber layer just after spin-coating is dark brown, and turns to black immediately after annealing for about 30 seconds.

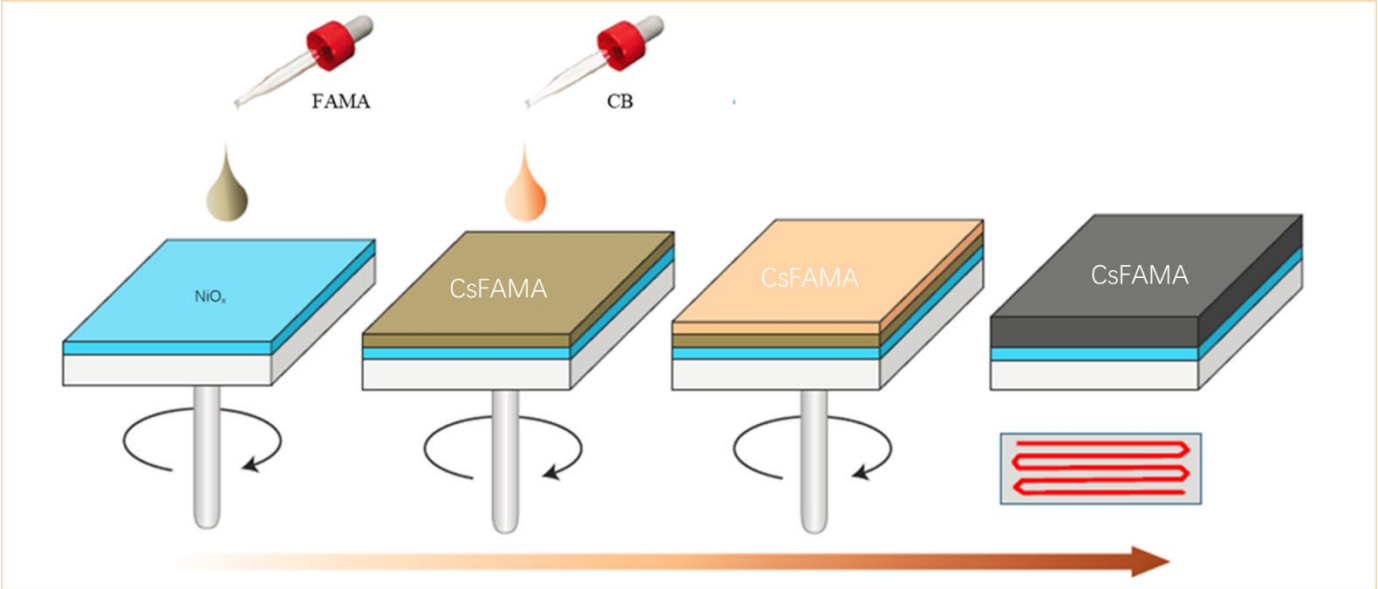

Figure 3.3 Schematic diagram of the deposition of a perovskite absorber layer by spin coating.

3.1.2.4. Electron transport layer (ETL)

Unless otherwise specified, we use [6,6]-Phenyl C61 butyric acid methyl ester ([60]PCBM) as the electron transport material. [60]PCBM solution was made by dissolving [60]PCBM in anhydrous chlorobenzene (CB) at a mass concentration of 20 mg/mL in a glove box. The solution was then stirred at room temperature for 1 hour in an argon atmosphere. After the annealing of the perovskite film is completed and the sample is cooled to room temperature, 60 µL of [60]PCBM CB solution is spin-coated onto the surface of the perovskite at a rotation rate of 2000 rpm for 45 seconds. The electron transport layer does not need further heat treatment. Similarly, the top end of the sample must be cleaned with a cotton swab soaked with acetonitrile to remove the covering perovskite layer and PCBM layer in order to expose the FTO back electrode.

To match the work function between the device and the metal electrode, an ultra-thin layer of the organic small molecule Bathocuproine is applied before the top electrode is deposited. The samples were placed inside chamber of the deposition device. With the internal air pressure below $1*10^{-6}$ mbar, 4 nm Bathocuproine were deposited (100 °C, 0.1nm/s).

3.1.2.5. Top electrode

We use the same sample holder for evaporating the top metal silver electrode. The thickness of the silver electrode was 200 nm to ensure the durability of the metal electrode. The sample was placed in the chamber of the evaporator. Evaporation was performed at a rate of 0.2 nm/s when the internal air pressure was below $1*10^{-6}$ mbar. The effective surface area of the cell was 0.09 cm^2.

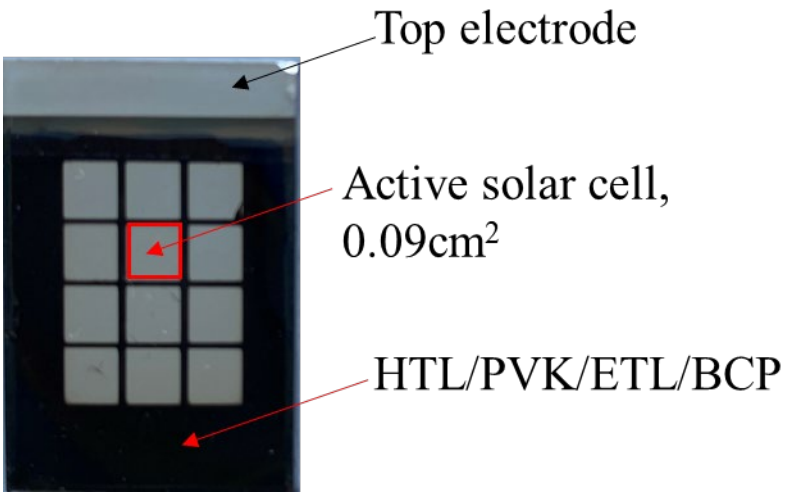

Figure 3.4 Picture of full device deposited with Ag electrode using a mask.

Figure 3.5 shows a flowchart depicting the various phases of the preparation equipment.

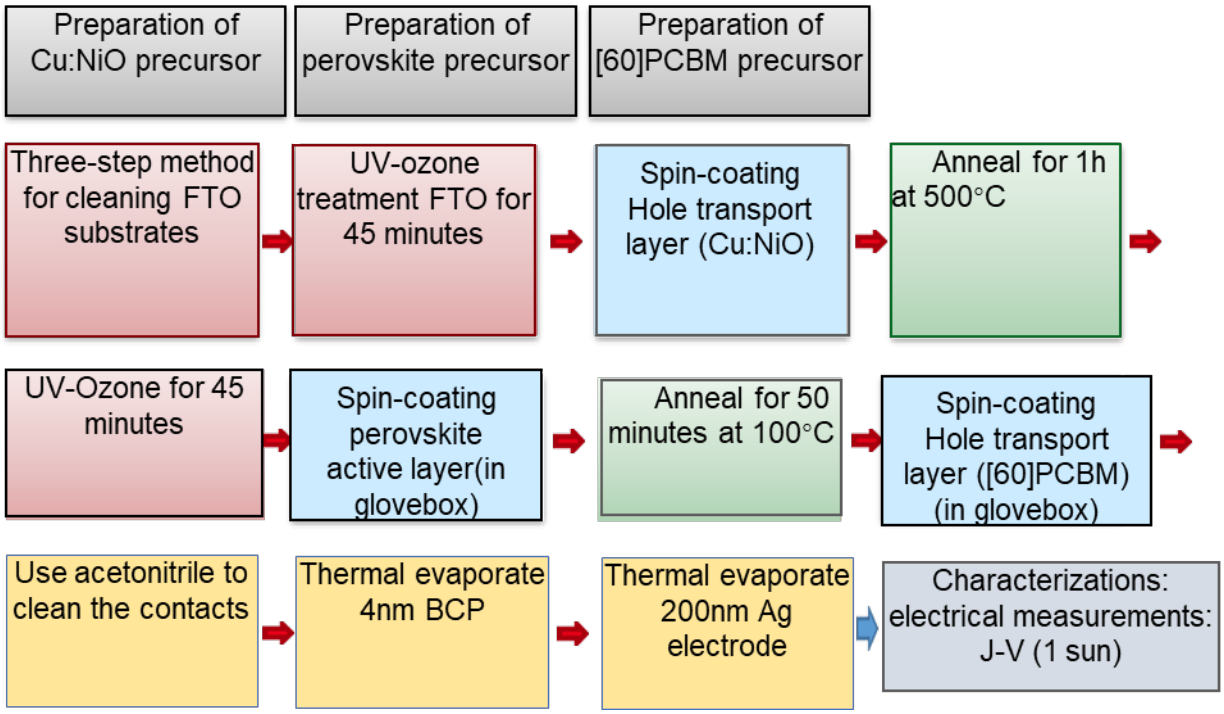

Figure 3.5 Schematic diagram of the complete process of preparing perovskite thin-film solar cells in the lab.

3.2. Methylammonium Chloride (MACl) modified perovskite

As mentioned above, the introduction of Cl^- plays a crucial role in perovskite based solar cells, especially for the increase of the device open circuit voltage. In addition, excess lead iodide has also been reported to have a role in enhancing the short-circuit current of solar cells. In this section we will investigate the effect of MACl and excess lead iodide on perovskite crystal and find the appropriate addition amount to maximize the solar cell efficiency. To create perovskite films modified with varying quantities of MACl, different amounts of MACl and PbI_2 were added to the perovskite precursors mentioned above. When the ratio of lead iodide to perovskite is 1.3, 0.3M of MACl is added; when the ratio of lead iodide to perovskite is 1.45, 0.45M of MACl is added; and when the ratio of lead iodide to perovskite is 1.6, 0.6M of MACl is added.

3.2.1. Structural study by XRD and morphology

The CsFAMA thin layer comprising various amounts of MACl and PbI_2 placed on the glass/FTO/Cu:NiO in the initial condition after spin coating and annealing is subjected to XRD measurements. The thin layer was put in a heat-sealed aluminized bag in a glove box and opened shortly before analysis to limit CsFAMA contact with ambient air, and the measurements were done in CEA/Grenoble and the characterizations are in $\theta/2\theta$ mode. As indicated in Figure 3.6, the XRD peaks cannot meet the α-$FAPbI_3$ perfectly, probably because of the introduction of MA^+ and Br^-. In the previous study, we successfully fabricated $FA_{0.85}MA_{0.15}Pb(I_{0.85}Br_{0.15})_3$ powder, and structural investigations based on this perovskite had been studied. The XRD patterns in my case can well meet the results in the previous research[2], showing a cubic phase at room temperature. No $MAPbCl_3$ phase is detected, which indicates that the introduction of Cl does not form another type of perovskite. However, after adding excessive PbI_2 and MACl, the XRD pattern of perovskite with MACl shows a slight shift towards larger 2ϑ angles, indicating a smaller lattice interplanar distance with increasing amount of MACl. The smaller lattice interplanar distance is due to the incorporation of chloride ions with a smaller radius.

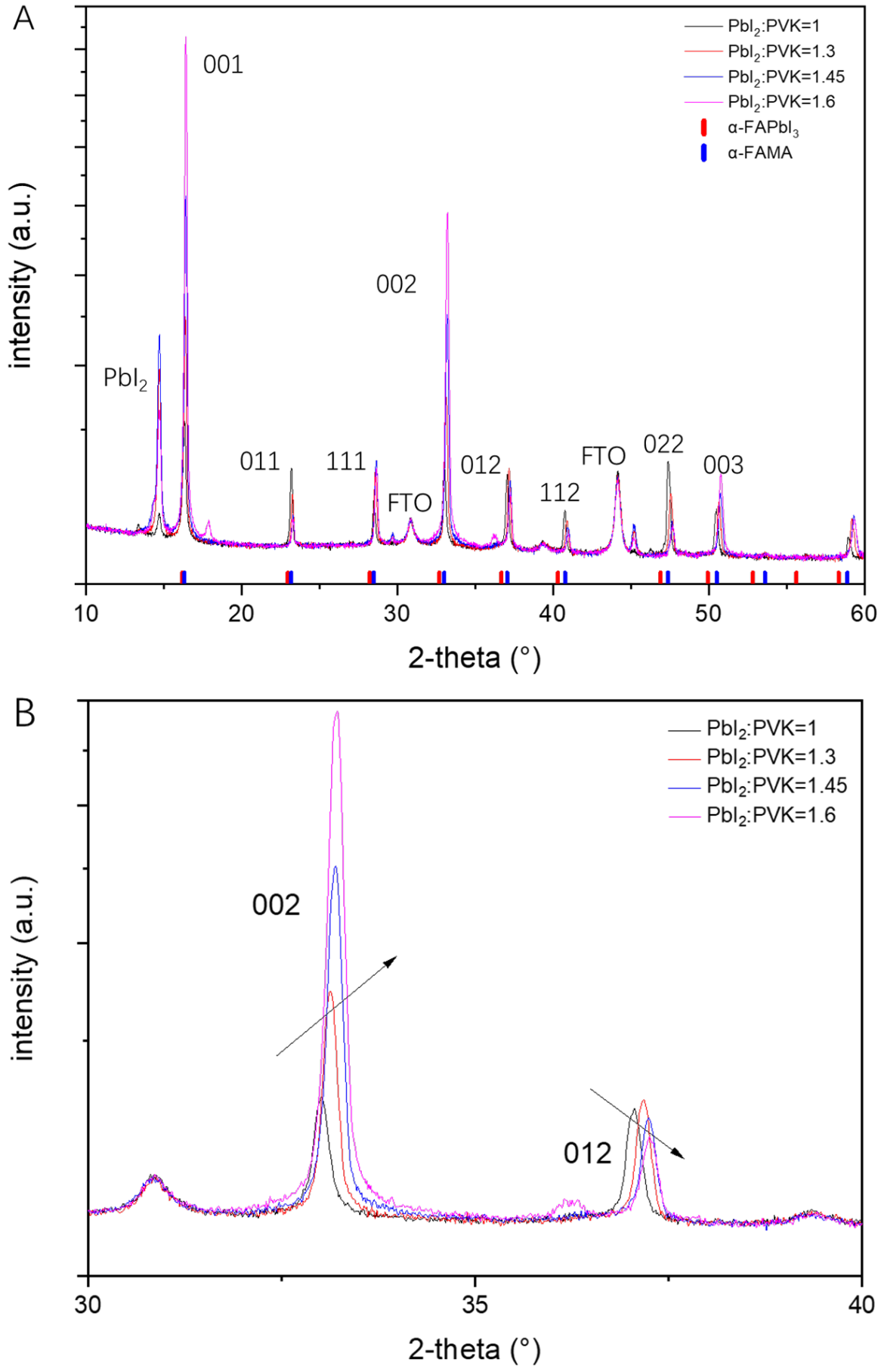

Figure 3.6 XRD patterns for perovskite layer with different amount of MACl and excess PbI_2

Figure 3.7 shows how MACl influences the lattice parameters of the perovskite. It is clear that the lattice parameter is decreasing with increasing MACl amount. However, the lattice parameters no longer changed when the excess amount of MACl exceeded to 0.6M. This indicates that the excess MACl is not involved in the formation of perovskite at this time, but is more likely to be ionized in the perovskite crystal. In previous study, it is found that only very few Cl^- can substitute I^- in the Cl introduced $MAPbI_3$ perovskite[11]. Here, a similar phenomenon can be observed. It seems like the lattice parameter becomes small due to the limited substitution between I^- and Cl^- as the introduced MACl in FAMA perovskite is few. As the amount of introduced MACl reaches 0.6 M, FAMA perovskite cannot accommodate more Cl-, and thus the lattice parameters no longer change.

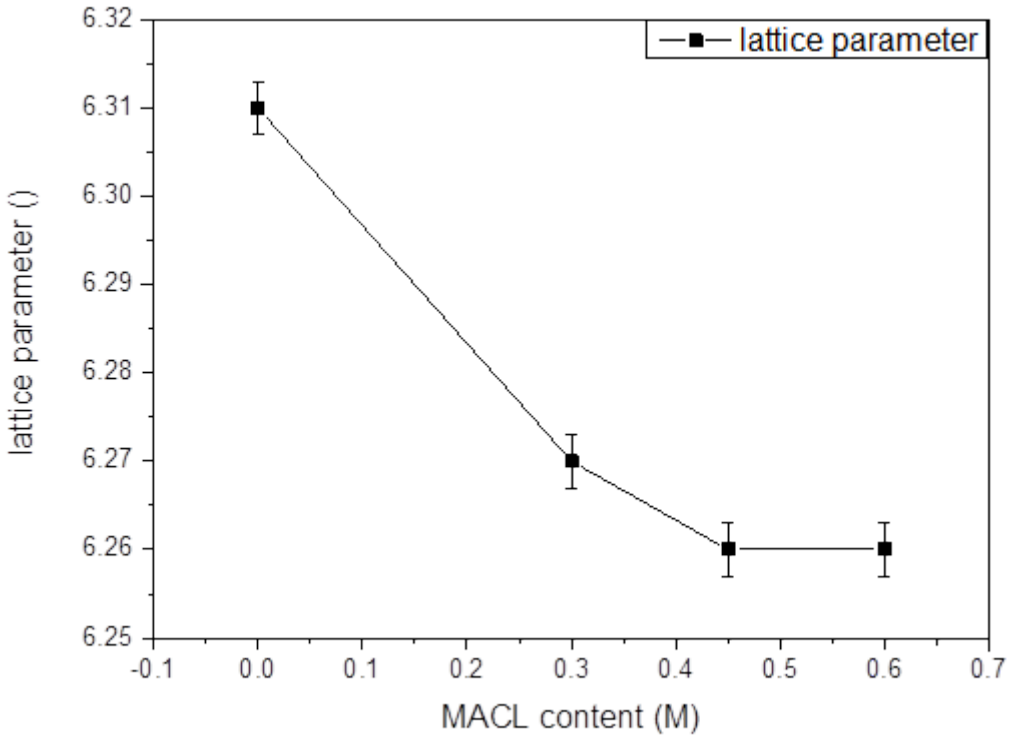

Figure 3.7 Lattice parameter of the CsFAMA perovskite using different amounts of MACl.

Moreover, a preferential orientation appears with adding MACl. Here the ratio between *(022)* and *(002)* is plotted in Figure 3.8 as examples. It is clear that the intensity of the *(00l)* peak family becomes stronger, meanwhile, the *(0kl)* peak family is weakened with increasing the MACl amount, which indicates that the *(00l)* peak is more preferred in the perovskite with MACl. Partial replacement of I^- with small halides of Br^- or Cl^-, can significantly promote the formation of high-quality perovskites. In particular, Cl^- doping can alter the crystallization kinetics, promote rapid nucleation and prolong the crystal growth process, allowing the growth of perovskites with larger grain size and preferential crystal orientation. By increasing the binding energy of each unit, the insertion of PbBr bonds in the lattice can improve crystal stability. As a result, remaining Cl^-

ions in perovskite have a restricted mobility[12].

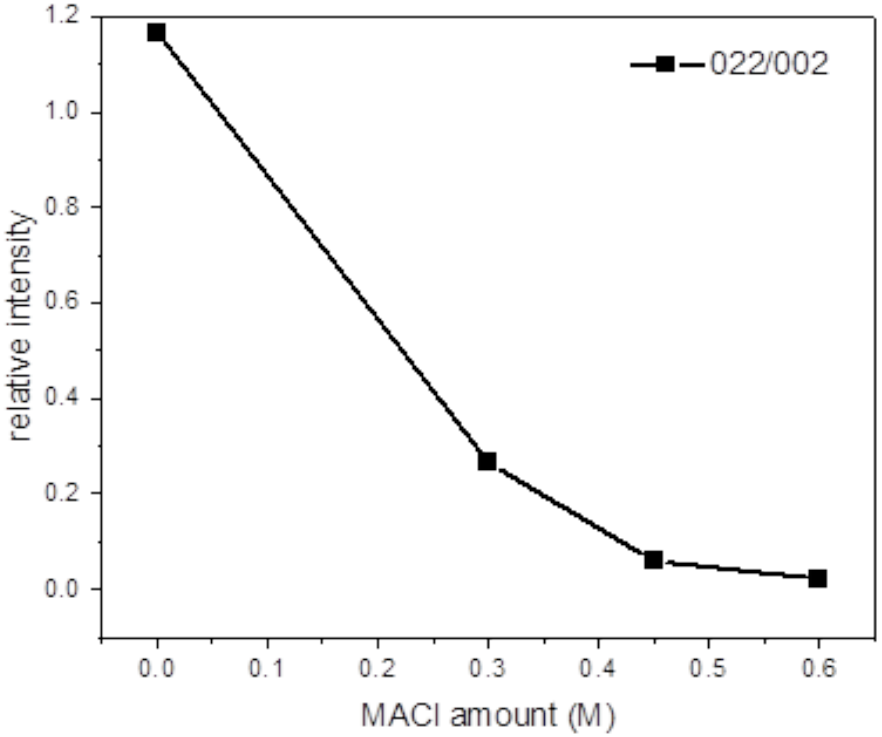

Figure 3.8 Relative intensity between (00l) and (0kl) peak family

Here, the effects of excess PbI_2 are discussed in detailed. From XRD (cf. Figure 3.6A), a significant PbI_2 peak at 14.8° is observed. The intensity of the PbI_2 peak is enhanced with the increase of the introduced amount of PbI_2. The sample used as a control (PbI2:PVK=1:1) exhibits only a weak PbI_2 signal. To distinguish the PbI_2 produced by perovskite decomposition, top-view SEM of fresh perovskite layer (cf. Figure 3.9A), and aged perovskite layer (cf. Figure 3.9C) were taken. In aged perovskite samples, needle-like PbI_2 can be clearly observed and the grain boundaries of perovskite crystals become blurred. In contrast, for the fresh samples, because of the high electronic density of Pb, we observed that PbI_2 presents as bright dots and the perovskite layer shows well-defined, tightly packed grains. The SEM results indicates the detected PbI_2 is not from decomposition and this excess of PbI_2 incorporated free in the perovskite layer instead of forming a new perovskite with MACl. As a result, the composition is formed based on a cubic FAMA phase with MACl and PbI_2 in excess. Figure 3.9B show the cross-section SEM images of perovskite, in which grain boundaries is perpendicular to the substrate. However, in our sample, in addition to the perovskite grains, we also see dots of PbI_2 especially located in the grain boundaries (GBs), as marked in red circles. In Figure 3.9B, grains of PbI_2 (circled in red) can be seen at the edge of grains.

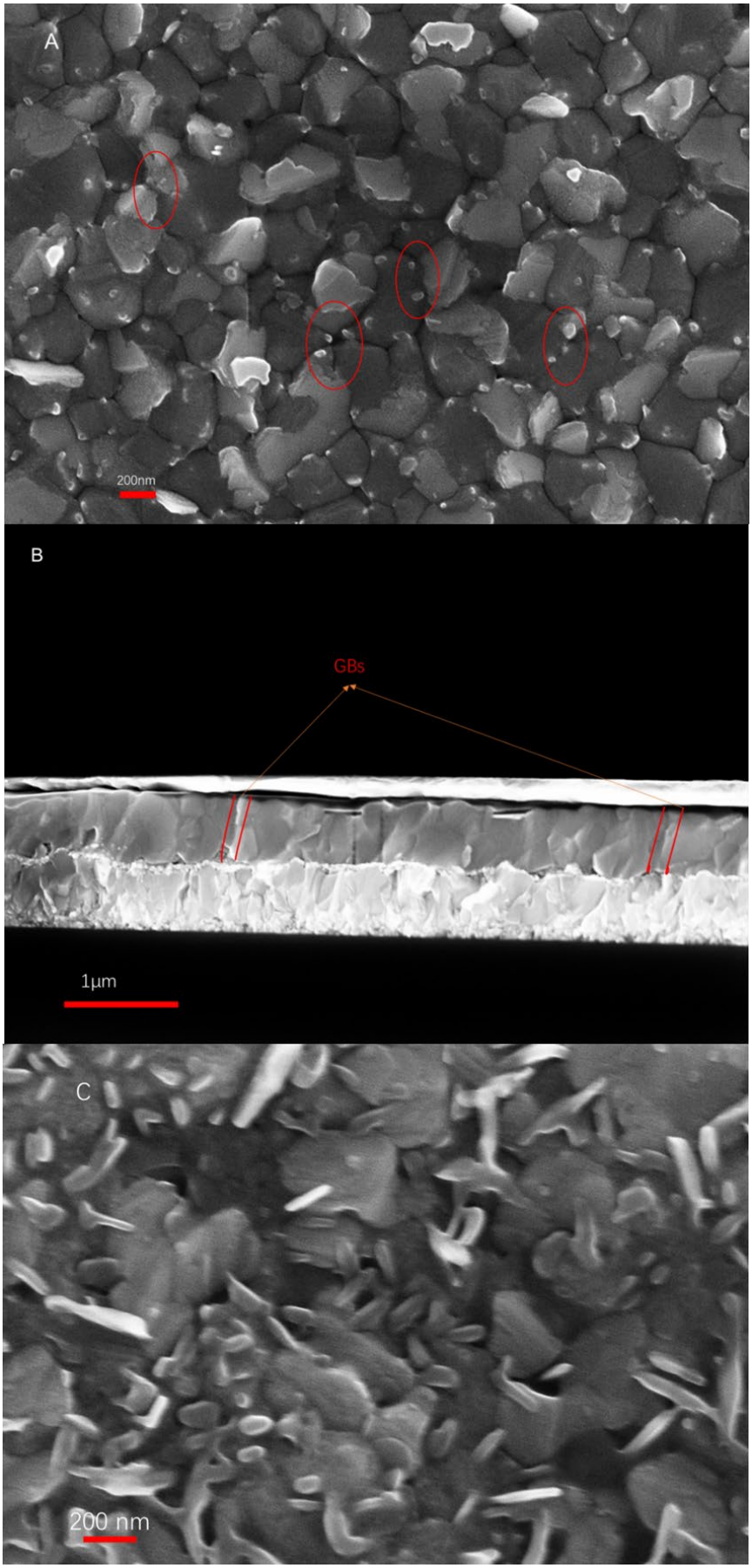

Figure 3.9 A) Top view and B) cross-section view SEM of perovskite with excess PbI_2 and MACl (GB: grain boundary), C) Top view SEM of aged perovskite with excess PbI_2 and MACl.

Following annealing at 100°C, the excess PbI_2 that develops at the grain boundaries of the perovskite films spreads through the grains until it reaches the perovskite surface, as shown schematically in Figure 3.10. Because of perovskite's high crystalline quality, surplus lead iodide will escape from the crystal to the grain boundaries, resulting in a PbI_2 rich area[13]. The small bright dots observed by SEM in Figure 3.9A should indeed be PbI_2 crystals that have grown through the layer, and the dots appear when the voids neighboring the PbI_2 reach the film surface. Because to perovskite's strong crystalline quality, defects may have a greater probability of occupying locations at the surface and in GBs. PbI_2 has a conduction band of 3.44 eV and a valence band of 5.79 eV, respectively[14]. Because PbI_2 has a wider bandgap than perovskite, the band difference between the two materials acts as an energy barrier, preventing excitons from forming due to surface defects and trap states. As a result, the film shows a carrier transmission route with fewer non-radiative channels. The self-induced transformation of PbI_2 can efficiently passivate the grains locally, reducing carrier reorganization and improving device performance.

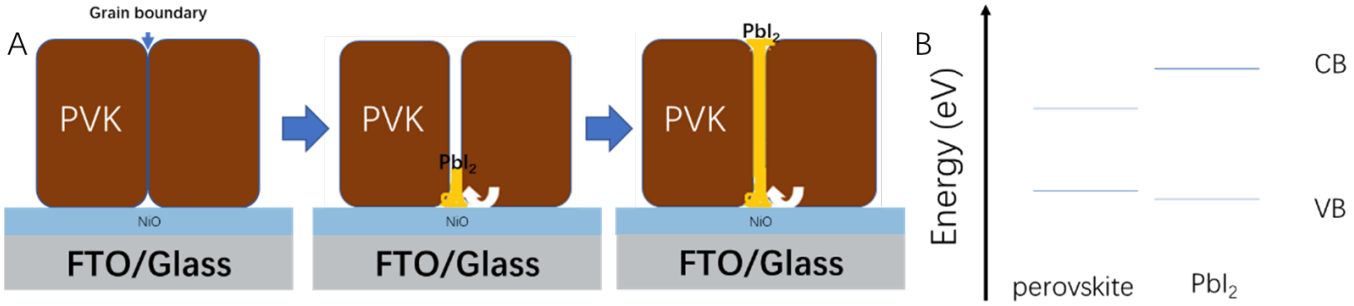

Figure 3.10 A) The schematic of PbI_2 passivated perovskite grain boundary; B) The coexistence of PbI_2 and perovskite in the film shows an energy barrier of the band edge, with the bandgap of 2.35 and 1.5 eV, respectively.

3.2.2. Optical property and devices performance

Figure 3.11A shows UV-visible absorption spectra of CsFAMA perovskite placed on the Cu:NiO hole transport layer with various MACl concentration. These spectra reveal a distinct transition at 725~760nm, as well as a significant blue shift as the proportion of MACl rises. The Tauc plot approach is used to obtain the band gap (Eg) of perovskite materials with varying MACl concentration. After calculating, the band gaps belonging to 0M, 0.3M and 0.45M MACl are 1.61eV 1.63eV and 1.66eV respectively as shown in Figure 3.11B.

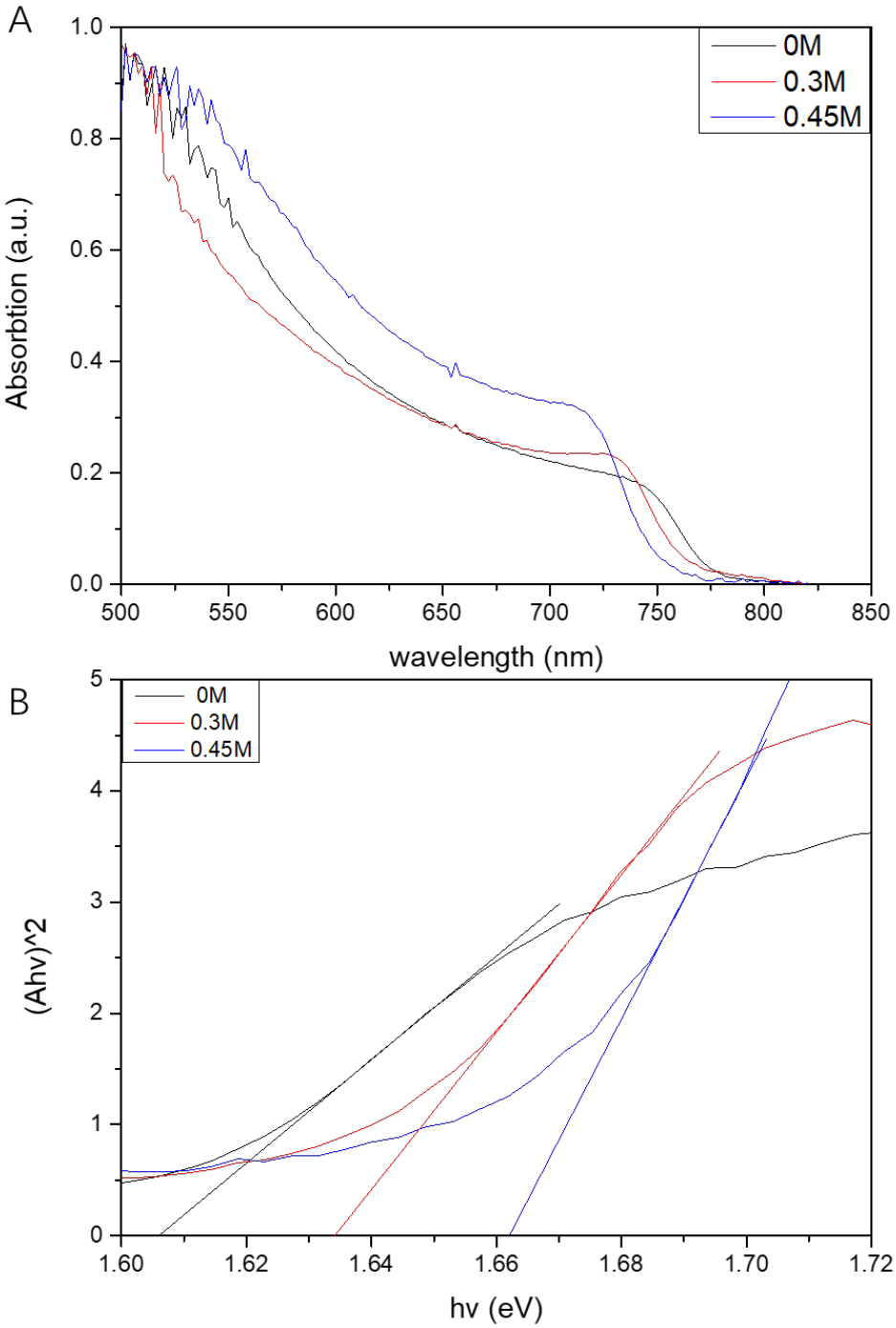

Figure 3.11 A) UV-visible absorption spectra of CsFAMA perovskite with different content of MACl deposited on Cu:NiO/FTO layer; B) Bandgap for perovskite with different amounts of MACl calculated by Tauc plot

In summary, we found that the introduction of MACl can significantly increase the forbidden band width of perovskite, which can bring higher open circuit voltage for perovskite solar cells. In addition, excessive lead iodide also plays a role in passivating the grain boundary, which will theoretically lead to an increase in short-circuit current. The photovoltaic performance of perovskite solar cells produced with the various formulations will next be tested.

A solar simulator in a glove box was used to measure the electrical performance of the cells, as detailed in Chapter 2. For Perovskite-based cells, it is critical to establish a uniform and consistent measuring methodology for all of the cells. Changes in measuring circumstances will have an impact on the device's photoelectric performance. The cells were then tested by changing the voltage at the devices terminals from 1.1 V to -0.1V in 0.02 V steps. The electrical parameters shown were acquired after cycling and stability under light. The cells active surface area is 0.09 cm^2. Table 3.3 shows the best electrical performance of the cells with different amount of MACl.

	Voc (V)	Jsc (mA/cm^2)	FF	PCE (%)
no MACl	1.05	18.96	0.61	12.15
MACl 20 mg (0.3mol)	1.08	20.9	0.62	13.99
MACl 30 mg (0.45mol)	1.1	21.6	0.61	14.49
MACl 40 mg (0.6mol)	0.98	14.12	0.38	5.26

Table 3.3 Performance for the device with different amounts of MACl

The efficiency of the solar cell significantly improves as the amount of PbI_2 and MACl rises. When the quantity of MACl is increased to 0.6M, however, it has a substantial detrimental influence on the device performance. We counted the efficiency of 18 solar cells for each formula in order to ensure consistency in efficiency, as shown in Figure 3.12.

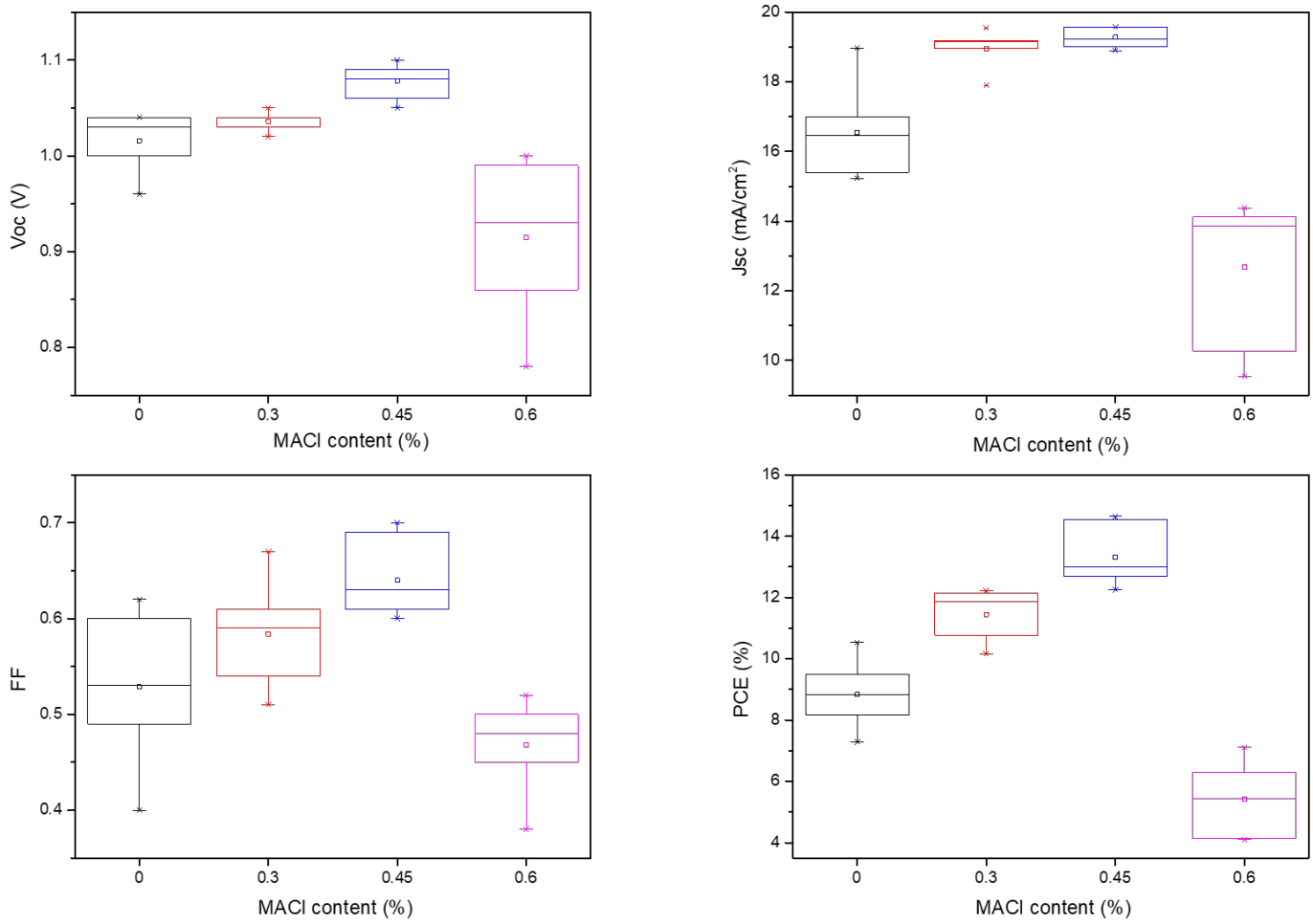

Figure 3.12 Comparison of the device performance distribution using different amounts of MACl in the CsFAMA perovskite preparation while keeping all other parameters constant.

It is observed that all parameters are significantly improved with the increase of MACl content. The improvement of *Voc* is due to the fact that the introduction of MACl increases the band gap of the perovskite. And because of the passivation effects of PbI_2 mentioned above, a significant increase *Jsc* occurs. However, when the introduced amounts of MACl and PbI_2 are too high, the free ions cause defects and increase the carrier recombination. This results in a significant decrease in solar cell performance when the amount of introduced MACl increases to 0.6 M. In addition, we observe a small dispersion of PCE from one series to another, which demonstrates the high reproducibility of the approach. To summarize, we will use in the following the perovskite precursors according to the proportions summarized below in order to maximize solar cell efficiency: PbI_2 (1.45 M), FAI (1.15 M), $PbBr_2$ (0.21 M), MABr (0.21 M), and MACl (0.45 M) in 1 mL of a mixed solvent of DMF/DMSO (4:1 v/v). Then 17.5 µL of CsI solution (2 M in DMSO) was added.

3.3. Engineering of the Cu:NiO HTL surface

As mentioned above, although the perovskite solar cell performances based on NiO_x hole transport layer has

been largely improved, there is still a gap compared to the performance of solar cells using the n-i-p structure. The reason seems to be related to the lower quality of the perovskite layer and the poor contact between NiO_x and perovskite caused by NiO_x surface defects. Surface modification can be considered as a simple and effective way to solve contact problems and adjust surface energy levels to improve charge extraction, thereby improving the cell *FF* and *Jsc* performance [15]. Many passivation materials for n-i-p structured perovskite solar cells have been reported to improve the *FF* and the photovoltaic performance of perovskite solar cells, such as phenethylammonium iodide (PEAI)[16]. However, its poor temperature stability and energy level mismatch make it difficult to be applied to the hole transport layer of the p-i-n structure. Only a few articles have reported passivation layers applied to the hole transport layer of the p-i-n structured perovskite solar cell, such as diethanol amine (DEA) and ferrocenedicarboxylic acid (FDA)[6,17]. In this work, we explore a novel small molecule as passivation agent on the surface of a sol-gel processed Cu:NiO layer, for improving the contact between the Cu:NiO layer and the perovskite, as well as perovskite crystal quality: dimethylamino(4-)pyridine (DMAP). Due to its bifunctional character, DMAP generates a strong connection between perovskite and the Cu:NiO HTL, which not only improves the perovskite crystalline quality but also fixes contact issues. Furthermore, this molecule changes the energy level at the Cu:NiO surface, making hole extraction more favorable. As a consequence, perovskite solar cells based on the structure of FTO/Cu:NiO/DMAP/PVK/PCBM/BCP/Ag presents better performances than reference cells without DMAP.

3.3.1. Passivation layer fabrication

The passivation precursor was made by dissolving 20mg 4-Dimethylaminopyridine (DMAP) in 1 ml isopropanol (IPA). The precursor needs to be stirred under ambient atmosphere at room temperature for 1h. The resulting solution does not need to be filtered. After UV-ozone treatment of the Cu:NiO HTL, the precursor was transferred into a glovebox, and spin-coating of the passivation layer was performed under Argon atmosphere by applying 80µL DMAP IPA solution under 3000rpm spinning speed. After spin-coating, the film needs to be annealed for 10 min at 100 °C. After heat treatment, the substrates were cooled down to room temperature before further deposition steps.

3.3.2. Interaction between DMAP and the perovskite

Figure 3.13A illustrates a DMAP layer modified Cu:NiO layer where the N atom of pyridine forms a chemical bond with Ni atoms in the Cu:NiO film surface. This interaction is very likely due to the high basicity of the pyridine function of DMAP owing to the resonance stabilization from the dimethylamino substituent. The latter is able to coordinate to Pb atoms of the subsequently deposited perovskite layer via the electron lone pair at the nitrogen atom. The favorable interaction between Pb^{2+} ions and organic functional group with lone pairs (e.g.,-OH) was reported previously[6]. Here, the possible interaction between DMAP and PbI_2 was

checked by mixing DMAP and PbI_2 directly. After annealing the mixture at 150°C, a new solid product of white color is formed, as shown in Figure 3.13B.

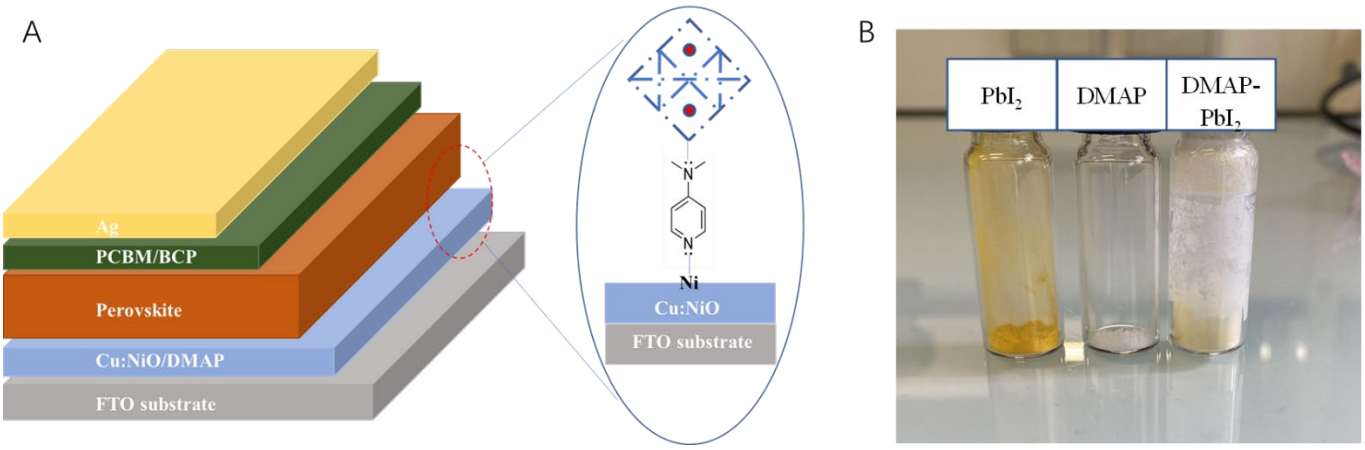

Figure 3.13 A) Schematic illustration of the device structure, where the Cu:NiO layer is modified by DMAP layer, highlighting an enhanced contact at interface though -$N(CH_3)_2$ and Pb in perovskite; B) Photos of DMAP, PbI_2 and mixed PbI_2 and DMAP (115mg PbI_2 mixed with 480mgDMAP, stir under 150° C)

The Fourier-transform infrared (FT-IR) spectra in the wavenumber range from 4000 cm^{-1} to 600 cm^{-1} are presented in Figure 3.14A to study the difference between DMAP and the mixture. To remove the effect of the pyridine group on the results, one pyridine-PbI_2 (py-PbI_2) powder was prepared in the same way. As shown in Figure 3.14A, the spectra of DMAP-PbI_2 shows a significant shift in the range of 3000-2800 cm^{-1} (indicated by the dashed line), which can be attributed to the coordination of the dimethylamino group to Pb center. In the case of the DMAP-PbI_2, slight shifts of the aromatic C-N bond stretching and amine C-N bond stretching were apparently observed, respectively, in the range of 1000 cm^{-1} to 1400 cm^{-1}, see Figure 3.14B. To further check the chemical state of N atom, the result of X-ray photoelectron spectra is shown in Figure 3.14C. It shows a slight shift to lower energy (-0.16 eV) after coordination to PbI_2, indicating a weak N reduction occurred. These phenomena combined with FT-IR spectrum results explain the interaction between PbI_2 and the DMAP layer. In the one-step perovskite deposition process, the precursor solution contains the iodide lead salt intermediate (PbI_n^{2-n}, n = 2-6) and lead-solvent complexes, including methyl ammonium iodide (MAI) and PbI_2[18,19]. The presence of these substances subsequently determines the defect density and morphology of the fully formed active layer[20]. The exposed -$N(CH_3)_2$ group of DMAP on the Cu:NiO surface would assist the assembly of PbI_2 and its coordination to the Cu:NiO surface. This favorable interaction will create benefits for achieving a uniform and complete coverage of the perovskite layer, thereby ensuring good contact with the interface between the Cu:NiO layer after the annealing process.

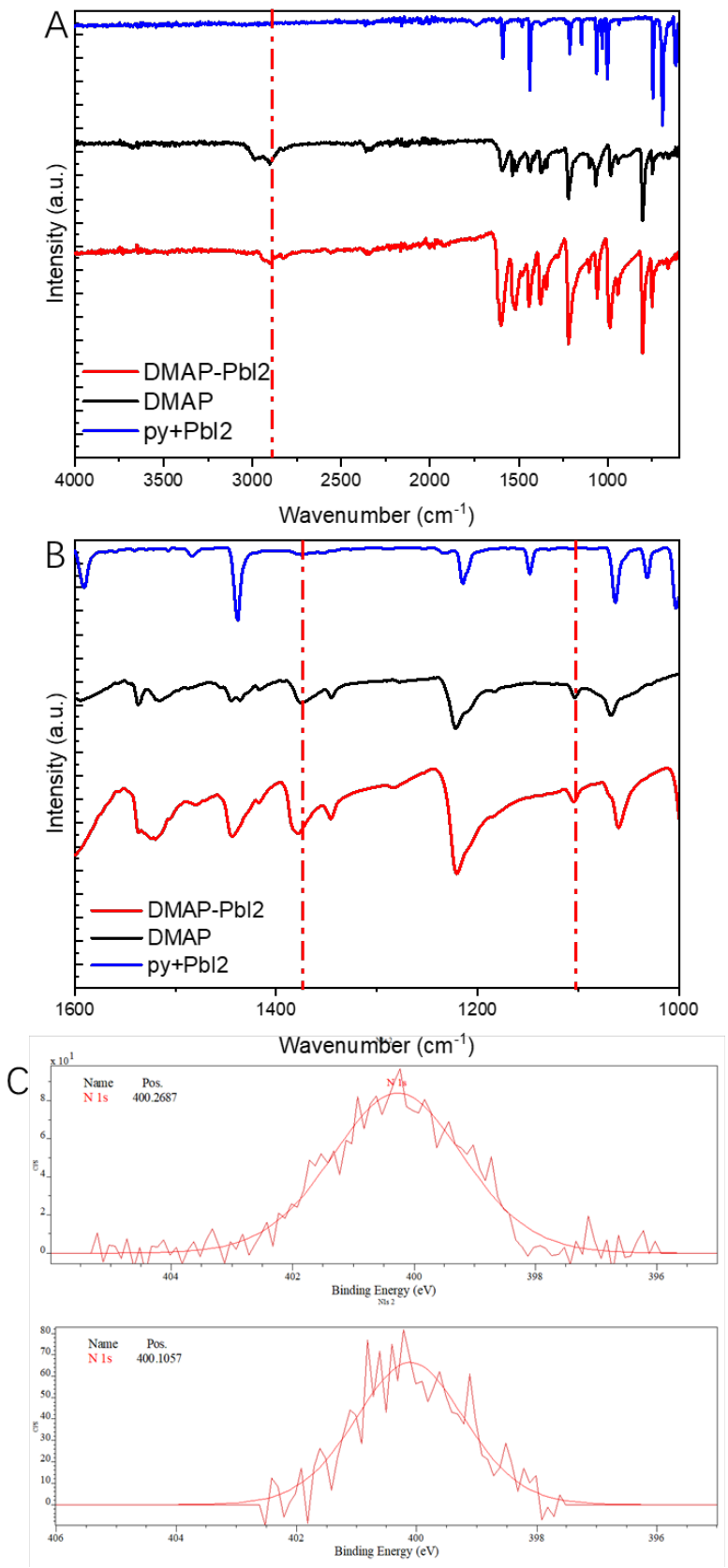

Figure 3.14 A) FT-IR spectra of pure DMAP molecular and DMAP combined PbI_2 in the range of 4000-600cm^{-1}; B) FT-IR spectra of pure DMAP molecular and DMAP combined PbI_2 and in the range of 1600-1000cm^{-1}, pyridine-PbI_2 powder are used as reference to remove the effects from pyridine group; C) High resolution N 1s XPS spectra for DMAP-PbI_2 powder

3.3.3. Interaction between DMAP and Cu:NiO layer

Besides the better contact between Cu:NiO layer and perovskite film by introducing DMAP passivation layer, the energy level of Cu:NiO layer could also be adjusted because of the chemical interaction between Cu:NiO layer and DMAP, which will influence the hole extraction process. To prove the effects on the energy level of HTL, ultraviolet photoelectron spectroscopy (UPS) was taken, as shown in Figure 3.15A-B. After applying DMAP layer, it can be seen that the work function (WF) decreases to 4.51eV. The lower WF of DMAP modified NiO results in a larger V_{bi} and a wider depletion region. Furthermore, this built-in field can help with charge separation, charge transport, and collection of photo-generated carriers, as well as suppressing the back transfer of holes from the NiO HTL to the perovskite layer[21]. Besides the shift of WF, the valence band of the HTL with DMAP passivation is also lowered to 5.26 eV, which is beneficial for the energy level alignment with the perovskite and improve the charge carriers extraction. The energy level scheme of the perovskite solar cell is shown in Figure 3.15C.

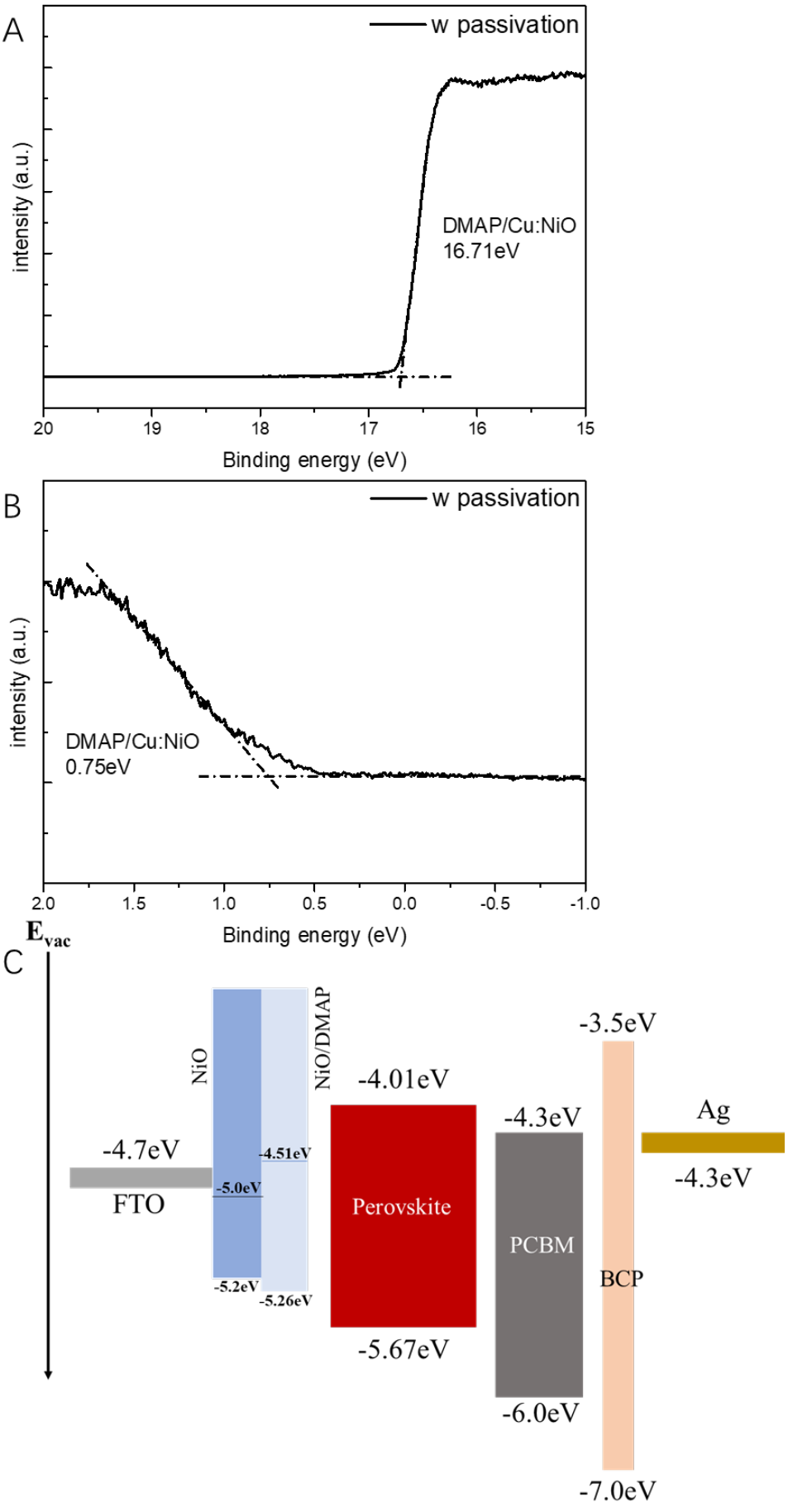
A
w passivation
intensity (a.u.)
DMAP/Cu:NiO
16.71eV
20
19
18
17
16
15
Binding energy (eV)
B
w passivation
intensity (a.u.)
DMAP/Cu:NiO
0.75eV
2.0
1.5
1.0
0.5
0.0
-0.5
-1.0
Binding energy (eV)
C
E vac
NiO
NiO/DMAP
-4.7eV
FTO
-4.51eV
-5.0eV
-5.2eV
-5.26eV
-4.01eV
Perovskite
-5.67eV
-4.3eV
PCBM
-6.0eV
-3.5eV
BCP
-7.0eV
Ag
-4.3eV

Figure 3.15 A,B) Ultraviolet Photoelectron spectra of the Cu:NiO/DMAP layer; C) Schematic energy levels of each layer in the perovskite solar cell. The Fermi levels of each type of Cu:NiO layer are marked with dashed lines.

XPS measurements were carried out to study the surface states of the Cu:NiO hole transport layer (HTL) with DMAP passivation, as shown in Figure 3.16A. On the survey spectra, appearance of N 1s (ca. 400 eV) peak after the passivation clearly indicates the presence of DMAP on the surface. High-resolution Ni 2p spectra recorded for both passivated and pristine NiO films have broad multipeak nature due to the complex shake-up losses typical for this transition metal (cf. Figure 3.16B). The spectra were fit using a model from previous paper[22].The signal for both films is overall similar and can be fit using a set of peaks for NiO demonstrating the absence of Ni^0 and Ni^{3+} contributions, with the main Ni 2p3/2 component situated at 853.55 eV for Cu:NiO and 853.43 eV for Cu:NiO/DMAP. As DMAP is a good electron donor due to its lone pairs[23], it can lower the WF of Cu:NiO[24]. The nucleophilic organic amine present in DMAP can coordinate to Ni^{2+} [25,26] donating electrons and thus inducing the shift of Ni 2p3/2 peak to lower binding energies for the passivated sample. Concomitantly, the decrease of free carrier concentration can reduce the conductivity of the passivated Cu:NiO layer[27]. However, this effect is potentially compensated by the improved hole extraction process, as discussed above.

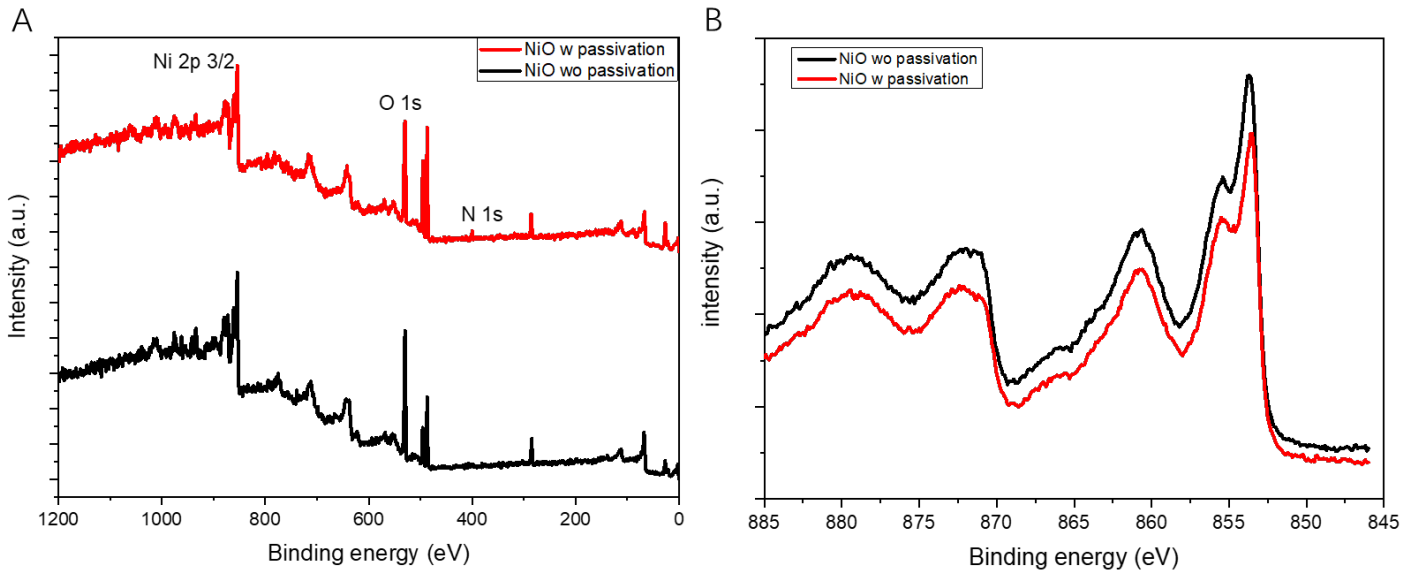

Figure 3.16 A) Overview XPS spectra of the Cu:NiO layer w/wo passivation; B) High resolution Ni 2p XPS spectra.

3.3.4. Structural study by XRD and optical properties

X-ray diffraction (XRD) measurements were performed to evaluate the effect of the presence of DMAP on the crystalline quality of this CsFAMA perovskite layer. Figure 3.17 displays the diffractograms obtained for

perovskite films grown on bare Cu:NiO HTL and DMAP passivated Cu:NiO HTL. In both cases, considering peaks positions, the data are coherent with the expected diffraction pattern for cubic α-phase (space group $Pm\vec{3}m$)[28] with a lattice parameter value of 6.260 ± 0.005 Å and 6.276 ± 0.005 Å, respectively. Besides perovskite phase contributions, peaks associated to polycrystalline FTO (ICDD PDF4 #04-008-8130) at 30.8° and 44.1° appear for both cases, indicating that the X-rays have penetrated the entire perovskite layer, and the components of the full perovskite layer were detected. Moreover, peak associated to *(00l)* textured PbI_2 (ICDD PDF4 #01-079-0803) is present. The relative intensities of the peaks are similar for the two perovskite patterns. Here the ratio between *(022)* and *(002)* is taken as sample. For perovskite based on bare Cu:NiO layer, the ratio is about 0.060,meanwhile, the ratio of perovskite based on passivated Cu:NiO layer is 0.064. This indicates that no indication of any preferential orientation changing with or without DMAP. As mentioned above, the present PbI_2 is not from perovskite degradation, and play a role on passivating grain boundaries to improve *Jsc*[29,30]

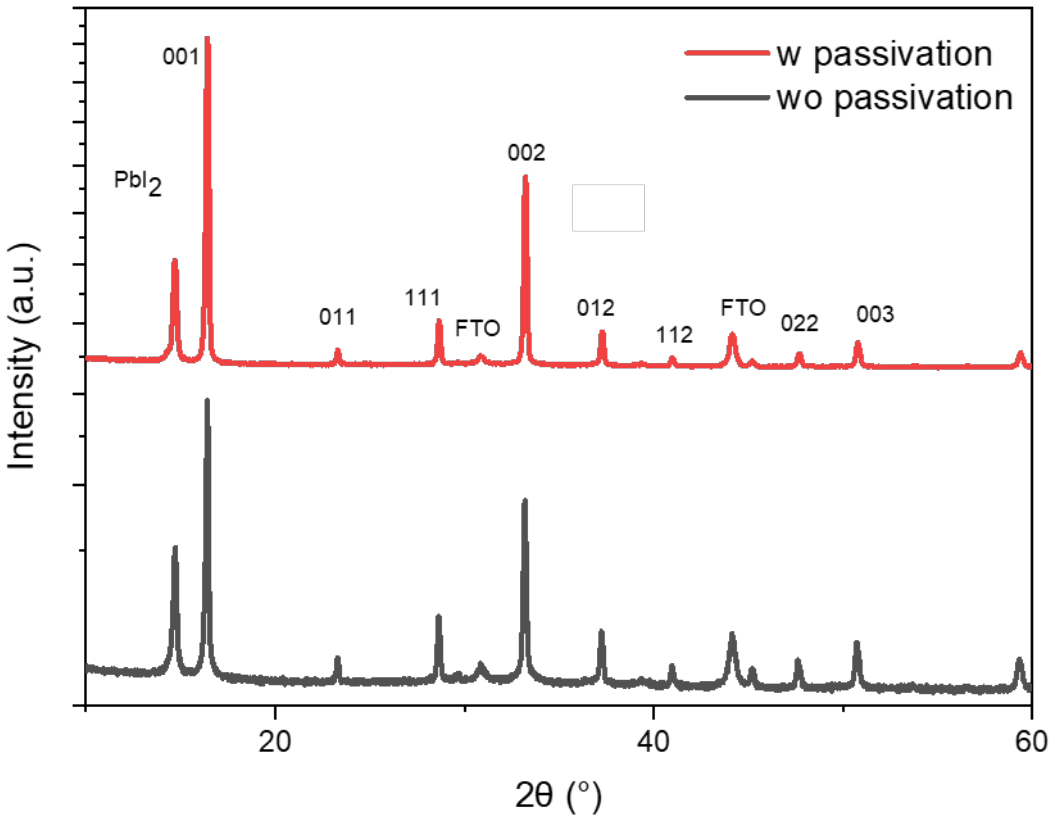

Figure 3.17 XRD patterns of CsFAMA/DMAP/Cu:NiO/FTO and CsFAMA/Cu:NiO/FTO samples.

The perovskite film microstructure, which can directly affect the performance of the full device, has to be considered [31]. In the present case, it mainly concerns the perpendicular crystallite size and strain (distorsion). For quantitative analysis of strain, the instrumental broadening cannot be neglected as it is of the same order of magnitude as the measured FWHMs. However, this instrumental resolution depends on the degree of preferential orientation presenting in perovskite sample, which cannot be determined. Thus, the instrumental

resolution of the configuration used for the XRD measurements does not allow to perform quantitative analysis. However, qualitative information can be obtained considering the evolution of the full width at half maximum (FWHM) of the peaks as a function of the scattering angle 2θ. From cross sectional SEM images the perpendicular crystallite size appears to be larger than 100 nm (cf Figure 3.23). Therefore, the peaks broadening can be considered as coming mainly from the presence of distortion in the perovskite lattice. This is confirmed by the 2θ dependency of the FWHMs displayed in Figure 3.18. In the case of dominant crystallite size contribution, the value of the FWHM would increase more slightly with 2θ (100 nm size crystallites induce a peak broadening of 0.10° and 0.12° respectively at 2θ = 30° and 70°). Hence for both types of perovskite layers, the peak broadening appears to come mainly from the presence of strain. However Figure 3.18 reveals that the passivation of the Cu:NiO film with DMAP improves the crystalline quality of the perovskite by reducing this strain.

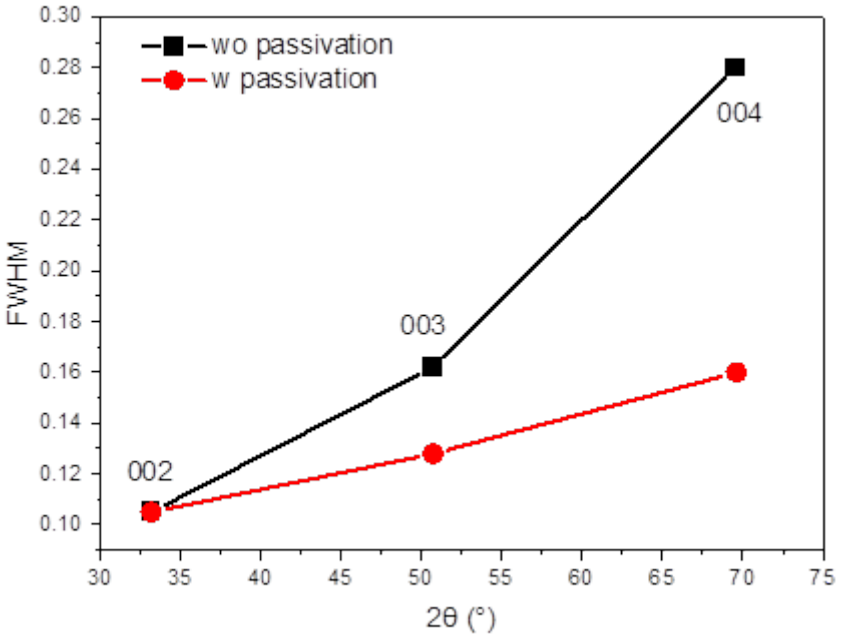

Figure 3.18 Peak full width at half maximum (FWHM) of the different (*00l*) perovskite diffraction peaks.

Since the thicknesses of the perovskite layers based on different substrates are similar (650nm), this better perovskite crystallization likely causes a positive effect on the light harvesting properties, as shown in Figure 3.19A. The UV-vis absorption spectra of Cu:NiO/PVK and Cu:NiO/DMAP/PVK indicates a slight enhancement of light absorption in the whole spectral range. Steady-state PL measurements were performed to study the hole extraction process. As shown in Figure 3.19B, the steady-state PL spectra with an excitation wavelength of 400 nm show that for both types of HTL, the emission band of the perovskite peaks at 760 nm. Although at least 90% of the light should be absorbed in the first 200 nm of the perovskite film (which is excited from the perovskite side and not from the glass substrate side)[32], significant differences can be seen between the two samples. In the case of the DMAP passivation layer, the PL intensity is greatly reduced,

revealing a significant quenching effect. While it presents a better perovskite crystallization for the Cu:NiO/DMAP sample, which in principle leads to a lower trap density for quenching and longer PL lifetime, the DMAP modified Cu:NiO layer has also a stronger interaction with perovskite layer, and therefore a better interface contact. As a consequence, this significant PL quenching behavior indicates that the perovskite film exhibits faster charge transfer kinetics and higher hole extraction ability than the non-passivated Cu:NiO layer, which can effectively reduce the radiative carrier recombination in the PSC active layer, thereby increasing the FF of the device.

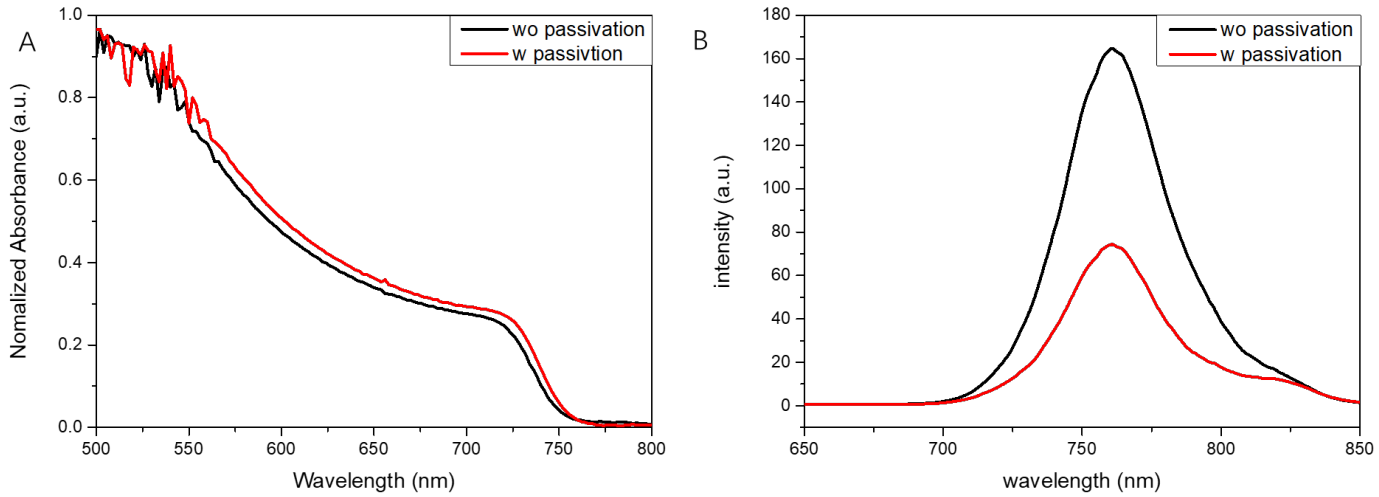

Figure 3.19 A) UV–vis spectra of the perovskite films based on bare Cu:NiO and DMAP/Cu:NiO layer; B) Steady-state photoluminescence (PL) spectra (the small bump at around 825 nm is a measurement artifact).

3.3.5. Morphology study of the perovskite layer

Top-view scanning electron microscope (SEM) images of the Cu:NiO/CsFAMA and Cu:NiO/DMAP/CsFAMA samples have been taken to evaluate the effects of DMAP on the morphology of the perovskite layers. As shown in Figure 3.20A, a large number of small dots appear on the perovskite surface for the sample without DMAP passivation, which correspond to excess PbI_2 crystals[33]. As discussed above, due to its higher electronic density, excess PbI_2 appears brighter than the perovskite in the dark-field images. Moreover, it can be seen clearly some holes present. After use of the DMAP passivation layer, the amount of PbI_2 over-excess on the surface reduces significantly, as shown in Figure 3.20C. The surface roughness of the perovskite based on the two types of substrates was investigated by using AFM, as illustrated in Figure 3.20B and D. The crystal sizes of perovskites grown on the Cu:NiO layer and the Cu:NiO/DMAP layers are around 410nm and 400nm respectively, which does not change much, but perovskite films on bare Cu:NiO layers have a higher roughness of 17.3±1.6 nm RMS, compared to those on Cu:NiO/DMAP layers exhibiting a roughness of 12.4±0.8 nm RMS. Concluding, SEM and AFM analyses show that the DMAP passivation layer not only maintains good perovskite morphology with a low surface roughness, but also results in a reduction

of the excess PbI_2 riched near perovskite surface. Because the conduction band of PbI_2 is relatively high (3.4eV)[14], strong over-excess of PbI_2 at the perovskite surface would build an energy barrier for charge extraction[34] and decrease the device stability under illumination[35]. It has been reported that only a little amount of unreacted PbI_2 near the perovskite surface is beneficial to decrease recombination at the perovskite/charge transport layer interface[36,37].

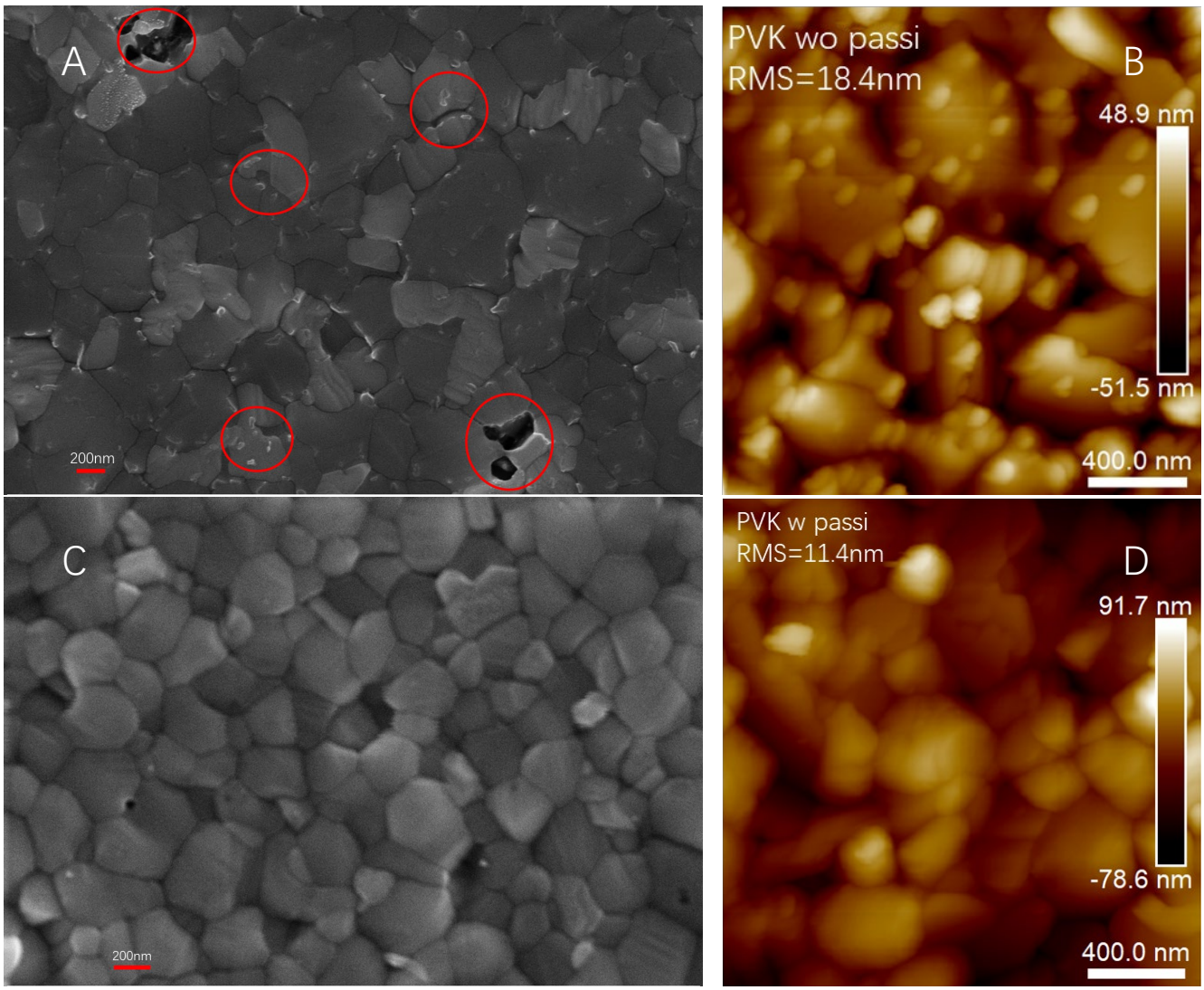

Figure 3.20 A, B) Top-view SEM and AFM images of the perovskite layer grown on bare Cu:NiO, excess PbI_2 is marked by red circles; C, D) Top-view SEM images AFM of the perovskite grown on the DMAP-passivated Cu:NiO layer.

3.3.6. In-plane measurement of the distribution of PbI_2 in the perovskite layer

In order to gain further insight into differences shown in the SEM images and how DMAP on the Cu:NiO layer would affect the PbI_2 distribution throughout the perovskite layer, grazing incidence X-ray diffraction (GIXRD) was performed. By changing the incident angle of the X-ray beam ω, compositions of the perovskite layer at different depths are detected (as shown in Figure 3.21).

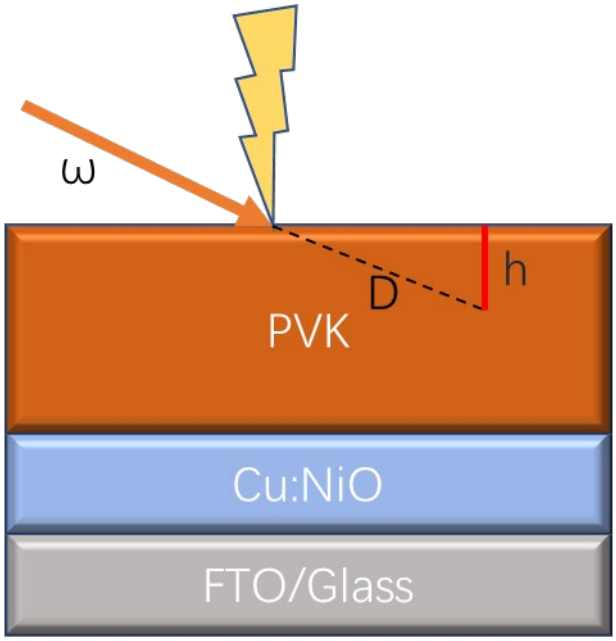

Figure 3.21 Diagram representative of the 'depth measurement' principle with the corresponding quantities ω, D and h

The detected depth can be described as following formula, where D is penetration depth and calculated from the mass absorption coefficient and the density of materials.

$$sin\omega = \frac{h}{D}$$

Scans varying the scattering angle 2θ are performed at fixed incident angle ω. The chosen value for ω determines the depth probed in the sample. Figure 3.22A presents the data obtained for values of the incident angle varying from 0.3° up to 1.0°, which correspond to probed thicknesses ranging between about 40 nm and 200 nm. As for θ/2θ data, diffraction peaks characteristic of the cubic perovskite phase are present, as well as the *(001)* PbI_2 Bragg peak. FTO contribution is missing due to the limited probed depths. For both types of samples, the relative intensities of the PbI_2 and perovskite contributions appear to vary with the value of the incident angle.

In order to quantify this evolution, the ratio of the intensities of the PbI_2 and a-phase CsFAMA (001) peaks was calculated; its evolution as a function of the probed depth is shown in Figure 3.22B. It needs to be noticed that the values at 650nm are from θ-2θ mode, which indicates all the PbI_2 phase and perovskite phase though the active layer are counted. At 650nm, the ratio of the peak area for the case of DMAP passivated Cu:NiO is similar to the one for the cell without passivation. This indicates that the total amount of PbI_2 and perovskite in the active layer does not change significantly due to the introduction of the passivation layer. For both types of samples, the amount of PbI_2 is maximum in the upper part of the layer. This indicates that the growth of the perovskite phase is bottom-up, with the excess lead iodide remaining near the surface. However, it clearly

appears that the amount of untransformed PbI_2 is notably higher in the case of the perovskite layer grown on bare Cu:NiO, in agreement with SEM observations.

Considering that DMAP can coordinate with PbI_2 (as described in the previous section), this surface-sensitive XRD technique proofs that the DMAP passivation layer influences the distribution of PbI_2 though the active layer, and promotes the formation of the perovskite phase near the surface. As illustrated in Figure 3.22C and D, for samples without DMAP passivation, excess PbI_2 precipitates from perovskite crystals and enriches to the surface of the perovskite layer in the process of annealing. After the introduction of the passivation layer, the coordination of DMAP molecules with PbI_2 could anchor the first few PbI_2 molecules, which can slow down the conversion of PbI_2 to perovskite at the initial deposition process. On the other hand, a relatively stable PbI_2 ultrathin layer can ensure the uniform growth of the perovskite layer in the following annealing step and reduce the enrichment of PbI_2 on the surface of the activated layer, which is beneficial for charge extraction and decreases the probability of charge recombination at the interface between the perovskite and top charge transport layer (ETL)[38].

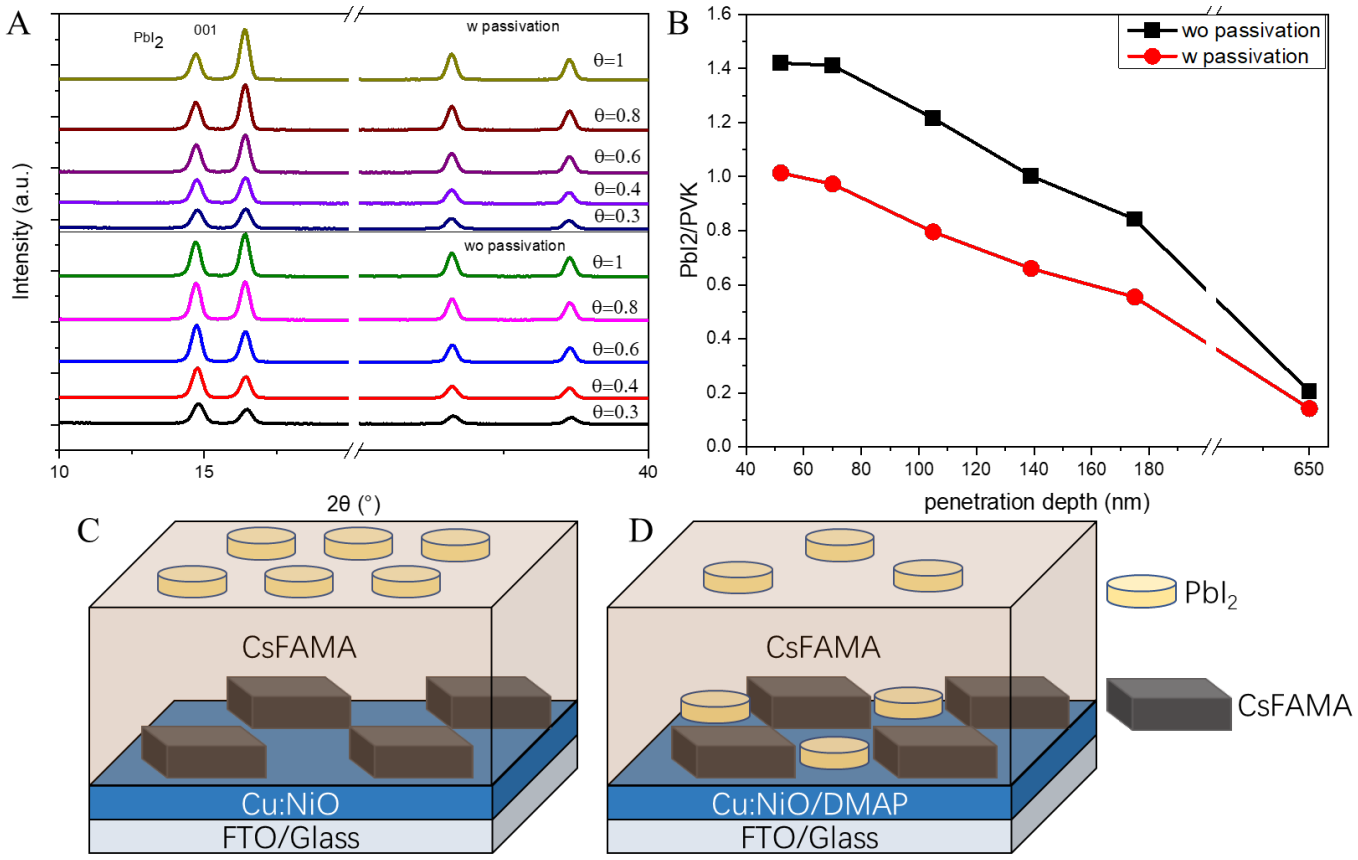

Figure 3.22 A) XRD patterns with different incident angles; B) relative intensities of the PbI_2 and α-phase CsFAMA (001) peaks of the samples w/wo passivation; C, D) Schematic illustration of the perovskite composition based on different HTL, noting the CsFAMA perovskite and PbI_2 in perovskite bulk are not mentioned to avoid misunderstanding.

3.3.7. Photovoltage performance

Based on the above analysis, the DMAP-modified Cu:NiO layer is expected to be beneficial for boosting the solar cell device performance, due to a better interface contact, improved crystallization of the perovskite layer and lower trap density at the perovskite/ETL interface. To get acceptable performance, the thicknesses of the different layers have been optimized: 40~60 nm HTL, around 650 nm for perovskite, 70 nm for [60]PCBM, 4 nm for BCP and 200 nm for Ag as the counter-electrode. Cross-section SEM images of both devices are shown in Figure 3.23 displaying the thickness of each layer.

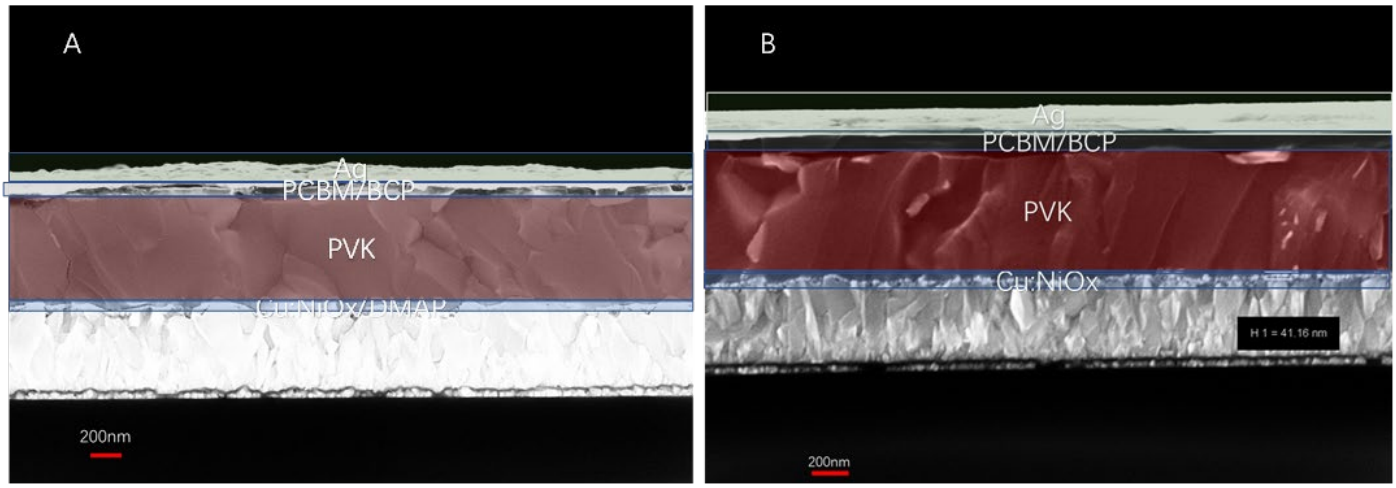

Figure 3.23 Cross-section SEM images of A) FTO/Cu:NiO-DMAP/PVK/PCBM/Ag; B) FTO/Cu:NiO/PVK/PCBM/Ag.

The corresponding J-V curves of devices obtained by low-temperature processing are shown in Figure 3.24A. For devices with the passivation layer, the PCE reaches 17.9% and the values recorded for *FF* were also higher than those containing the non-treated HTL (15.73% PCE). Furthermore, Figure 3.24B shows that the J-V hysteresis almost disappeared after applying the passivation layer. The detailed J–V parameters are illustrated in Table 3.4.

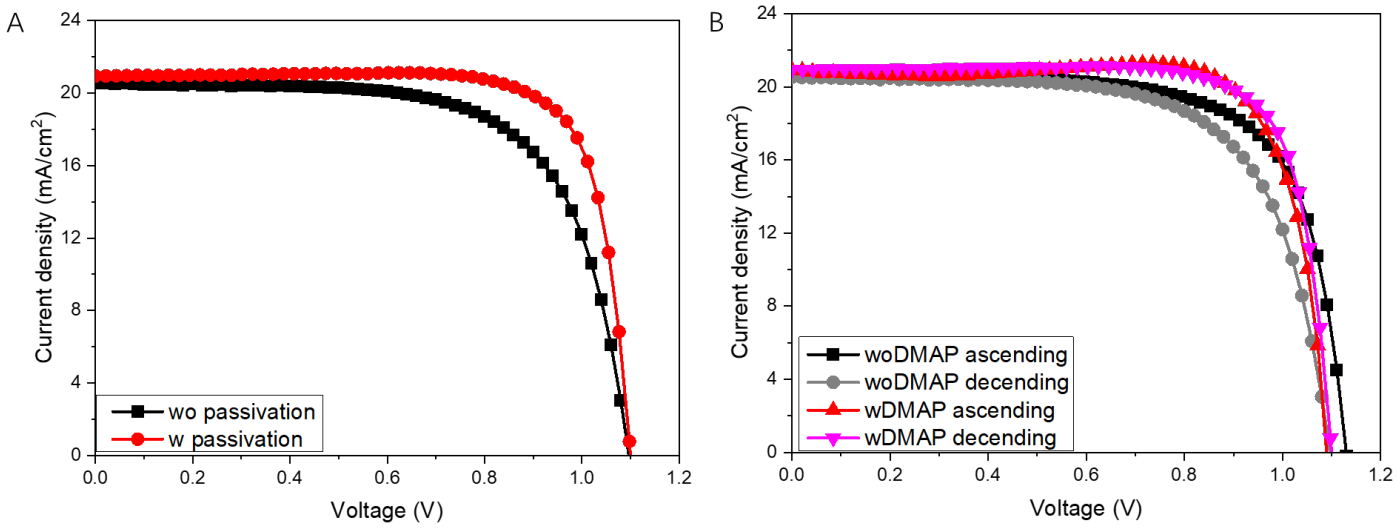

Figure 3.24 A) J/V curves of devices containing Cu:NiO HTLs w/wo DMAP passivation; B) J–V curves of the reverse and forward scans demonstrating the hysteresis behavior.

	Voc (V)	Jsc (mA/cm^2)	Fill Factor (%)	Efficiency (%)	Average	Hysteresis index
wo DMAP descending	1.13	20.80	68.93	16.2	15.73%	6.04%
wo DMAP ascending	1.1	20.55	67.46	15.25		
w DMAP descending	1.10	20.94	78.46	17.98	17.9%	0.9%
w DMAP ascending	1.09	20.91	78.22	17.82		

Table 3.4: Device parameters and hysteresis index of the best performing PSCs using passivated and non-passivated HTLs

The statistical distribution of the efficiencies of the devices tested is shown in Figure 3.25. As a marker in Figure 3.25C, the devices based on the DMAP-modified Cu:NiO layer obviously present a higher FF. For the cells based on bare Cu:NiO layers, most FF values are around 0.63, whereas the FF for devices based on the DMAP/Cu:NiO devices is in the range of 0.75, with highest value being 0.78. This confirms the diverse

advantages of DMAP passivation of the HTL discussed before: lower trap density near the surface, improved perovskite crystallization and enhanced light absorbance of the devices. Also, the higher FF and smaller hysteresis indicate a better extraction of the charge carriers, which is caused by the better energy level alignment and less nonradiative recombination at the interface between the perovskite and the charge transport layer.

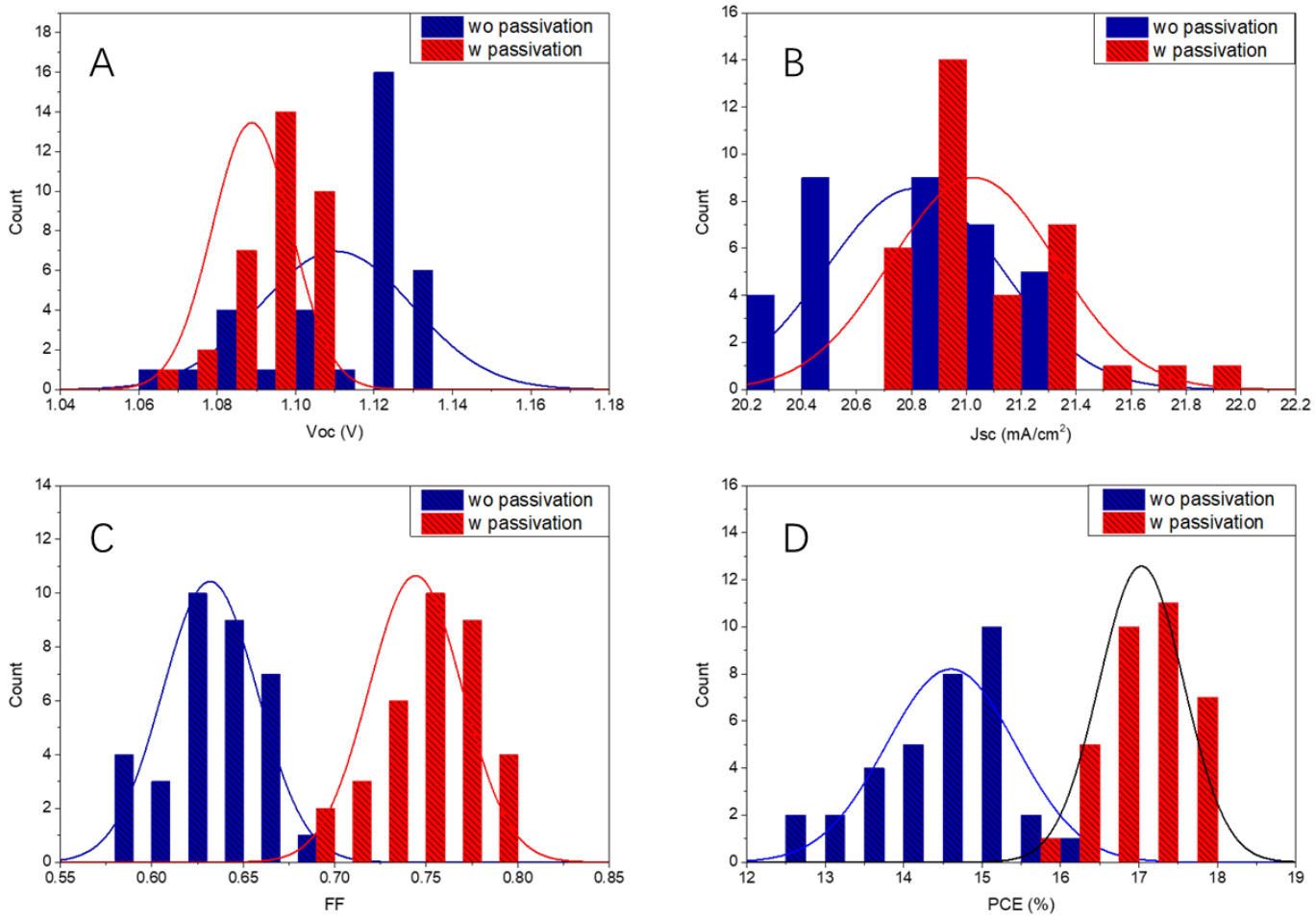

Figure 3.25 Comparison of the device performance distribution on each HTL.

Next, by examining the link between V_{oc} and light intensity, I was able to learn more about the device charge carrier recombination mechanisms (see Figure 3.26). If recombination of free electrons and holes in the active layer dominates, the slope of *Voc* against light intensity is often larger than kT/q, and *Voc* is significantly dependent on the incident light intensity, where q is the electron charge, k is the Boltzmann constant, and T is the Kelvin temperature[39]. The slope of the device without DMAP passivation layer is 2.1 kT/q, whereas the slope of the device containing the DMAP layer is lower (1.19 kT/q). This result is strong evidence that there is no noticeable charge barrier at the interface when the passivation layer is applied. These findings support the idea that carrier recombination is largely suppressed in the passivation layer, which can be attributed to a combination of factors, including reduced perovskite crystal strain/better perovskite crystalline quality, and in this case, better carrier extraction due to the modified HTL/perovskite interface.

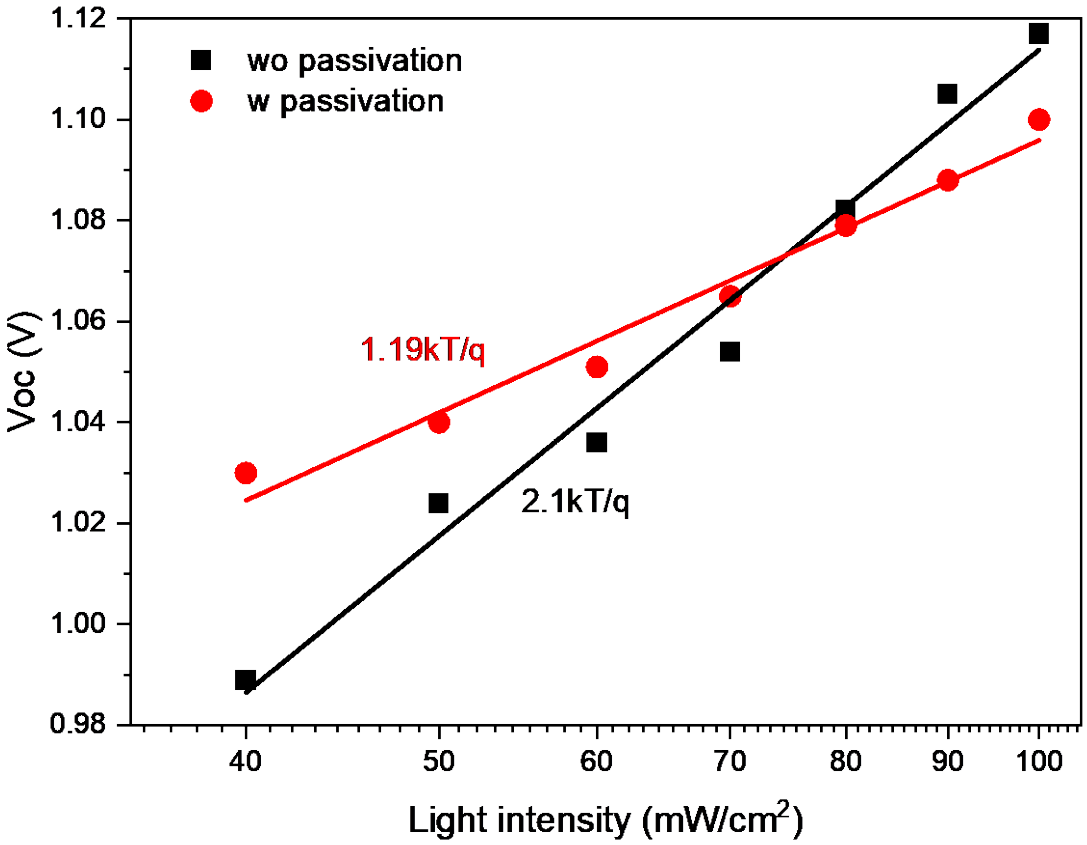

Figure 3.26 Device Voc vs. light intensity for perovskite solar cells w/wo DMAP passivation layer.

Long-term stability is another key parameter to be evaluated for the economic value of perovskite solar cells. As shown in Figure 3.27, the DMAP-modified device maintained 87% of its initial PCE after 72h storage in the ambient air (50% humidity, 25°C) and dark environment, while the cell without DMAP modification lost 22% of its initial PCE. The greater crystalline quality and lower strain of the perovskite crystals formed on the passivation layer compared to the non-passivated HTL may account for the enhanced stability. Furthermore, the presence of the passivation layer at the interface between the electron transport layer and the perovskite alters the distribution of lead iodide inside the perovskite crystal, resulting in fewer pinholes and defects. Over time, these defects may extend, which has a negative impact on performance[40]. We point out that this stability test just serves for the comparison of the behavior of perovskite solar cells fabricated under identical conditions with the only difference being the DMAP passivation layer. As for other types of perovskite solar cells, their operational stability could be further strongly enhanced by employing appropriate encapsulation techniques.

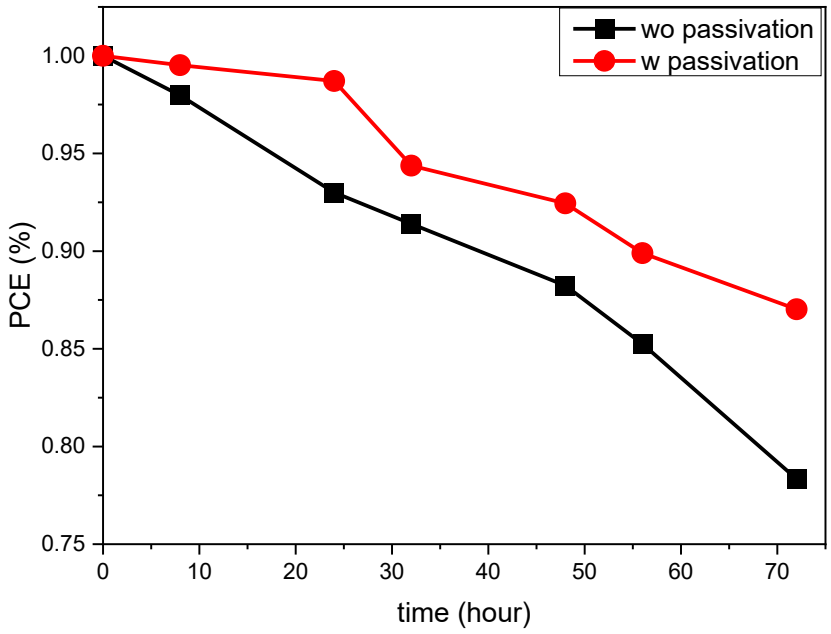

Figure 3.27 Stability measurements of devices based on the two types of HTL exposed to ambient atmosphere (50% humidity, 25°C).

Conclusion

In this chapter, I presented the perovskite system related to my work, its optimization for use in p-i-n solar cells and the entire preparation process of the devices. By using custom FTO conductive glass and molds, I set the standard for perovskite solar cell preparation. In addition, optimization was performed for the perovskite precursors. MACl and excess of PbI_2 were introduced to improve the photovoltaic conversion efficiency of the solar cells. The presence of MACl directly affects the crystallization of perovskite. In fact, as the amount of MACl increases, I find that the lattice parameter of perovskite crystals appear to shrink to some extent and present preferential orientation. More precisely, with the increase of MACl, the (*00l*) crystallographic orientation of the cubic phase CsFAMA perovskite becomes preferred. In addition, with the increase of MACl, I increased the band gap of the perovskite to 1.66 eV., which can improve the *Voc* of the solar cell. On the other hand, the introduction of too much MACl and PbI_2 has a negative effect on the photovoltaic performance of the solar cells, the optimum amount has been determined.

In order to improve the interface quality between the HTL and the perovskite layer, our study established a simple passivation molecule, DMAP, for enhancing the performance and stability of planar perovskite solar cells. This bifunctional molecule can cross-link the Cu-doped NiO hole transport layer with the triple-cation perovskite (CsFAMA) layer by forming chemical interactions, i.e., pyridine-NiO, $N(CH_3)_2$-Pb. These interactions induce several beneficial properties, including enhanced perovskite crystallization and film morphology, absence of pinholes in the perovskite layer, and a better energy level alignment with the CsFAMA perovskite. These improvements combined with enhanced crystal quality and better PbI_2 distribution throughout the perovskite layer significantly enhance charge carrier extraction and transport, and reduce undesired charge recombination processes. By consequence, the *Jsc* and *FF* values were improved in the PSCs, and a PCE over 17.5% was obtained with negligible hysteresis, significantly higher than that in the case of reference PSCs without DMAP (maximum 15.7%). Furthermore, the DMAP passivation has also improved solar cell stability, with about 90% PCE retention after storage in high humidity environment, most probably because of the better crystalline quality of the perovskite and less PbI_2 near the surface and interface with the ETL. Therefore, this study brings new insights into the surface modification of the technologically important HTL NiO for improving the photovoltaic performance and stability of perovskite solar cells and pave the way for future work on inorganic hole transport material based perovskite solar cells.

References

1. Slimi, B. *et al.* Perovskite FA1-xMAxPbI3 for Solar Cells: Films Formation and Properties. *Energy Procedia* 102, 87–95 (2016).
2. Medjahed, A. A. Structure-properties correlation in hybrid perovskite for photovoltaics. (2021).
3. Xie, F. *et al.* Vertical recrystallization for highly efficient and stable formamidinium-based inverted-structure perovskite solar cells. *Energy Environ. Sci.* 10, 1942–1949 (2017).
4. Saliba, M. *et al.* Cesium-containing triple cation perovskite solar cells: Improved stability, reproducibility and high efficiency. *Energy Environ. Sci.* 9, 1989–1997 (2016).
5. Xue, Q. *et al.* Dual Interfacial Modifications Enable High Performance Semitransparent Perovskite Solar Cells with Large Open Circuit Voltage and Fill Factor. *Adv. Energy Mater.* 7, 1–9 (2017).
6. Bai, Y. *et al.* Effects of a Molecular Monolayer Modification of NiO Nanocrystal Layer Surfaces on Perovskite Crystallization and Interface Contact toward Faster Hole Extraction and Higher Photovoltaic Performance. *Adv. Funct. Mater.* 26, 2950–2958 (2016).
7. Chen, W. *et al.* Understanding the Doping Effect on NiO: Toward High-Performance Inverted Perovskite Solar Cells. *Adv. Energy Mater.* 8, 1–10 (2018).
8. Manders, J. R. *et al.* Solution-Processed Nickel Oxide Hole Transport Layers in High Effi ciency Polymer Photovoltaic Cells. *Adv. Funct. Mater.* 23, 2993–3001 (2013).
9. Zhao, L. *et al.* Optical and electrochemical properties of Cu-doped NiO films prepared by electrochemical deposition. *Appl. Surf. Sci.* 257, 3974–3979 (2011).
10. Birnie, D. P. A model for drying control cosolvent selection for spin-coating uniformity: The thin film. *Langmuir* 29, 9072–9078 (2013).
11. Dally, P. Cellules Solaires à base de Matériaux Pérovskites : De la caractérisation des matériaux à l'amélioration des rendements et de la stabilité. (2019).
12. Zhang, H. *et al.* Influence of Cl Incorporation in Perovskite Precursor on the Crystal Growth and Storage Stability of Perovskite Solar Cells. *ACS Appl. Mater. Interfaces* 11, 6022–6030 (2019).
13. Chen, Q. *et al.* Controllable self-induced passivation of hybrid lead iodide perovskites toward high performance solar cells. *Nano Lett.* 14, 4158–4163 (2014).
14. Cho, K. T. *et al.* Highly efficient perovskite solar cells with a compositionally engineered perovskite/hole transporting material interface. *Energy Environ. Sci.* 10, 621–627 (2017).
15. Xu, L. *et al.* Inverted perovskite solar cells employing doped NiO hole transport layers: A review. *Nano Energy* 63, 103860 (2019).
16. Lee, D. S. *et al.* Passivation of Grain Boundaries by Phenethylammonium in Formamidinium-Methylammonium Lead Halide Perovskite Solar Cells. *ACS Energy Lett.* 3, 647–654 (2018).

17. Zhang, J. *et al.* Efficient and ultraviolet durable planar perovskite solar cells: Via a ferrocenecarboxylic acid modified nickel oxide hole transport layer. *Nanoscale* 10, 5617–5625 (2018).
18. Hamill, J. C., Schwartz, J. & Loo, Y. L. Influence of Solvent Coordination on Hybrid Organic-Inorganic Perovskite Formation. *ACS Energy Lett.* 3, 92–97 (2018).
19. Rahimnejad, S., Kovalenko, A., Forés, S. M., Aranda, C. & Guerrero, A. Coordination Chemistry Dictates the Structural Defects in Lead Halide Perovskites. *ChemPhysChem* 2795–2798 (2016) doi:10.1002/cphc.201600575.
20. Stewart, R. J., Grieco, C., Larsen, A. V., Doucette, G. S. & Asbury, J. B. Molecular Origins of Defects in Organohalide Perovskites and Their Influence on Charge Carrier Dynamics. *J. Phys. Chem. C* 120, 12392–12402 (2016).
21. Yang, G. *et al.* Interface engineering in planar perovskite solar cells: Energy level alignment, perovskite morphology control and high performance achievement. *J. Mater. Chem. A* 5, 1658–1666 (2017).
22. Biesinger, M. C., Payne, B. P., Lau, L. W. M., St, R. & Smart, C. X-ray photoelectron spectroscopic chemical state quantification of mixed nickel metal , oxide and hydroxide systems. *Surf. Interface Anal. An Int. J. devoted to Dev. Appl. Tech. Anal. surfaces, interfaces thin Film.* 324–332 (2009) doi:10.1002/sia.3026.
23. Garnier, J., Kennedy, A. R., Berlouis, L. E. A., Turner, A. T. & Murphy, J. A. Structure and reactivity in neutral organic electron donors derived from 4-dimethylaminopyridine. *Beilstein J. Org. Chem.* 6, 4–11 (2010).
24. Lindell, L. *et al.* Characterization of the interface dipole at the paraphenylenediamine-nickel interface: A joint theoretical and experimental study. *J. Chem. Phys.* 122, (2005).
25. Hercules, D. M. Electron spectroscopy for chemical analysis. *Proc. Soc. Anal. Chem.* 10, 193–194 (1973).
26. Grim, S. O., Matienzo, L. J. & Swartz, W. E. X-Ray Photoelectron Spectroscopy of Some Nickel Dithiolate Complexes. *J. Am. Chem. Soc.* 94, 5116–5117 (1972).
27. Qiu, Z. *et al.* Enhanced physical properties of pulsed laser deposited NiO films via annealing and lithium doping for improving perovskite solar cell efficiency. *J. Mater. Chem. C* 5, 7084–7094 (2017).
28. Zheng, G. *et al.* Manipulation of facet orientation in hybrid perovskite polycrystalline films by cation cascade. *Nat. Commun.* 9, 1–11 (2018).
29. Du, T. *et al.* Formation, location and beneficial role of PbI2 in lead halide perovskite solar cells. *Sustain. Energy Fuels* 1, 119–126 (2017).

30. Wang, L., Mccleese, C., Kovalsky, A., Zhao, Y. & Burda, C. Femtosecond Time-Resolved Transient Absorption Spectroscopy of CH3NH3PbI3 Perovskite Films: Evidence for Passivation Effect of PbI2. *J. Am. Chem. Soc.* 136, 12205–12208 (2014).
31. Zou, Y. *et al.* Reduced Defects of MAPbI 3 Thin Films Treated by FAI for High-Performance Planar Perovskite Solar Cells. *Adv. Funct. Mater.* 29, 1–7 (2019).
32. De Wolf, S. *et al.* Organometallic halide perovskites: Sharp optical absorption edge and its relation to photovoltaic performance. *J. Phys. Chem. Lett.* 5, 1035–1039 (2014).
33. Jiang, Q. *et al.* Planar-Structure Perovskite Solar Cells with Efficiency beyond 21%. *Adv. Mater.* 29, 1–7 (2017).
34. Bi, D., El-Zohry, A. M., Hagfeldt, A. & Boschloo, G. Unraveling the effect of PbI2 concentration on charge recombination kinetics in perovskite solar cells. *ACS Photonics* 2, 589–594 (2015).
35. Schoonman, J. Organic-inorganic lead halide perovskite solar cell materials: A possible stability problem. *Chem. Phys. Lett.* 619, 193–195 (2015).
36. Liu, F. *et al.* Is Excess PbI2 Beneficial for Perovskite Solar Cell Performance? *Adv. Energy Mater.* 6, 1–9 (2016).
37. Merdasa, A. *et al.* Impact of Excess Lead Iodide on the Recombination Kinetics in Metal Halide Perovskites. *ACS Energy Lett.* 4, 1370–1378 (2019).
38. Wolff, C. M., Caprioglio, P., Stolterfoht, M. & Neher, D. Nonradiative Recombination in Perovskite Solar Cells: The Role of Interfaces. *Adv. Mater.* 31, (2019).
39. Jiang, Q. *et al.* Surface passivation of perovskite film for efficient solar cells. *Nat. Photonics* 13, 460–466 (2019).
40. Sherkar, T. S. *et al.* Recombination in Perovskite Solar Cells: Significance of Grain Boundaries, Interface Traps, and Defect Ions. *ACS Energy Lett.* 2, 1214–1222 (2017).

Chapter IV. Hole transport layer fabrication by an innovative method

In Chapter 3, we established a bunch of standard procedures for making perovskite solar cells and optimizing the formulation of perovskite precursors. The hole transport layer Cu:NiO is produced using the spin-coating method. Despite the high photoelectric conversion efficiency of perovskite solar cells based on this hole transport layer, limited repeatability remains an issue. This could be owing to the lack of homogeneity of the layers produced by the spin-coating method, which can include pinholes and uncontrolled contaminants. These factors may have an impact on the carrier transport within the hole transport layer (HTL).

To solve these issues, we propose a novel approach for realizing the HTL using electrostatic spray deposition (ESD). This method not only enables the development of NiO films with fewer defects, but also enables the facile introduction of dopants. It also enables the exact control of the film thickness, which is critical for light transmission. In this study Cu:NiO films produced by spin-coating and ESD are compared as hole transport layers in perovskite solar cells. To increase the charge extraction efficiency and promote perovskite crystallization, copper was used as a dopant[1]. Prior research has revealed that cells based on Cu-doped NiO perform better than cells made with undoped NiO, and that an optimal value of 5 mol. % Cu dopant exists for NiO films[2,3].

This chapter is devoted to the optimization of the microstructure and composition of the HTL by ESD and spin-coating. The objectives are to fabricate a thin and dense HTL to enhance the performances of the perovskite solar cell. The principle of ESD is detailed in Chapter 2. By varying the ESD conditions such as precursor concentration, substrate temperature, deposition time, etc., the morphology and thickness of the ESD Cu:NiO HTL are optimized to maximize the photovoltaic efficiency of the perovskite solar cell.

In addition, we also tried to dope the NiO layer using other elements, such as Li^+. We analyzed the surface morphology of the Li:NiO layer, the optimum doping concentration, and the photovoltaic conversion efficiency of perovskite solar cells based on this Li:NiO HTL. The problems of this system are also discussed.

4.1. Cu:NiO hole transport layer by ESD

4.1.1. Deposition conditions

FTO conductive glasses from SOLARONIX (Switzerland) were used as the substrates for ESD. These 25 mm x 17 mm substrates are fully coated with FTO and have a square resistance of 10 Ω/sq. Their transmittance in the visible light region can reach 75%. Their total thickness is 3 mm, of which 200 nm is FTO. To remove contaminants on the transparent conductive glass, these substrates were first immersed in an acetone washing solution using an ultrasonic bath for 30 minutes. Then they were cleaned with a cleaning agent and soaked in deionized water for 10 minutes in an ultrasonic bath. Finally, the conductive glasses were immersed in isopropanol for ultrasonic cleaning for 30 minutes. After washing, the substrates were dried in a clean oven at 70°C and ambient humidity for at least 30 minutes. The dried substrates should be stored in a dry and clean environment. Before being applied to ESD, the FTO layer needs to be treated under UV-Ozone for 30 min. Noticing that the FTO used here was NOT the same as the FTO used in Chapter III, and that this can cause differences in the device performances, making it impossible to directly compare the results of the different chapters. The roughness of FTO used here is over 60nm.

For the deposition of Cu:NiO layers through electrostatic spray deposition, different Cu:NiO precursor solutions varying the concentration from 0.02, 0.01 M to 0.005 M for a 5 atomic percent of copper are prepared by dissolving nickel (II) nitrate hexahydrate ($Ni(NO_3)_2{\cdot}6H_2O$, Sigma Aldrich, 99.00 %) along with copper (II) nitrate trihydrate ($Cu(NO_3)_2{\cdot}3H_2O$, Sigma Aldrich, 99.00%) in 30 ml of diethylene glycol mono butyl ether ($CH_3(CH_2)_3OC_2H_2)_2OH$, Sigma Aldrich, 99+%, referred to as butyl carbitol). Cleaned FTO substrates were mounted on the metallic sample holder moving on X and Y axes to favor the homogeneity of the coatings. The samples connected to the ground were facing the nozzle (Figure 4.1) that was linked to a positive high voltage ranging from 6 to 8 kV to get a stable Taylor cone. Note that the electrostatic spray deposition method is very sensitive to the substrate surface temperature that was varied from 350°C to 300°C in this study. The real deposition temperature (Set Temperature) was adjusted versus the instrumental set-point thanks to a previous thermal calibration.

Figure 4.1 Picture of electrostatic spray deposition setup

A syringe pump (KDS scientific) was used to control the flow rate of the precursor solution at 1.5 mL h^{-1}. The nozzle-to-substrate distance was fixed at 30 mm. To get coatings with different thicknesses, the deposition time was varied from 35, 20 to 15 minutes. The prepared films were subsequently calcined at 500 °C for 60 minutes in air with a heating ramp of 10 °C min^{-1}.

4.1.1.1. Deposition time dependency

This part is focused on the investigation of the influence of the ESD deposition time on the microstructure of Cu:NiO coating, and consequently on the solar cell efficiency.

As described in Chapter 2, during electrostatic spray deposition, droplets fly towards the substrate under the action of an electrostatic field. In this paragraph, the deposition time was varied from 35 to 15 min. keeping the substrate temperature constant at 350 °C, the nozzle-to-substrate distance at 30 mm, the flow rate at 1.5 mL h^{-1}, and the precursor concentration at 0.02 M with 5 mol% of Cu dopant.

To ensure a complete coverage of the FTO surface, we first applied a long deposition time of 35 min. The other parameters for the electrostatic spray deposition are listed in Table 4.1.

Electrostatic-spray deposition			
Parameters	Value	Value	Value
Precursor Concentration (M)	0.02	0.02	0.02
Substrate Temperature (°C)	350	350	350
Set Temperature (°C)	500	500	500
Substrate-nozzle distance (mm)	30	30	30
Horizontal moving distance (mm)	30	30	30
Duration (min)	35	20	15
Steps (mm)	20	20	20
Speed per step (2mm/s)	2	2	2
Spraying rate (1.5mL/h)	1.5	1.5	1.5
Voltage (kv)	6-7	6-7	6-7
Thickness (nm)	100 ± 19.5	80 ± 8.1	52 ± 5.3

Table 4.1 Parameters used to fabricate Cu:NiO HTLs using the ESD method.

The surface morphology of the ESD Cu:NiO layer was evaluated using SEM. The SEM micrograph (Figure 4.2A) shows that at the aforementioned parameters, ESD Cu:NiO can completely cover the FTO substrate surface and there are practically no voids/pinholes on the surface. As shown in Chapter 2, the morphology of the coating is fully dependent on the size of the droplets impacting the heated substrate. Since butyl carbitol is a slow-evaporating solvent, the droplets are quite liquid and spread on the heated substrate forming a dense sub-layer. However, the surface of the entire ESD Cu:NiO layer is exceptionally heterogeneous, and many Cu:NiO particles are aggregated in some places, as seen in the top-view SEM. Indeed, when the deposition time is increased, the next charged droplets impact the already coated substrate surface and land preferentially on the more pronounced curvatures. This phenomenon is known as the preferential landing effect (see Chapter 2). It arises because the surfaces with the strongest curvature have the strongest electric fields, as the charges tend to be more concentrated in these areas. As a result, the preferential landing of these droplets causes particles to accumulate on the substrate. This preferential landing area leads to a change in the film morphology, i.e., beyond a certain thickness a dense film will no longer form. Therefore, the deposition time is a critical parameter to be optimized. The roughness on the film surface is caused by the regions of particle aggregation. This morphology is expected to limit the performance of the solar cells because it causes imperfections at the HTL/perovskite interface, which can induce carrier recombination. In addition, the rough Cu:NiO surface is

expected to increase the concentration of defects inside the perovskite layer. Finally, the thickness of the ESD Cu:NiO layer is determined to be around 100 ± 19.5nm, according to the cross-sectional SEM image (Figure 4.2B). A hole transport layer that is too thick causes a variety of issues, including an increased resistance and a higher probability for carrier recombination.

The obtained ESD Cu:NiO layers were tested in perovskite solar cells. Only the parameters of the highest efficiency cell are displayed in Table 4.2. We attribute the low PCE of 1.47 % and poor other values to the extreme roughness of the ESD Cu:NiO layer, inducing too many defects at the interface with and inside the perovskite layer leading among other shortcomings to extensive carrier recombination. Because of the high resistance caused by the thick ESD Cu:NiO layer *Jsc* is also comparably low.

Voc (V)	*Jsc* (mA/cm^2)	*FF* (%)	Efficiency (%)
0.36	10.46	39	1.47

Table 4.2 Best performance of the devices based on an ESD Cu:NiO HTL with 35 min deposition time.

Summarizing, the ESD Cu:NiO film on FTO has a high coverage but a rough surface, which has to be adjusted in the following. To enhance *Jsc*, one straightforward method is to reduce the thickness of the ESD Cu:NiO layer, which should lead to a lower resistance. Thus, time deposition was decreased to 20 min keeping constant the other ESD parameters such as substrate temperature of 350 °C, the nozzle-to-substrate distance of 30 mm, the flow rate of 1.5 mL h^{-1}, and the precursor concentration of 0.02 M (Table 4.1). SEM surface and cross-section micrographs are shown in Figure 4.2C-D. With the given settings, ESD Cu:NiO completely covers the surface of the FTO substrate improving the surface morphology quality. However, surface inhomogeneity throughout the ESD Cu:NiO layer and some Cu:NiO particle aggregation can still be seen (shown with a red circle). As visible in the cross-sectional SEM image (Figure 4.2D), the thickness of the ESD Cu:NiO layer is about 80 ± 8.1 nm. This shows that reducing the deposition time can effectively reduce the thickness of ESD Cu:NiO layer and help to improve the surface morphology quality of the film.

A 15-minute deposition duration was used to further increase the quality of ESD Cu:NiO film while also reducing its thickness, keeping constant the other ESD parameters. As shown in Figure 4.2E, ESD Cu:NiO does not entirely cover the surface of the FTO substrate under the specified conditions. Many fractures can be seen in Figure 4.2E, and some Cu:NiO particles are still visible as aggregates (shown as red circles). In the

cross-sectional SEM picture shown in Figure 4.2F, the thickness of the ESD Cu:NiO layer is decreased to around 52± 5.3nm. The above experiments demonstrate that the deposition time plays a key role in the quality of the film surface morphology and the thickness of the deposited layer. By decreasing the deposition time, the thickness of the film is effectively controlled. Note that the surface morphology of the film is not only affected by the deposition time but also other factors such as substrate temperature and precursor concentration are important to improve the surface morphology of the film.

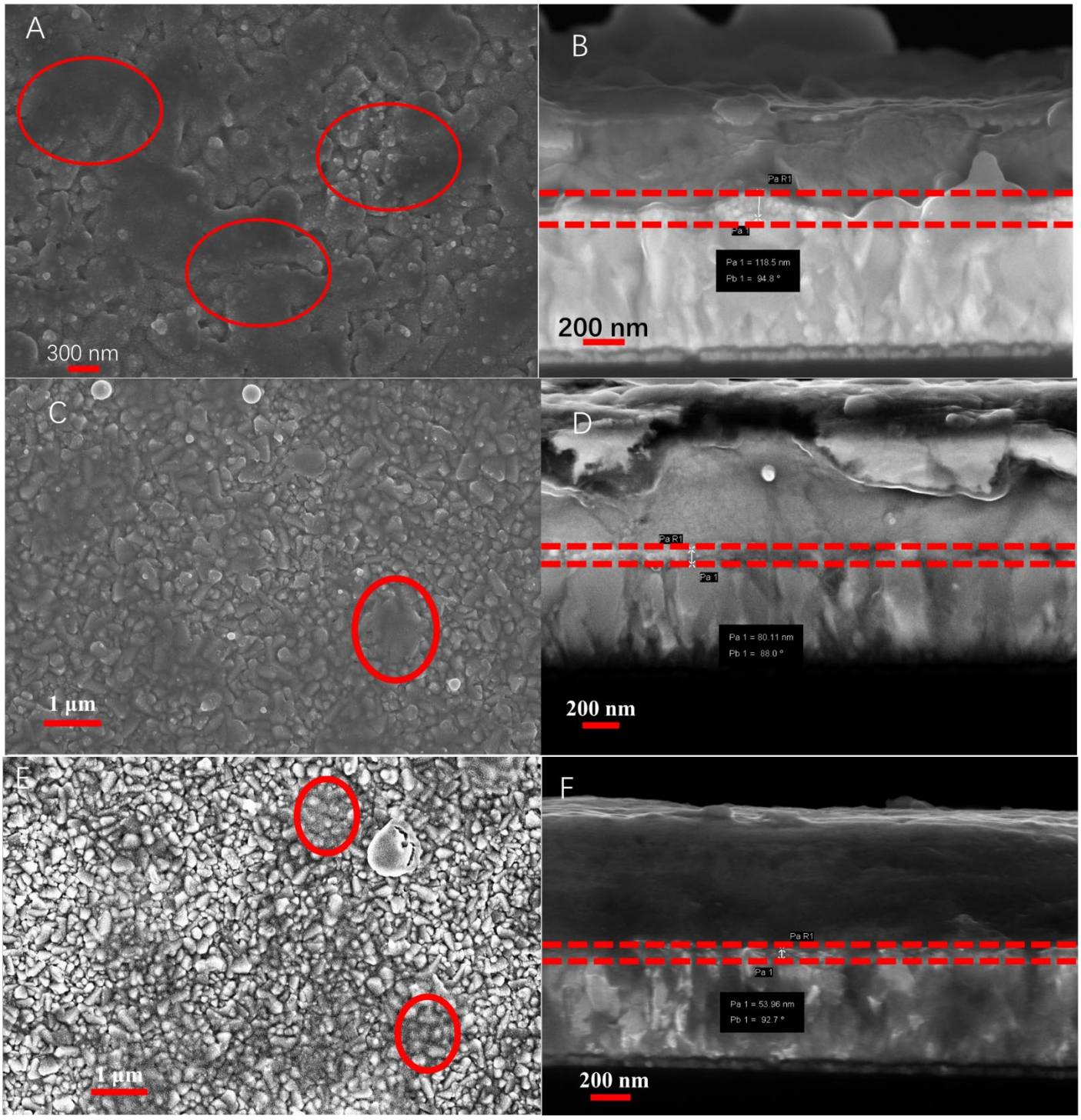

Figure 4.2: ESD Cu:NiO films obtained using 35 min, 20 min, and 15 min deposition time: A, C, E) surface views and B, D, F) cross-section images.

4.1.1.2. Substrate temperature dependency

The influence of the substrate temperature has been investigated to increase the quality of film formation. The precursors' solution progressively evaporates as the charged droplets fly to the substrate, as explained in Chapter 2, and is influenced by the temperature and the travel time. Lowering the substrate temperature should theoretically minimize solution evaporation. As a result, bigger droplets reach the substrate. Thus, the substrate temperature was decreased from 350 °C to 300 °C and the deposition time was selected to an intermediate value of 20 minutes keeping all other ESD parameters such as the nozzle-to-substrate distance of 30 mm, the flow rate of 1.5 mL h^{-1}, and the precursor concentration of 0.02 M constant. The different parameters are listed in Table 4.3.

Electrostatic-spray deposition	
Parameters	Value
Precursor Concentration (M)	0.02
Substrate Temperature (°C)	300
Set Temperature (°C)	400
Substrate-nozzle distance (mm)	30
Horizontal moving distance (mm)	30
Duration (min)	20
Steps (mm)	20
Speed per step (2mm/s)	2
Spraying rate (1.5mL/h)	1.5
Voltage (kv)	6-7 kv
Thickness (nm)	107± 4.6

Table 4.3: Parameters used to fabricate the ESD Cu:NiO film at lower temperature.

As shown in SEM images (Figure 4.3A) we can observe a full coverage of the ESD Cu:NiO film on the FTO substrate under the specified conditions. There are much smaller voids on the surface compared to previous ESD Cu:NiO layers, and the surface morphology is considerably improved in terms of regularity. The grain size of about 24.6 ± 4.3 nm is homogeneously distributed even at higher magnification, as illustrated in the right panel of Figure 4.3B.

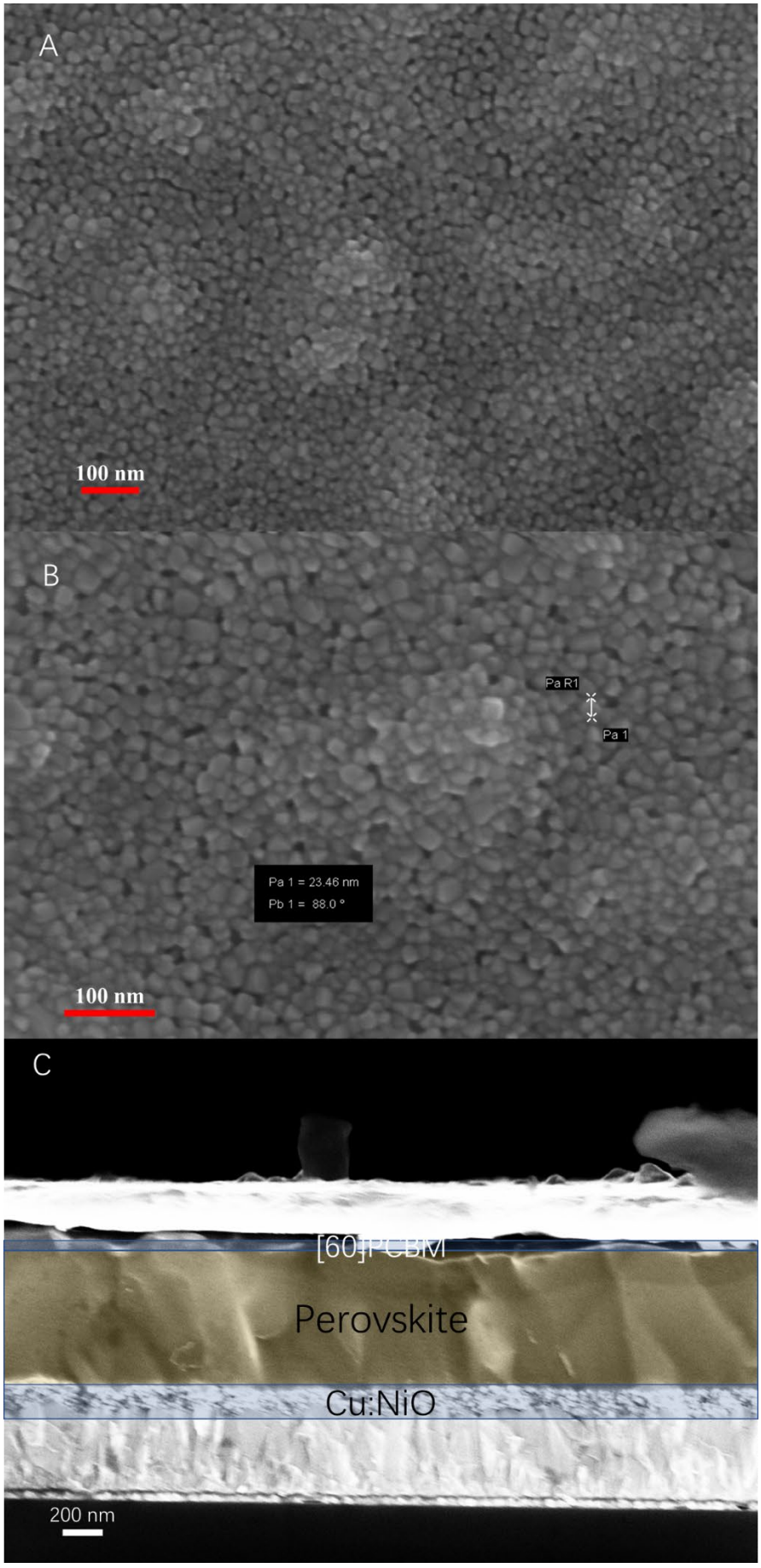

Figure 4.3: SEM images of an ESD Cu:NiO film deposited at 300 °C for 20 min: A) surface view, B) surface view with larger magnification, and C) Cross-section view of the corresponding PSC.

We have used this ESD Cu:NiO film to prepare perovskite solar cells. Again, only the highest efficiency is shown in Table 4.4. Because of the extremely homogenous ESD Cu:NiO layer, the PSCs have a higher fill factor than in the previous experiments. *Jsc*, on the other hand, remains low. As illustrated in Figure 4.3C, the thickness of this ESD Cu:NiO layer is 107± 4.6 nm. *Jsc* is greatly affected by the high resistance of this comparably thick hole transport layer.

Voc (V)	Jsc (mA/cm^2)	Fill Factor (%)	Efficiency (%)
0.81	14.53	71	8.36

Table 4.4 Best performance of the device based on EDS Cu:NiO film with 300°C substrate temperature

Summarizing, these results show that decreasing the substrate temperature significantly improves the surface morphology of the films. Perovskite solar cells based on ESD Cu:NiO hole transport layers typically have a high fill factor.

4.1.1.3. Concentration of the precursors' solution dependency

The concentration of the precursors' solution is another parameter that affects the quality of ESD films. Based on the research findings in the previous two sections, to study the influence of precursors' solution concentration from 0.02 M to 0.01 M, and 0.005 M, we have selected a lower substrate temperature of 300°C and an appropriate deposition period of 15 minutes that were found beneficial to favor a homogeneous surface morphology and to minimize the thickness of the films (Table 4.5).

Electrostatic-spray deposition			
Parameters	Value	Value	Value
Precursor Concentration (M)	0.02	0.01	0.005
Substrate Temperature (°C)	300	350	350
Set Temperature (°C)	400	400	400
Substrate-nozzle distance (mm)	30	30	30
Horizontal moving distance (mm)	30	30	30
Duration (min)	15	15	15
Steps (mm)	20	20	20
Speed per step (2mm/s)	2	2	2
Spraying rate (1.5mL/h)	1.5	1.5	1.5
Voltage (kv)	6-7	6-7	6-7
Thickness (nm)	76 ±6.8 nm	50±5.3 nm	

Table 4.5: Parameters used to fabricate the ESD Cu:NiO film with different precursors' solution concentration.

The surface morphology of ESD Cu:NiO layer using the 0.02 M precursor solution, investigated by SEM, shows that the FTO surface is completely coated without cracks and voids (Figure 4.4A). The Cu:NiO particles are consistent in size with an average value of around 30 nm and there are no apparent regions of particle agglomeration. According to the cross-sectional SEM image in Figure 4.4B, the hole transport layer is roughly 76 ±6.8 nm thick.

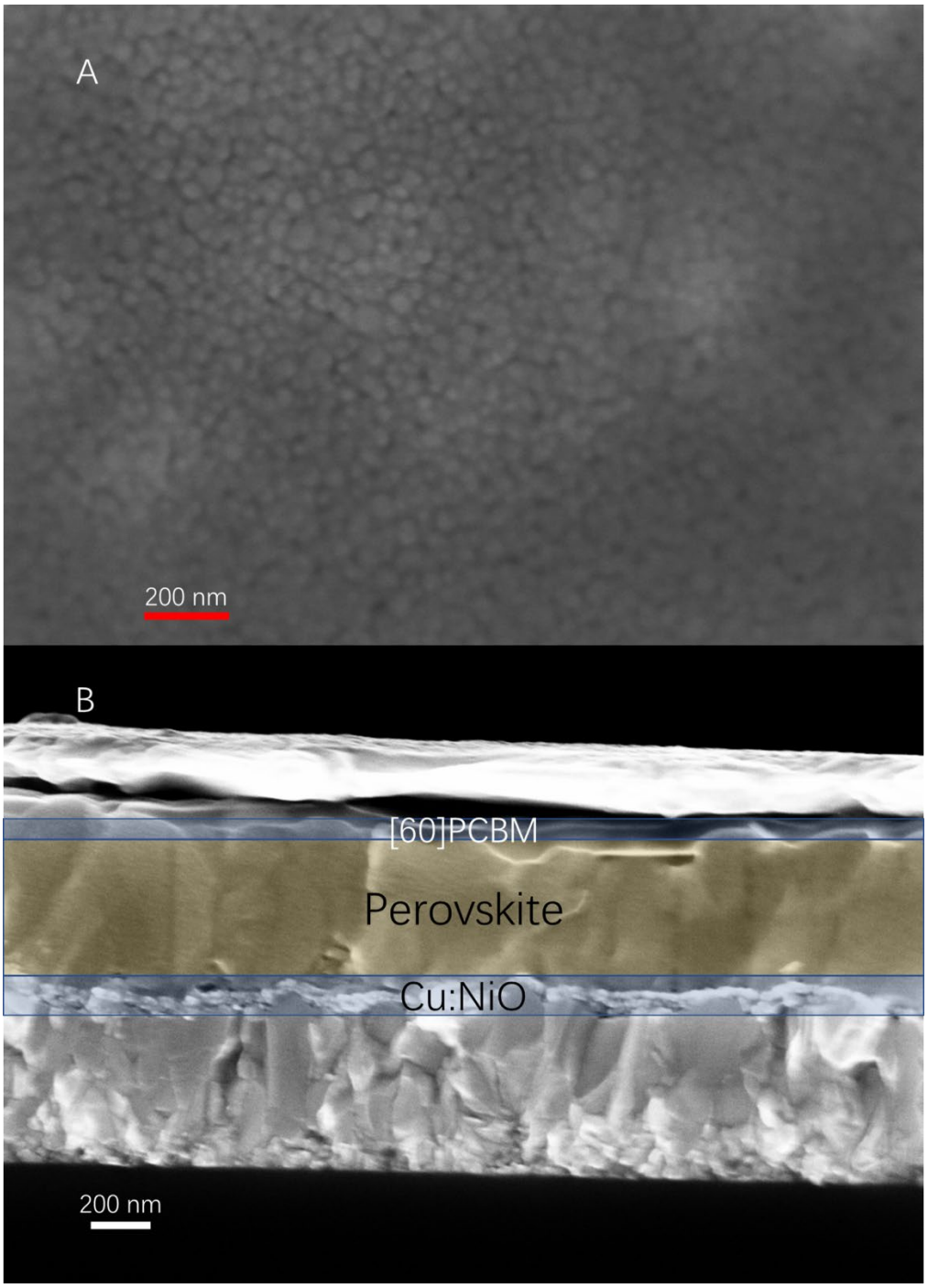

Figure 4.4: SEM images of an ESD Cu:NiO film deposited at 300 °C for 15 min with a precursors' solution concentration of 0.02 M: A) surface view, B) cross-section view of the corresponding PSC.

When the precursors' solution was diluted by a factor of 2 (0.01 M) while maintaining the other electrostatic spray deposition parameters, the contour of the FTO surface can be readily seen in the top-view SEM (Figure 4.5A), suggesting a substantial reduction in the thickness of the ESD Cu:NiO deposited layer. Indeed, reducing the concentration of the precursors' solution makes it possible to decrease the conductivity of the solution and also decrease the viscosity of the solution according to the Gañan-Calvo's relationship (Chapitre 2). Thus, a

spread of diluted droplets of larger size is expected. The stresses on the surface of the deposited thin layer are increased and consequently, cracks begin to develop, mostly near the FTO crystal's border, as illustrated in Figure 4.5A by the red circles. Short circuits and current leakage may occur as a result of these tiny cracks, probably lowering the efficiency of perovskite solar cells. According to the cross-sectional SEM image in Figure 4.5B, the thickness of the hole transport layer is about 50±5.3 nm

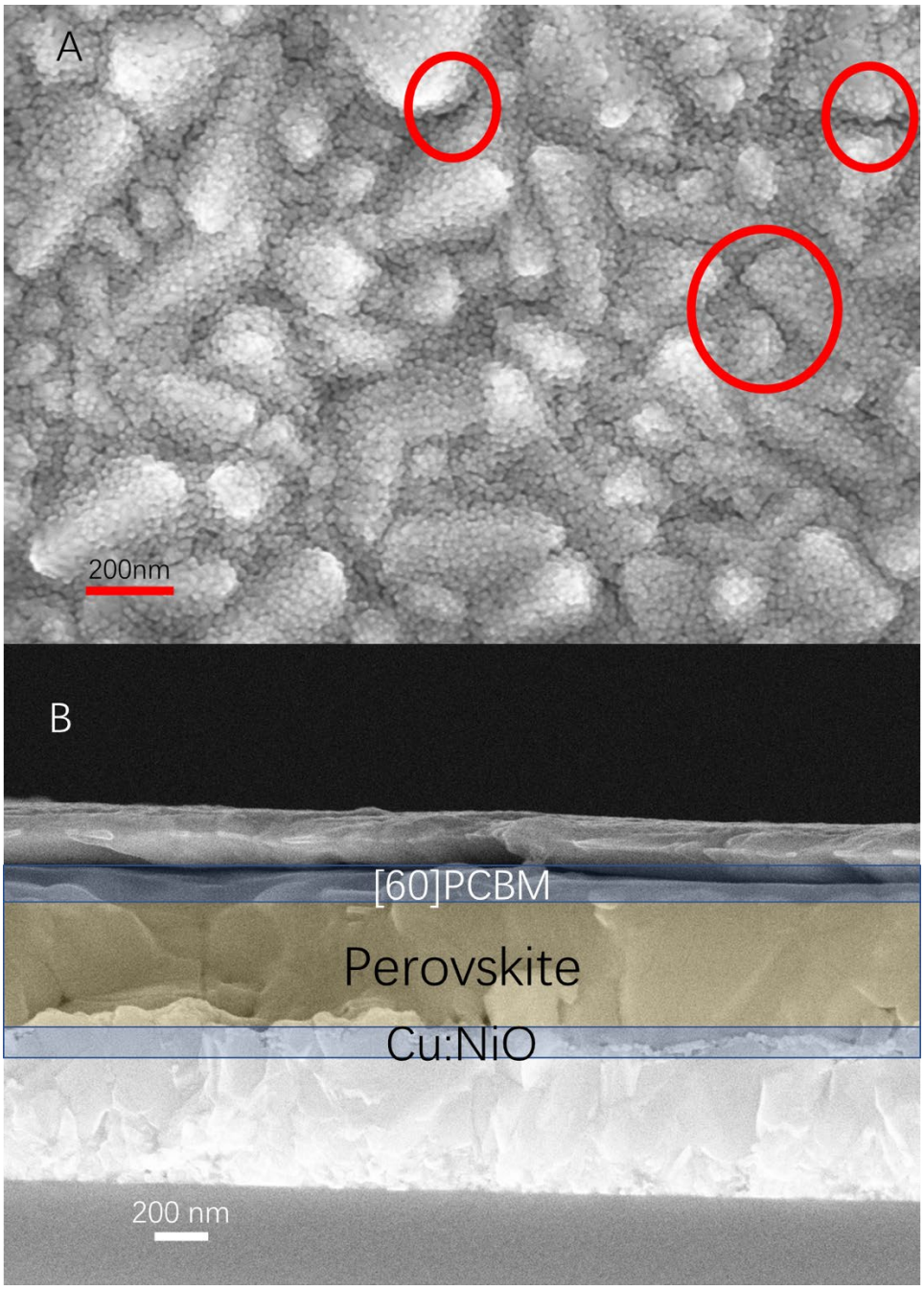

Figure 4.5: SEM images of an ESD Cu:NiO film deposited at 300 °C for 15 min with a precursors' solution concentration of 0.01 M: A) surface view, B) cross-section view of the corresponding PSC.

AFM images of the Cu:NiO films produced with a precursors' solution concentration of 0.02 M and 0.01 M are shown in Figure 4.6. The roughness of the 0.02 M-deposited layer is only 16.7 nm, which is around half of the roughness of the 0.01M-deposited layer (35.5 nm). The smoother surface covering obtained with a precursors' solution concentration of 0.02 M sprayed for 15 minutes at 300 °C is preferred for the subsequent deposition of the other layers, to avoid recombination sites, and to minimize detrimental carrier losses[4].

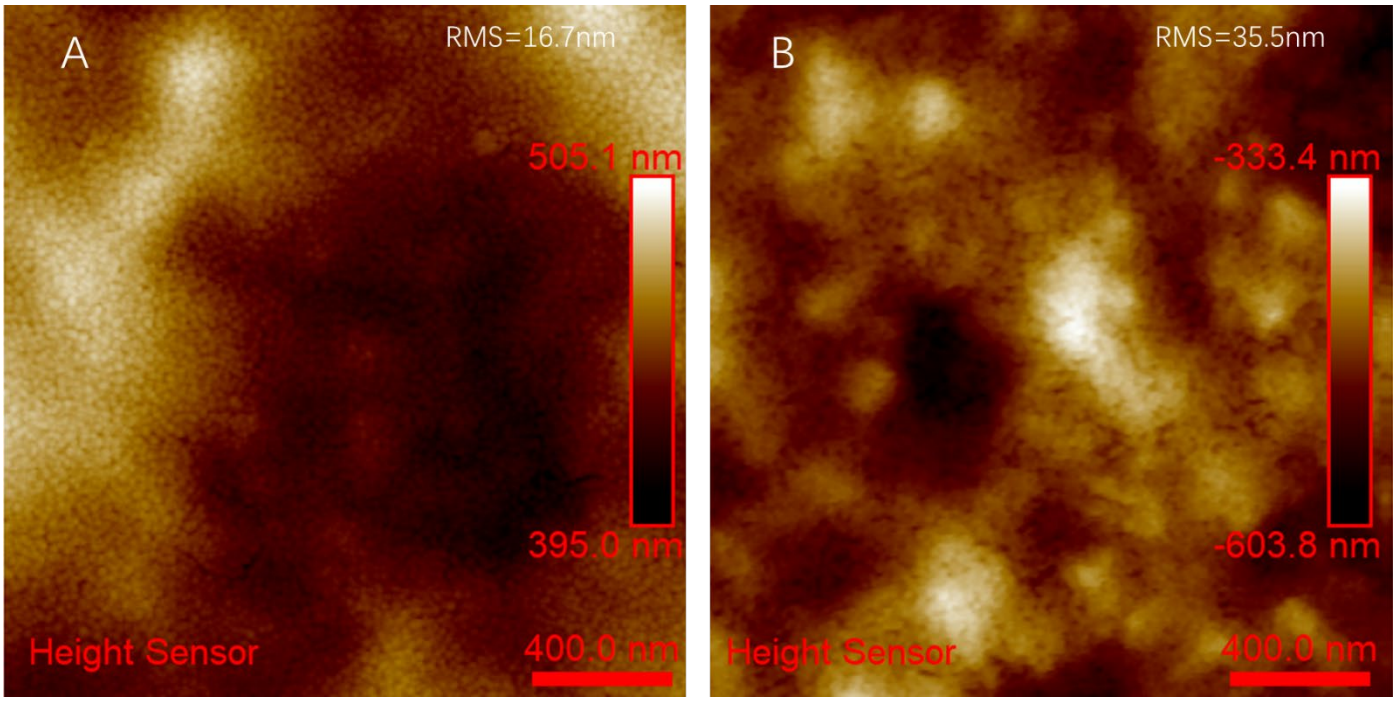

Figure 4.6: AFM images of the ESD Cu:NiO layers deposited on FTO substrates and surface roughness (root mean square average). Depositions were performed at 300 °C for 15 min with a precursors' solution concentration of A) 0.02 M; B) 0.01 M.

For completing the series, the precursor was further diluted to a concentration of 0.005 M while keeping the other ESD parameters constant. The ESD Cu:NiO layer did no longer cover completely the FTO surface and several regions of particle aggregation occurred, as shown in Figure 4.7. This might be owing to a lack of material sprayed onto the substrate as a result of the low precursors' solution concentration. Particles flying to the substrate are so diluted that the amount of material deposited is two times lower than in the previous case. As a result, we can observe isolated islands on FTO substrate.

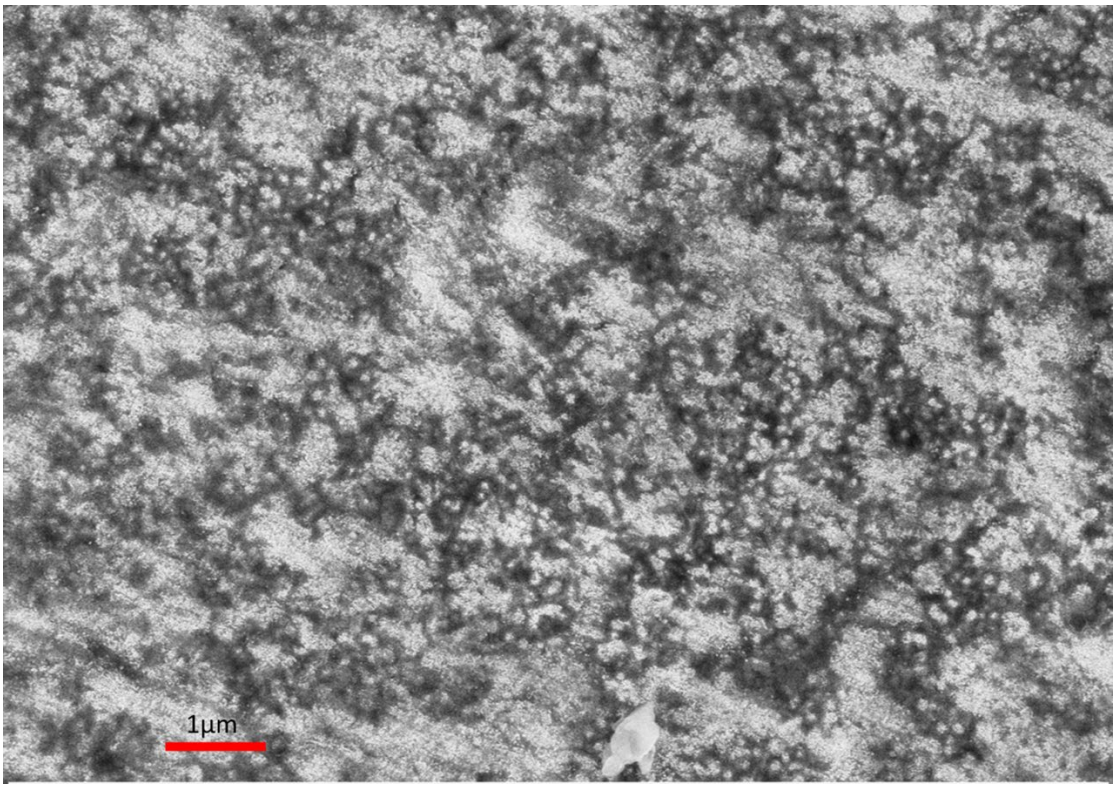

Figure 4.7 Surface SEM micrograph of an ESD Cu:NiO film deposited at 300 °C for 15 min with a precursors' solution concentration of 0.005 M.

In conclusion, when the substrate temperature was adjusted to 300 °C and the deposition time was 15 minutes using a 0.02 M precursor, the nanostructured ESD Cu:NiO coatings showed smooth surface morphology and an optimum thickness of 80 nm. For this layer deposited under optimized conditions, we will perform further investigations.

4.1.2. ESD Cu:NiO layer vs. spin-coated Cu:NiO layer

4.1.2.1. Study of the morphology of the Cu:NiO thin films

The perovskite solar cell performance is highly dependent on the surface morphology and root mean square (RMS) surface roughness of the NiO HTL[5]. Figure 4.8A shows the top view of a spin-coated Cu:NiO layer. The SP Cu:NiO layer obtained by spin-coating is unable to completely cover the substrate surface, resulting in a considerable number of cracks, which may be caused by the FTO substrate's high roughness. These fractures allow current to leak from the perovskite layer, causing contact problems between the Cu:NiO layer and the perovskite layer. The problem of leaking current and insufficient contact between the Cu:NiO layer and the perovskite layer might considerably reduce the fill factor (FF)[6]. The surface SEM picture of the

electrosprayed Cu:NiO layer (Figure 4.8B) reveals complete coverage of ESD Cu:NiO on the FTO substrate with practically no voids. The FTO crystals are visible beneath the Cu:NiO layer, and the surface shape of this ESD Cu:NiO layer is identical to that of the bare FTO surface, implying that the Cu:NiO nanocrystals are covering the FTO surface conformally. The substrates are fully covered by compacted Cu:NiO nanoparticles on this continuous, homogeneous, and crack-free surface, which inhibits current leakage from the perovskite layer.

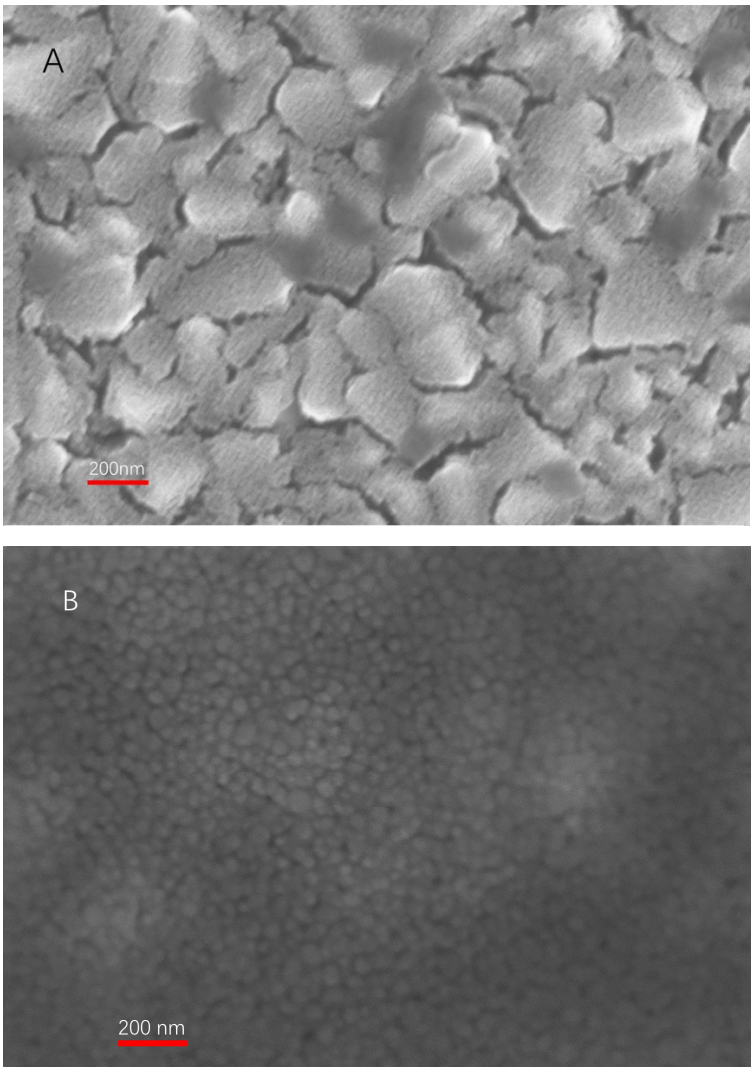

Figure 4.8: Top-view SEM images of Cu:NiO layers prepared using A) spin-coating SP; B) ESD.

At the same time, AFM shows that the ESD method can also considerably reduce surface roughness. The root-mean-square (RMS) of the ESD Cu:NiO layer is only 16.7 nm, which is almost two times smoother than the SP Cu:NiO layer (34.8 nm), as illustrated in Figure 4.9A and B. The development of high-quality perovskite layers is promoted by smoother ESD Cu:NiO layers[7].

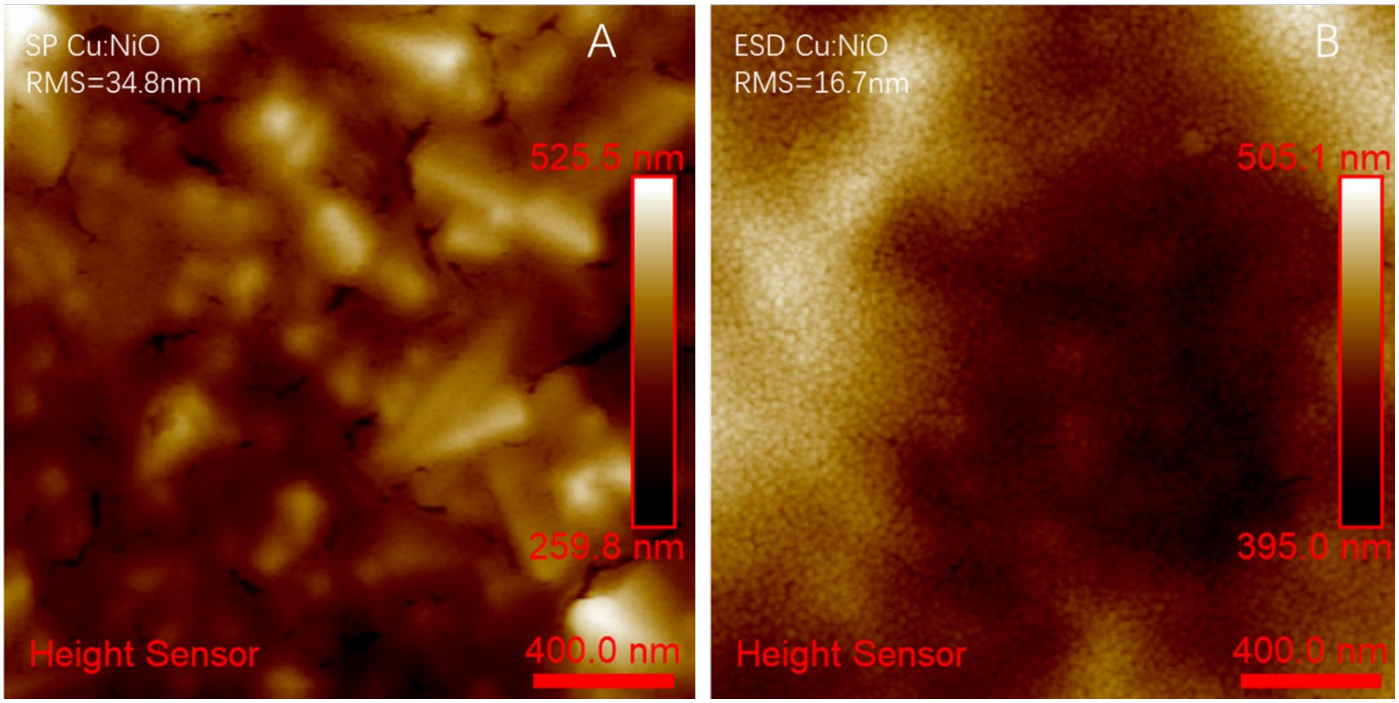

Figure 4.9: AFM images of Cu:NiO layers prepared by: A) SP; B) ESD.

4.1.2.2. A structural study by XRD and optical properties of ESD and SP-Cu:NiO layers

X-ray diffraction (XRD) was used to analyze the phase purity and crystalline quality of a Cu:NiO layer produced by electrostatic spray deposition (ESD) and spin-coating (SP) with 5 mol% Cu dopant. Because the Cu:NiO layers are ultra-thin (80 nm, as shown in Figure 4.4B), grazing incidence X-ray diffraction (GIXRD) was utilized, as shown in Figure 4.10. The characteristic cubic phase NiO (space group $Fm\bar{3}m$) diffraction peaks (*111*), (*200*), (*220*), and (*311*) can be readily distinguished (JCPDS card numbers 00-047-1049), which indicates a high crystalline quality of Cu:NiO layer[2]. Because of the ultra-thin Cu:NiO layer employed, even at a small XRD incidence angle θ of 0.3°, it still exhibits a significant signal from the FTO substrate. The relative intensities of those peaks are similar for each pattern, suggesting that the fabrication method does not change the growth direction and keeps a similar preferential orientation. There are no secondary phases such as CuO, Ni, or Cu_2O. We note that Cu^{2+} ions can be doped by substitution into the NiO lattice structure and replace Ni^{2+} without altering considerably the Cu:NiO crystal structure[8].

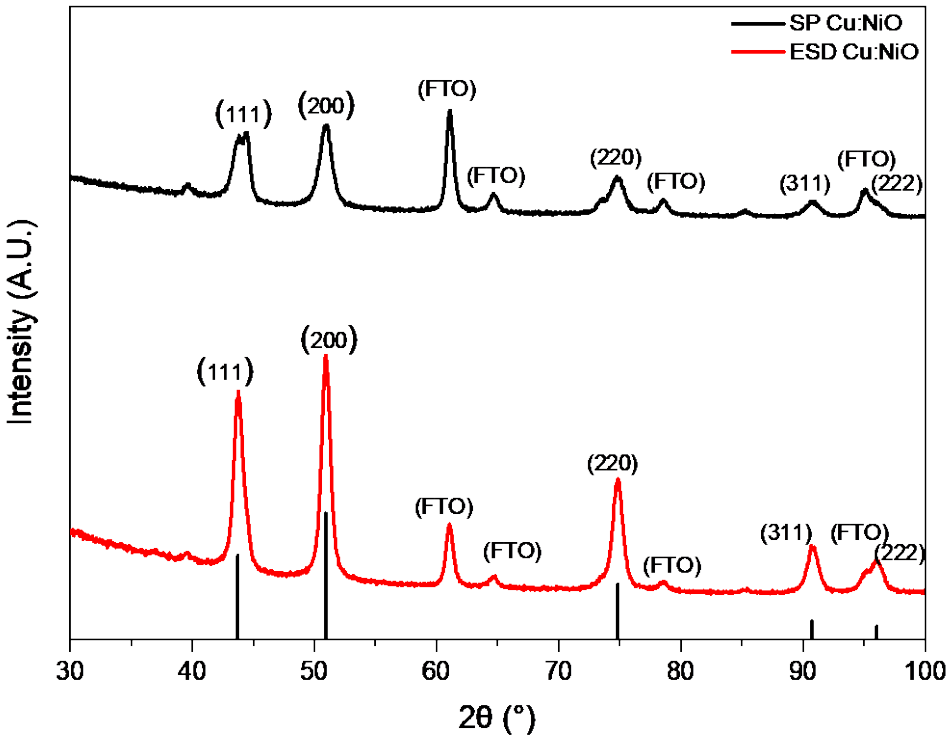

Figure 4.10: XRD patterns of Cu doped-NiO layers fabricated by ESD and spin-coating (SP).

Figure 4.11A shows the optical transmittance of Cu:NiO layers made using ESD and SP. Above 450 nm, both layers have great optical transparency, making them suitable candidates for hole transport layers (HTLs) in perovskite solar cells (PSCs)[9]. Meanwhile, as compared to Cu:NiO films produced by spin-coating, the transparency of Cu:NiO films manufactured by the ESD technique decreases slightly. This might be the result of a slightly thicker Cu:NiO layer[10]. The values for the bandgap (Eg) were calculated using the Tauc plot method[11]. Figure 4.11B indicates that the bandgap of the ESD Cu:NiO layer is reduced by 0.06 eV, ensuring a good optical transmittance in the visible range.

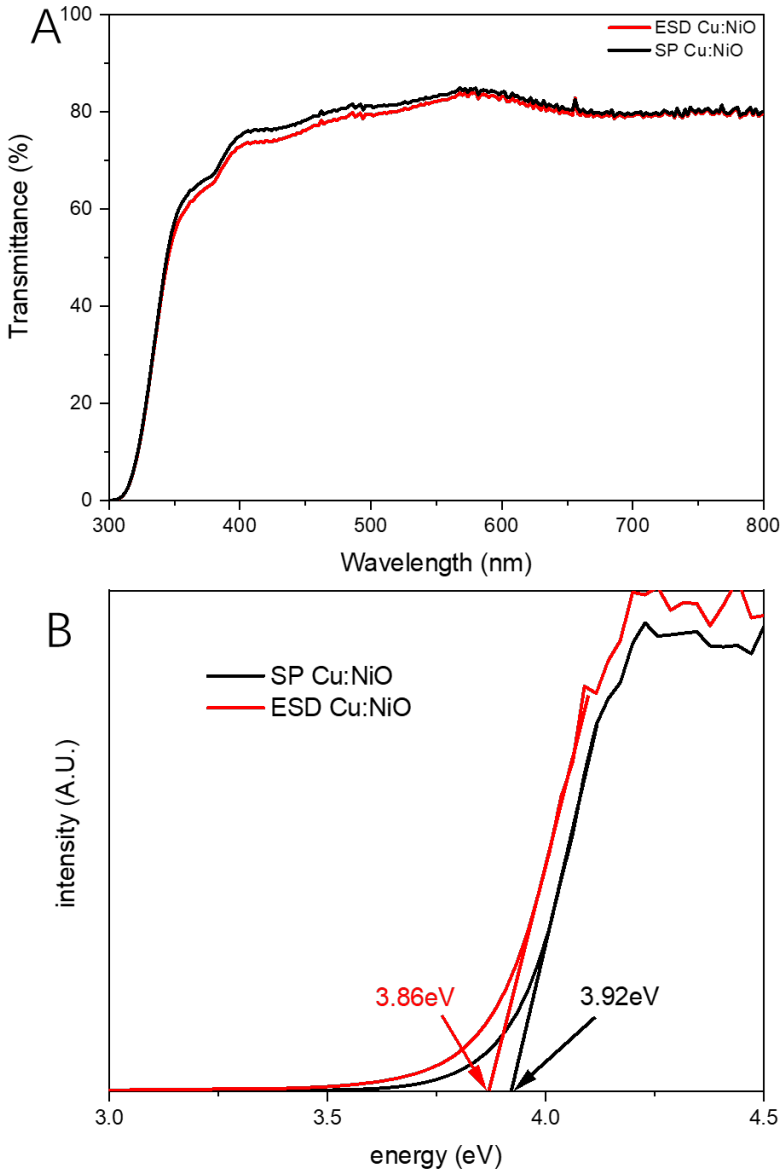

Figure 4.11 A) Optical transmittance spectra of Cu doped-NiO layers fabricated by ESD and spin-coating (SP)); B Tauc plots of the same layers.

4.1.2.3. Electrical properties of ESD and SP-Cu:NiO layers

Table 4.6 shows Hall measurements for the electrical characteristics of NiO layers with various Cu doping levels and fabrication methods. The electrical conductivity of the films can be increased by doping with Cu ions, as predicted, with the maximum value of 40.3 S/cm achieved in the ESD Cu:NiO layer with 5 mol% Cu dopant. When the dopant concentration exceeds 10 mol%, the conductivity begins to drop, which might be due a decrease of the hole carrier mobility. When the dopant concentration is increased from 5 mol. % to 10 mol%, more and more Cu^{2+} ions substitute the sites of Ni^{2+} in the lattice, thus providing a higher hole carrier concentration. The scattering centers of a 10 mol. % Cu:NiO layer, on the other hand, increase due to lattice distortion, resulting in a reduction of carrier mobility. This explains why the concentration of hole carriers

continues to rise when the doping concentration rises from 0 mol% to 10 mol%. When the dopant concentration is raised to 10 mol%, the mobility declines. At high Cu doping concentrations, crystal disorder may play a major impact in decreasing carrier mobility and conductivity[6]. When the Cu ion doping concentration is the same (5 mol%), both the mobility and the electrical conductivity of Cu:NiO films using ESD is higher than that of Cu:NiO films prepared using the spin-coating method (cf. Table 4.6). This may be due to the higher quality of Cu:NiO crystals prepared by ESD with few lattice defects and lattice distortion at the same hole carrier concentration, thus improving the mobility of the hole carriers.

Sample	T(°C)	Resistivities(Ω·cm)	Conductivity(S/cm)	Mobility(cm^2/V.s)	Carrier concentration($1/cm^3$)
SPCu5%	25	2.78E-02	3.60E+01	0.2270	1.07E+21
ESD0%	25	2.57E-02	3.89E+01	0.2627	8.83E+20
ESD5%	25	2.48E-02	4.03E+01	0.2676	1.02E+21
ESD10%	25	2.76E-02	3.63E+01	0.2144	1.17E+21

Table 4.6 Electrical parameters of Cu:NiO layers prepared with different Cu doping concentrations and different fabrication methods. For these measurements, the Cu:NiO films were deposited on normal glass substrates.

Tuna AFM measurements were also performed, as shown in Figure 4.12, to further demonstrate the enhanced conductivity as a result of the fabrication technique. In comparison with the films generated by the spin-coating approach, the tuna AFM findings indicate a clear increase in conductivity when employing the ESD method, which is consistent with the Hall measurement results. The above measurements indicate that the 5 mol% Cu doped NiO layer produced by the ESD method possesses the highest conductivity among all of the prepared films with an only very slightly reduced optical transmittance.

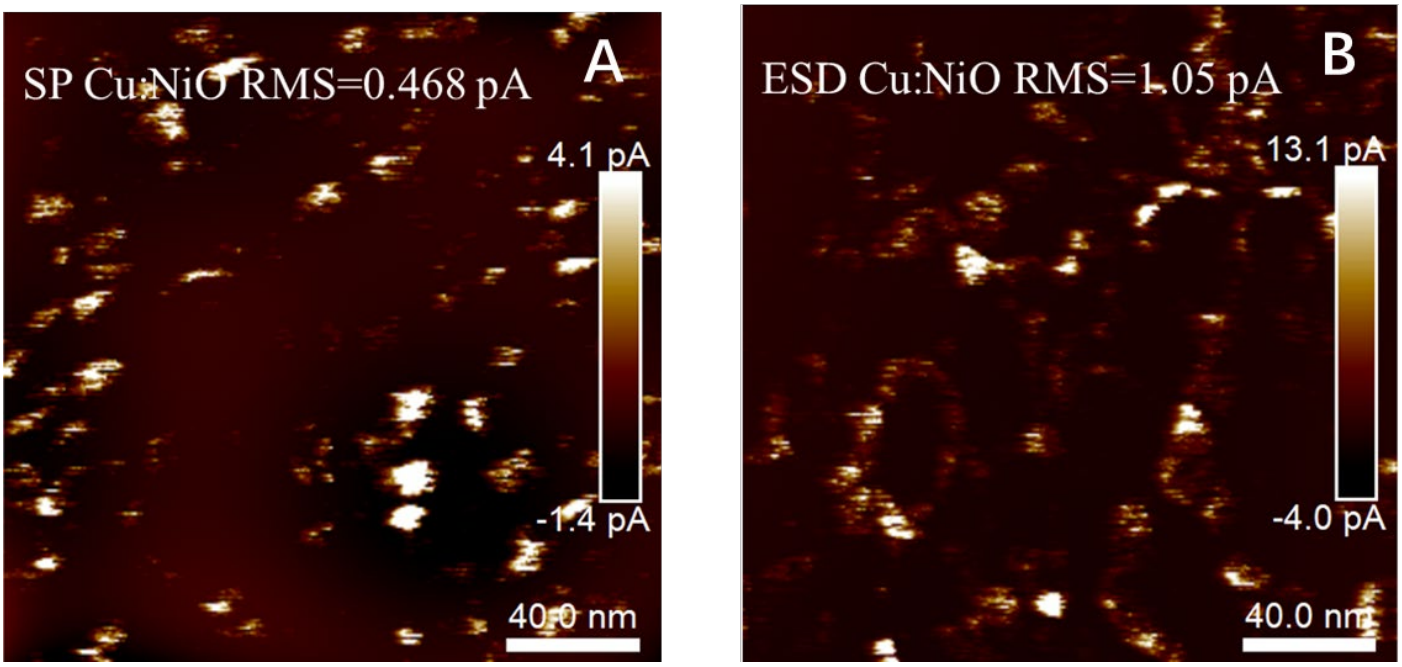

Figure 4.12 Tuna AFM images of Cu doped-NiO layer fabricated by A) spin-coating; B) ESD.

4.1.2.4. Composition analysis of ESD and SP-Cu:NiO layers

X-ray photoelectron spectroscopy (XPS) was used to study the compositions and valence states of Cu-doped NiO layers produced by spin-coating and ESD methods. Figure 4.13 shows the complete spectra of both Cu:NiO layers. It should be noticed that in the XPS spectra of the Cu:NiO layers produced by the ESD method, no Sn peak was observed. The XPS spectrum of the Cu:NiO layer produced by the spin-coating technique, on the other hand, shows a strong Sn peak (marked in red in Figure 4.13). This suggests that the Cu:NiO spin-coated films did not completely cover the FTO substrate.

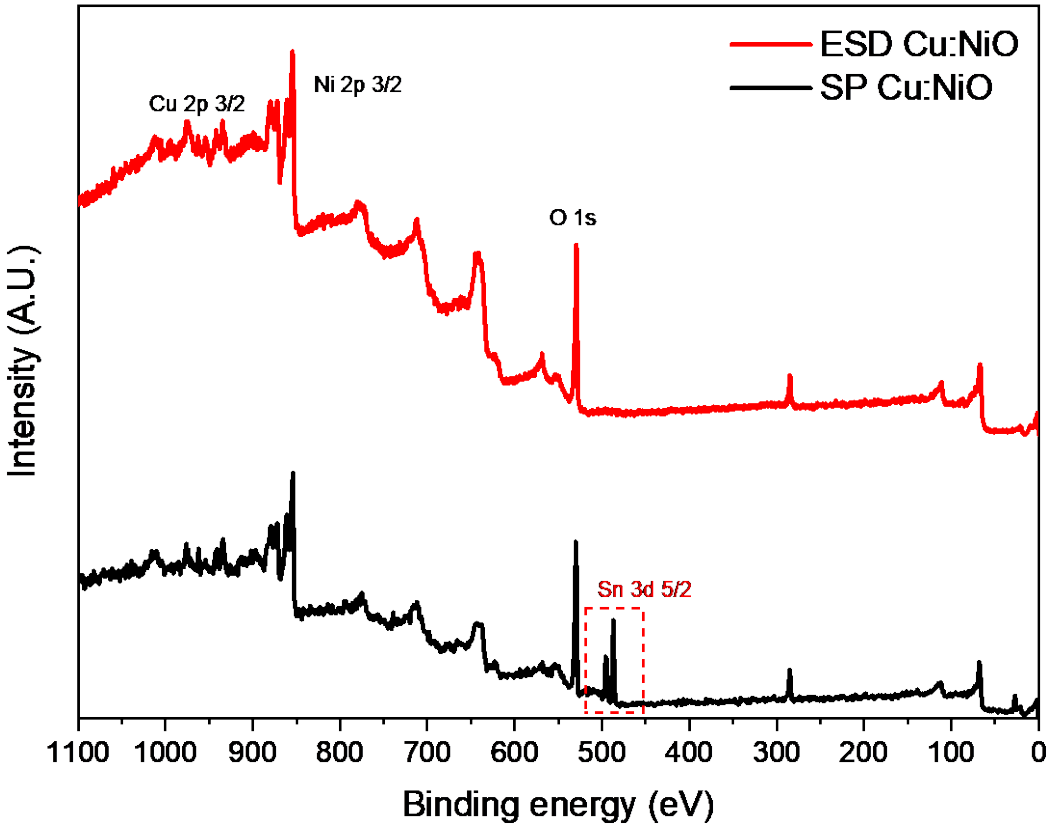

Figure 4.13: XPS spectra of Cu:NiO films produced by ESD and SP.

Cu peaks could well be detected in the Cu:NiO films made with both techniques. This is due to the proximity of the atomic radii of Cu and Ni, which is predicted to effectively promote Cu substitutional incorporation[12–14]. Cu, on the other hand, depends on whether it is integrated as Cu^{+} or Cu^{2+} to contribute to the enhanced hole density. High-resolution XPS measurements, which offer significant information on the chemical states of the elements, can be used to get this information. Doping can result in an increase in carrier concentration owing to substitutional incorporation of a suitable dopant or changes in native defects (nickel vacancies) as a result of dopant incorporation. Since Cu was introduced in its divalent form[1,3], it was previously reported that changes in native defect concentrations caused an increase in conductivity in Cu:NiO[6,8]. Nickel vacancies V_{Ni2+}, which have the lowest formation energy, are the most likely acceptors in NiO[15,16]. As a result, we investigated the XPS spectra of Ni and Cu. As shown in Figure 4.14, the Ni 2p3/2 peak typically consists of the main peak at ≈854 eV, a shoulder at ≈856 eV, and a shake-up satellite peak at ≈862 eV[17]. The main peak is generally assigned to Ni^{2+} in the cubic rock salt NiO (NiO_6 octahedral bonding)[18]. Ni-vacancy generated Ni^{3+} ions[19,20], nickel hydroxides and oxyhydroxides[18], nonlocal screening and surface states[17] have all been attributed to the shoulder as reported before.

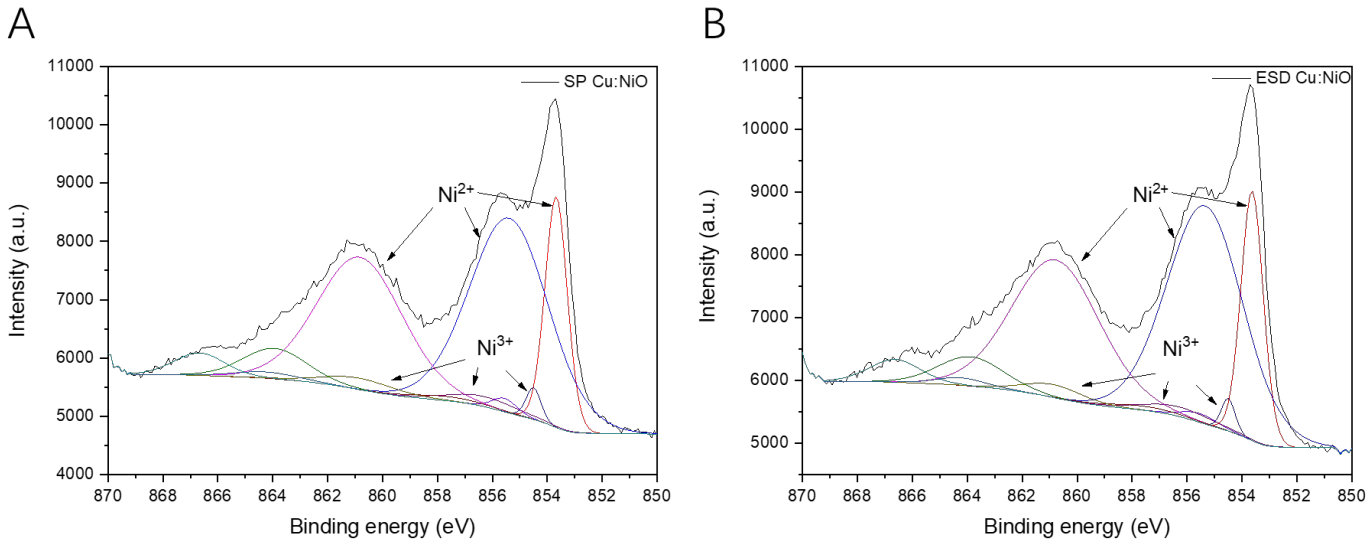

Figure 4.14: High-resolution Ni 2p XPS spectra of Cu:NiO layers: A) SP; B) ESD.

We compared the normalized spectra since the Ni 2p peak fitting is complicated and the Ni^{3+} concentration is likely overestimated by the XPS fitting[21]. We can see that the Ni 2p peaks do not change significantly, indicating that the commonly suggested mechanism of enhanced conductivity owing to increased Ni vacancy concentration does not apply to our samples, as shown in Figure 4.15.

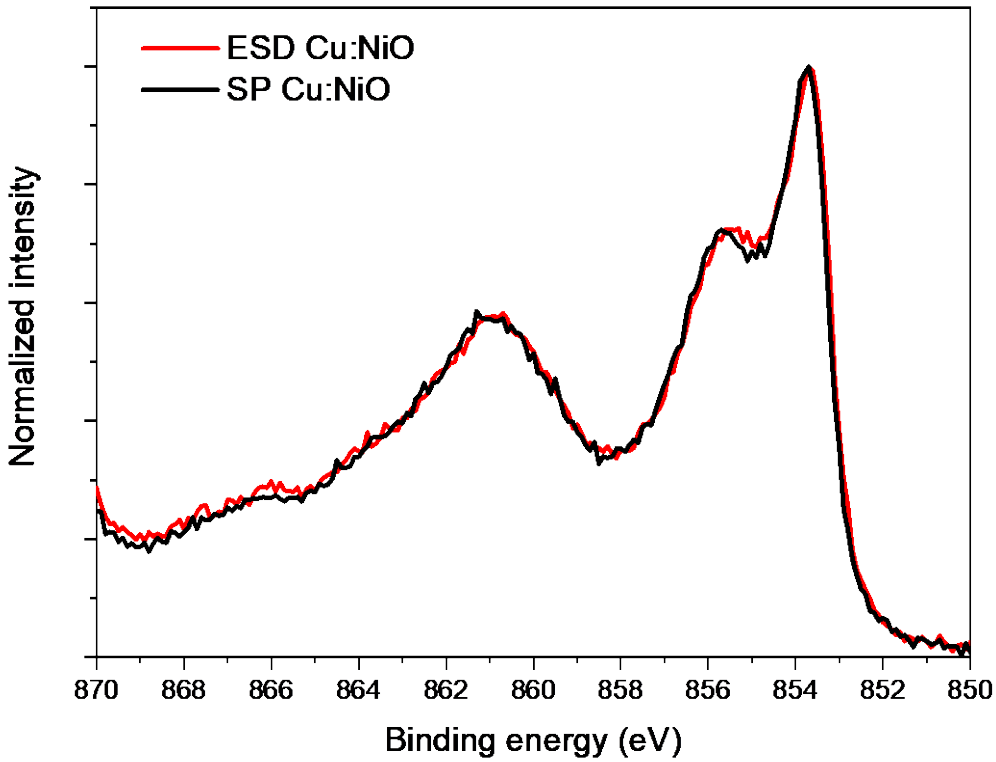

Figure 4.15: Normalized XPS spectra of the Ni 2p 3/2 peaks of Cu:NiO ESD and SP.

Because the Ni 2p peak remained unchanged, we focused next on the analysis of the Cu signal peak. High-

resolution Cu 2p XPS spectra were carried out revealing that the Cu peaks are dominated by Cu^{2+} [22] as previously reported on Cu:NiO[1]. However, unlike earlier research, which showed exclusively the presence of Cu^{2+}, we could identify traces of Cu^{+}. Figure 4.16 shows a high-resolution XPS spetrum of Cu 2p 3/2. Two core level peaks at 934.4 eV and 932.2 eV correspond to Cu^{2+} $2p_{3/2}$ and $Cu^{+}2p_{3/2}$, respectively[23]. It is clear that the ratio of Cu^{+} to Cu^{2+} changes with the change of preparation method. In both Cu-doped NiO films, no substantial shift in the Cu 2p peak location is detected, as shown in Table 4.7. As reported before, the Cu^{2+} ion is commonly used as a dopant in NiO layers to increase the conductivity and charge carrier mobility[1], whereas Cu^{+} has been applied in perovskite solar cells for reducing recombination and transport losses[24]. The proportion of Cu^{+} was significantly reduced in the Cu:NiO films prepared by ESD. As a result, we can conclude that variations in carrier concentration and conductivity in our samples are caused by the Cu dopant, which is present mostly in the Cu^{2+} state but also as Cu^{+} in a minority, presumably as a result of changes in the surface adsorbate. Cu^{2+} is the oxidation state that contributes mostly to the increase in conductivity.

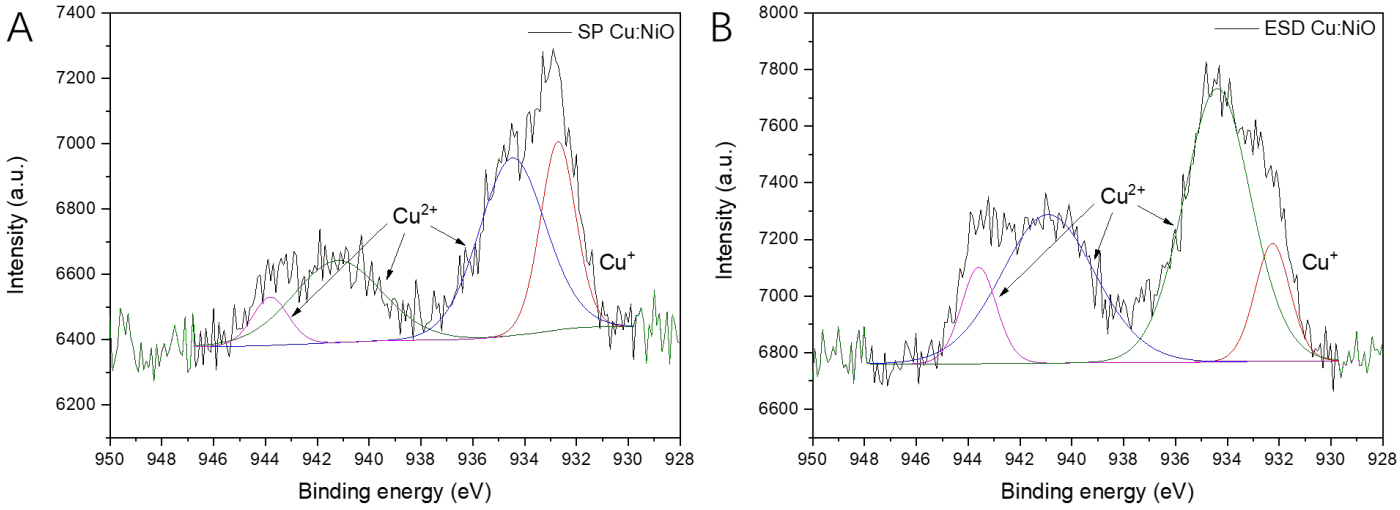

Figure 4.16. High-resolution Cu 2p XPS spectra for A) spin coated; B) ESD-deposited Cu:NiO layers.

Fabrication method	Cu^{+} position (eV)	Cu^{2+} position (eV)	$Cu^{+}/(Cu^{+}+Cu^{2+})$
Spin-coating	932	934.5	24.20%
ESD	932.2	934.4	10.40%

Table 4.7 Cu 2p analysis of Cu:Cu:NiO film fabricated by different methods.

With the change of the Cu^{+} ions dopant level, the work function of the ESD Cu:NiO layer is slightly increased. The work functions of ESD Cu:NiO layer and SP Cu:NiO layers were determined by Photoelectron Spectroscopy in Air (PESA). As shown in Figure 4.17, the work function of ESD Cu:NiO is increased to 5.56

eV, compared to the 5.4 eV for the SP Cu:NiO layer. This increased work function can give rise to a higher open circuit voltage for inversed perovskite solar cells[25].

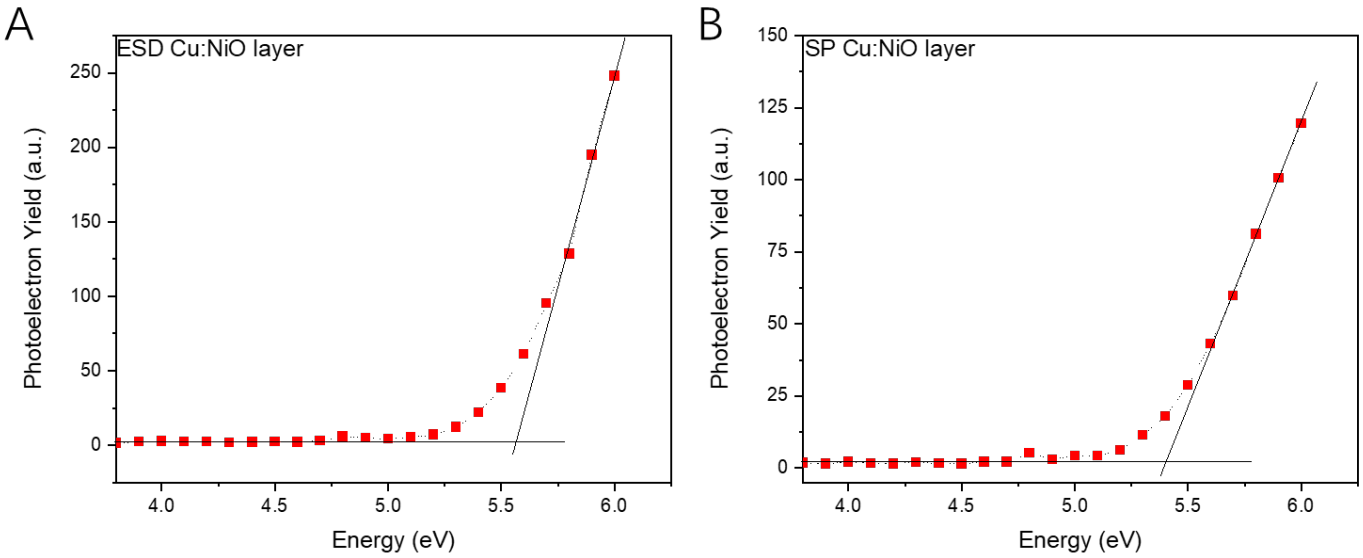

Figure 4.17: Work function determined with PESA for (A) ESD Cu:NiO and (B) SP Cu:NiO layers.

It has been reported that the spin-coating method can cause inhomogeneous films due to the Marangoni effect caused by the different evaporation rates of the solvent on the substrate, especially when the roughness of the substrate is high[26,27]. To explore the homogeneity of the film composition, we used Energy-dispersive X-ray spectroscopy (EDX). For each sample, we randomly selected three points for the elemental analysis to investigate the homogeneity of the film composition. For the Cu:NiO films prepared by ESD, we detected Cu signals at all three points. The calculated ratio of Cu to Ni is about 5.1 atom. %, which is similar to the ratio of Cu/Ni in the precursors. Moreover, these three points showed similar Cu/Ni values, indicating that the Cu:NiO films prepared using ESD are homogeneous in composition. However, for the Cu:NiO films prepared using the spin-coating method, we did not detect the signal of Cu at one of the points. In addition, the ratio of Cu to Ni in the other two points was more than 10%, which was much larger than the concentration of Cu in the precursors. This difference is a sign of the uneven film composition obtained with the spin-coating process.

Spectrum	C	N	O	F	Si	Ni	Cu	Sn	Cu/Ni
ESDNi01	1.92	12.78	55.36	1.08	-	13.49	0.69	14.67	0.051149
ESDNi02	5.34	13.99	56.12	3.18	2.27	4.04	0.19	14.86	0.04703
ESDNi03	1.6	13.41	59.36	1.4	2.7	3.65	0.19	17.68	0.052005
SPNi01	3.95	20.07	52.15	2.49	2.59	0.86	-	17.89	-
SPNi02	1.66	18.34	54.1	1.65	4.04	1.29	0.21	18.7	0.162791
SPNi03	4.05	19.87	53.35	1.64	3.42	1.14	0.12	16.41	0.105263

Table 4.8: EDX analysis of ESD Cu:NiO and SP Cu:NiO layers (in atomic percent).

4.1.2.5. XRD study and optical properties of perovskite layers deposited on ESD and SP-Cu:NiO layers

The aforementioned results show that using the ESD approach reduces the roughness of the Cu:NiO layer and improves electrical conductivity. All of these are necessary for the perovskite layer to have good crystalline quality and fast extraction of charge carriers. The effect of the Cu:NiO layer on the perovskite crystallinity was studied using X-ray diffraction (XRD). As shown in Figure 4.18, in both cases, clear substrate peaks assigned to FTO are detected at 30.8° and 44.1°, indicating that the X-rays have penetrated the perovskite layer throughout its entire thickness. The triple-cation perovskite ($CsFAMAPbI_{3-x}Br_x$) films formed on the SP Cu:NiO and ESD Cu:NiO HTLs exhibits main diffraction peaks at 16.41°, 33.23°, and 37.29° corresponding to the (*001*), (*002*), and (*012*) reflections of the cubic crystalline phase (space group $Pm\bar{3}m$)[28]. At 23.30°, 28.66°, 47.66°, and 50.78°, respectively, are the reticular planes (*011*), (*111*), (*022*), and (*003*) of the CsFAMA cubic crystalline phase. The lattice parameters of the cubic triple-cation perovskite on the ESD Cu:NiO HTL and on the SP Cu:NiO HTL are 6.279 and 6.273 Å, respectively. The presence of excess lead iodide (PbI_2), which can eventually passivate grain boundaries and improve the perovskite solar cell performance[29,30], is also indicated by a strong diffraction peak at 14.69°. Because the relative intensities of those peaks are identical for each pattern, the ESD Cu:NiO layer is unlikely to change the growth direction of the perovskite layer and maintains the preferred orientation also observed with SP Cu:NiO. However, the absolute intensity of the *(001)* and *(002)* peaks of the perovskite layer grown on the ESD Cu:NiO HTL is higher than that of the perovskite on the SP Cu:NiO HTL. As the perovskite layers based on different HTLs have identical thicknesses, around

650nm (cf. Figure 4.23), this higher absolute intensity implies that the presence of the ESD NiO layer is favoring higher crystallinity[31].

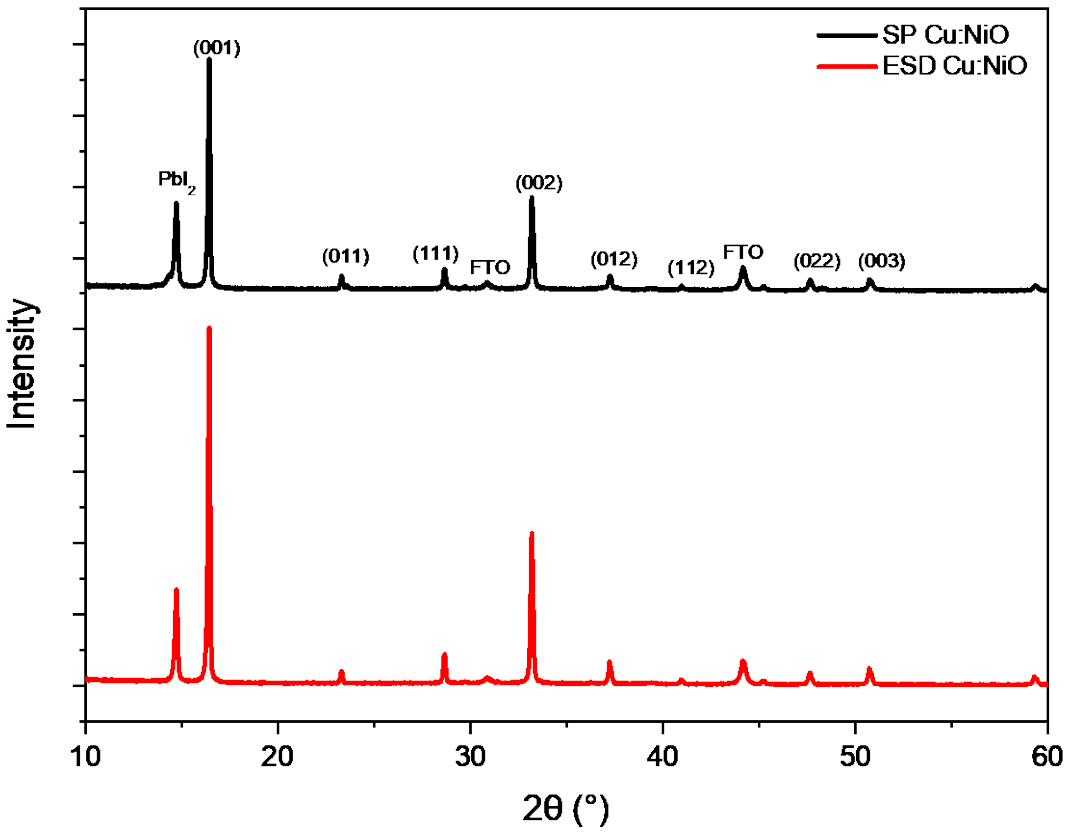

Figure 4.18: XRD patterns of CsFAMA/SP Cu:NiO/FTO and CsFAMA/ESD Cu:NiO/FTO samples.

The overall performance of PSCs is directly influenced by the crystalline quality of the perovskite. The level of inhomogeneous strain in the perovskite, as indicated by XRD peak broadening, is an excellent predictor of crystalline quality. The results, however, cannot be utilized to precisely and quantitatively assess crystallite size and distortion (strain), which both contribute to peak broadening, due to the instrumental resolution. Strain is the major driver of peak broadening since the perpendicular crystallite size of the perovskite film obtained by SEM is more than 100 nm, suggesting that the relative full width at half maximum (FWHM) is proportional to strain. The existence of deformation (strain) in the crystal lattice is indicated by the observed increase in FWHM value at higher diffraction orders. This distortion appears to be lower for the perovskite film grown on the Cu:NiO film formed via ESD, as shown in Figure 4.19, evidencing improved perovskite crystalline quality.

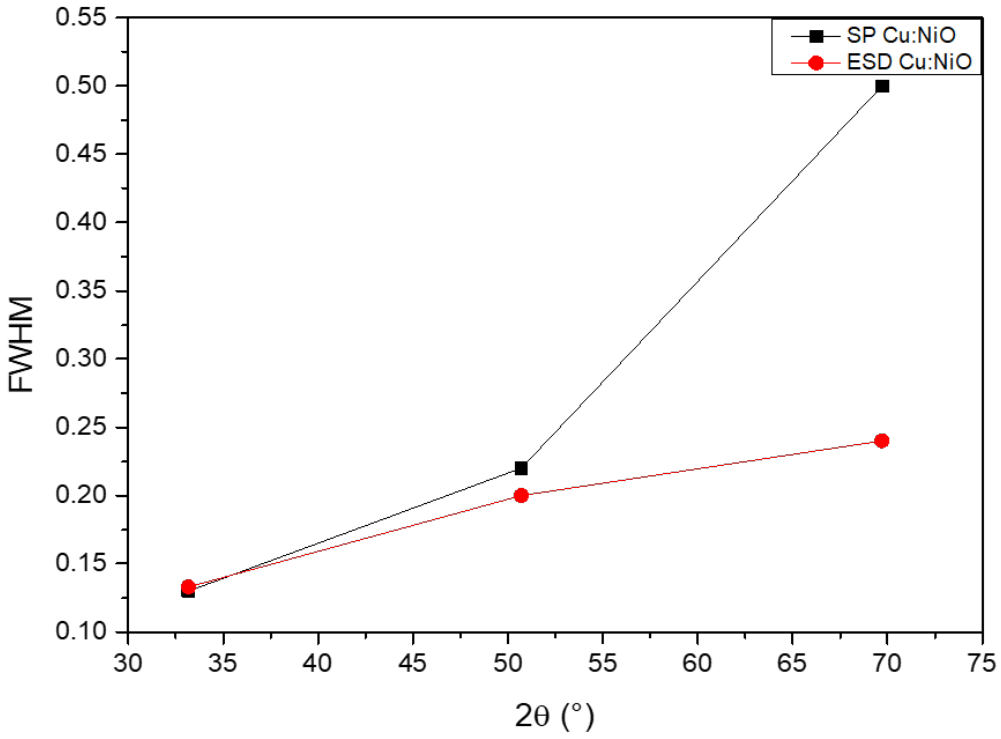

Figure 4.19: Peak full width at half maximum (FWHM) of the different (00l) perovskite diffraction peaks.

Because the thicknesses of the perovskite layers grown on the different substrates are very similar, around 650 nm (cf. Figure 4.23), enhanced perovskite crystalline quality is expected to have a positive impact on UV-vis absorption (cf. Figure 4.20A). In the characteristic wavelength range of 500 nm to 750 nm, the UV-vis absorption spectra of SP Cu:NiO/PVK and ESD Cu:NiO/PVK are essential identical. Steady-state PL measurements were conducted to study the hole extraction process. The emission band of the perovskite peaks at about 760 nm for both types of HTL, as demonstrated in the PL spectra using an excitation wavelength of 420 nm, as shown in Figure 4.20B. Even though in the first 200 nm of the perovskite layer, at least 90% of the light should be absorbed due to the excitation from the perovskite side[32], there are substantial differences between the two samples. In the case of the ESD NiO layer, the PL intensity significantly reduced. As shown above, the ESD Cu:NiO sample has a better perovskite crystallization, which should result in a lower trap density and hence reduced PL quenching and a longer PL lifetime. On the other hand, an improved quality of the Cu:NiO / PVK interface in the case of the ESD HTL could be at the origin of enhanced hole transfer, reducing radiative recombination of the photogenerated carriers.

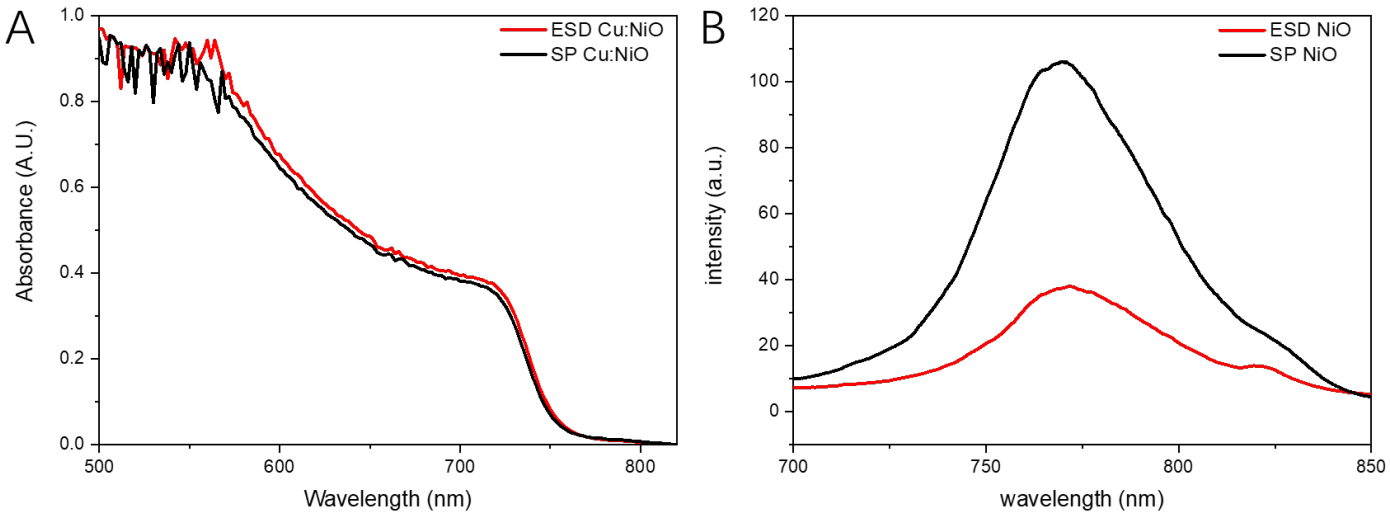

Figure 4.20: A) UV–vis spectra of the perovskite films deposited on SP Cu:NiO and on ESD Cu:NiO layers; B) Steady-state photoluminescence (PL) spectra.

To learn more about the device's charge carrier recombination mechanisms we analyzed the relationship between *Voc* and light intensity (see Figure 4.21). If free electron and hole recombination predominate in the active layer, the slope of *Voc* versus light intensity is greater than kT/q. In this case, *Voc* is highly reliant on the light intensity, where q is the electronic charge, k is the Boltzmann constant, and T is the Kelvin temperature. The device based on spin-coated Cu:NiO layer has a slope of 2.1 kT/q, whereas the device based on ESD Cu:NiO layer has a slope of 1.4 kT/q indicating that charge carrier recombination is strongly reduced. As a result, the perovskite film has faster charge transfer kinetics and a greater hole extraction capacity for the ESD Cu:NiO layer, which can significantly minimize carrier recombination in the PSC active layer, therefore enhancing the devices FF.

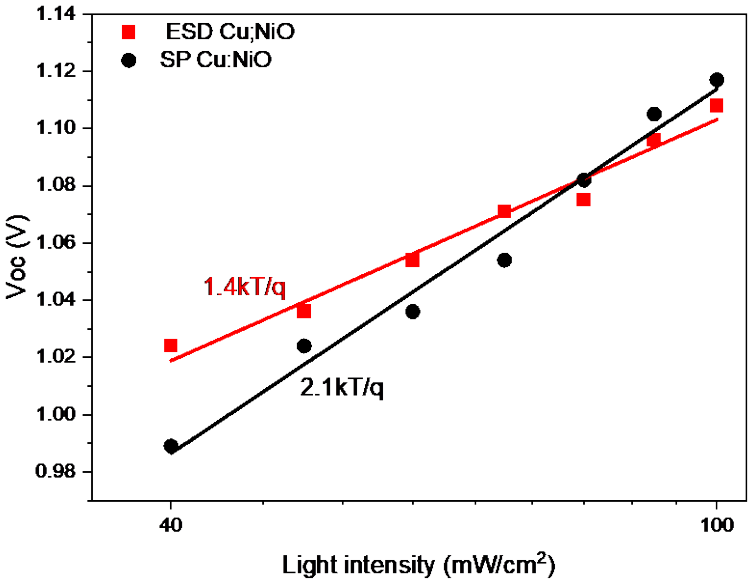

Figure 4.21: *Voc* of PSCs based on ESD Cu:NiO and SP Cu:NiO HTLs as a function of light intensity.

4.1.2.6. Morphology of the perovskite layer grown on ESD and SP Cu:NiO layers

To assess the influence of the underlying HTL on the morphology of the perovskite layers, top-view SEM images of SP Cu:NiO/PVK and ESD Cu:NiO/PVK samples were acquired. We found a high number of dotted crystals in the perovskite films prepared on both HTLs, as shown in Figure 4.22A. These dotted crystals were caused by an excess of lead iodide[33]. The spin-coated Cu:NiO layer on the perovskite film has a much larger number of pinholes than in the sample based on the ESD Cu:NiO (Figure 4.22B). This demonstrates that ESD Cu:NiO hole transport layer thus contributes to the uniform crystallization of the perovskite layer and greatly reduces defects such as pinholes. This may be attributed to the fact that the smoother HTL is beneficial to the growth of perovskite.

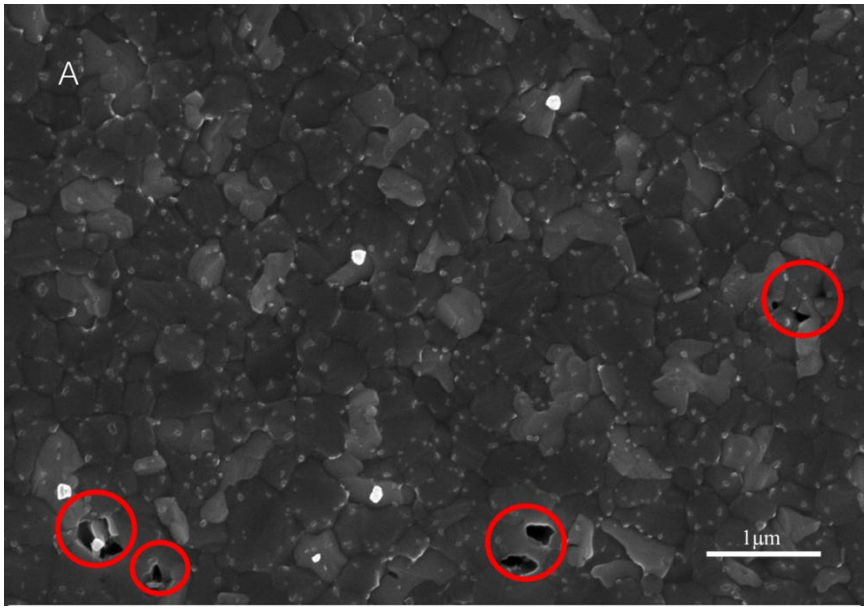

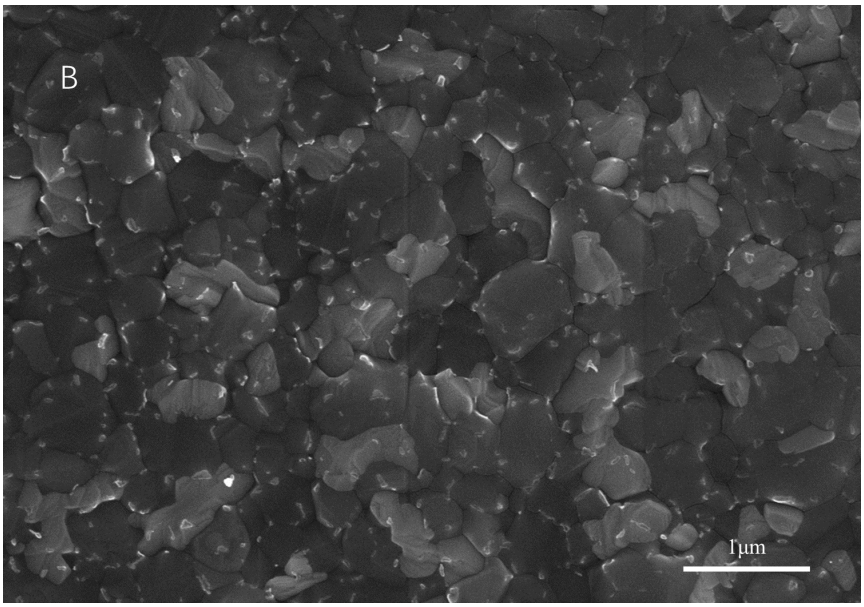

Figure 4.22: Top-view SEM images of perovskite layers grown on Cu:NiO layers prepared by A) SP - pinholes are marked by red circle; B) ESD.

4.1.2.7. Photovoltaic performance

Based on the above analysis, the ESD Cu:NiO layer is expected to be beneficial for boosting the device performance, as a result of the better interface contact, improved crystallization of the perovskite, and lower trap density at the perovskite/ETL interface. The thicknesses of the different layers of both devices are shown in Figure 4.23 revealing that the perovskite layers are 650 nm to 700 nm, and the ETLs (PCBM) are 70 nm. Finally, we deposited 4 nm of BCP on top of PCBM via thermal evaporation and a 200 nm thick Ag electrode on the top. From the cross-section SEM images, the thickness of the SP Cu:NiO HTL was estimated to be around 50 nm, while it was a little bit thicker (around 80 nm) for the ESD HTL.

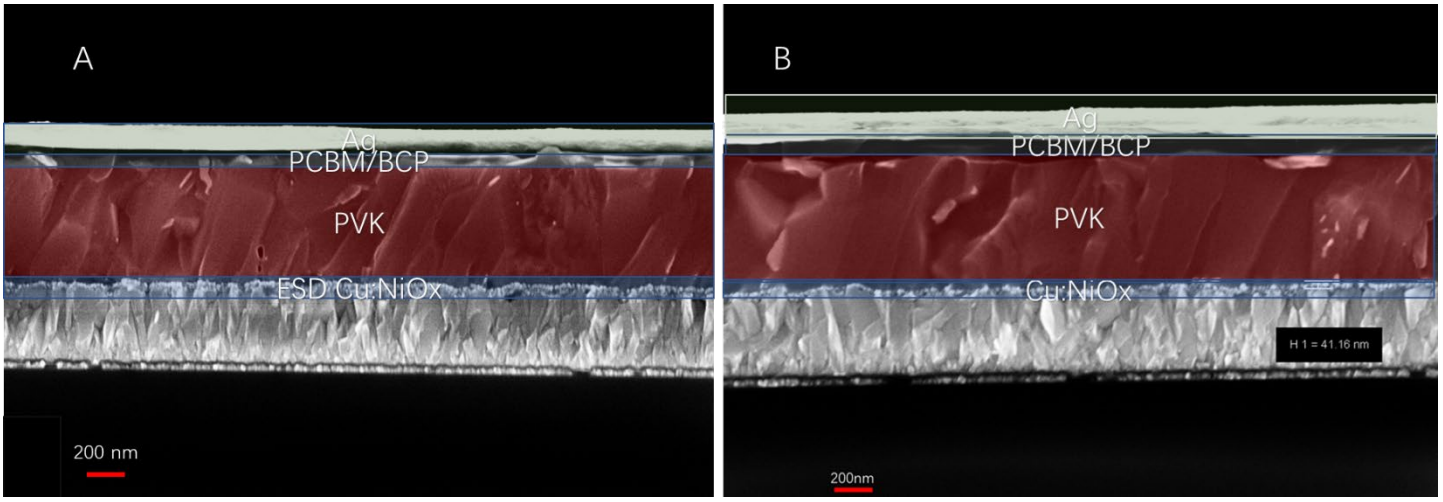

Figure 4.23: Cross section SEM images of A) FTO/ESD Cu:NiO /CsFAMA/PCBM/Ag; B) FTO/SP Cu:NiO/ CsFAMA /PCBM/Ag (scale bar: 200 nm).

The corresponding *J*/*V* curves of devices obtained by low-temperature processing are shown in Figure 4.24A. For devices with the ESD Cu:NiO layer, the PCE reaches 17.11% and the values recorded for FF were also higher than those containing the spin-coated HTL (14.55% PCE). Furthermore, Figure 4.24B shows that the *J*-*V* hysteresis almost disappeared when applying the ESD Cu:NiO HTL. The detailed *J*–*V* parameters are summarized in Table 4.9.

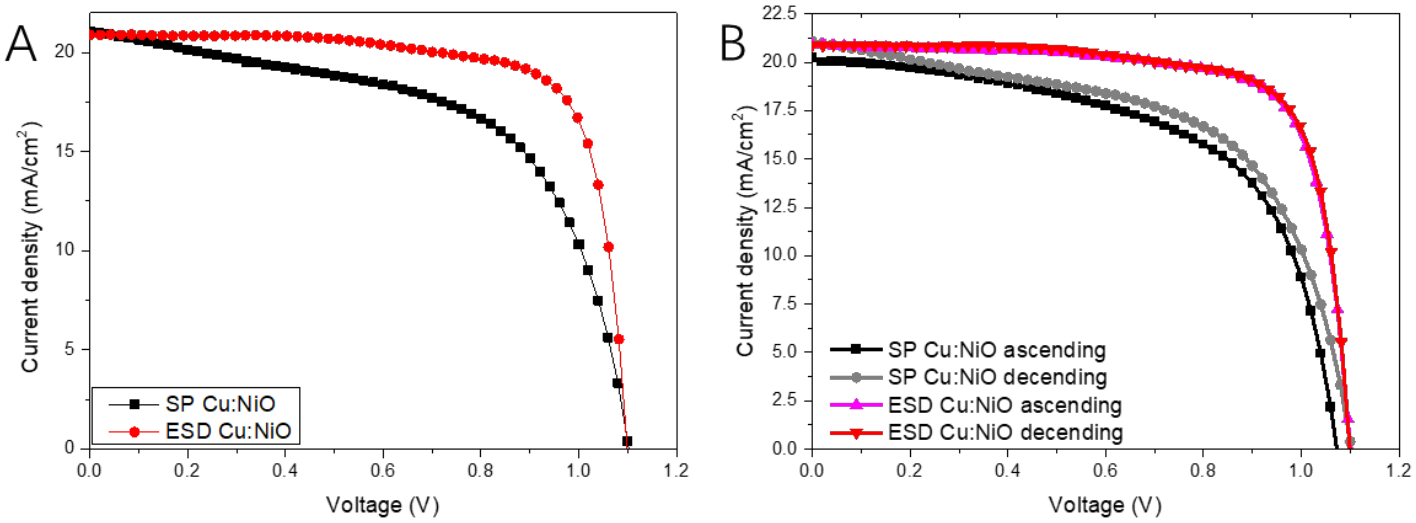

Figure 4.24: *J*/*V* curves of A) devices using the two different HTLs; B) reverse and forward scans for revealing strongly reduced hysteresis with the ESD HTL.

	Voc (V)	Jsc (mA/cm^2)	Fill Factor (%)	Efficiency (%)	Average efficiency (%)	Hysteresis index (%)

SP Cu:NiO descending	1.12	21.07	61.65	14.55	14.12	6.0
SP Cu:NiO ascending	1.07	20.24	63.15	13.68		
ESD Cu:NiO descending	1.10	20.90	74.43	17.11	16.99	1.4
ESD Cu:NiO ascending	1.09	20.88	74.15	16.87		

Table 4.9: Device parameters and hysteresis index of the best performing PSCs using ESD and SP HTLs.

The statistical distribution of the efficiencies of the devices tested is shown in Figure 4.29. As marker in Figure 4.25C, the devices based on ESD Cu:NiO layer present a strongly enhanced FF. For the cells based on SP Cu:NiO layer, most of the FF values are around 0.61, whereas the FF for devices based on ESD Cu:NiO is in the range around 0.72, with the highest value being 0.75. This demonstrates that the ESD Cu:NiO HTL brings advantages of lower trapping density near the surface and improved perovskite crystallization to the devices. Also, the higher FF and smaller hysteresis indicate better extraction of charge carriers, which is caused by better energy level alignment, higher mobility and conductivity, and less nonradiative recombination at the interface between the perovskite and the charge transport layer. However, it is necessary to notice that the relatively thick ESD Cu:NiO layer (70-80 nm) can be at the origin of performance limitations (generally inorganic HTLs are as thin as possible, just around 20-30 nm).

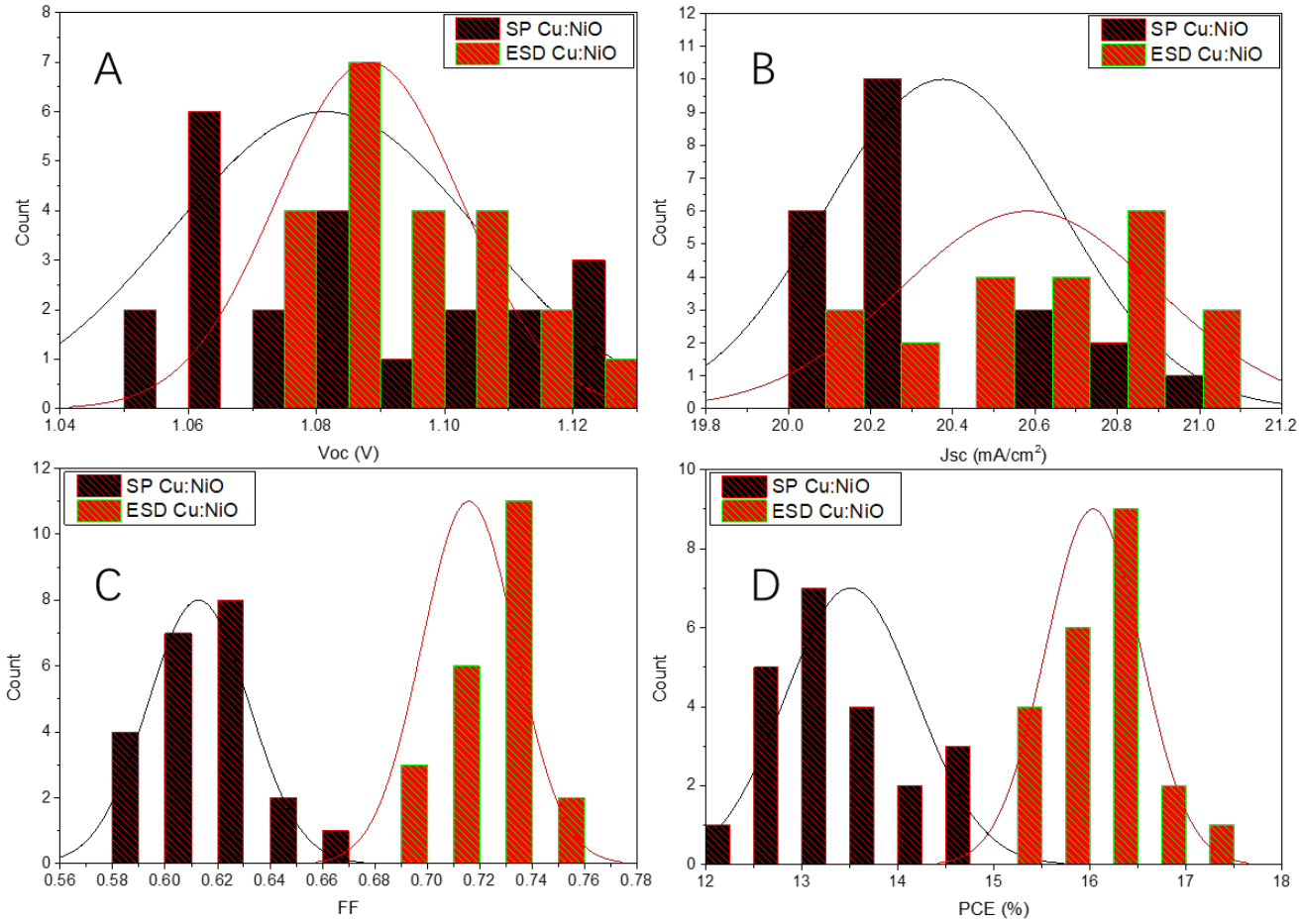

Figure 4.25: Comparison of the device performance distribution for both HTLs.

Apart from high efficiency the long-term stability of PSCs is another important prerequisite for their practical use. To find out, we examined the environmental stability of the solar cells (*Voc*, *FF*, and PCE) for 360 h, as illustrated in Figure 4.26A-C. The PSCs using inorganic Cu:NiO HTLs are expected to be more stable than devices using organic HTLs such as spiro-OMeTAD in ambient oxygen and moisture conditions. However, there is a large difference in ambient stability between the PSCs using the two different HTLs (SP and ESD): After 15 days of storage, the PCE values of PSCs with ESD Cu:NiO and SP Cu:NiO HTLs were 92.1 % and 61.5 % of their initial efficiency, respectively. The *Voc* of the PSCs with ESD Cu:NiO HTLs remained nearly constant. The small drop in PCE was mostly attributable to a small reduction in *FF*. To th contrary, the *Voc* and *FF* of devices utilizing SP Cu:NiO HTLs are significantly reduced. This could be due to the smaller grain size of the perovskite films when using SP Cu:NiO, which is not favorable for preventing water penetration at grain boundaries. Furthermore, SP Cu:NiO-based devices display more pinholes and defects at the ETL/perovskite interface, and these defects could be extended with time. This process raises the proportion of grain boundaries and speeds up the rate of deterioration, both of which deteriorate the performance[34].

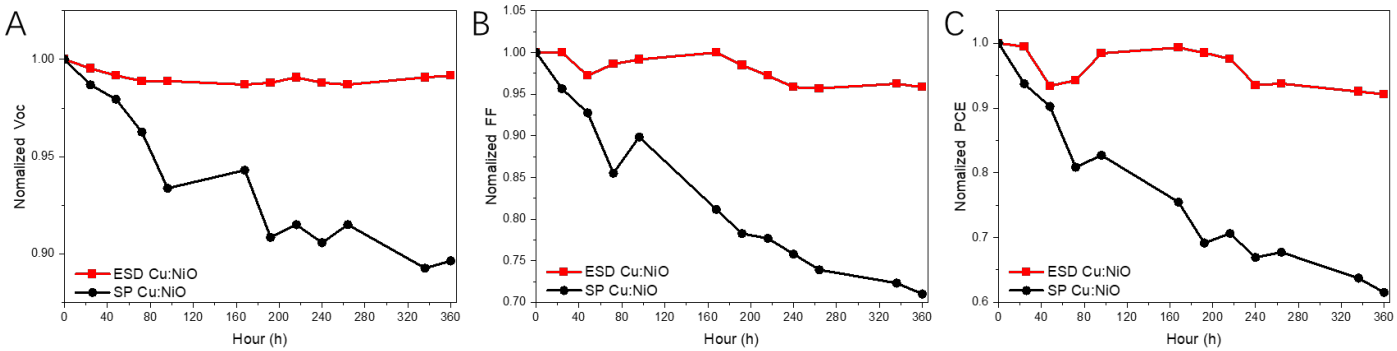

Figure 4.26: Environmental stability of the photovoltaic parameters (A) *Voc*; (B) FF; and (C) PCE of PSCs using ESD Cu:NiO and SP Cu:NiO HTLs under ambient conditions (20% humidity, 25°C). All devices were kept in opaque aluminum bags.

4.2. Lithium doped NiO hole transport layers prepared by ESD

In addition to the p-type metal ion Cu^{2+} doping, monovalent alkali metals, such as lithium (Li^{+}) ions, can also be used as dopants to increase the electrical conductivity of NiO films. Since the ionic radius of Li^{+} (0.76 Å) is similar to that of Ni^{2+} (0.70 Å), NiO can be effectively doped into the NiO lattice[35]. Its introduction leads to an increase in Ni^{3+} ion concentration and a decrease in the resistivity of NiO films. Unlike Cu^{2+} dopants, the most interesting feature of monovalent alkali metal doping is that they can improve electrical conductivity while producing negligible effects on the light transmission properties of NiO HTL[8,36].

Previously, Qiu and his colleagues reported that a maximum PCE of 15.41% was achieved with NiO when doping with 5 mol% lithium[15]. Therefore, we first attempted to prepare 5 mol% Li-doped NiO films using ESD. We have transferred our experience based on the above ESD Cu:NiO investigation to fabricate Li-doped NiO using the optimized ESD parameters. Practically, we prepared a precursor solution of 0.02 M, dissolving nickel (II) nitrate hexahydrate salt ($Ni(NO_3)_2{\cdot}6H_2O$, Sigma Aldrich, 99.00 %) along with 2.5, 5, 7.5, and 10 mol% of lithium nitrate ($LiNO_3$, Sigma Aldrich, 99.99 %) in 30 ml of butyl carbitol. We selected a substrate temperature of 300 °C, a deposition time of 15min, a flow rate of the precursor solution of 1.5 mL h^{-1}, a nozzle-to-substrate distance of 30 mm, and a voltage of 6-8 kV.

4.2.1. XRD study and optical properties of ESD Li:NiO

The phase purity and crystalline quality of doped NiO layers generated by electrostatic spray deposition (ESD) with 5 mol% Li dopant concentration were investigated using X-ray diffraction (XRD) and compared to layers

prepared with 5 mol% Cu dopant. Due to the thin NiO layers (around 80 nm), grazing incidence X-ray diffraction (GIXRD) was used, as illustrated in Figure 4.27. The diffraction peaks (*111*), (*200*), (*220*), and (*311*) of the cubic phase NiO (space group $Fm\bar{3}m$) are easily distinguishable, indicating a good crystalline quality of the NiO layers. Even at a small XRD incidence angle of 0.4°, the FTO substrate displays a substantial signal. The relative intensities of the NiO peaks are comparable for each case, implying that the nature of the dopant does not induce any kind of anisotropy or preferential orientation. For a more detailed comparison of the the NiO films using the two different dopants, we compared the positions of the (*200*) and (*220*) peaks, which do not overlap with substrate peaks. No shifts in the peak positions were found indicating that doping with Li^+ instead of Cu^{2+} does not affect the crystal structure or lattice parameters of the NiO host, which is expected considering the similar ionic radii of Li^+ and Cu^{2+}.

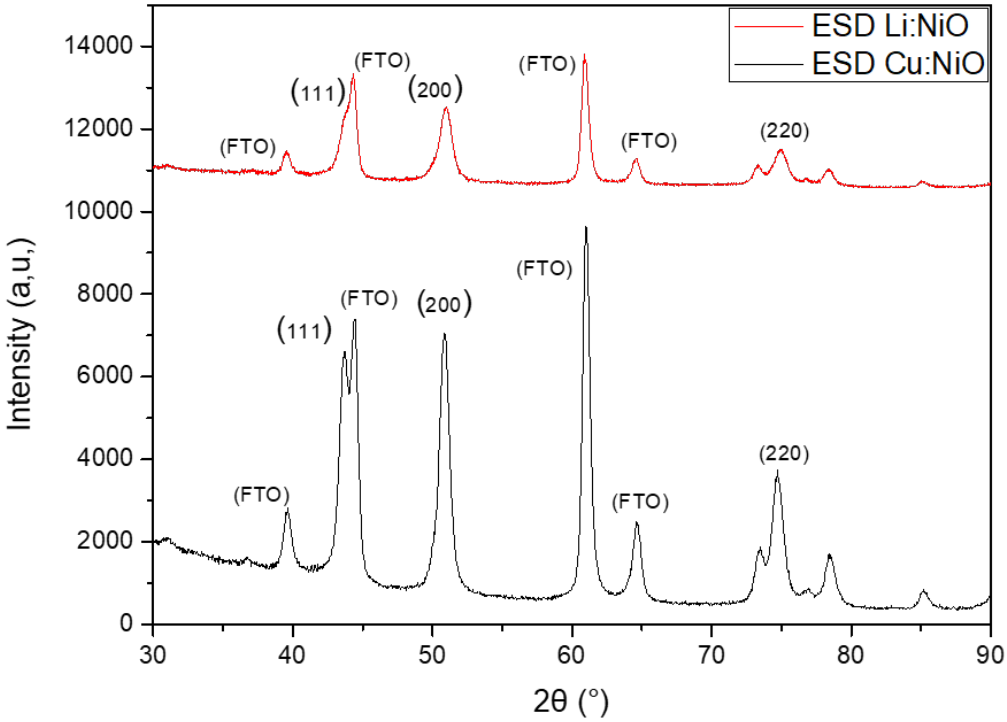

Figure 4.28: XRD patterns of NiO layers on FTO-coated glass substrates fabricated by ESD using 5 mol% of Cu^{2+} and Li^+ dopants.

Figure 4.28 shows the optical transmittance of ESD Cu:NiO and Li:NiO layers. Above 450 nm, both layers have high optical transparency, making them suitable candidates for HTLs in PSCs. Meanwhile, as compared to NiO films doped by Li^+, the transparency of NiO films doped by Cu^{2+} is slightly lower. This might be the result of the optical bandgap change caused by different dopants[8]. However, it is noteworthy that when testing

the optical properties of Li-doped NiO films, the experimental results showed extremely low reproducibility. The results shown here occurred only a few times.

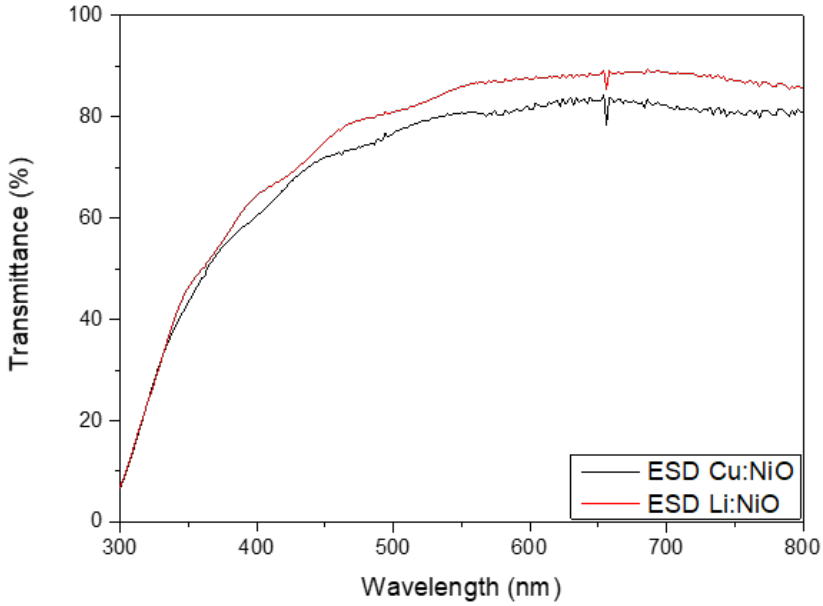

Figure 4.29: Optical transmittance spectra of 5 mol% Cu-doped and Li-doped NiO layers.

4.2.2. Morphological properties of ESD Li:NiO layers

Figure 4.29A-D shows top-view SEM images of NiO films using different concentrations of Li^+ dopant. In all cases, the ESD Li:NiO completely covered the FTO substrate with almost no voids. The FTO crystal contours can be seen below the Li:NiO layer, and the surface shape of the ESD Li:NiO layer is the same as that of the bare FTO surface, which means that the Li:NiO nanocrystals are conformally covering the FTO surface. On this continuous, uniform, and crack-free surface, the substrate is completely covered by compact Li:NiO nanoparticles. However, with increasing dopant concentration, for NiO layers doped with 5 mol%, 7.5 mol%, and 10 mol% Li, some cubic crystals appear on the NiO surface. The origin of these cubic crystals must still be confirmed.

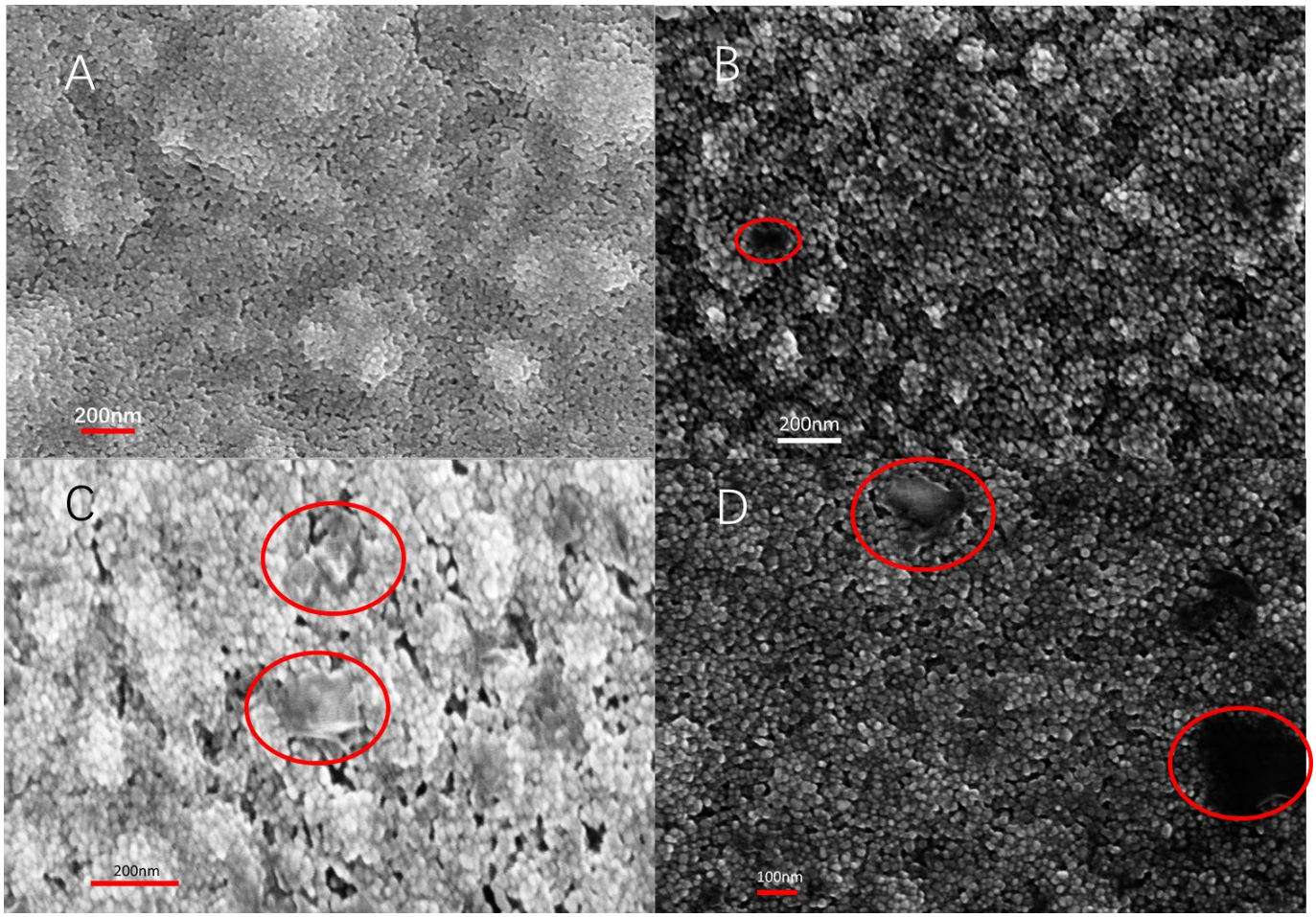

Figure 4.30: Top-view SEM images of x mol% Li-doped NiO layers deposited by ESD: A) x=2.5; B) x=5; C) x=7.5; D) x=10

Based on these four Li:NiO layers we prepared perovskite solar cells using the optimized conditions for the deposition of each layer described above. Table 4.10 shows the device parameters of the solar cells prepared using the different HTLs. It can be seen that the efficiency of the perovskite solar cell is improved as the concentration of Li doping increases but reaches a maximum at 5 mol%. This behavior is mostly originating from an increase in *Jsc* and *FF*, which is related to the fact that lithium-doped NiO films considerably enhance conductivity, hence decreasing carrier transport losses in HTL[36]. However, when the concentration of Li^+ was further increased to 7.5 mol%, the PCE of started to decrease and at 10 mol%, it dropped to 10.77%. Excessive lithium doping introduces more defects and degrades the crystal quality of the Li:NiO thin film. In addition, as the dopant concentration increases, the lithium ions not only occupy Ni sites but also interstitial sites, which annihilates holes after the photo-generation of charge carriers[37].

	Voc(V)	Jsc(mA/cm²)	FF	PCE
2.5mol%Li^+	1.09	20.17	0.59	12.97
5mol%Li^+	1.09	21.85	0.64	15.24
7.5mol%Li^+	1.02	20.33	0.62	12.86
10mol%Li^+	0.93	19.96	0.58	10.77

Table 4.10: Best performance of the devices based on ESD Li:NiO HTLs with different Li concentrations.

The above results demonstrate that the use of 5 mol% Li^+ doped NiO HTLs can improve the photovoltaic conversion efficiency of the device with respect to undoped NiO HTLs. However, we note a serious problem of reproducibility for these devices. Figure 4.30 displays the dispersion of each parameter of the PSCs, all of which show a very large dispersion.

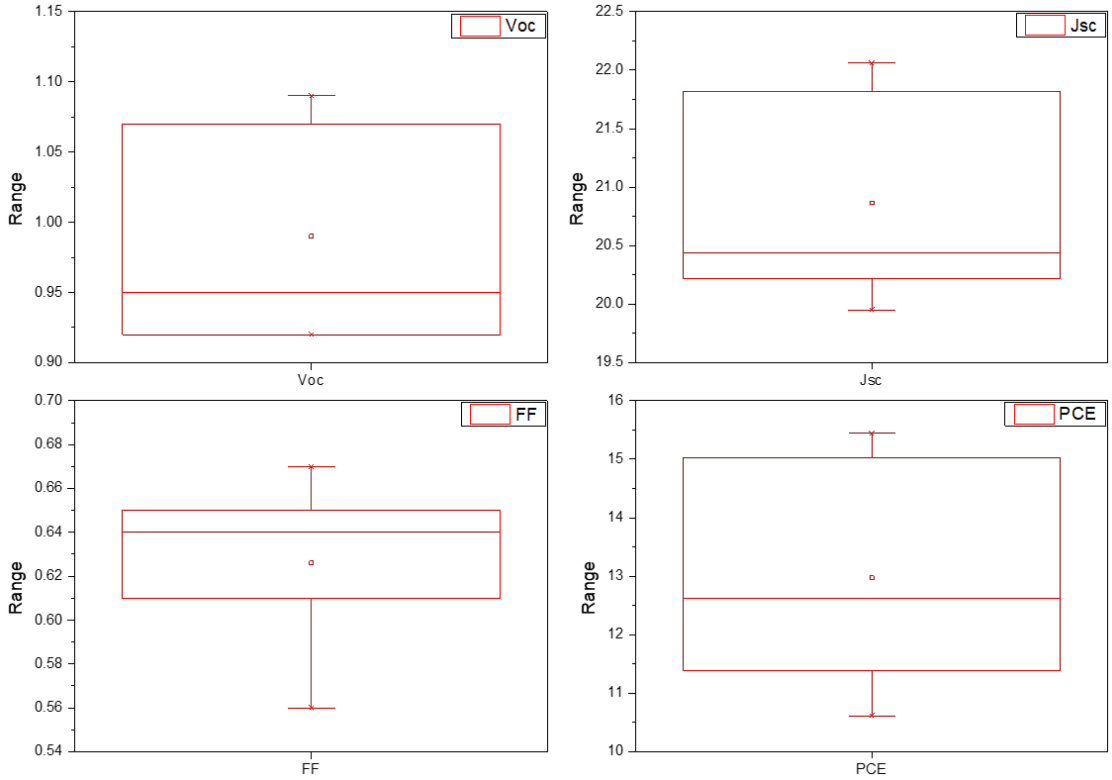

Figure 4.31: Device performance distribution of PSCs using a 5mol% Li:NiO HTL (statistics of 18 devices).

4.2.3. Li:NiO film composition analysis

To investigate the reason of the unreproducible device performance, we used XPS to study the elemental composition of the Li:NiO films. Figure 4.31 shows the complete spectrum of the Li:NiO layer produced by

ESD. Again, we did not observe an Sn peak confirming that the ESD Li:NiO film completely covered the FTO substrate. Usually, the Li signal in XPS appears at 45-55 eV[38]. Unexpectedly we did not find any signal of Li. This indicates that the doping with Li^+ is not uniform.

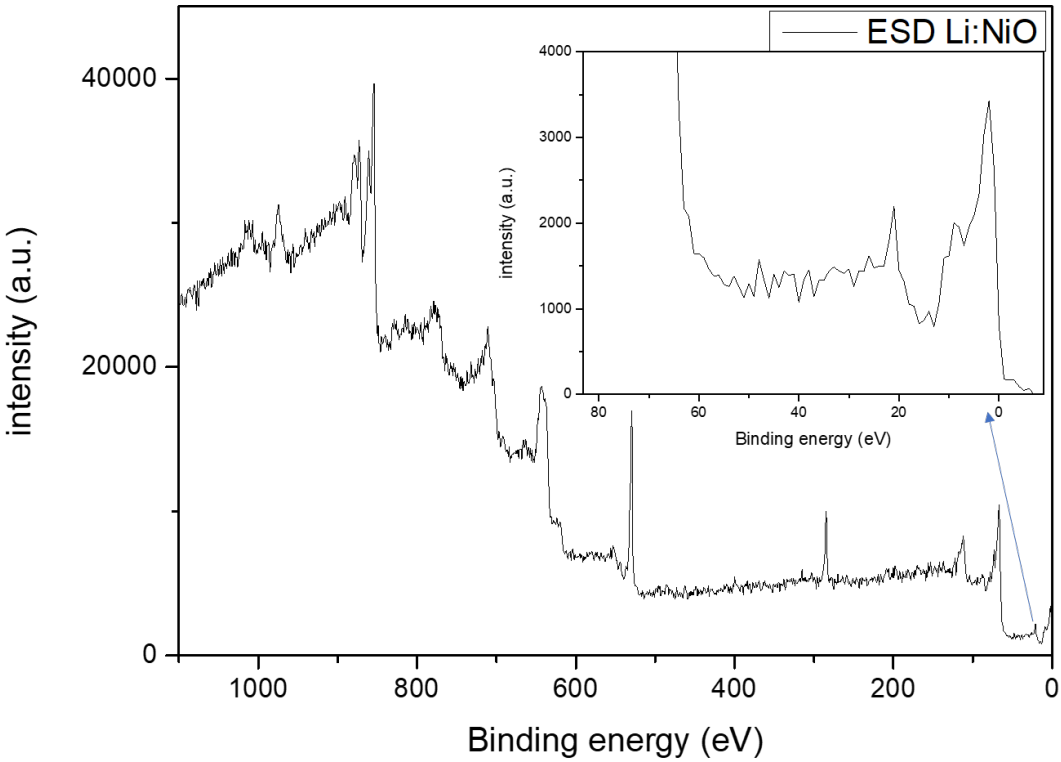

Figure 4.32: XPS spectrum of the 5 mol% Li doped NiO layer produced by ESD.

The reason for this phenomenon may be due to the very low solubility of $LiNO_3$ in butyl carbitol. Figure 4.32 shows a photograph of the $LiNO_3$ butyl carbitol suspension with the concentration of 0.5 mol/L after stirring for 24 hours at 60° C. We expect that the $LiNO_3$ dispersion in the precursor solution will be inhomogeneous due to the poor solubility. Furthermore, the charged droplets will fly to the substrate during electrostatic spray deposition, as stated previously. This process is accompanied by the volatilization of the solution. $LiNO_3$ precipitates early and has difficulties diffusing on the substrate surface due to its low solubility, leading to localized Li-enriched regions. This might explain the cubic crystal impurities shown in the top-view SEM images above. We tried other common Li sources, such as lithium acetate and lithium chloride, however, all of these Li salts exhibited poor solubility in the ESD solvent. Overall, Li-doping can be a very interesting perspective as the encountered solubility problems can likely be overcome by investing more time in the study of novel Li precursor/solvent couples.

Figure 4.33: Photograph of $LiNO_3$ in butyl carbitol with a concentration of 0.5 mol L^{-1}.

Conclusion

In this chapter, we explored an innovative method, electrostatic spray deposition, for the preparation of thin films of the inorganic semiconductor metal oxide NiO to be used as HTL in PSCs. Dense Cu-doped NiO films with a well-controlled thickness of 80 nm were successfully coated on FTO by optimizing the deposition time from to 15 min, the substrate temperature to 300 °C, and the precursors' solution concentration to 0.02 M. We note that the comparably low processing temperature of 300°C may be compatible with the use of ITO-coated glass substrates, which commonly show higher performance in PSCs.

Importantly, the ESD Cu:NiO films are characterized by a higher conductivity and hole mobility as well as smoother surface morphology than classic spin-coated Cu:NiO films. When deposited by electrostatic spraying, the Cu dopant is more evenly distributed in the NiO film than in the case of spin-coating provided that each droplet obtained by electrostatic atomization is containing the stoichiometric precursors' solution. This requirement has been evidenced when switching from Cu to Li used as the dopant: in the latter case, the inhomogeneous ESD precursor solutions led to a non-uniform dopant distribution in the NiO HTLs, and ultimately to a low reproducibility of the resulting PSCs.

The PCE of perovskite solar cells using ESD Cu:NiO HTLs with an optimized doping level of 5 mol% reached values above 17% (best device: 17.43%), accompanied by low hysteresis, enhanced environmental stability, and excellent repeatability. The newly developed ESD process for NiO HTL deposition opens up new opportunities for PSCs. For industrial fabrication of PSCs, not only high efficiency and environmental stability are required, also the scale-up to larger device areas while keeping excellent uniformity of each leayer are necessary. In this context, electrostatic spray deposition may be a viable approach for the preparation of uniform large-area HTLs (end ETLs) with excellent optical and electrical characteristics.

References

1. Kim, J. H. *et al.* High-performance and environmentally stable planar heterojunction perovskite solar cells based on a solution-processed copper-doped nickel oxide hole-transporting layer. *Adv. Mater.* 27, 695–701 (2015).
2. Chen, W. *et al.* Understanding the Doping Effect on NiO: Toward High-Performance Inverted Perovskite Solar Cells. *Adv. Energy Mater.* 8, 1–10 (2018).
3. Jung, J. W., Chueh, C. C. & Jen, A. K. Y. A Low-Temperature, Solution-Processable, Cu-Doped Nickel Oxide Hole-Transporting Layer via the Combustion Method for High-Performance Thin-Film Perovskite Solar Cells. *Adv. Mater.* 27, 7874–7880 (2015).
4. Ye, J. *et al.* Doped Bilayer Tin(IV) Oxide Electron Transport Layer for High Open-Circuit Voltage Planar Perovskite Solar Cells with Reduced Hysteresis. *Small* 17, 1–9 (2021).
5. Park, J. H. *et al.* Efficient CH3NH3PbI3 Perovskite Solar Cells Employing Nanostructured p-Type NiO Electrode Formed by a Pulsed Laser Deposition. *Adv. Mater.* 27, 4013–4019 (2015).
6. Feng, M. *et al.* High-Efficiency and Stable Inverted Planar Perovskite Solar Cells with Pulsed Laser Deposited Cu-Doped NiOxHole-Transport Layers. *ACS Appl. Mater. Interfaces* 12, 50684–50691 (2020).
7. Zhang, M. *et al.* Acceptor-Doping Accelerated Charge Separation in Cu2O Photocathode for Photoelectrochemical Water Splitting: Theoretical and Experimental Studies. *Angew. Chemie - Int. Ed.* 59, 18463–18467 (2020).
8. Xu, L. *et al.* Inverted perovskite solar cells employing doped NiO hole transport layers: A review. *Nano Energy* 63, 103860 (2019).
9. Tang, L. J. *et al.* A Solution-Processed Transparent NiO Hole-Extraction Layer for High-Performance Inverted Perovskite Solar Cells. *Chem. - A Eur. J.* 24, 2845–2849 (2018).
10. Zhao, L. *et al.* Optical and electrochemical properties of Cu-doped NiO films prepared by electrochemical deposition. *Appl. Surf. Sci.* 257, 3974–3979 (2011).
11. Makuła, P., Pacia, M. & Macyk, W. How To Correctly Determine the Band Gap Energy of Modified Semiconductor Photocatalysts Based on UV-Vis Spectra. *J. Phys. Chem. Lett.* 9, 6814–6817 (2018).
12. Rahm, M., Hoffmann, R. & Ashcroft, N. W. Atomic and Ionic Radii of Elements 1–96. *Chem. - A Eur. J.* 22, 14625–14632 (2016).
13. Kim, K. H., Takahashi, C., Abe, Y. & Kawamura, M. Effects of Cu doping on nickel oxide thin film prepared by sol-gel solution process. *Optik (Stuttg).* 125, 2899–2901 (2014).

14. Nag, S., Banerjee, K. & Datta, D. Estimation of the van der Waals radii of the d-block elements using the concept of bond valence. *New J. Chem.* 31, 832–834 (2007).
15. Qiu, Z. *et al.* Enhanced physical properties of pulsed laser deposited NiO films via annealing and lithium doping for improving perovskite solar cell efficiency. *J. Mater. Chem. C* 5, 7084–7094 (2017).
16. Wang, K. *et al.* Low-Temperature Sputtered Nickel Oxide Compact Thin Film as Effective Electron Blocking Layer for Mesoscopic NiO/CH3NH3PbI3 Perovskite Heterojunction Solar Cells. *ACS Appl. Mater. Interfaces* 6, 11851−11858 (2014).
17. Seo, S. *et al.* An ultra-thin, un-doped NiO hole transporting layer of highly efficient (16.4%) organic-inorganic hybrid perovskite solar cells. *Nanoscale* 8, 11403–11412 (2016).
18. Cui, J., Meng, F. & Zhang, H. CH3NH3PbI3-Based Planar Solar Cells with Magnetron-Sputtered Nickel Oxide. *Appl. Mater. Interfaces* 6, 22862–22870 (2014).
19. Kwon, U. *et al.* Solution-Processible Crystalline NiO Nanoparticles for High-Performance Planar Perovskite Photovoltaic Cells. *Sci. Rep.* 6, 1–10 (2016).
20. Chen, W. *et al.* Cesium Doped NiOx as an Efficient Hole Extraction Layer for Inverted Planar Perovskite Solar Cells. *Adv. Energy Mater.* 7, 1–8 (2017).
21. Natu, G. *et al.* Valence band-edge engineering of nickel oxide nanoparticles via cobalt doping for application in p-type dye-sensitized solar cells. *ACS Appl. Mater. Interfaces* 4, 5922–5929 (2012).
22. Zhang, Z. & Wang, P. Highly stable copper oxide composite as an effective photocathode for water splitting via a facile electrochemical synthesis strategy. *J. Mater. Chem.* 22, 2456–2464 (2012).
23. Swadźba-Kwaśny, M. *et al.* Facile in situ synthesis of nanofluids based on ionic liquids and copper oxide clusters and nanoparticles. *Dalt. Trans.* 41, 219–227 (2012).
24. Huang, A. *et al.* Minimizing the energy loss of perovskite solar cells with Cu+ doped NiOx processed at room temperature. *Sol. Energy Mater. Sol. Cells* 182, 128–135 (2018).
25. Yan, W. *et al.* Increasing open circuit voltage by adjusting work function of hole-transporting materials in perovskite solar cells. *Nano Res.* 9, 1600–1608 (2016).
26. Mouhamad, Y., Mokarian-Tabari, P., Clarke, N., Jones, R. A. L. & Geoghegan, M. Dynamics of polymer film formation during spin coating. *J. Appl. Phys.* 116, (2014).
27. Birnie, D. P. A model for drying control cosolvent selection for spin-coating uniformity: The thin film. *Langmuir* 29, 9072–9078 (2013).
28. Zheng, G. *et al.* Manipulation of facet orientation in hybrid perovskite polycrystalline films by cation

cascade. *Nat. Commun.* 9, 1–11 (2018).

29. Du, T. *et al.* Formation, location and beneficial role of PbI2 in lead halide perovskite solar cells. *Sustain. Energy Fuels* 1, 119–126 (2017).
30. Wang, L., Mccleese, C., Kovalsky, A., Zhao, Y. & Burda, C. Femtosecond Time-Resolved Transient Absorption Spectroscopy of CH3NH3PbI3 Perovskite Films: Evidence for Passivation Effect of PbI2. *J. Am. Chem. Soc.* 136, 12205–12208 (2014).
31. Wang, S. *et al.* Smooth perovskite thin films and efficient perovskite solar cells prepared by the hybrid deposition method. *J. Mater. Chem. A* 3, 14631–14641 (2015).
32. De Wolf, S. *et al.* Organometallic halide perovskites: Sharp optical absorption edge and its relation to photovoltaic performance. *J. Phys. Chem. Lett.* 5, 1035–1039 (2014).
33. Jiang, Q. *et al.* Planar-Structure Perovskite Solar Cells with Efficiency beyond 21%. *Adv. Mater.* 29, 1–7 (2017).
34. Sherkar, T. S. *et al.* Recombination in Perovskite Solar Cells: Significance of Grain Boundaries, Interface Traps, and Defect Ions. *ACS Energy Lett.* 2, 1214–1222 (2017).
35. Li, Y., Li, X., Wang, Z., Guo, H. & Li, T. One-step synthesis of Li-doped NiO as high-performance anode material for lithium ion batteries. *Ceram. Int.* 42, 14565–14572 (2016).
36. Dutta, T., Gupta, P., Gupta, A. & Narayan, J. Effect of Li doping in NiO thin films on its transparent and conducting properties and its application in heteroepitaxial p-n junctions. *J. Appl. Phys.* 108, (2010).
37. Jia-heng Zhang, Guo-fa Cai, Ding Zhou, Hong Tang, Xiu-li Wang, C. G. and J. Co-doped NiO nanoflake array films with enhanced electrochromic properties. *J. Mater. Chem. C* (2017).
38. Wood, K. N. & Teeter, G. XPS on Li-Battery-Related Compounds: Analysis of Inorganic SEI Phases and a Methodology for Charge Correction. *ACS Appl. Energy Mater.* 1, 4493–4504 (2018).

Chapter V. NiO nanoparticles synthesis

In Chapters 3 and 4 we reported the preparation of metal oxide semiconductor NiO thin films using the conventional spin-coating method and an innovative electrostatic spray deposition method. Based on these two methods we have successfully prepared perovskite solar cells with good photovoltaic conversion efficiency (>17%) and considerable environmental stability. However, the NiO films prepared based on both methods need to be annealed at a high temperature of around 500°C. This high-temperature treatment obviously limits the application of NiO thin films: they cannot be used on heat-sensitive substrates (e.g., flexible substrates, ITO) and such high temperatures are also incompatible with the integration as a top-cell into tandem devices (e.g., Si/perovskite). Furthermore, nanostructuring and shrinking the crystal size to the nanoscale can generally improve the characteristics of NiO. The observed NiO nanomorphs often exhibit outstanding performance in applications requiring charge transfer and charge transport processes due to the substantially increased interface and significant reduction in size relative to the bulk[1]. Colloidal nanocrystal dispersions can be utilized to regulate the deposition of crystalline nickel oxide at ambient temperature or to fabricate hole transport layers in polymer solar cells[2], making crystalline non-agglomerated dispersible nanoparticles of nickel oxide attractive. Furthermore, shrinking the crystal size to a few nanometers is predicted to change the electrical, optical, and magnetic properties of nanocrystals, as well as their surface properties.

Several other metal oxides can be produced as colloidal non-agglomerated nanocrystals[34], however only very scarce report can be found on the preparation of nickel oxide nanoparticles. Sol-gel[5], hydrothermal[6], and solution thermal processes[7] allow for the control of the nanoparticle size, shape, and aggregation state, enabling the production of nanoparticles as tiny as a few nanometers. In this chapter, we report the exploration of different methods for the preparation of ultra-small, crystalline and dispersible NiO nanoparticles. Among them, we have developed a novel thermal decomposition method in an organic solvent for the preparation of NiO nanoparticles of tunable size in a range of 3 nm to 8 nm.

5.1. Sol-gel synthesis of NiO nanoparticles

Metal oxides can be made by precipitating metal ions in the presence of OH^- ions from metal salts forming first a sol of ultrasmall nanoparticles / nanoclusters, which subsequently transform to a gel/more viscous phase in the course of the reaction. The latter is generally transformed to the final metal oxide nanoparticles by thermal treatment. NH_4OH and NaOH are commonly utilized as sources of hydroxide ions in this sol-gel procedure. The precipitation reaction can be represented by:

$$M^{n+} + nOH^- \rightarrow M(OH)_n \rightarrow M_xO_y \cdot zH_2O \rightarrow M_xO_y + zH_2O$$

The produced metal oxides M_xO_y are frequently seen to be coupled with H_2O molecules adsorbed on the surface of the particles. These can be eliminated by adding acetone to the sample or heating it to around 200°C. In other situations, however, even heating to 600°C is insufficient to eliminate the ligated water molecules. To create materials with greater densities, dehydrated samples in pellet form are generally sintered at higher temperatures (>1000°C).

Fei Jiang and coworkers reported a typical method for synthesizing NiO nanoparticles. Chemical precipitation of NPs was achieved utilizing commercially available materials $Ni(NO_3)_2{\cdot}6H_2O$ and NaOH. In deionized water, the raw material is easily soluble. The clear green aqueous colloidal solution becomes cloudy after adding NaOH dropwise. By keeping the pH of the solution at 10, ultrafine nickel hydroxide $Ni(OH)_2$ was produced in large quantities. The resulting apple green product was dried in the air and calcined for 2 hours at various temperatures to produce black NiO NPs. The calcination technique was developed to create non-stoichiometric NiO NPs and was based on the thermal decomposition of $Ni(OH)_2$.

$$Ni(NO_3)_2 + 2NaOH \rightarrow Ni(OH)_2 \downarrow + 2NaNO_3 \qquad (1)$$

$$Ni(OH)_2 \xrightarrow{\Delta} NiO + H_2O \qquad (2)$$

5.1.1. Experimental section

In my experiments, I followed the reported procedure[8] and the dark green solution was made by dissolving $Ni(NO_3)_2{\cdot}6H_2O$ (0.5 mol) in 100 mL deionized water. By adding a NaOH solution (10 mol L^{-1}) to the solution, the PH was adjusted to 10. The colloidal precipitation was thoroughly rinsed twice with deionized water after swirling for 5 minutes, and then dried for 6 hours at 80 °C. After that, the green powder was calcined for 2

hours at various temperatures to produce a dark-black powder.

5.1.2. Results and discussion

To ensure the complete decomposition of $Ni(OH)_2$, I set the calcination temperature at 500°C. Figure 5.1 shows the XRD pattern of the black powder obtained after calcination.

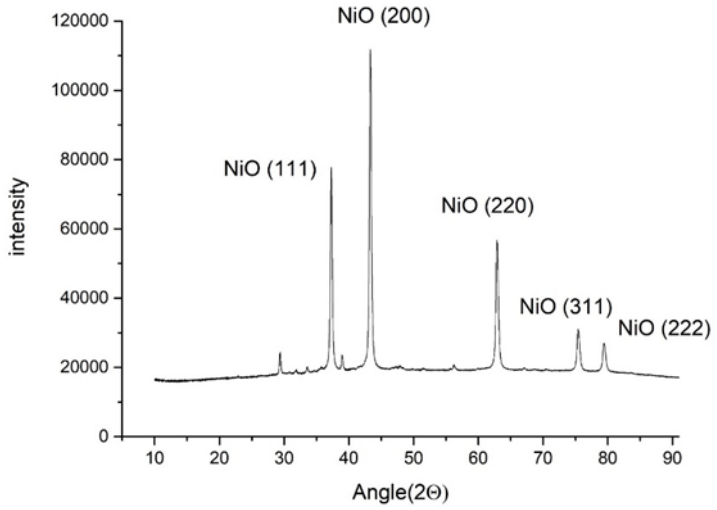

Figure 5.1: XRD of the black powder obtained after calcination 500°C

From the XRD results, it can be concluded that after calcination at 500°C we end up with very pure NiO powder with no secondary phase. We used Scherrer's formula to calculate the particle size of the powder, as shown below.

$$D = \frac{K\gamma}{B\cos\theta}$$

In which K a dimensionless shape factor, with a value close to unity. The shape factor has a typical value of about 0.9, but varies with the actual shape of the crystallite; D is the average thickness of the grain in the direction perpendicular to the grain plane (Å). B is the half-height width of the diffraction peak of the measured sample (bilinear correction and instrumental factor correction must be performed), which needs to be converted into radians (rad) in the process of calculation. θ is the Bragg diffraction angle in angles (in degrees) γ is the X-ray wavelength. By measuring the FWHM of different peaks of NiO, we obtained that the average particle size of NiO powder obtained after calcination at 500°C was 23.3 ± 5.9 nm.

hkl	B obs. [°2Th]	B std. [°2Th]	Peak pos. [°2Th]	B struct. [°2Th]	Crystallite size [Å]
111	0.44	0.066	36.653	0.374	224
200	0.531	0.066	43.328	0.465	184
220	0.396	0.078	62.391	0.318	292

Table 5.1 Scherrer's formula calculation of the NiO powder obtained after calcination at 500°C

In order to study the morphology of the powder, we used SEM. As shown in Figure 5.2, the SEM image shows that the obtained particle size is very irregular and often on the order of hundreds of nm or even µm. These sizes are much larger than those calculated from XRD. This discrepancy is attributed to the irreversible agglomeration phenomenon under high temperature calcination. The Scherrer formula gives the average *crystallite* size, which can be considered as a lower limit for the actual particle size, in particular if bigger particles are formed through the agglomeration of smaller ones.

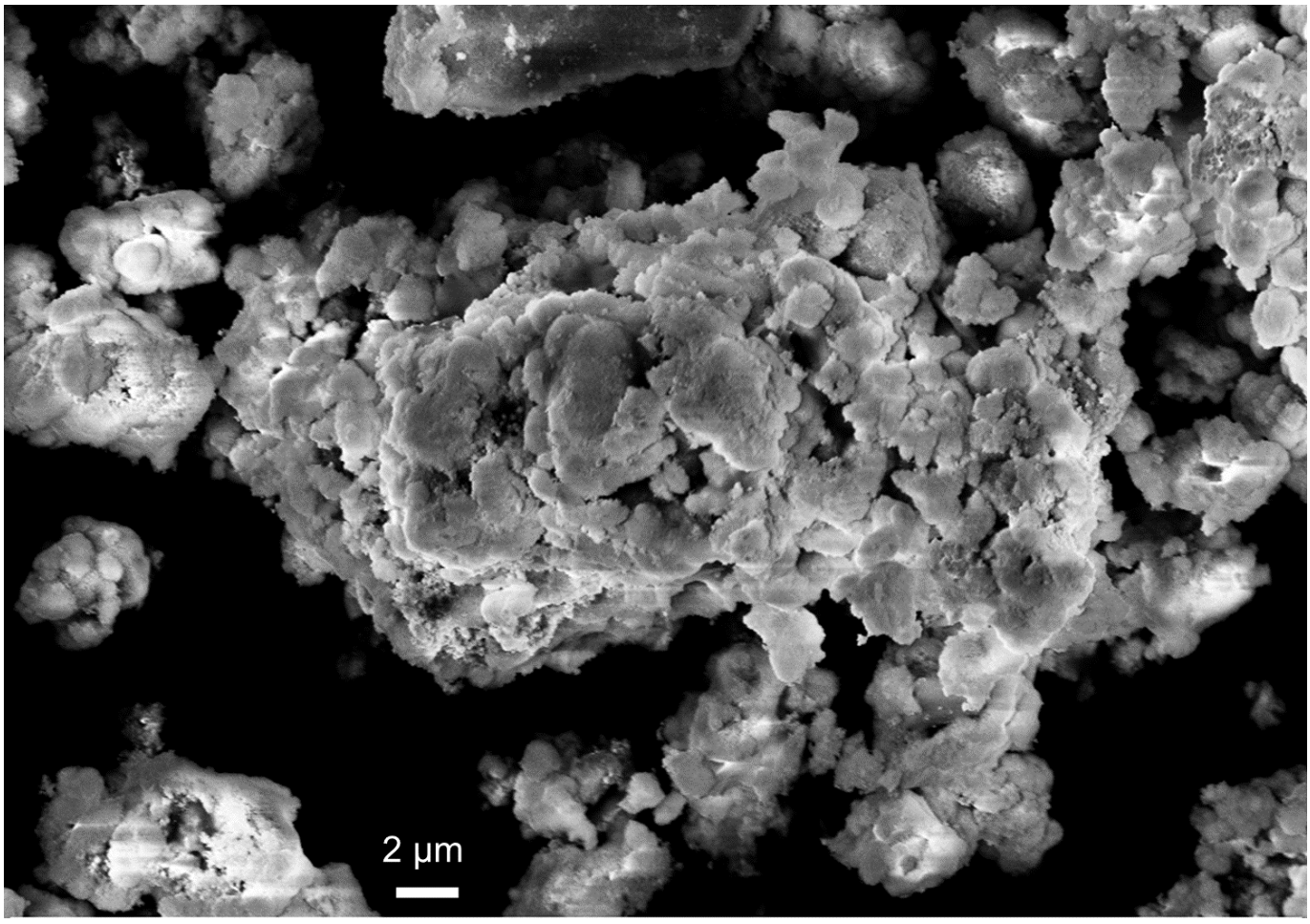

Figure 5.2: SEM image of the NiO powder obtained after calcination at 500°C.

To reduce irreversible agglomeration, we lowered the calcination temperature to 275°C, which is the minimum decomposition temperature of $Ni(OH)_2$[9]. XRD shows that $Ni(OH)_2$ has been completely decomposed to NiO at this temperature. No other secondary products, such as $Ni(OH)_2$ was found, as shown in Figure 5.3.

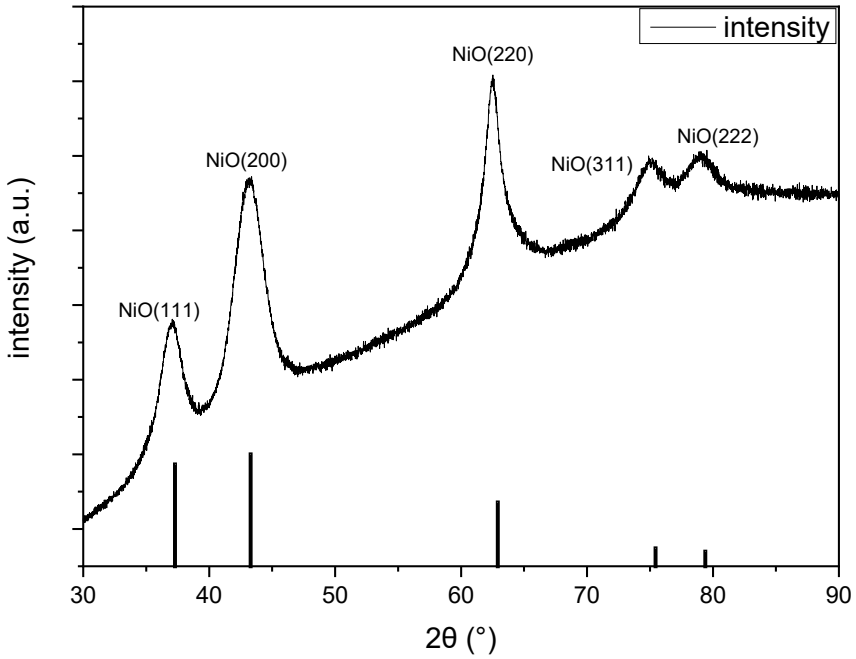

Figure 5.3: XRD of black powder obtained after 275°C calcination

Again, we use Scherrer's formula to calculate the grain size of NiO. We obtained an average grain size of 4.1 nm, as indicated in Table 5.2. This finding shows that reducing the calcination temperature reduces the grain size of NiO efficiently. However, when we examined the powder using a SEM, we once again discovered that uncontrolled agglomeration took place, as illustrated in Figure 5.4.

hkl.	B obs. [°2Th]	B std. [°2Th]	Peak pos. [°2Th]	B struct. [°2Th]	Crystallite size [Å]
111	2.2	0.066	36.934	2.134	39
200	2.798	0.066	43.121	2.732	31
220	1.83	0.078	62.465	1.752	53

Table 5.2: Scherrer's formula calculation of the NiO powder obtained after calcination at 275°C.

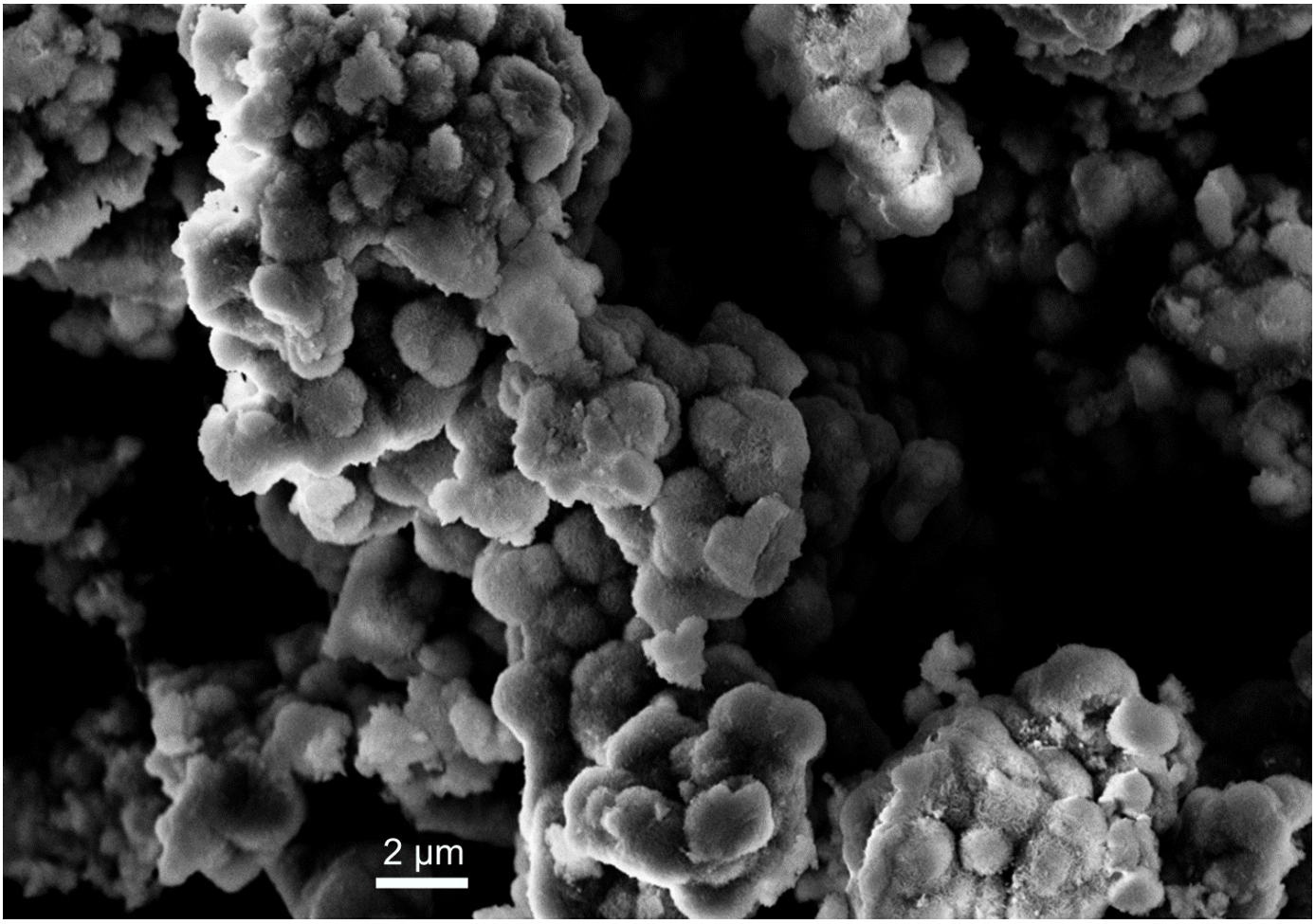

Figure 5.4: SEM of the NiO powder obtained after calcination at 275°C.

We tried to disperse the NiO powders obtained at different calcination temperatures in water. Not surprisingly, the prepared dispersions were extremely unstable at any concentration and settled down quickly, as shown in Figure 5.5.

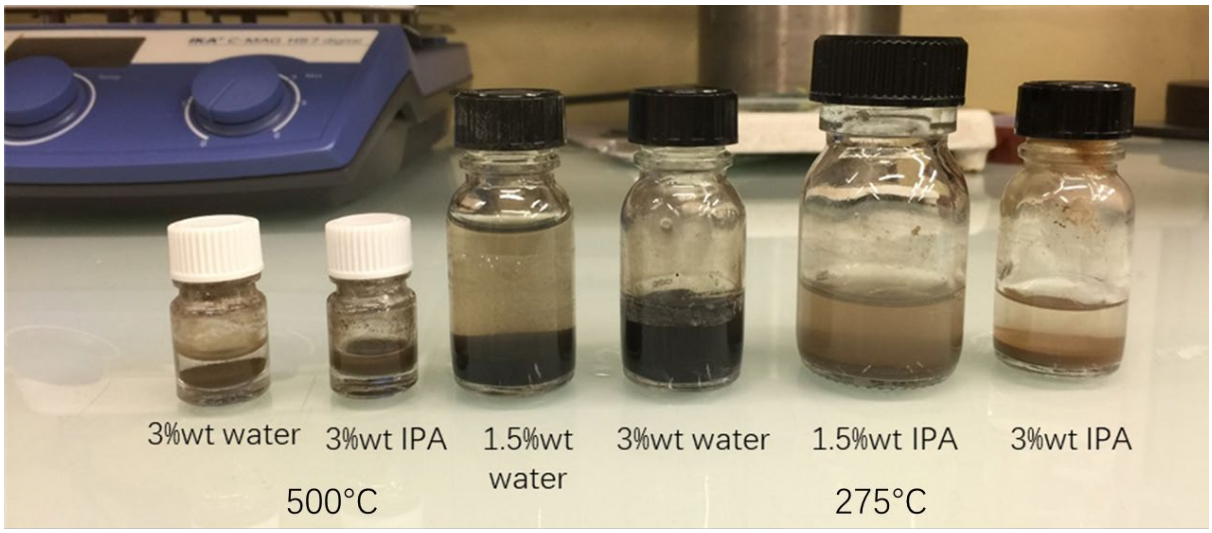

Figure 5.5: Photograph of NiO powders dispersed in water and IPA using different concentrations.

To improve the dispersibility of the powder, we used more viscous isopropyl alcohol (IPA) instead of water and diluted the concentration of the dispersion to 0.6 wt% (4.7 mg/mL). The resulting dispersion is stabilized for about 1h without precipitation, as shown in Figure 5.6A. It has been spin-coated onto the surface of ITO-coated glass substrates. As visible in Figure 5.6B, SEM shows that the particles are forming a homogeneous layer of isolated islands on the ITO surface. The reason for this phenomenon is the very poor dispersion of the powder.

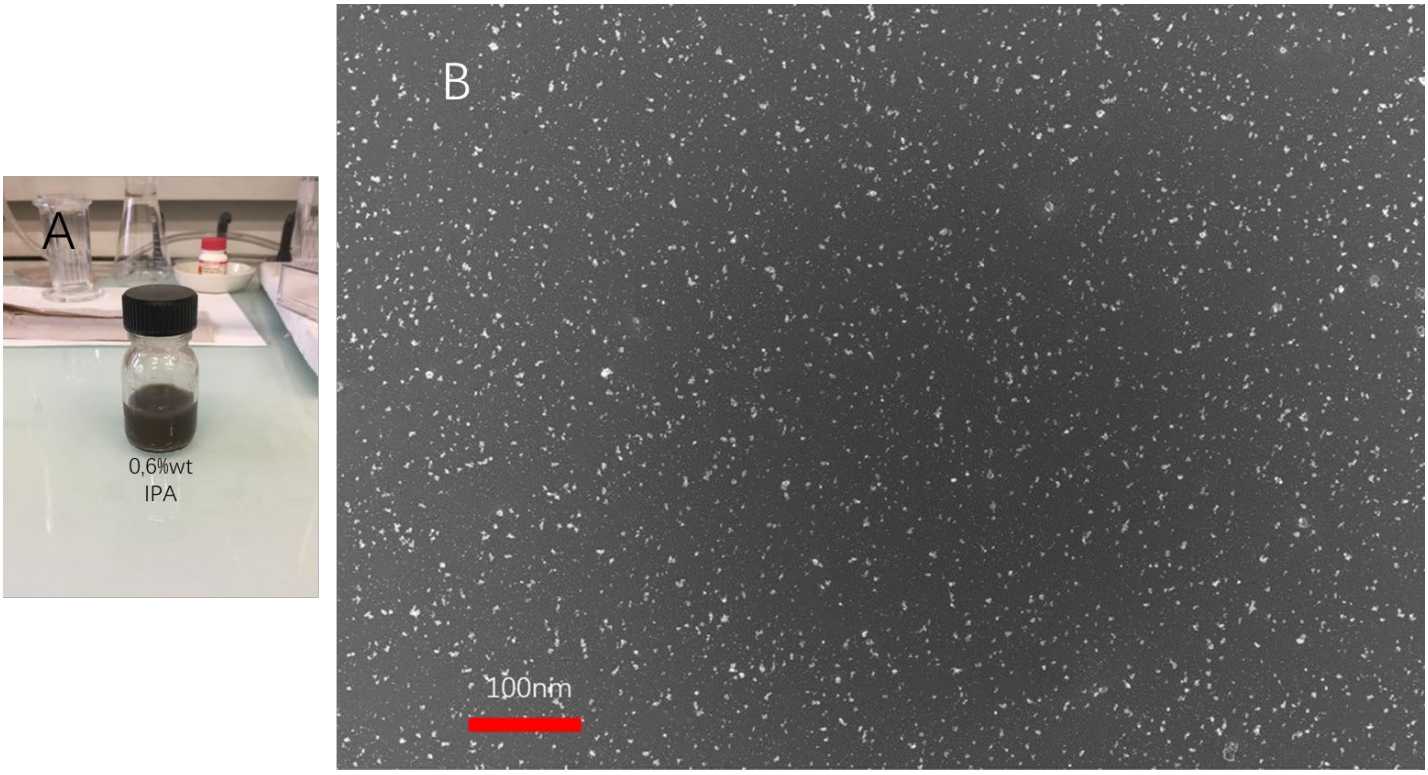

Figure 5.6: A) Photograph of NiO NPs dispersed in IPA (0.6 wt%); B) Top view SEM image of the ITO surface after spin-coating the NiO NPs/IPA dispersion.

5.2. NiO nanoparticles prepared using solvothermal reactions

Solvothermal processes are chemical reactions that take place in a closed vessel at a pressure and temperature higher than the ambient. The reaction vessel or autoclave in the solvothermal technique runs at a temperature of 100 to 1000 °C and a pressure of 1 to 10,000 bar[10]. The interaction between the reactants is aided by the high pressure and temperature, resulting generally in products of high crystallinity. In terms of purity, crystallinity, and morphology, the products obtained using this technique are extremely selective. The medium used in solvent thermal synthesis can be anything from water (hydrothermal) to alcohol or any other organic or inorganic solvent[3]. Metal oxide nano powders of various sizes and shapes can be produced by changing the reaction parameters (ratio of ligands to metal precursors, temperature, pressure, reaction time, etc.). Due to the lack of information on the nucleation and growth kinetics, as well as their relationship with the metal precursor conversion rate, the data acquired for the synthesis of different specific metal oxides cannot be linked with one another. Despite the fact that the solvothermal synthesis produces highly crystalline materials and has the potential to produce monodisperse and homogeneously shaped metal nanoparticles, this approach remains complex and can give uncontrollable results due to the high temperature and high pressure conditions.

5.2.1. Experimental section

The synthesis process was followed as reported before[7]. To get a murky, light green solution, 13 g (0.50 mmol) nickel acetylacetonate ($Ni(acac)_2$) was added to 14 mL of tert-butanol (0.147 mol) at room temperature. The reaction mixture was agitated for 10 minutes before being placed to the autoclave and sealed. The autoclave was kept at 200°C in a laboratory oven. The powder was air dried at 60°C in a laboratory oven. The mass transfer conditions in the autoclave reactor, which are significantly impacted by the geometry of the autoclave, are particularly important for the repeatability of reaction. In this experiment, an 80 mL cylindrical autoclave was utilized (as shown in Figure 5.7). Under these conditions, phase-pure nickel oxide particles were obtained after 24 h of reaction time.

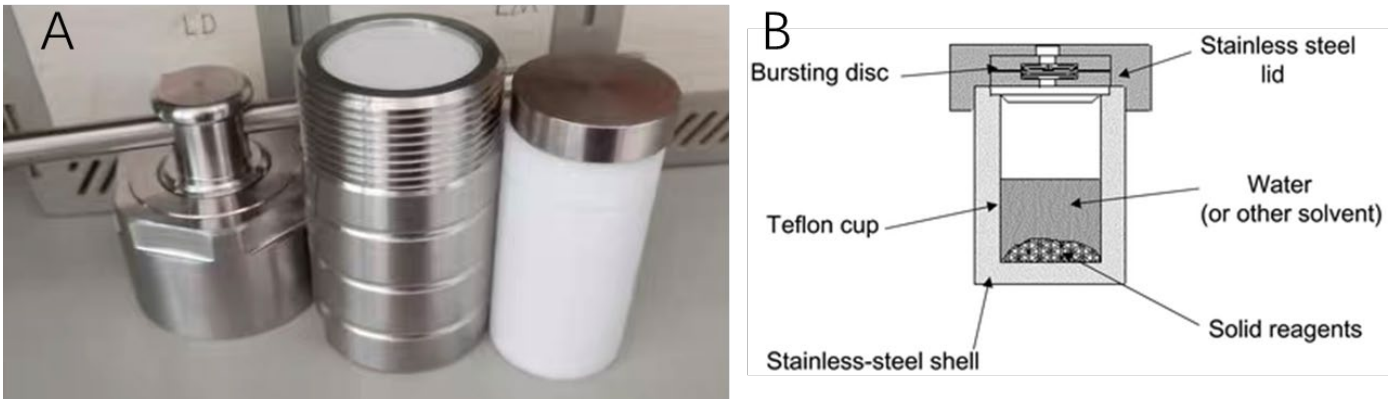

Figure 5.7 A) Photograph of the used autoclave; B) schematic of a Teflon™-lined, stainless-steel autoclave typically used in the laboratory to perform solvothermal synthesis. Adapted from Ref 10[10].

5.2.2. Results and discussion

Only NiO reflections are exclusively observed in the XRD pattern, as shown in Figure 5.8A. After a 24 h reaction period at 200 °C, the size of the obtained NiO nanocrystals estimated from line broadening in the XRD pattern corresponds to 5 nm. SEM imaging shows that in contrast to what is described in the literature, we observe severe agglomeration and a very non-uniform particle size distribution, as shown in Figure 5.8B. We observed that the smallest nanoparticles were about 10 nm and the largest nanoparticles were more than 200 nm.

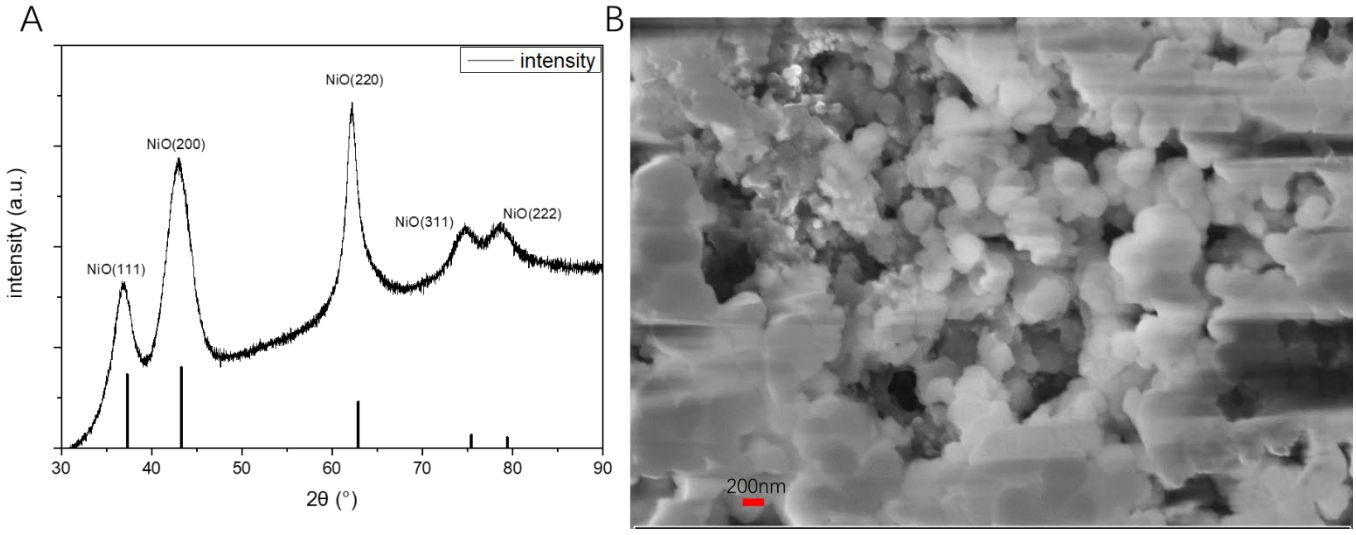

Figure 5.8: A) XRD pattern of the NiO nanoparticles obtained by solvothermal reaction; B) SEM image of the same sample.

To overcome the problems of particle agglomeration and broad particle size distribution, we used cetyltrimethylammonium bromide (CTAB) as a surfactant. S.H. Wu and coworkers reported that 0.3 Mm added CTAB is beneficial for controlling the size distribution in the solvothermal reaction[11]. Similarly, as in this work, CTAB was added to the nickel acetylacetonate precursor. Figure 5.9A shows the XRD pattern of the final product. By comparison with reference patterns, it becomes clear that both NiO and $Ni(OH)_2$ phases were synthesized. Meanwhile, SEM analysis shows the serious agglomeration of the obtained particles, which leads to a poor dispersibility in common solvents, as visible in Figure 5.9B. Concluding, although pure nickel oxide particles can be obtained by autoclave synthesis, the surfactant must be carefully selected to suppress agglomeration phenomena and the formation of heterogeneous phases.

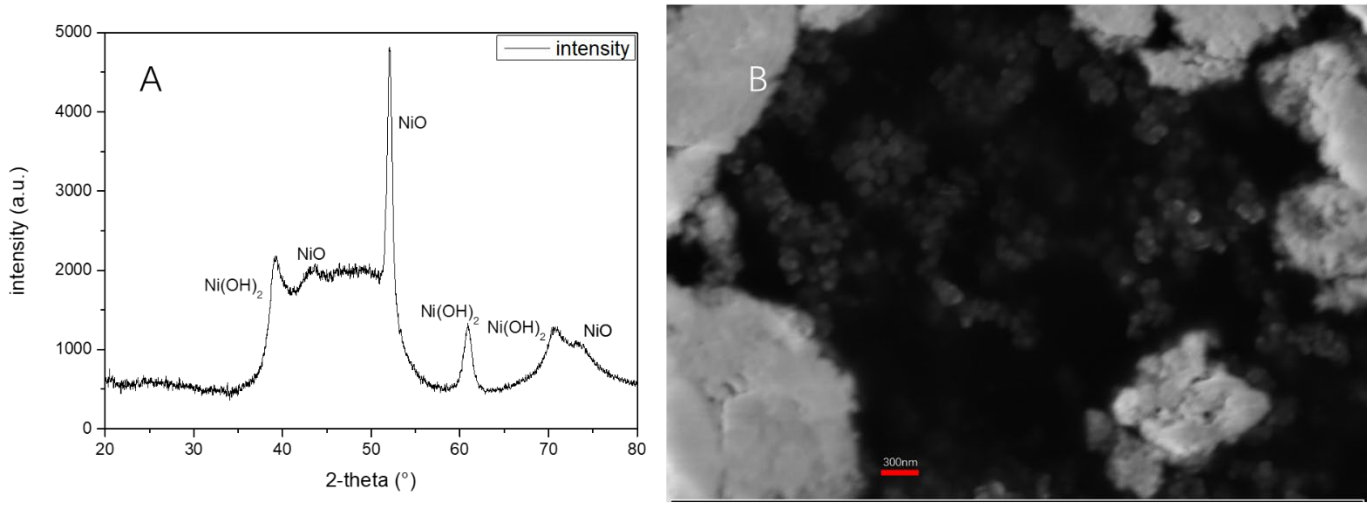

Figure 5.9: A) XRD pattern of the nanoparticles obtained by the solvothermal reaction with CTAB addition; B) SEM image of the same sample.

5.3. NiO nanoparticles prepared by thermal decomposition in non-aqueous solvents

5.3.1. Polyol synthesis reaction

The liquid-phase synthesis in high-boiling, multivalent alcohols is known as the polyol synthesis, and represents a widely used method for the preparation of metal and metal oxide nanoparticles[12]. Polydispersity, agglomeration, and poor crystallinity are common problems when using aqueous and volatile solvents to prepare metal oxides. The polyol synthesis produces metal and metal oxide nanoparticles that do not require post-synthesis thermal treatments to be monocrystalline. Furthermore, the obtained particles are generally monodispersed in size and shape and the process is very simple, as the polyol can act in many cases as both the solvent and stabilizing agent/surface ligand. On the other hand, polyols can also act as reducing agents, and therefore, the process is mostly used for metal nanoparticles. Nonetheless it has been also successfully applied to a range of metal oxide nanoparticles, albeit not to nickel oxide[13]. The nucleation and growth rates of metal oxide nanoparticle production via the polyol synthesis are well characterized, and small adjustments of the reaction parameters have been shown to give a considerable control over particle size and shape. Organometallic precursors mixed in an organic solvent (polyol) and a surface stabilizing agent are used to make most metal oxide nanoparticles using this technique, which is done at a high temperature in an inert atmosphere. The presence of multiple reagents and their ionic forms during decomposition complicates the elucidation of the reaction mechanisms.

Diethylene glycol (DEG) is an ideal solvent for the synthesis of oxide nanoparticles due to its water-comparable (high polarity) and chelating properties. Simple metal salts (e.g., halides, nitrates, acetates, alcohol salts) can be used as starting materials. In addition, the polyol solvent immediately coordinates with the formed particle nuclei, allowing for excellent control of particle size, size distribution and dispersion/absence of agglomeration. Moreover, following the synthesis, low molecular weight polyols such like DEG can be easily removed from the particle surface by washing (i.e., repeated centrifugation and redispersion) with water[14] or by exchanging with stronger ligands (e.g., amines and carboxylates)[15].

5.3.1.1. Experimental section

In this study, 1 mmol nickel acetate tetrahydrate ($Ni(OAc)_2 \cdot 4\ H_2O$) was dissolved in 10 mL of DEG (Diethylene glycol) and stirred for 30 min at 80°C under vacuum to get a homogeneous solution. This green solution was kept at 230°C for 1 h under Ar flow. After reaction, the dark solution was cooled to room temperature. The particles were collected by adding 5 mL ethanol and centrifuged at 10 000 rpm for 4 min. The reaction setup is shown in Figure 5.10.

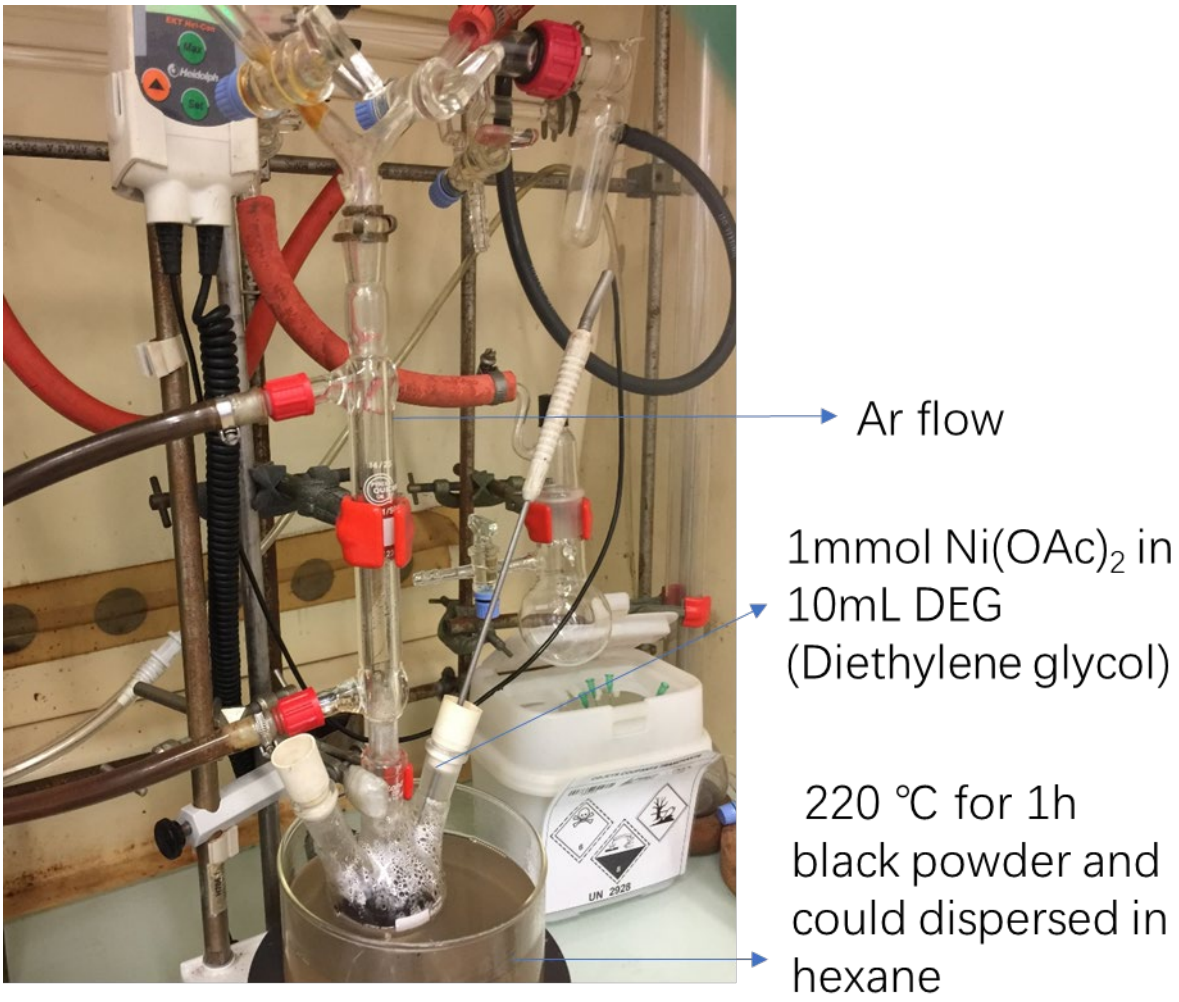

Figure 5.10: Photograph of the reaction setup used for thermal decomposition reactions.

5.3.1.2.Results and discussion

Figure 5.11 shows the characteristic X-Ray diffractogram of the obtained black powder showing that the final product is a mixture of the hexagonal and cubic phase of Ni metal (JCPDS card numbers 00-36-1451 and 00-

04-0850).

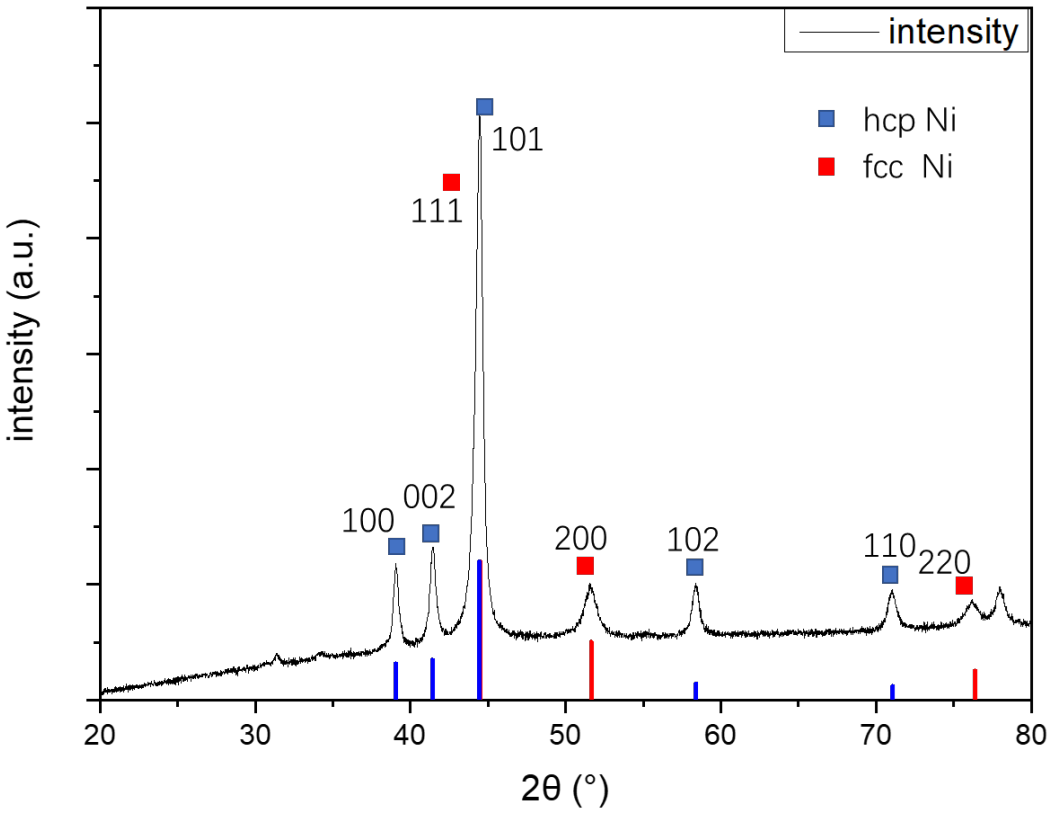

Figure 5.11: XRD pattern of the nanoparticles obtained with the polyol synthesis reaction.

Crystallite sizes are calculated with the Scherrer formula. As judged from the Scherrer formula, the *hcp* NPs have a larger size with average value of 23.1±4.6nm, while ,the *fcc* NPs are only 9.7±0.4nm, as shown in Table 5.3. Due to the large particle size, the synthesized nickel nanoparticles are difficult to be oxidized subsequently to nickel oxide, e.g., by thermal treatment under air.

hcp	B obs. [°2Th]	B std. [°2Th]	Peak pos. [°2Th]	B struct. [°2Th]	Crystallite size [Å]
100	0.373	0.066	39.038	0.307	275
002	0.408	0.066	41.411	0.342	248
102	0.489	0.071	58.332	0.418	218
110	0.610	0.083	70.930	0.527	185
fcc	B obs. [°2Th]	B std. [°2Th]	Peak pos. [°2Th]	B struct. [°2Th]	Crystallite size [Å]
200	0.947	0.071	51.545	0.876	101
220	1.170	0.083	76.087	1.087	93

Table 5.3 Scherrer's formula calculation of the NiO powder obtained with the polyol synthesis reaction.

Figure 5.12 shows SEM of NiO powder obtained with the polyol synthesis reaction. No significant agglomeration occurs. However, two different sizes of nanoparticles were observed, presumably belonging to different crystalline phases of Ni nanoparticles, respectively.

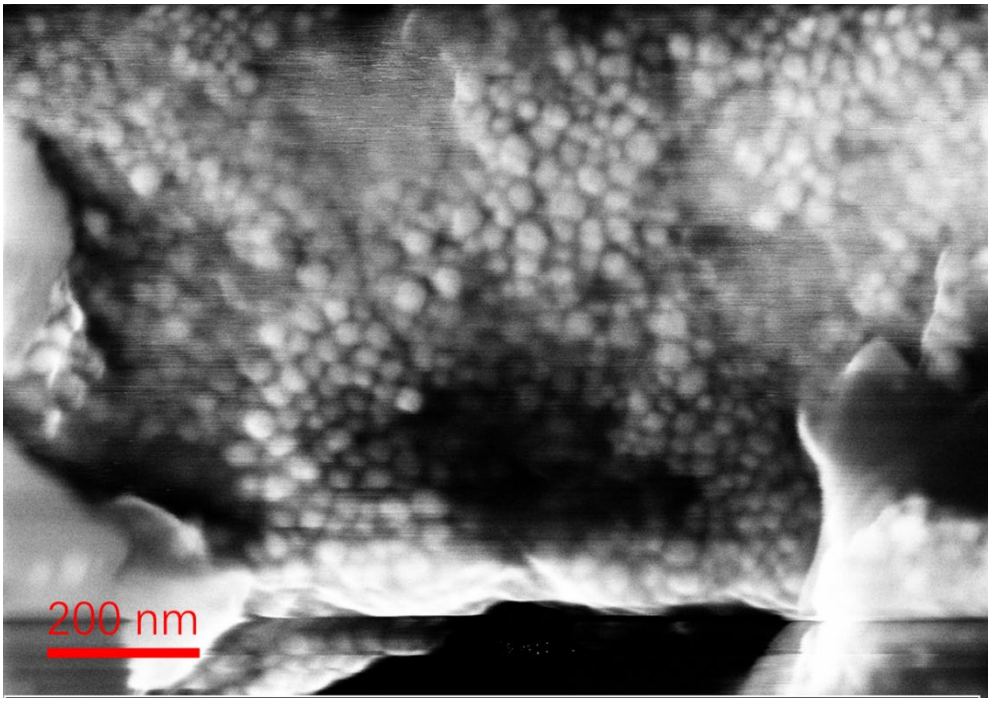

Figure 5.12 SEM of NiO powder obtained with the polyol synthesis reaction.

As DEG is a good reducing agent at high temperatures[16] and the reduction potential of nickel ions is only - 0.25eV[17] nickel acetate is readily reduced to Ni metal at 220-230°C under argon atmosphere. Therefore, we need to use other non-reducing organic solvents with high boiling point to replace DEG.

$$Ni^{2+} + 2e^{-} \leftrightarrow Ni \qquad -0.25eV$$

5.3.2. Thermal decomposition reactions in alternative organic solvents

In the previous section we tried to synthesize NiO nanoparticles using the polyol synthesis. However, due to the reducing character of DEG, we only ended up with metallic Ni particles. Therefore, we need to find other capping ligands. The thermal decomposition reaction with the assistance of capping ligands can lead to a similar control of the size and size distribution as in the polyol synthesis, because the nucleation and growth stages of the nanoparticles in solution are controlled by the interaction of the metal species with the capping molecules. During the reaction the surface atoms are passivated by the dynamically binding capping molecules, which prevent the particles from aggregation while also assuring the colloidal stability of the final product[18]. Therefore, the choice of the capping molecules is crucial. An important factor is the strength of the binding between the capping molecule and the metal precursor. If the capping molecule is too weakly bound to the

metal, the growth of the particles becomes uncontrollable and larger microcrystals tend to form. Conversely, if the binding of the capping molecule to the precursor is too strong, the growth of the nanoparticles will be blocked. In the formation reaction, the rate of adsorption and desorption of capping molecules affects the growth rate of the nanoparticles and thus controls the final particle size. In addition, the reaction temperature, reactant concentration, etc. are also important[19]. Based on our experience with other types of nanoparticles we selected trioctylphosphine oxide (TOPO)[20] and octadecylamine (ODA)[21] as two candidates, which can serve as coordinating solvents in the thermal decomposition reactions. Figure 5.13 shows a schematic diagram of the thermal decomposition reaction with the help of capping ligands

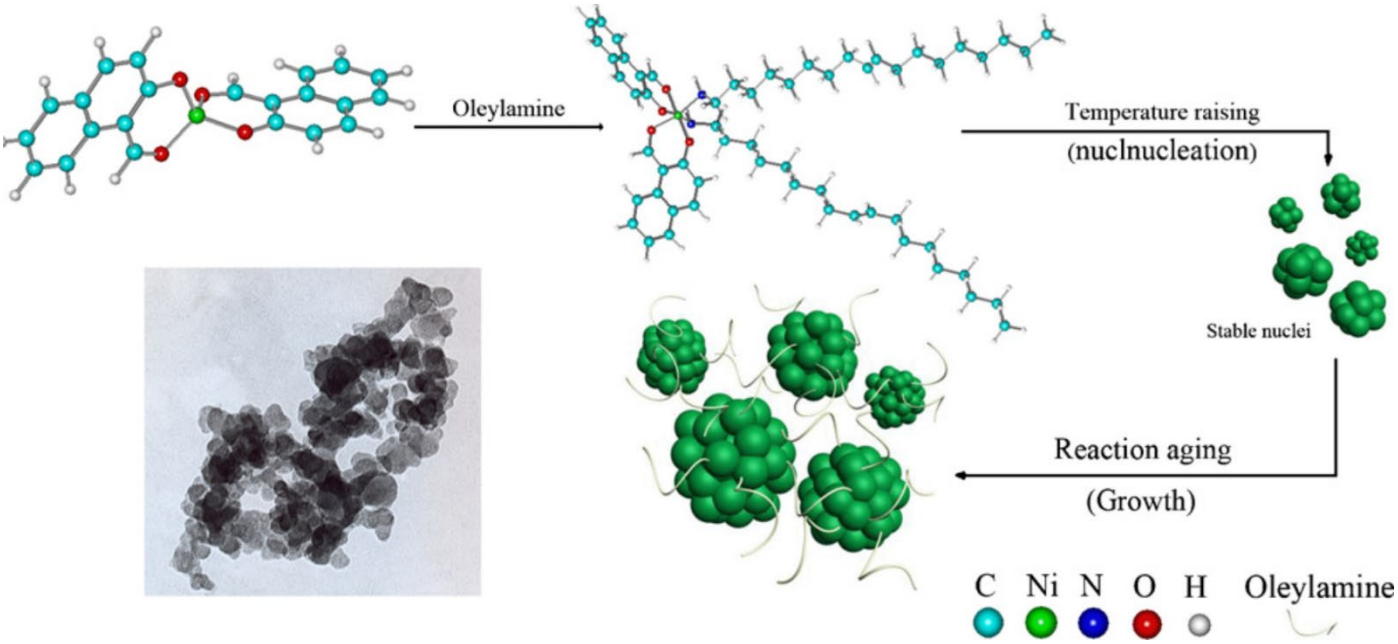

Figure 5.13: Schematic diagram of the thermal decomposition reaction with the help of capping ligands (Adapted from Ref 22[22])

As an amine, ODA can be used as a ligand to coordinate with metal ions and act as a surfactant as well as a solvent. Thus, this molecule can limit the crystal growth and provide stability of the nanoparticles in solution. ODA, having a boiling point of 349°C has been applied in the synthesis of many nanoparticles[21]. Similarly, TOPO (boiling point: 201°C at 2 mbar) has a good affinity for metal ions as a capping molecule. Moreover, the steric demand provided by the bulky properties of TOPO allows the growth of nanocrystals to be well controlled: the longer the chain of the capped molecule, the lower the diffusion coefficient of the [metal-capped ligand] compound[23]. Oleyamine (OAm) and trioctylphosphine (TOP) were introduced into the reaction as additional surface ligands. OAm is a very versatile ligand in metal, oxide and semiconductor nanocrystal synthesis[24] and TOP is often used to control the growth of nanoparticles[25]. The introduction of OAm and TOP can thus further control the size and particle size distribution of the final nanoparticles obtained.

5.3.2.1. Experimental section

In this study, 1mmol nickel acetate tetrahydrate ($Ni(OAc)_2 \cdot 4\ H_2O$) was mixed with 5 g ODA or 5 g TOPO and stirred for 30 min at 80°C under vacuum to get a homogeneous solution. Oleylamine (OAm) and Trioctylphosphine (TOP) are used as additional surfactants/ligands. The green solution was kept at 240°C for 1h under Ar flow. After reaction, the dark solution was cooled to room temperature. The particles were collected by adding 10 mL ethanol and centrifuged at 10000 rpm for 4min. The reaction setup is the same as for the polyol synthesis. In our case, the obtained nanoparticles were dispersed in hexane under air to form a stable dispersion using ultrasound. with following method: 10 mg Ni NPs was added into 1 mL Hexane and took an ultrasonicated bath for 10 min. For the oxidization process, the dispersion was stirred under air overnight in the room temperature. The obtained nanoparticles were collected by adding excess antisolvent ethanol into Hexane dispersion and centrifuged at 8000rpm for 5min.

5.3.2.2.Results and discussion

Figure 5.14 shows the characteristic Xray diffractogram of the black powder obtained with the different solvents (TOPO or ODA). The XRD patterns of both powders showed that the end product obtained in each case was Ni rather than NiO, crystallizing in different phases: the Ni nanoparticles are in the cubic phase when TOPO was used as solvent, as shown in Figure 5.14A (JCPDS card number 00-04-0850), while with ODA they crystallized in the hexagonal structure (JCPDS card number 00-36-1451, Figure 5.14B). We also note that the Ni nanoparticles obtained in the two different solvents have different particle sizes. The width of the diffraction maximum from the ODA-Ni XRD pattern is very narrow, indicating a large grain size, determined as 58±4nm using the Scherrer formula. In contrast, the Ni nanoparticles prepared in TOPO show comparably broad peaks, with crystallite sizes corresponding to 6.5±0.8nm. We attribute the small nanoparticle size in this case to the high steric demand of TOPO, strongly modifying the nucleation and growth kinetics. Due to the ultra-small particle size, these nanoparticles are more likely to fully oxidize subsequently to nickel oxide.

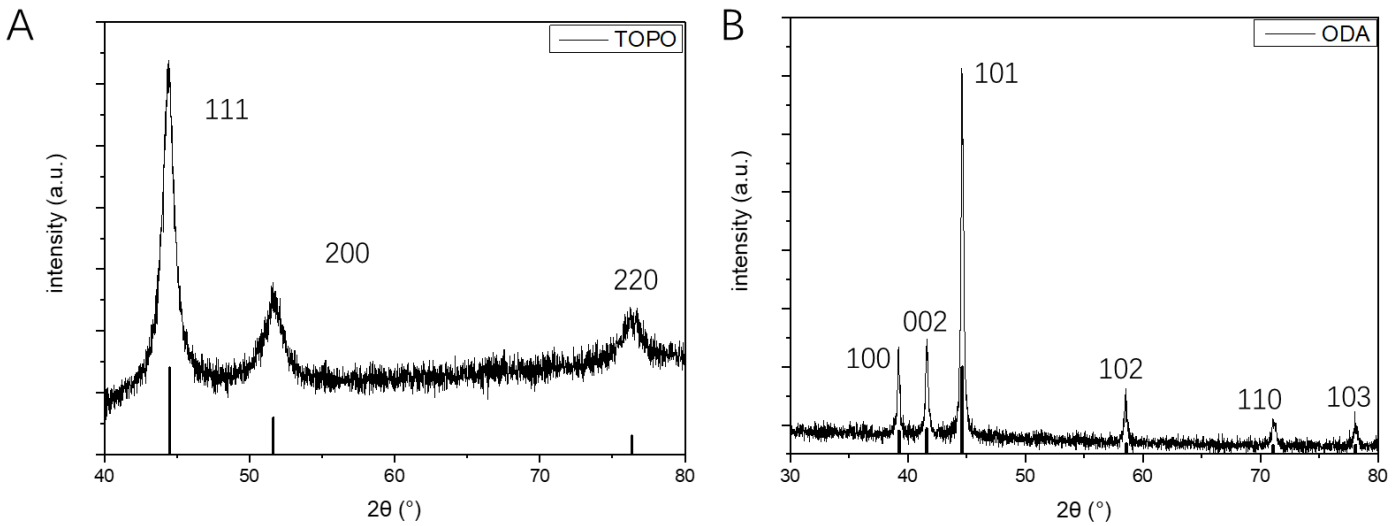

Figure 5.14: XRD patterns of the Ni nanoparticles obtained in thermal decomposition reactions conducted in A) TOPO and B) ODA.

Considering the size of the nanoparticles we obtained, we chose to use TOPO as the solvent for the subsequent oxidization experiments. Sako Sanshiro and coworkers successfully oxidized very small metallic Ni nanoparticles to NiO nanoparticles by exposure to air[26]. XRD was used to evaluate the success of the oxidation process of the nanoparticles, cf. Figure 5.15. In the X-ray diffraction pattern, we found diffraction peaks corresponding to the cubic phase of NiO and to the cubic phase of Ni, respectively. This indicates that very small Ni nanoparticles can be only partially oxidized to NiO at room temperature. It has suggested that the oxidized nanoparticles could be actually Ni(core)/NiO(shell) structures[27].

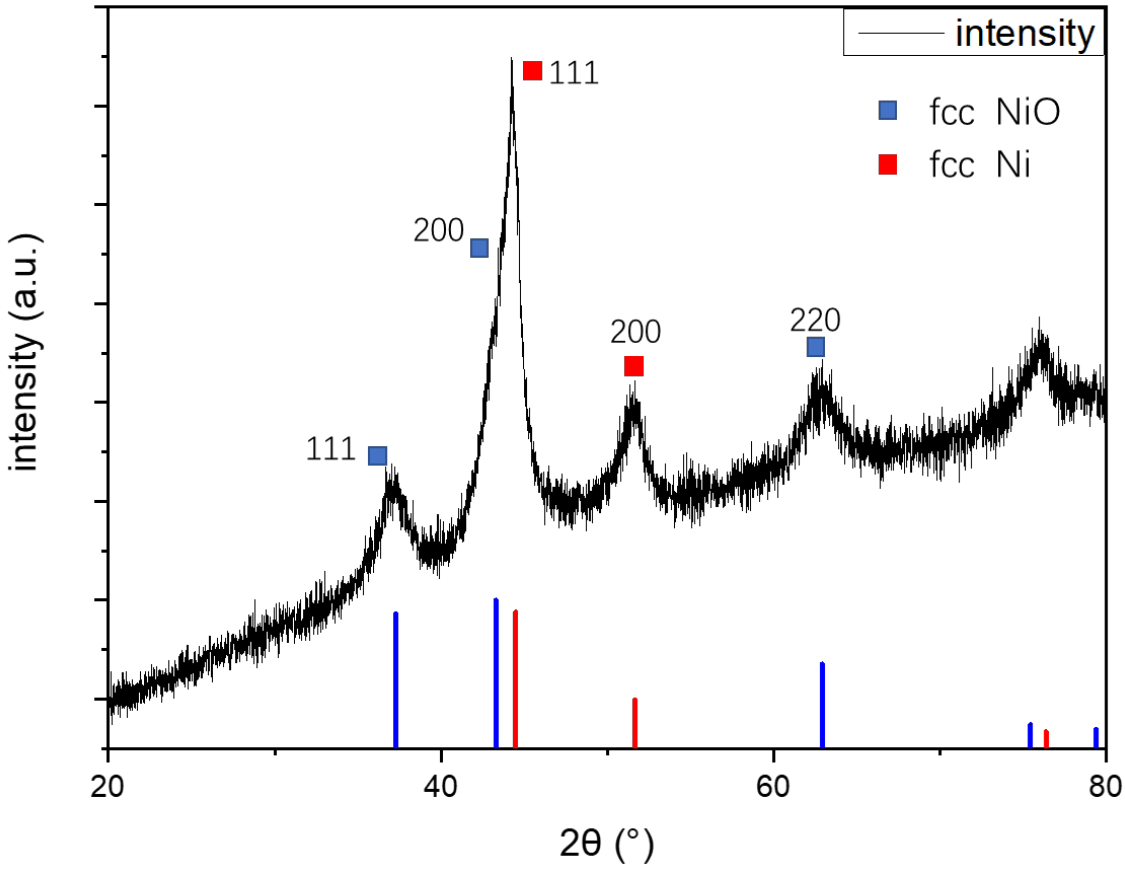

Figure 5.15: XRD pattern of the Ni nanoparticles oxidized by air exposure at room temperature.

In order to maximize the oxidation of Ni to NiO nanoparticles, we spin-coated the unoxidized particles dispersion onto an ITO-coated glass substrate and annealed the obtained film at 300°C for 1 h. The top-view SEM image in Figure 5.16A shows that although the nanoparticles do not completely cover the ITO surface, they exhibit a uniform size distribution with an average size of 10 nm. The high-resolution Ni 2p 3/2 XPS data is shown in Figure 5.16B. After high-temperature annealing, the Ni nanoparticles are almost completely oxidized to NiO. The hydrophobicity of the TOPO ligands is probably at the origin of the difficulty of forming a homogeneous Ni-TOPO particles film on the hydrophilic ITO surface. To avoid the post-synthetic treatment at high temperature, we need to modify our synthetic route to have direct access to NiO nanoparticles.

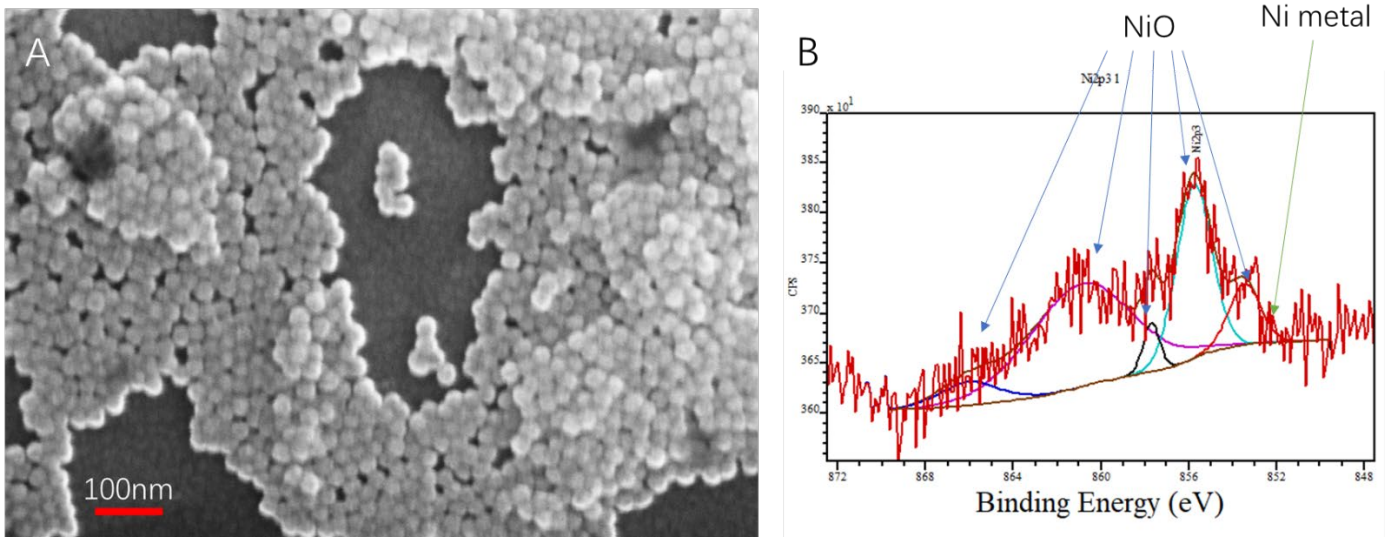

Figure 5.16 A) Top-view SEM image of Ni nanoparticles spin-coated on an ITO-coated glass substrate after annealing at 300°C for 1 h; B) High-resolution Ni 2p 3/2 XPS spectrum.

5.3.3. Modification of thermal decomposition reaction to get fully NiO Nps

In the above experiments, all synthesis reactions were carried out under argon atmosphere. The inert gas protection is beneficial for the formation of metal monomers. To directly obtain NiO nanoparticles, in the following, we carried out the reactions under air in order to rapidly oxidize the formed Ni nuclei to NiO.

5.3.3.1. Experimental section

In this study, 1mmol Nickel(II) bis(acetylacetonate) ($Ni(AcAc)_2$) was mixed with 5g TOPO and 0.4ml TOP/oleic acid (OA). The solution was stirred for 30min at 80°C under air atmosphere and stirred strongly to get homogeneous solution. Oleylamine (OAm) were add into precursor when temperature of precursor raised up to 200°C. The green solution was kept at 240°C for different time under air. The particles were collected by adding 10 mL ethanol and centrifuged at 9000rpm for 5min. The final products can be easily dispersed in Hexane or other non-polar solvent.

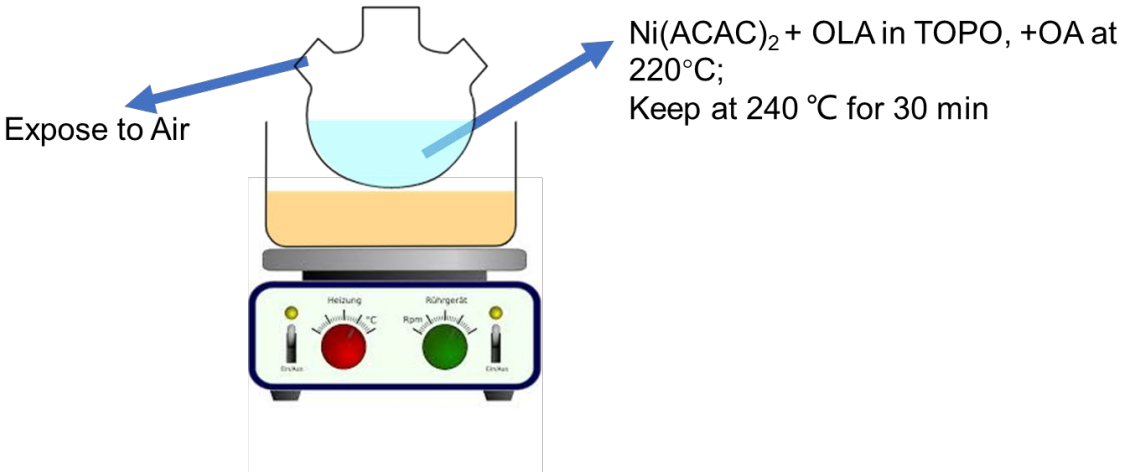

Figure 5.17: Photograph of the reaction setup (the used salt bath is partially molten).

5.3.4.1. Results and discussion

XRD was used to assess the crystal structure of the resulting nanoparticles (cf. Figure 5.18). By changing the reaction atmosphere, we successfully obtained nanoparticles with NiO as the main crystalline phase with only a small amount of Ni, as shown in Figure 5.18A. The diffraction peaks are quite broad, indicating a small particle size. The obtained nanoparticles were coated on conductive adhesive tape for SEM imaging to evaluate the particle size and size distribution. As shown in Figure 5.18B, the obtained nanoparticles are about 16 nm, however, it can be seen that the particle size distribution is in a wide range (Figure 5.18C). Moreover, TOP has been reported to be able to act as mild reducing agent in some reactions[24,28], eventually being at the origin of the observed fraction of unoxidized to NiO.

The above experiments demonstrate that exposing the reaction to air helps the formation of NiO nanoparticles. However, it is shown that the nature of the surface ligands needs to be carefully selected to achieve a low size distribution and to assure simultaneously quantitative oxidation.

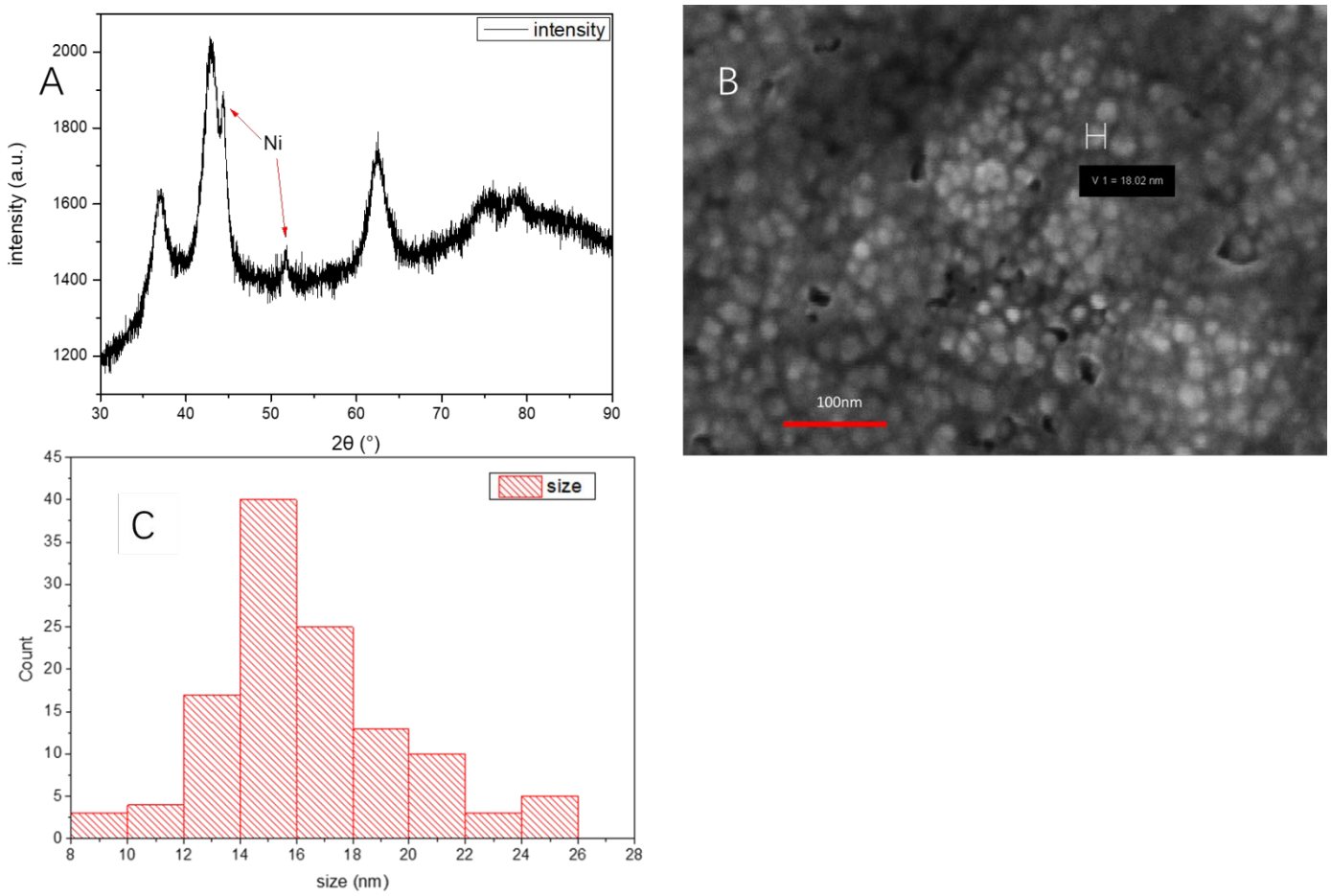

Figure 5.18: A) XRD patterns of oxidized nanoparticles; B) Top-view SEM image; C) size distribution of the obtained nanoparticles.

To stabilize magnetic nanoparticles, oleic acid (OA) is one of the most widely employed surface ligands among other capping agents. As an example, a strong chemical interaction between the carboxylic acid function and the surface of iron oxide nanoparticles is provided by oleic acid, necessary for producing monodisperse and highly uniform samples[29]. In the following, we utilize oleic acid instead of TOP and leave the rest of the parameters the same. The XRD pattern of the obtained nanoparticles are shown in Figure 5.19A. It demonstrates that in this case we were able to generate NiO nanoparticles in pure phase (cubic, space group $Fm\bar{3}m$) by changing the surfactant and exposing the reaction to air. The particle size of the NiO NCs is calculated to be 3.5±0.3 nm using the Scherrer equation. Transmission electron microscopy (TEM) images exhibit non-agglomerated, well-crystallized and round shaped particles with narrow particle size distribution, as shown in Figure 5.19B. In the high-resolution image shown in Figure 5.19C, well-defined lattice planes are visible confirming the high crystallinity of the product.

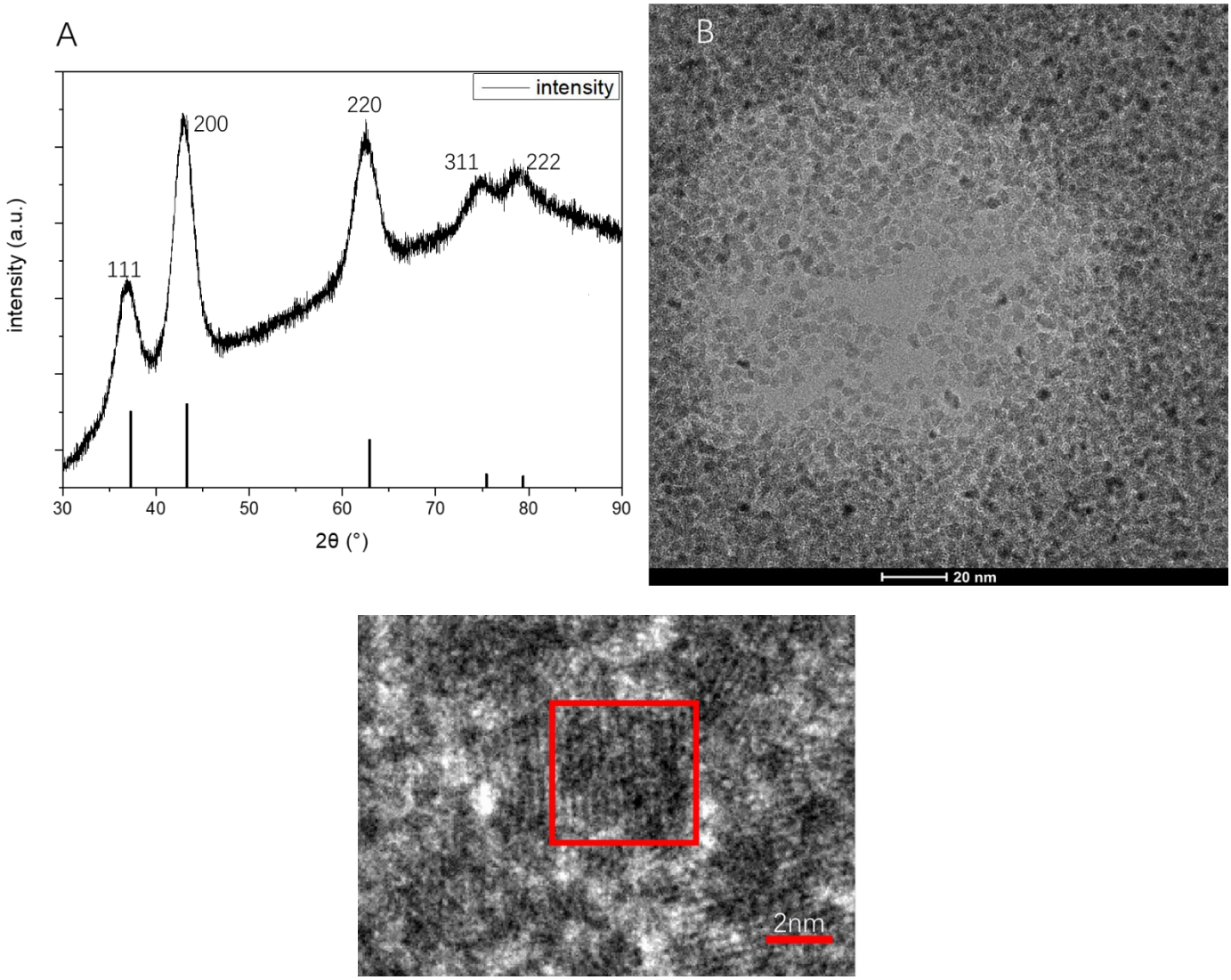

Figure 5.19 A) XRD pattern of the NiO nanoparticles obtained using OA/OAm ligands in TOPO solvent; B) TEM image of the NiO nanoparticles; C) HRTEM image of a single NiO nanoparticle (red square).

The cubic crystal structure of the NiO NCs is further confirmed by the selected-area electron diffraction (SAED) pattern shown in Figure 5.20A, which is in accordance with the X-ray diffraction data. The average particle size determined from the TEM images is 4.8±1.2 nm, which is slightly bigger than the 3.5±0.3 nm derived from the XRD pattern, as shown in Figure 5.20B. The existence of a thin layer of poor crystallinity on the surface of the NiO nanoparticles, not contributing to the crystallite size determined by XRD, might be the cause of this discrepancy.

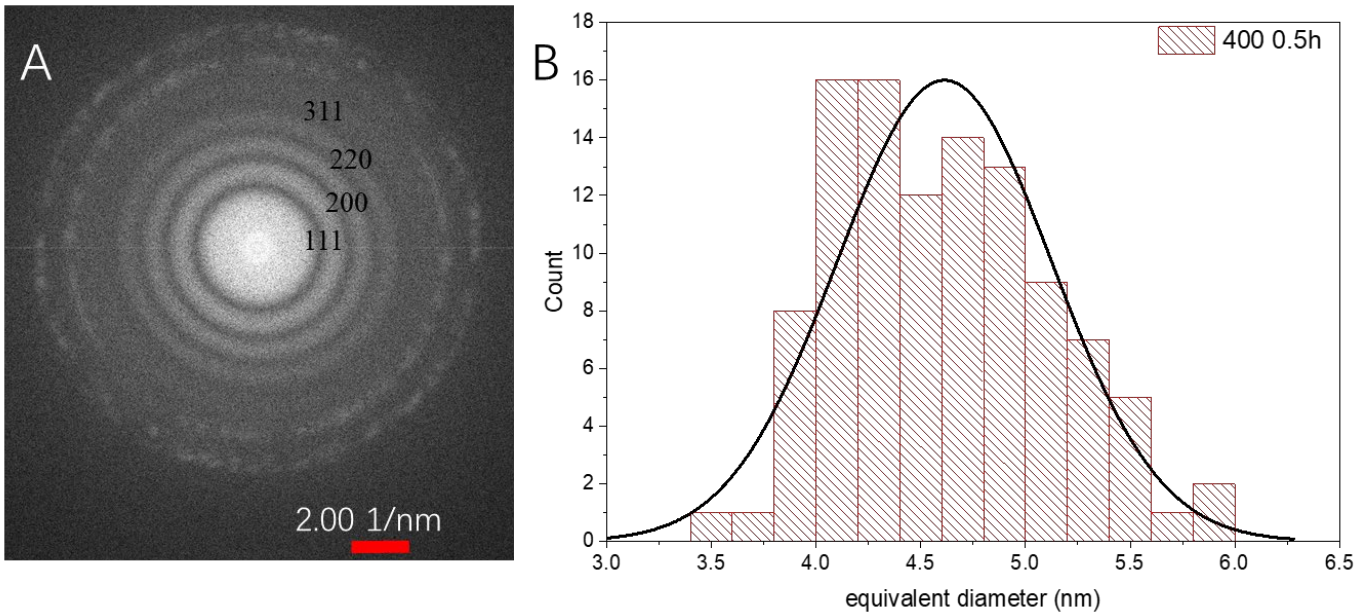

Figure 5.20 A) Selected-area electron diffraction pattern of the NiO nanoparticles. The corresponding d-values are 2.4 Å (111), 2.08 Å (200), 1.47 Å (220) and 1.26 Å (311), respectively; B) Size distribution of NiO NPs with an average size of 4.8±1.2 nm.

In order to obtain nanoparticles with different particle sizes, we need to change the reaction conditions. Obviously, the most straightforward way is to extend the reaction time. As the reaction time increases, the NiO nanocrystals have more time to grow and thus increase the particle size of the final product.

Considering the effect of the surfactant oleic acid, we first conducted experiments to compare the obtained products with and without 400 µL of oleic acid added. The reaction time was 0.5 h and 1 h for each group. Figure 5.21 shows TEM images of aliquots taken at different reaction times: 0 µl oleic acid / 0.5 h reaction time, 0 µl oleic acid / 1 h reaction time, 400 µl oleic acid / 0.5h reaction time, and 400 µl oleic acid / 1 h reaction time are represented in the panels A, B, C, D, respectively. All of the TEM pictures demonstrate that the produced NiO nanoparticles are non-agglomerated and well-crystallized.

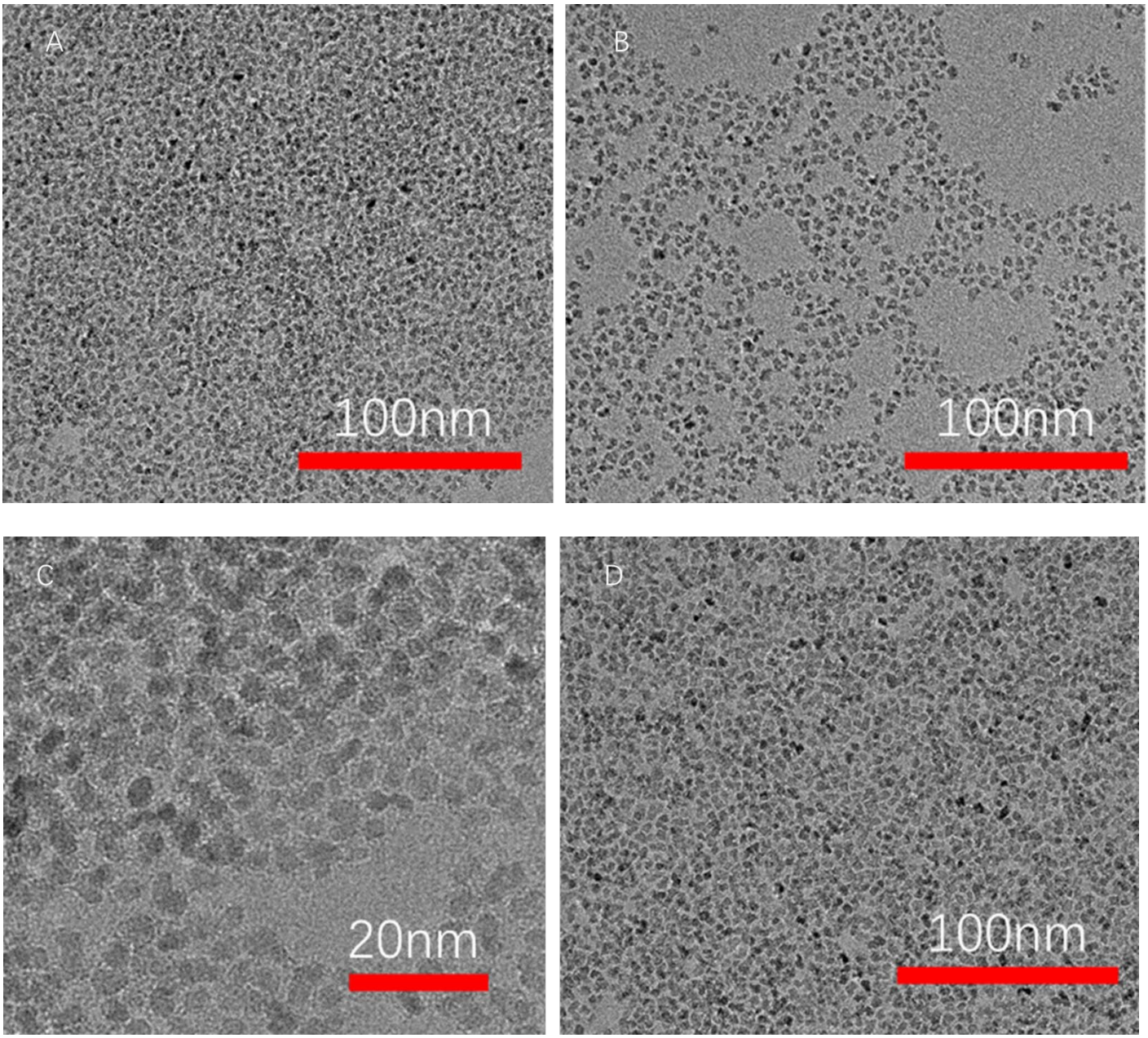

Figure 5.21 TEM images of the NiO nanoparticles obtained with A) 0 µl oleic acid and 0.5 h reaction time; B) 0 µl oleic acid and 1 h reaction time; C) 400 µl oleic acid and 0.5 h reaction time; D) 400 µl oleic acid and 1 h reaction time

The variation of the particle size distribution is shown in Figure 5.22. For NiO nanoparticles not capped by oleic acid, the size of the nanoparticles increased from 4 nm to 5 nm with the increase of reaction time, as shown in Figure 5.22A. On the contrary, the particle size of NiO nanoparticles with oleic acid capping was almost unaffected by the reaction time (Figure 5.22B). We also observed the effect of oleic acid on the morphology of NiO nanoparticles. NiO nanoparticles capped with oleic acid showed spherical or nearly spherical particles at any reaction time. However, the NiO particles without oleic acid addition exhibit irregular

shapes with increasing reaction time. Moreover, the particle size distribution of uncapped NiO nanoparticles increased as the reaction time became longer. This suggests that oleic acid acts indeed as a surface ligand preventing the NiO nanoparticles from uncontrolled ripening, leading to a broader size distribution and irregular shapes.

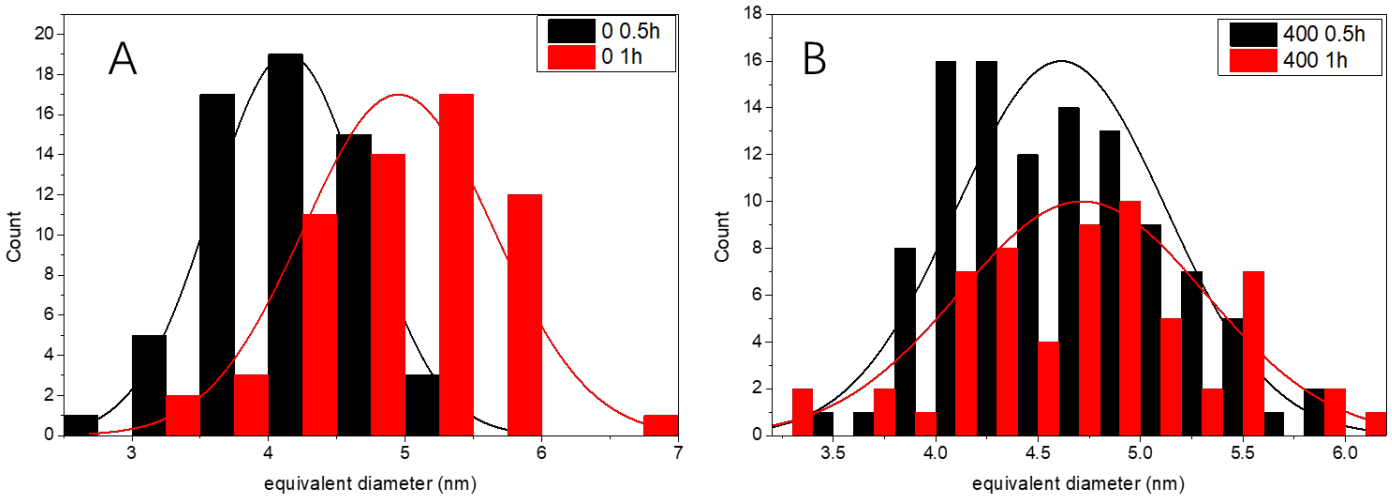

Figure 5.22 Size distribution of NiO NPs synthesized with A) 0 µl oleic acid and B) 400 µl oleic acid at different reaction times.

In the above experiments we observed the effect of oleic acid on the morphology and particle size of the nanoparticles. We further studied the effect of the amount of added oleic acid with the reaction time set to 0.5h.

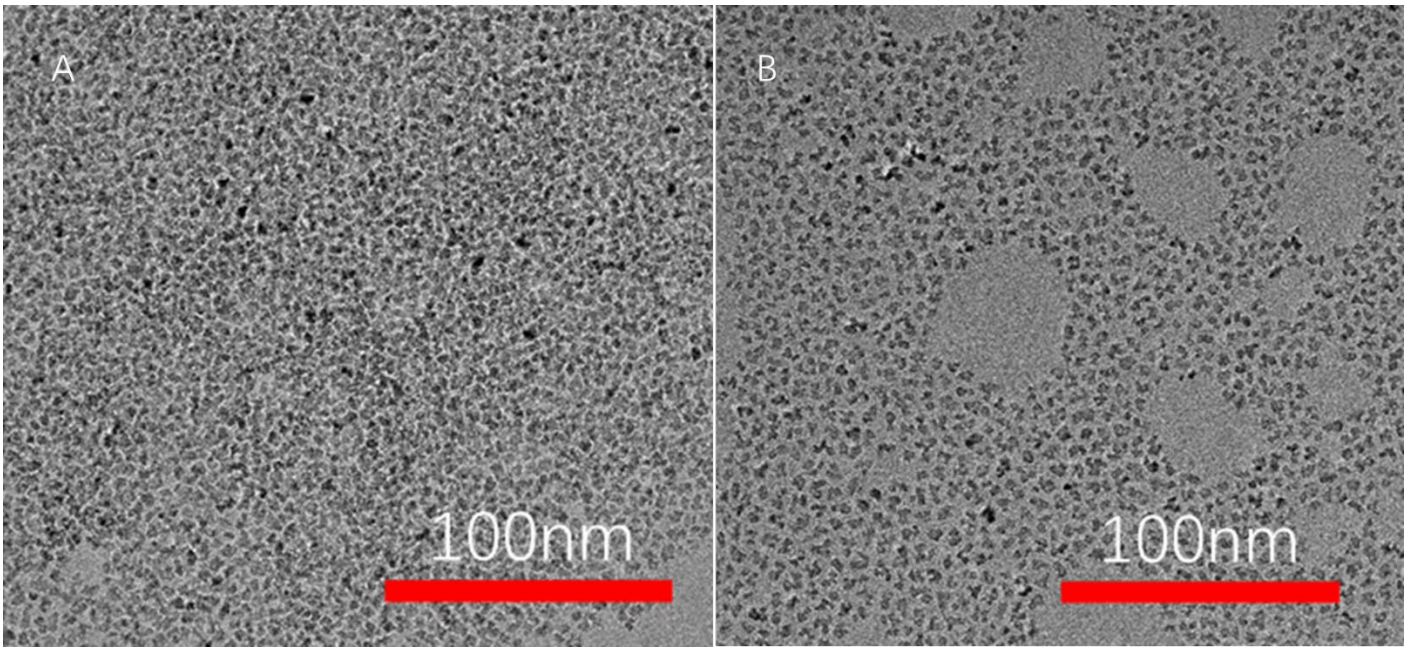

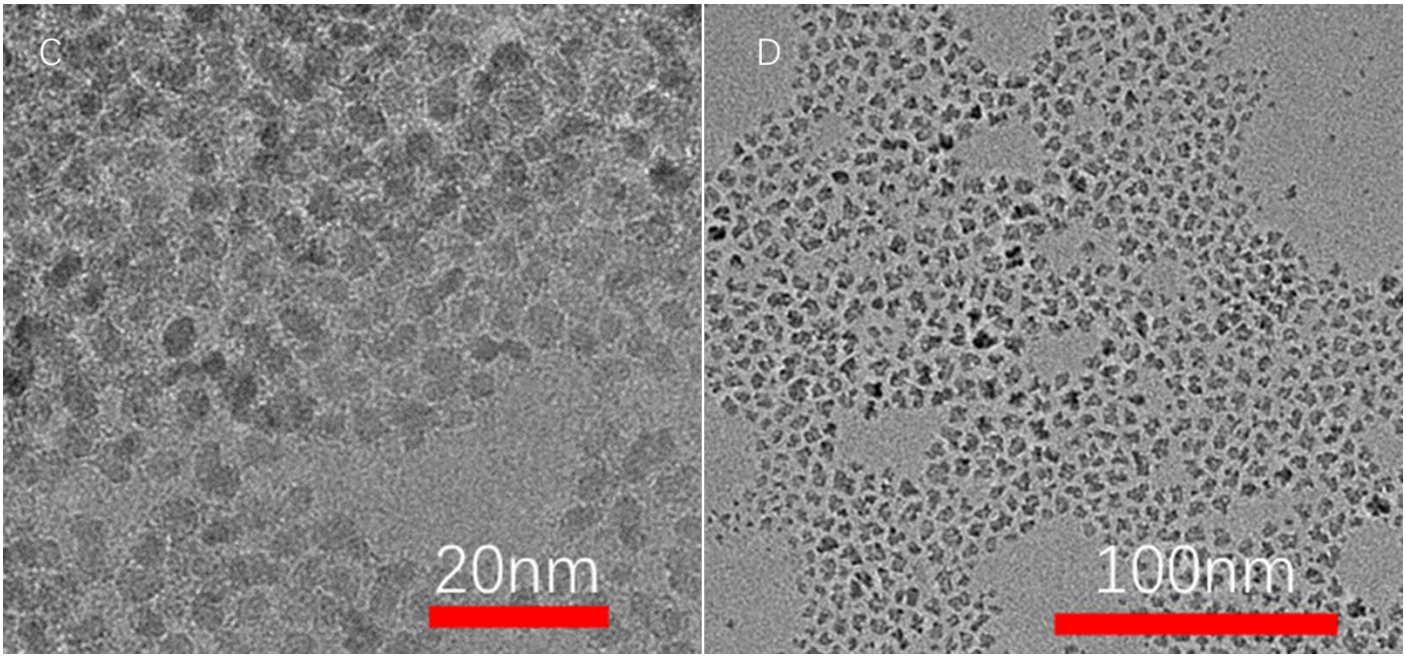

Figure 5.23 TEM images of the NiO nanoparticles with A) 0 µl oleic acid; B) 200 µl oleic acid; C) 400 µl oleic acid; D) 600 µl oleic acid

Figure 5.23 shows the TEM images of the NiO NPs produced with various oleic acid concentrations. They reveal a correlation between the amount of oleic acid added and particle size. Figure 5.24 displays the particle size distribution statistics. NiO NPs produced with 0, 200 µl, 400 µl, and 600 µl had mean diameters of 4.0 ± 1.5 nm, 4.4 ± 1.2 nm, 4.8 ± 1.2 nm, and 5.5 ± 2 nm, respectively. The TEM study further indicates that the amount of oleic acid has an impact on the particle shape and aggregation. Nanoparticles tend to develop a spherical shape in samples generated from 0 to 400 µl oleic acid (Figure 5.23A to C). In particular the nanoparticles in the sample containing 400 µl of oleic acid a well-defined spherical shape and a low particle size distribution are observed. The nanoparticles grew uneven and the particle size dispersion got bigger as the oleic acid concentration was increased to 600 µl.

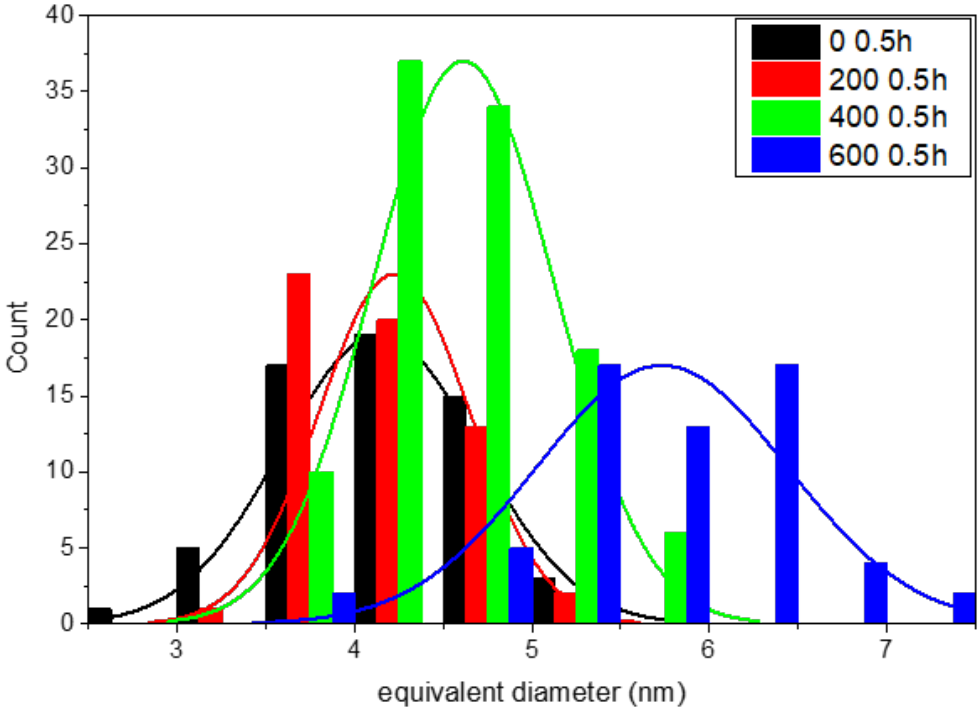

Figure 5.24 Size distribution of NiO nanoparticles synthesized with different amounts of oleic acid (given in microliters) and a reaction time of 0.5 h.

5.3.4. Application of NiO nanoparticles in perovskite solar cells

In the previous section we successfully developed the synthesis of NiO nanoparticles. We obtained spherical particles with an average size of 4.8 nm and good particle size distribution when using 400 µl of oleic acid and setting the reaction time of 0.5 h. The control of the size and size distribution is assured by the complex interplay of the different capping molecules present in the reaction medium. In this case we have to consider three species: oleic acid, oleylamine and TOPO, which can act as a coordinating solvent. The hydrophobicity of these compounds makes the nanoparticles more easily dispersed in non-polar organic solvents (e.g., chloroform, toloune), difficult to apply to hydrophilic ITO-coated glass surfaces. Furthermore, the application of such insulating organic surfactants is very likely to have a negative impact on the electrical conductivity of the NiO layer. By consequence, we need to modify the surface of the produced NiO nanoparticles. Here, we first focus on ligend exchange method by the hydrophilic small molecule 5-amino-1-pentanol (AP), which was shown to be efficient for replacing capping molecules like oleic acid and binding to metal nanoparticles[30]. Francesca Porta and coworkers reported that the NH_2 group is the predominant binding site for the nanoparticles and not the OH group. The free hydroxy group can then render the nanoparticle surface more hydrophilic[31]. We then used another method to remodify the NiO Nps surface by using organic bases to fully

remove the bulky ligands from the nanoparticles, which is named as modification method.

By using NiO Nps, perovskite solar cells based on fully inorganic charge transport layers are possible. We have reported double-layered SnO_2-structure perovskite solar cells[45]. As a good electron transport layer, SnO_2 can be prepared as a good thin film at low temperatures while guaranteeing the performance of the device. By combining SnO_2 and NiO Nps, perovskite solar cells based on an all-inorganic charge transport layer are possible.

5.3.4.1.Experimental section

Ligand exchange was performed using the following method. 20 mg of pristine NiO nanoparticles were dispersed in 1 ml of chloroform with 5-amino-1-pentanol (1mg/ml) and vigorously stirred overnight. After ligand exchange, excess hexane was added as anti-solvent to precipitate the nanoparticles. The final product was collected via centrifuging at 9000 rpm for 5 min and drying at 70°C.

For modification method, 70 mg of pristine NiO nanoparticles were dissolved in 1 ml of n-hexane to form a stable dispersion. Subsequently 3 ml of tetrabutylammonium hydroxide (1 M in methanol) was added dropwise to the dispersion. The hydrolysis reaction was immediately promoted, leading to the rapid desorption of the initial ligand molecules from the surface of the NiO nanoparticles. The ligand-stripped NiO nanoparticles were collected by centrifugation at 4000 rpm for 5 min. Purification of the nanoparticles was carried out by rinsing several times using methanol to remove residual organic matter followed by centrifugation. Note that the bare NiO nanoparticles should not be dried, otherwise irreversible aggregation occurs. The obtained nanoparticles can be directly dispersed in water or isopropanol to form a stable colloidal dispersion. To further stabilize the dispersion of NiO nanoparticles in IPA, a small amount of acetylacetone (ACAC) was added. The addition of 1µl/ml of ACAC to 20 mg/ml of NiO/IPA dispersion can increase the colloidal stability. Schematic illustration of this method is shown in Figure 5.25.

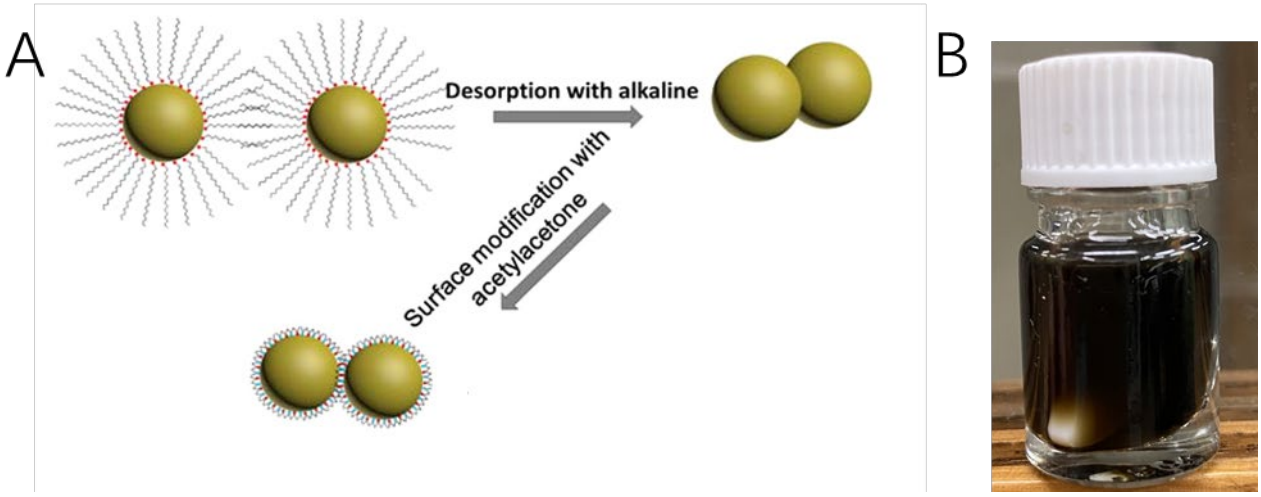

Figure 5.25 A) Schematic illustration of the modification procedure.[32]; B) photograph of a 20 mg/ml NiO nanoparticles dispersion in IPA using 1µl/ml ACAC as surfactant.

The double-layered SnO_2-structure perovskite solar cells were prepared as described in our report[45], in brief as follows. To generate the L-SnO_2 and H-SnO_2 precursor solutions, 1 mL of the SnO_2 colloid dispersion was diluted six times with deionized water containing various concentrations of NH_4Cl (20 and 40 mmol). The B-SnO_2 layer was produced by spin-coating the H-SnO_2 solution after depositing the L-SnO_2 solution on the ITO substrate (5 s between steps, no heating process). These solutions were spin-coated on ITO-coated glass substrates to obtain each of the ETLs (100 L solution, 2000 acceleration, 4000 speed, and 30 s). All ETL films were annealed for 1 hour at 70°C in the air. The deposition of perovskite active layer is described in Chapter 3. The 25 mg/ml NiO Nps IPA dispersion was spin-coated on top of the chalcogenide to replace the Spiro-OMeTAD as the hole transport layer. 100 gold was thermally evaporated as the top electrode.

5.3.4.2. Results and discussion

Fourier transform infrared spectroscopy (FTIR) was used to detect ligand exchange. The –CH2– stretching modes of the alkyl chains in TOPO,OA,OAm can be seen in at 2850 and 2919 cm^{-1} (Figure 5.26A red, green and blue). At 1146 cm^{-1} and 1465 cm^{-1}, the typical P=O and P-C stretching modes of TOPO were detected[33], respectively. At 1710 $cm^{-1,}$ the typical C=O stretching of carboxylic acid is identified, which belongs to OA. After fabrication and purification of the nanoparticles, FTIR spectroscopy (Figure 5.26 black) shows that the P=O vibration is still visible around 1200 cm^{-1}, but the band becomes broad and weak. Moreover, the C-H stretching vibration becomes strong, indicating the NiO nanoparticles are capped with TOPO molecular via

P=O group. Meanwhile, the typical C=O stretching of carboxylic acid is shifted from 1710 cm^{-1} to 1702 cm^{-1}, indicating the NiO nanoparticles are capped with OA molecular. A broad peak at around 1060 cm^{-1} is typical peak belonging to C-N stretching, indicating the NiO nanoparticles are also capped with OAm molecular. FTIR results reveal all three ligands are successfully capped with NiO nanoparticles, which can efficiently control the size of final products.

The FTIR spectrum of AP-exchanged NiO nanoparticles is presented in Figure 5.26B (black). In the range of 3500 cm^{-1} to 3200 cm^{-1}, the stretching signal from the N-H group and the O-H group of 5-amino-1-pentanol are overlapping. The FTIR spectrum did not reveal any peaks at 1146 cm^{-1} and 1465 cm^{-1}, which are characteristic peaks of TOPO and OA. Furthermore, the peaks related to the CH-vibrations are strongly reduced. These observations indicate that the original ligands have been successfully removed from the surface of the NiO nanoparticles during the ligand exchange. At the same time, the peaks in the range of 3500 cm^{-1} to 3200 cm^{-1} disappear, which corresponds to the -NH and -OH groups in the alcoholamine molecule.

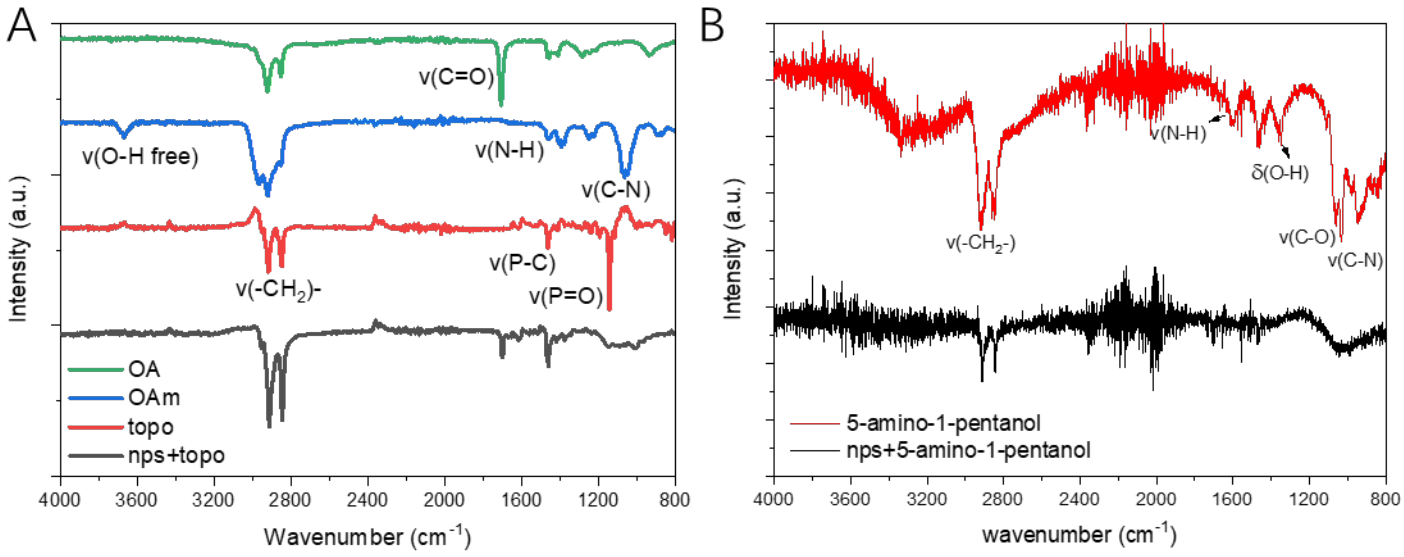

Figure 5.26 FTIR spectra of A) TOPO and pristine NiO nanoparticles; B) 5-amino-1-pentanol (AP) and NiO nanoparticles after ligand exchange with AP.

We redispersed the surface-modified NiO nanoparticles in polar solvents (isopropanol and water) to make dispersions of different concentrations, as shown in Figure 5.27A. The resulting dispersions were stable at room temperature for about 2 days after filtration using 0.2 μm PTFE filters. A 2.4mg/ml dispersion of NiO nanoparticles in IPA was spin-coated on an ITO-coated glass substrate and annealed at 150°C for 1 h to serve as a candidate for the hole transport layer of perovskite solar cells. As shown in Figure 5.27B, the obtained

NiO films are very blurred in the top-view SEM image and individual nanoparticles cannot be discerned. This may be due to the introduction of a large amount of 5-amino-1-pentanol used during ligand exchange, which has perhaps not been completely removed during purification. Due to the insulating character of 5-amino-1-pentanol, in the cross-sectional SEM image (Figure 5.27C) we observe a black layer between the NiO and the perovskite layer. Also, a serious contact problem between the perovskite layer and the hole transport layer can be observed in the cross-sectional SEM. The device characterization of the perovskite solar cell prepared with the above-described NiO hole transport layer shows an extremely low Voc and FF, which are associated with excessive carrier recombination phenomena. In addition, we expect that the low Jsc is mainly due to the residual organic matter that raises the resistance of the hole transport layer.

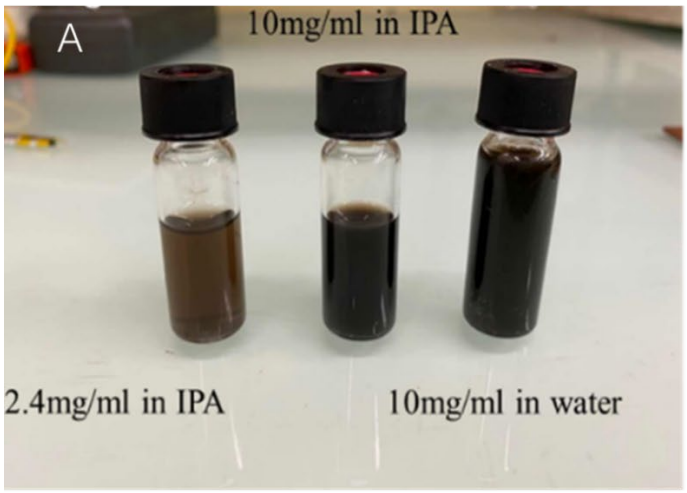

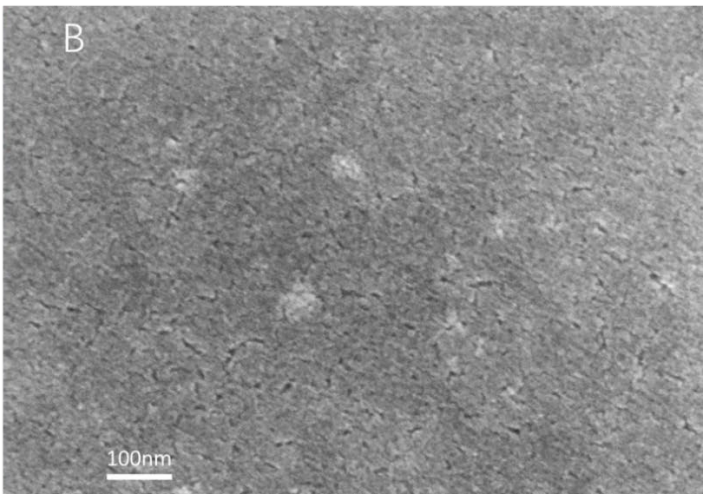

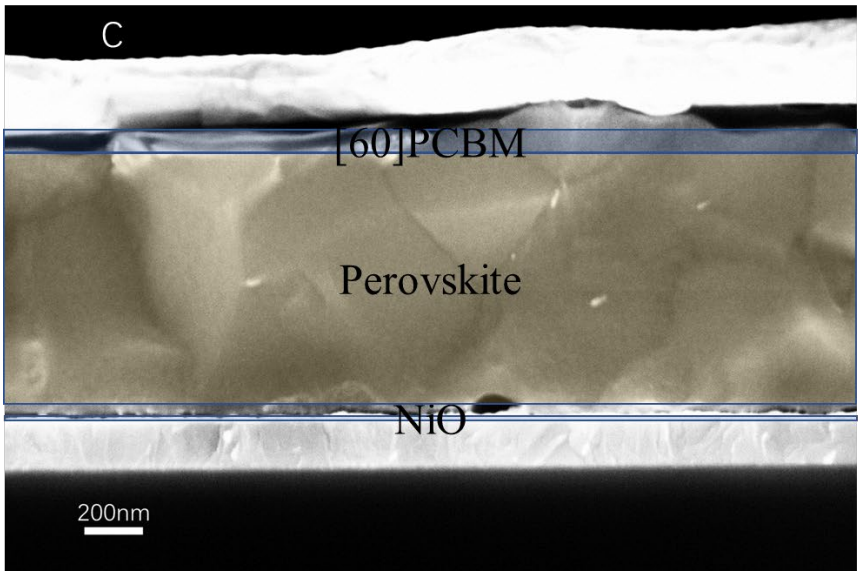

Voc (V)	Jsc (mA/cm²)	Fill Factor (%)	Efficiency (%)
0.72±0.14	14.98±1.56	22±11	1.9±0.48

Figure 5.27 A) Photograph of AP-functionalized NiO NPs dispersed in IPA and water at different concentrations; B) Top-view SEM image of the NiO layer obtained by spin coating onto ITO-

coated glass; C) cross-section SEM image of the perovskite solar cell based on this NiO layer; Table: solar cell parameters.

The above experiments demonstrated that the hydrophobic organic groups such as TOPO on the surface of NiO nanoparticles could be effectively replaced by using 5-amino-1-pentanol. However, due to inefficient purification of the exchanged particles, a large amount of 5-amino-1-pentanol and eventually other organic compounds remain and have a negative impact on the performance of NiO layer. To overcome this problem, we used in the following a two-step process. In the first step, to remove the initial surface ligands more effectively, we used tetrabutylammonium hydroxide as a stripping agent following[32].Simplely, pristine NiO nanoparticles were dissolved in n-hexane to form a stable dispersion. Then, tetrabutylammonium hydroxide (1 M in methanol) was added to the dispersion. The ligand-stripped NiO nanoparticles were collected by centrifugation. Purification of the nanoparticles was carried out by rinsing several times using methanol to remove residual organic matter followed by centrifugation. Note that the bare NiO nanoparticles should not be dried, otherwise irreversible aggregation occurs. The obtained nanoparticles can be directly dispersed in water or isopropanol to form a stable colloidal dispersion, which can be kept for 1 day without visible precipitation. To further stabilize the dispersion of NiO nanoparticles in IPA, a small amount of acetylacetone (ACAC) was added. The addition of 1µl/ml of ACAC to 20 mg/ml of NiO/IPA dispersion can increase the colloidal stability up to 5 days.

The characteristic bands of the organic ligands were no longer detected in the FTIR spectrum of the ligand-stripped nanoparticles (see Figure 5.28 black spectrum). The weak signals at 1500 and 2800-2950 cm^{-1} are probably due to residual tetrabutylammonium hydroxide. The FTIR spectrum of the sample treated with acetylacetone exhibits characteristic peaks in the range of 2850-2950 cm^{-1} belonging to the $-CH_2-$ vibrational band of acetylacetone molecules[34]. According to the literature, other characteristic ACAC related peaks at 1520 and 1394cm^{-1} can be attributed to the asymmetric and symmetric stretching vibrations of propionate ($C_2H_5COO^-$), respectively, due to the chelation of NiO by acetylacetone[35].

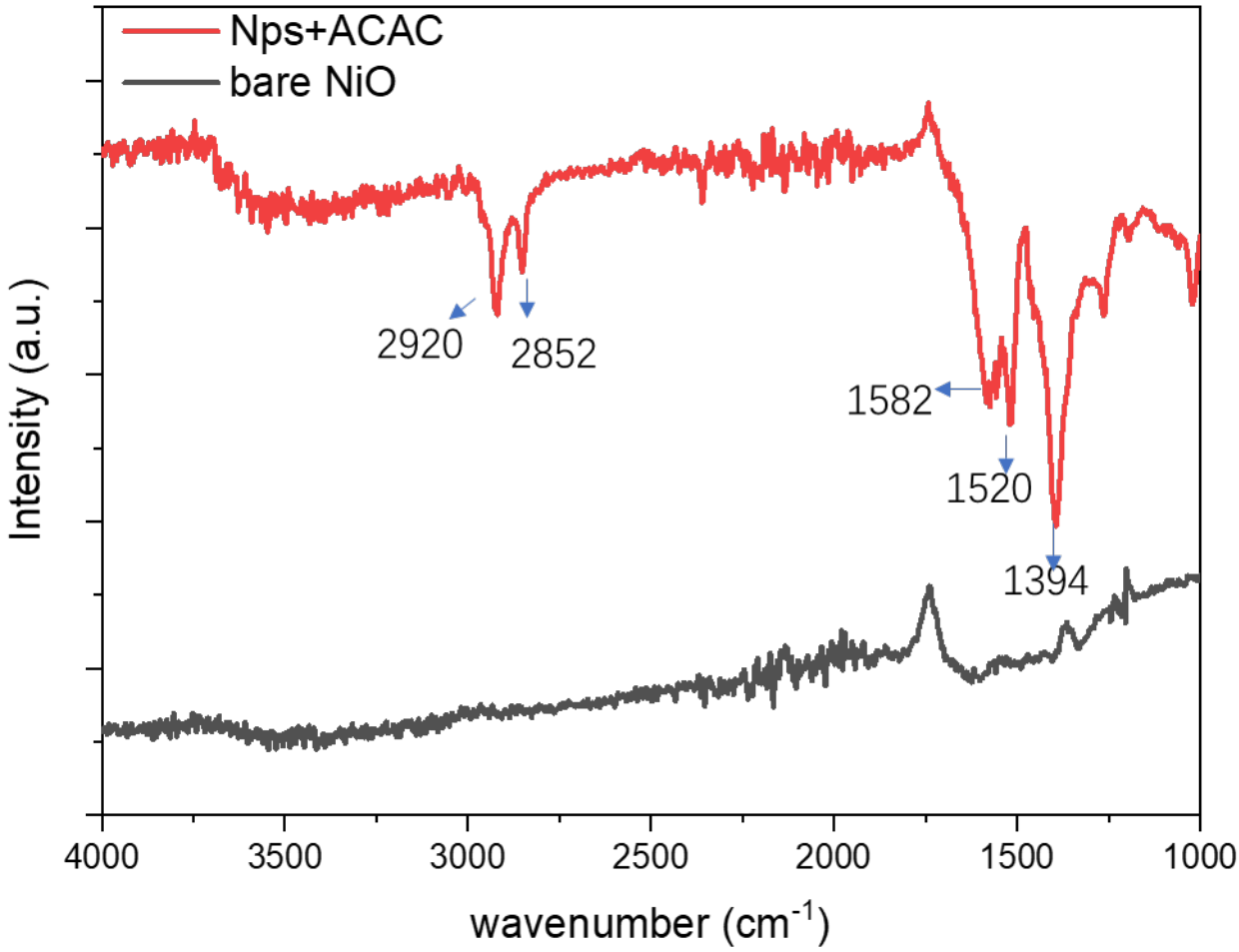

Figure 5.28 FTIR spectra of bare NiO NPs(black) and of ACAC-treated NiO NPs (red).

Summarizing, we successfully removed the initial capping molecules from the surface of NiO nanoparticles by alkaline treatment. The obtained bare NiO nanoparticles can be effectively dispersed in a polar solvent and the colloidal stability of this dispersion in isopropanol can be further enhanced by adding acetylacetone as a new capping molecule. This dispersion can be easily spin-coated on ITO-coated glass substrates. After spin coating, the substrate is annealed at 150°C and tested as the transparent electrode / hole transport layer of perovskite solar cells. As shown in Figure 5.29A, the top view SEM image reveals an ITO surface completely covered by nanoparticles and showing no particle agglomeration or pinholes. This improvement with respect to the earlier attempts can be attributed to the hydrophilic character of the ACAC-capped NiO nanoparticles, assuring a better interaction with the polar ITO surface, and to the use of IPA as the solvent, resulting in a better wettability than hexane or similar unipolar solvents. The AFM image shows that the roughness of this NiO layer is only 2.22 nm RMS. It has been shown that the obtained smother surface and good coverage results in the reduction of recombination sites, preventing from detrimental carrier losses in perovskite solar cells[36].

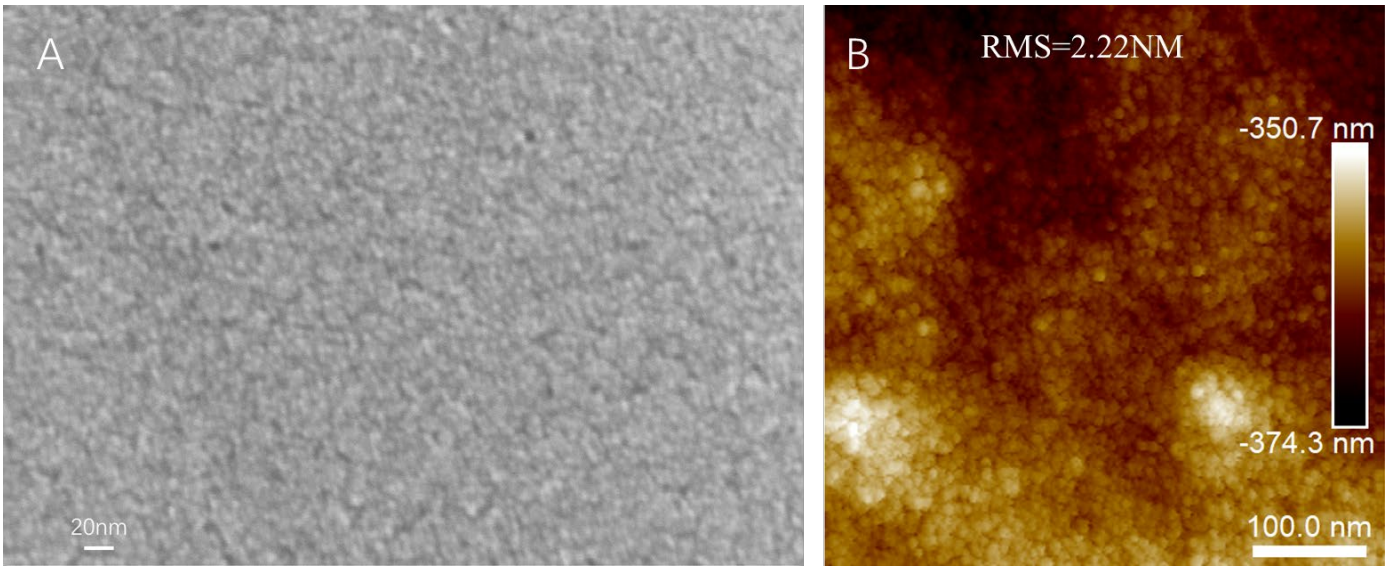

Figure 5.29 A) Top-view SEM image of the NiO layer by spin-coating NiO-ACAC NPs onto ITO; B) AFM image of the same layer.

We used this NiO thin film as the hole transport layer (HTL) in a perovskite solar cell. As shown in Figure 5.30A, the thickness of this HTL is 33 nm. From the cross-sectional SEM, it can be observed that the NiO film has high smoothness and does not show defects such as voids. The remarkably smooth NiO HTL should provide a good platform for the growth of perovskite layer. As shown in Figure 5.30B, the appearance of punctate crystals on the chalcogenide surface is caused by an excess of lead iodide[37]. The samples based on the NiO NPs layer do not exhibit morphological defects such as pinholes. This indicates that the flat NiO HTL contributes to the uniform crystallization of the perovskite layer and greatly reduces defects such as pinholes.

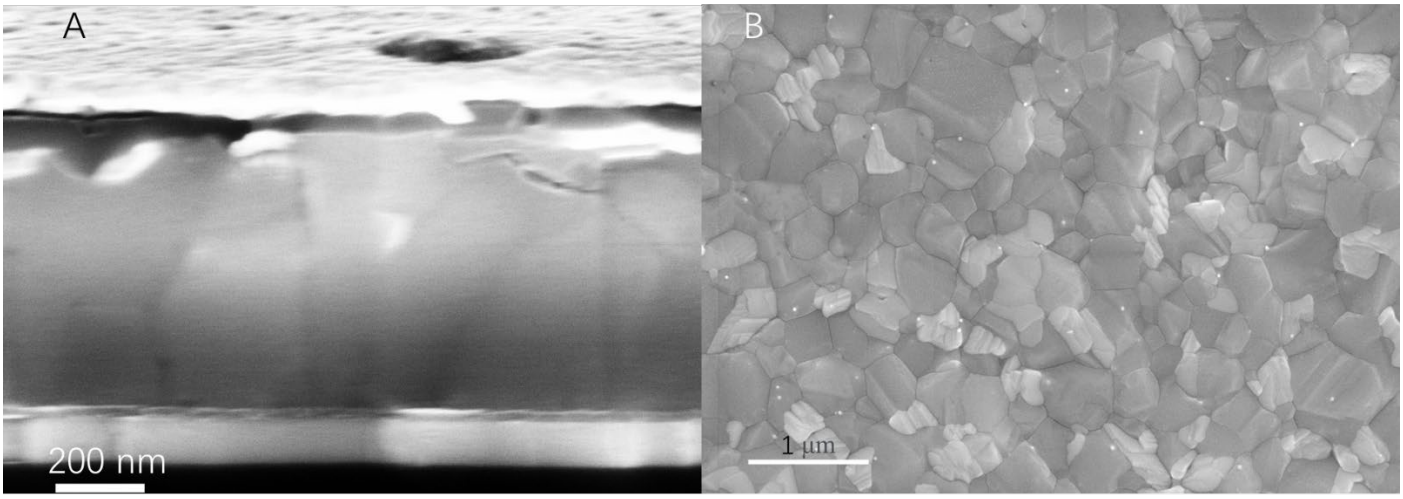

Figure 5.30 A) Cross-section SEM image of a PSC using NiO NPs as the hole transport layer (thickness: 33nm); B) Top-view SEM image of the perovskite layer grown on the NiO NPs hole transport layer.

Despite these very encouraging results from the morphological studies of the NiO HTL and the perovskite layer, the photovoltaic performance of the resulting PSCs was unfortunately disappointing (Figure 5.31). In particular, extremely low *FF*s in the range of 34-38% were found and also the values of *Jsc* were comparably low (15-18 mA/cm^2). Considering the regularity of the perovskite crystals obtained in SEM, the decrease of J_{SC} may be due to a too high series resistance.

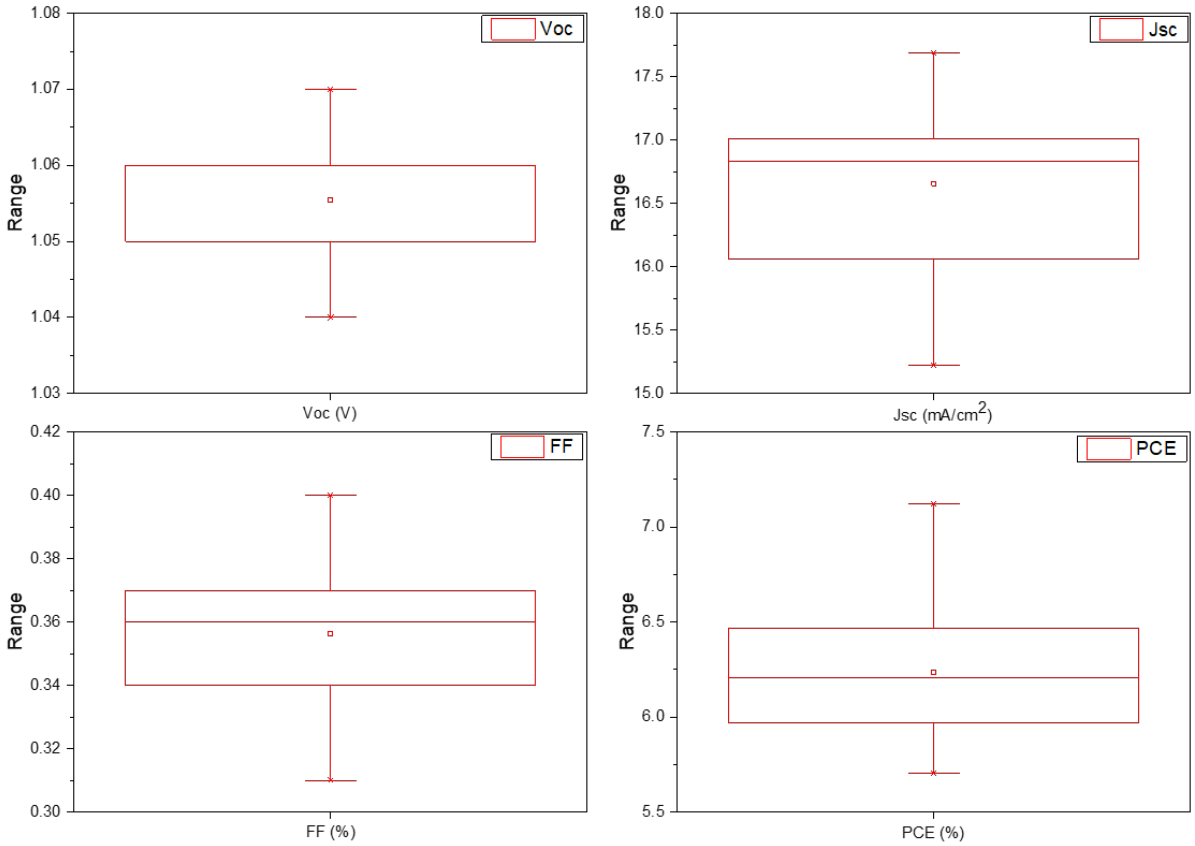

Figure 5.31 Device characteristics of PSCs using the NiO NPs HTL (statistics of 18 cells).

To further understand the origin of this behavior, we examined the *J-V* curves of the PSCs under dark and light conditions. As shown in Figure 5.32A (black), the dark *J-V* measurement produces an exponential curve characteristic of a diode. Figure 5.32B shows the dark *JV* plot on a semilogarithmic scale demonstrating a very low dark current density. Hence the *J-V* characteristics in the dark indicate a good heterojunction structure of the solar cell and no significant leakage currents. Under light conditions (Figure 5.32A, red curve), however, the *J-V* curve exhibits a distinct S-shape. Such curve shapes are usually associated with pronounced carrier recombination[38,39].

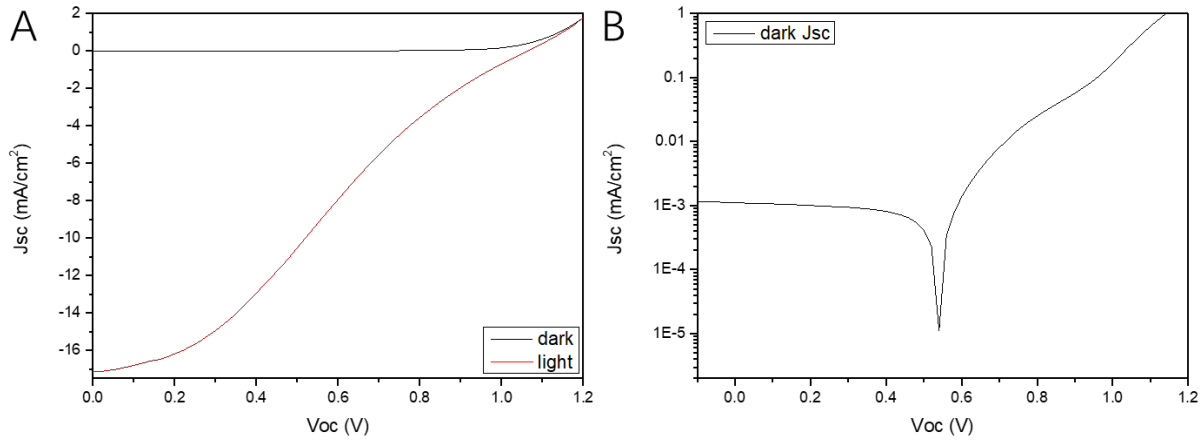

Figure 5.32 A) Typical J-V curves of the NiO NPs based PSCs in the dark (black) and under simulated sunlight (red); B) Dark J-V curve plotted on a semilogarithmic scale with the absolute value of the current density (negative current densities cannot be plotted on a log scale).

To investigated whether charge transport in the NiO NPs based HTL was the limiting factor, annealing at higher temperature was performed on FTO-coated glass substrates. Practically, 20 mg/ml of NiO NPs / IPA dispersion were spin-coated onto FTO-coated glass substrates and annealed at 500°C for 1h. As shown in Figure 5.1A, the top-view SEM image reveals that the NiO particles homogeneously cover the FTO surface, and individual nanoparticles can be clearly distinguished. Cross-sectional SEM imaging shows that this NiO film has a thickness of 35 nm and has good contact with the perovskite layer. We measured the photovoltaic performance of 18 PSCs, as shown in Table 5.4. These results demonstrate that the NiO NPs films annealed at 500°C have a much better performance, as the efficiency of the PSCs based on this HTL reaches values up to 14%.

Voc (V)	Jsc (mA/cm²)	Fill Factor (%)	Efficiency (%)
1.07±0.21	20.38±0.88	60±4	13.98±0.41

Table 5.4 Photovoltaic device characteristics of PSCs using a NiO NPs hole transport layer annealed at 500°C (statistics from 18 devices).

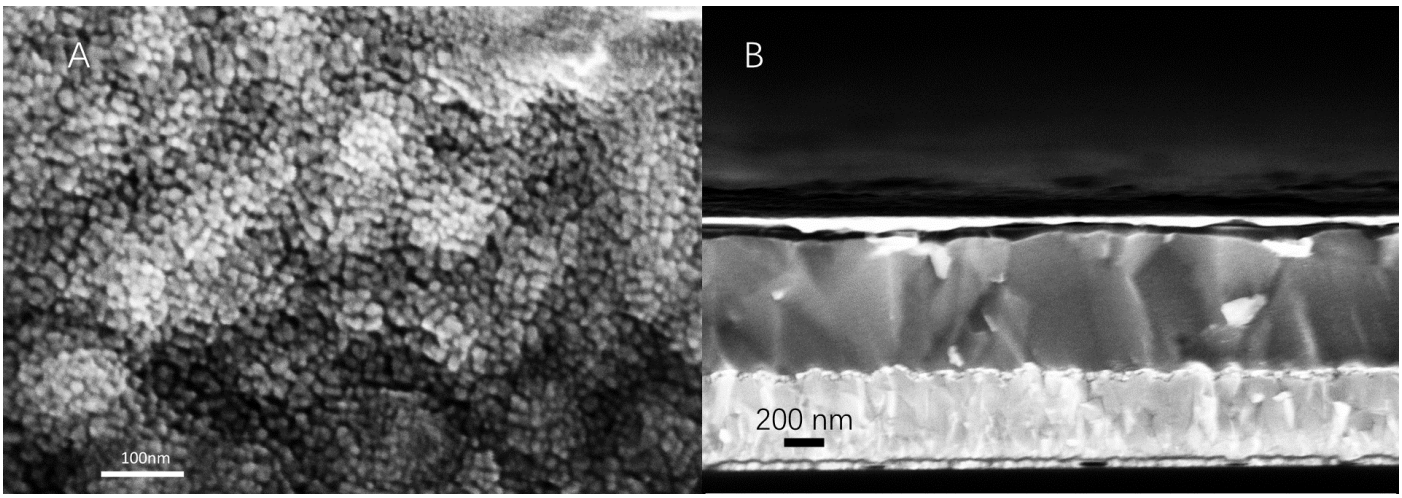

Figure 5.33 A) Top-view SEM image of the perovskite layer grown on the NiO NPs hole transport layer annealed at 500°C; B) Cross-section SEM image of the corresponding PSC.

Hall-effect measurements were used to investigate the electrical properties of the NiO nanoparticles thin films prepared at different annealing temperatures. For these measurements, the NiO NPs dispersion was spin-coated on two non-conductive glass slides and annealed at 500°C and 150°C, respectively for 1 h. NiO films prepared by the sol-gel method as described in Chapter 3 were also measured for comparison. Table 5.5 summarizes the results. The electrical conductivity is relatively poor for the samples with NiO NPs annealed at 150°C, likely due to the low carrier concentration. According to the following equations, defects in nickel oxide are likely generated under an excess oxygen environment[40].

$$2Ni^{2+} + \frac{1}{2}O_2(g) \rightarrow O^{2-} + V_{Ni}^{0} + 2Ni^{3+}$$

$$V_{Ni}^{0} \rightarrow V_{Ni}^{'} + h^{\cdot}$$

$$V_{Ni}^{'} \rightarrow V_{Ni}^{''} + h^{\cdot}$$

Therefore, the oxygen doping concentration affects the hole concentration and thus the electrical properties of NiO. When the annealing temperature is low, the oxygen doping concentration of NiO is low thus limiting the production of majority charge carriers. The weakening of the built-in electric field between the NiO and perovskite layers, as well as the wider depletion region is caused by the low concentration of majority charge carriers. The weaker built-in field in the depletion region is not only detrimental to suppress the reverse reaction of charge carriers from the NiO HTL to the perovskite layer, but also makes the charge separation, charge transport and collection of photogenerated charge carriers challenging[41,42,43]. As the annealing

temperature increases, the oxygen doping increases and provides NiO with better electrical properties. Their characteristics are then comparable to those of NiO films produced by the sol-gel process when annealed at 500°C.

Sample	T(°C)	resistivities(ohm-cm)	mobility(cm^2/V.S)	carrier concentration(1/cm^3)	Hall coefficient (cm^3/C)
NPS500	25	3.88E-04	2.74E+01	5.886E+20	1.06E-02
NPS150	25	2.48E-04	2.07E+01	1.31E+01	5.12E-03

Table 5.5 Electrical parameters of NiO layers with different treatment.

Elemental analysis of NiO treated with different annealing temperatures was carried out. The high-resolution XPS spectrum of Ni 2p 3/2 is shown in Figure 5.34, where we indicate the different valence states of Ni. From the above equation it can be concluded that the V_{Ni} defect concentration can be determined by the ratio of Ni^{3+}/Ni^{2+}, and the concentration of V_{Ni} defects can further influence the concentration of majority charge carriers in the NiO layer. Because the Ni 2p peak fitting is complicated and the Ni^{3+} concentration is likely overestimated by the XPS fitting[44], we abandon quantitative analysis about the ration of Ni^{3+}/Ni^{2+}. However, changes in the chemical and electronic states of NiO can still be observed in the XPS spectra, which is likely due to the doping of excess oxygen exacerbated at high temperatures, thus affecting the electrical properties of NiO films.

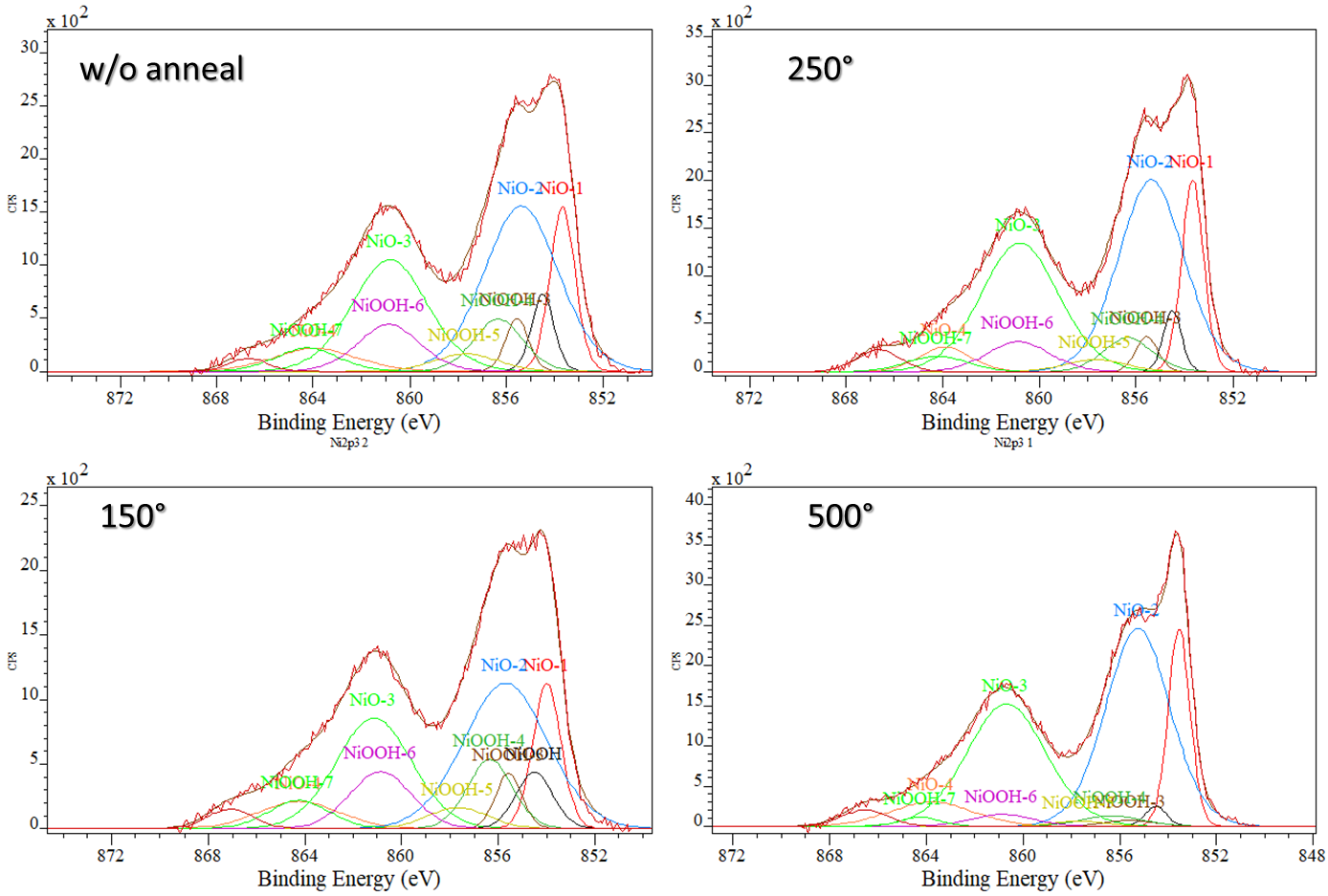

Figure 5.34 High-resolution Ni 2p 3/2 spectrum for thin films made of NiO nanoparticles using different annealing temperatures.

In the previous sections, we have developed a novel synthesis method for 4-5 nm NiO nanoparticles that can be stably dispersed in IPA. This important feature also allows the NiO particles to be deposited *on top* of the pervoskite layer (within an n-i-p PSC architecture) to replace the organic hole transport materials such as spiro-OMeTAD or PTAA. In previous studies we have published the use of bilayer SnO_2 as a very promising electron transport layer to obtain efficient perovskite solar cells[36]. In combination with the successful preparation of NiO nanoparticle dispersions, perovskite solar cells using entirely inorganic charge transport layers are possible, which could lead eventually to improved operational stability of the devices.

The top-view SEM image in Figure 5.35A depicts the surface morphology of the bare FAMA perovskite film with the perovskite crystals being clearly visible. The top-view SEM image in Figure 5.35B indicates that the NiO NPs have been successfully deposited on the perovskite surface without altering the morphology of the latter. This is also confirmed by EDX; the Ni signal can be clearly seen in the NiO-treated perovskite layer, as

shown in Figure 5.35D.

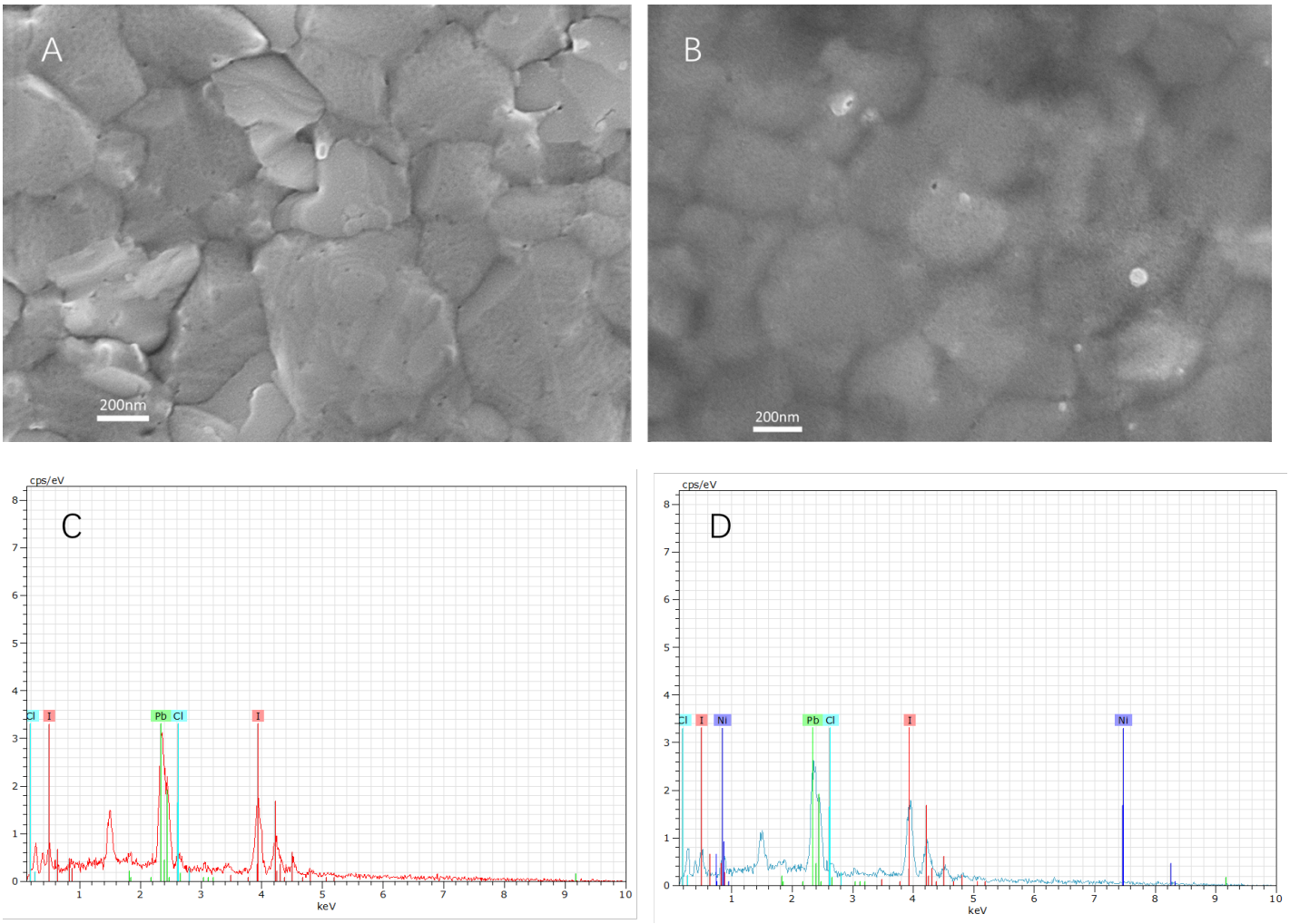

Figure 5.35 Top-view SEM images and EDX spectra of A, C) the bare perovskite layer; B, D) the perovskite layer covered with NiO NPs.

We expect that the NiO layer significantly enhances the chemical stability of the underlying perovskite layer. To confirm this, we produced two control samples, one with the bare perovskite (sample A) and the other with the NiO-covered perovskite layer (sample B), and rinsed them with water. The bare perovskite layer turns yellow (the color of PbI_2, in few seconds) because the perovskite structure decomposes and loses its organic cations in contact with water (cf. Figure 5.36). On the contrary, the perovskite/NiO sample remained brown. The decomposition of perovskite was only observed when a drop of water was placed on the perovskite/NiO surface and kept there for at least 30 s (yellowing in the lower left corner). This indicates that the NiO layer indeed protects the perovskite layer against the action of moisture, at least to some extent.

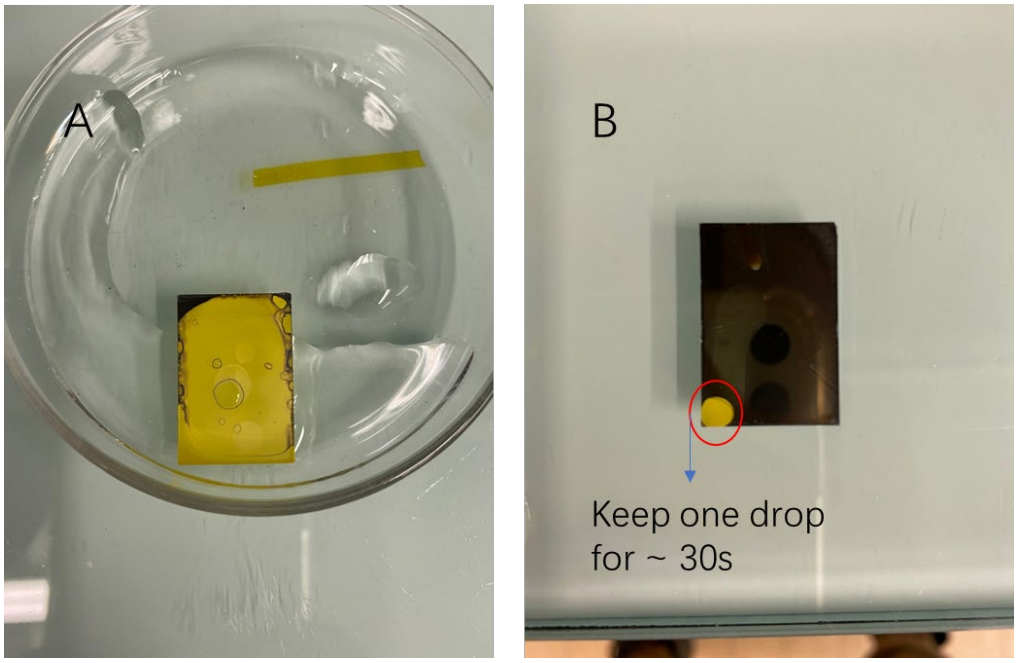

Figure 5.36 Photographs of A) half-cell with the bare perovskite on top; B) half-cell with NiO-covered perovskite layer on top, both rinsed with water after preparation.

Although we successfully deposited NiO NPs on the surface of perovskite layers and imparted perovskite water resistance, the performance of perovskite solar cells based on fully inorganic charge transport layers has not been studied in detail (due to time limitations). Only one set of samples with the device parameters listed in Table 5.6 is shown here. These parameters are not ideal, which may be due to the poor electrical properties of the NiO layer mentioned above. In addition, a Schottky contact may occur between NiO NPs and the Au electrode thus reducing the FF.

Voc (V)	Jsc (mA/cm^2)	Fill Factor (%)	Efficiency (%)
0.86	16.54	0.39	5.55

Table 5.6 Device characteristics of a (non-optimized) PSC using an SnO_2 bilayer ETL and NiO NPs HTL.

Conclusion

In this chapter, we explore the preparation of NiO nanoparticles using different methods and their integration into PSCs as HTL. The NiO nanoparticles obtained by conventional solvothermal and other solution-based methods showed uncontrolled agglomeration. To better control the particle size, size distribution and aggregation state of the nanoparticles, we finally explored thermal decomposition methods and investigated the influence of different types of capping/ligand molecules. First, we successfully synthesized Ni nanoparticles of 22 nm and very small particle size distribution with the help of Diethylene glycol (DEG). However, post-synthetic reduction to NiO NPs was not quantitative and the direct formation of NiO was not possible due to the reductive character of DEG. To obtain NiO NPs directly, we replaced DEG with trioctylphosphine oxide (TOPO) as a solvent and octadecylamine (ODA) as a ligand. We obtained a mixture of cubic-phase and hexagonal-phase Ni nanoparticles under Ar atmosphere. Considering the small particle size of these products, we finally kept TOPO as a coordinating solvent and carried out the reaction under air so that the resulting Ni nuclei could be rapidly oxidized to NiO. Oleylamine (OAm) and oleic acid (OA) were introduced as surfactants to regulate the particle size distribution and morphology of the nanoparticles. Using 2 ml of OAm and 400 µl of OA with a reaction time setting at 0.5 h, we obtained spherical NiO nanoparticles with an average particle size of 4.8 nm and uniform particle size distribution.

To improve the compatibility of the obtained NiO NPs with the highly polar surfaces of transparent conducting oxides (FTO, ITO), we performed ligand exchange on the NiO surface. The organic base tetrabutylammonium hydroxide was used to remove the initial hydrophobic capping molecules from the NiO surface, and the resulting bare NiO NPs could be dispersed in polar solvents. To further improve the stability of the dispersion, acetylacetone (ACAC) was used as a new surfactant. The resulting NiO NPs / IPA dispersion can be easily spin-coated on ITO-coated glass substrates to form dense NiO films of low surface roughness and controlled thickness. Nonetheless, the performance of the perovskite solar cells prepared with theses low-temperature processed NiO HTLs was poor. Using Hall-effect measurements we could infer that the low performance is caused by the poor electrical properties due to the low oxygen doping concentration of the NiO nanoparticles.

Finally, in a completely new approach, we deposited NiO NPs on the surface of the perovskite layer and made perovskite solar cells using fully inorganic charge carrier transport layers. The presence of NiO NPs gives the

perovskite layer some (limited) “waterproof” properties, which indicate that improved stability against moisture can be expected in PSCs using a NiO-covered active layer. Further improvement of the device performances of these PSCs would have required additional optimizations, which could not be made in the duration of this thesis.

Reference

1. Yuan, Y. F. *et al.* Hierarchically ordered porous nickel oxide array film with enhanced electrochemical properties for lithium ion batteries. *Electrochem. commun.* 12, 890–893 (2010).
2. Manders, J. R. *et al.* Solution-processed nickel oxide hole transport layers in high efficiency polymer photovoltaic cells. *Adv. Funct. Mater.* 23, 2993–3001 (2013).
3. Nikam, A. V., Prasad, B. L. V. & Kulkarni, A. A. Wet chemical synthesis of metal oxide nanoparticles: A review. *CrystEngComm* 20, 5091–5107 (2018).
4. Ueda, K., Tabata, H. & Kawai, T. Magnetic and electric properties of transition-metal-doped ZnO films. *Appl. Phys. Lett.* 79, 988–990 (2001).
5. Pilban Jahromi, S., Huang, N. M., Muhamad, M. R. & Lim, H. N. Green gelatine-assisted sol-gel synthesis of ultrasmall nickel oxide nanoparticles. *Ceram. Int.* 39, 3909–3914 (2013).
6. Mishra, A. K., Bandyopadhyay, S. & Das, D. Structural and magnetic properties of pristine and Fe-doped NiO nanoparticles synthesized by the co-precipitation method. *Mater. Res. Bull.* 47, 2288–2293 (2012).
7. Fominykh, K. *et al.* Ultrasmall dispersible crystalline nickel oxide nanoparticles as high-performance catalysts for electrochemical water splitting. *Adv. Funct. Mater.* 24, 3123–3129 (2014).
8. Chen, W. *et al.* Understanding the Doping Effect on NiO: Toward High-Performance Inverted Perovskite Solar Cells. *Adv. Energy Mater.* 8, 1–10 (2018).
9. Jiang, F., Choy, W. C. H., Li, X., Zhang, D. & Cheng, J. Post-treatment-free solution-processed Non-stoichiometric NiOx nanoparticles for efficient hole-transport layers of organic optoelectronic devices. *Adv. Mater.* 27, 2930–2937 (2015).
10. Walton, R. I. Subcritical solvothermal synthesis of condensed inorganic materials. *Chem. Soc. Rev.* 31, 230–238 (2002).
11. Wu, S. H. & Chen, D. H. Synthesis of high-concentration Cu nanoparticles in aqueous CTAB solutions. *J. Colloid Interface Sci.* 273, 165–169 (2004).
12. Fievet, F. *et al.* The polyol process: a unique method for easy access to metal nanoparticles with tailored sizes, shapes and compositions. *Chem. Soc. Rev.* 47, 5187–5233 (2018).
13. Dong, H., Chen, Y. C. & Feldmann, C. Polyol synthesis of nanoparticles: status and options regarding metals, oxides, chalcogenides, and non-metal elements. *Green Chem.* 17, 4107–4132 (2015).

14. Hammarberg, E. & Feldmann, C. In0 nanoparticle synthesis assisted by phase-transfer reaction. *Chem. Mater.* 21, 771–774 (2009).

15. Hammarberg, E. & Feldmann, C. Laux-type oxidation of In0 nanoparticles to In2O 3 retaining particle size and colloidal stability. *Zeitschrift fur Anorg. und Allg. Chemie* 639, 887–891 (2013).

16. Zhai, Y. N. *et al.* A Facile Diethylene Glycol Reduction Method for the Synthesis of Ultrafine Pd/C Electrocatalyst with High Electrocatalytic Activity for Methanol Oxidation. *Fuel Cells* 16, 771–776 (2016).

17. *Map: Chemistry (Zumdahl and Decoste) - Chemistry LibreTexts*.

18. Jung, D. R. *et al.* Review paper: Semiconductor nanoparticles with surface passivation and surface plasmon. *Electron. Mater. Lett.* 7, 185–194 (2011).

19. Wuister, S. F. & Meijerink, A. Synthesis and luminescence of (3-mercaptopropyl)-trimethoxysilane capped CdS quantum dots. *J. Lumin.* 102–103, 338–343 (2003).

20. Chopra, N., Claypoole, L. & Bachas, L. G. Morphological control of Ni/NiO core/shell nanoparticles and production of hollow NiO nanostructures. *J. Nanoparticle Res.* 12, 2883–2893 (2010).

21. Wang, D. & Li, Y. Effective octadecylamine system for nanocrystal synthesis. *Inorg. Chem.* 50, 5196–5202 (2011).

22. Salavati-Niasari, M., Mir, N. & Davar, F. A novel precursor in preparation and characterization of nickel oxide nanoparticles via thermal decomposition approach. *J. Alloys Compd.* 493, 163–168 (2010).

23. Manna, L., Scher, E. C. & Paul Alivisatos, A. Shape control of colloidal semiconductor nanocrystals. *J. Clust. Sci.* 13, 521–532 (2002).

24. Mourdikoudis, S. & Liz-Marzán, L. M. Oleylamine in nanoparticle synthesis. *Chem. Mater.* 25, 1465–1476 (2013).

25. Sharma, V. *et al.* Dominant role of trioctylphosphine on the particle size and various properties of CoO nanoparticles. *J. Magn. Magn. Mater.* 166000 (2019) doi:10.1016/j.jmmm.2019.166000.

26. Sako, S. Magnetic property of NiO ultrafine particles with a small Ni core. *J. Vac. Sci. Technol. B Microelectron. Nanom. Struct.* 15, 1338 (1997).

27. Johnston-Peck, A. C., Wang, J. & Tracy, J. B. Synthesis and structural and magnetic characterization of Ni(Core)/NiO(Shell) nanoparticles. *ACS Nano* 3, 1077–1084 (2009).

28. Mbewana-Ntshanka, N. G., Moloto, M. J. & Mubiayi, P. K. Role of the amine and phosphine groups

in oleylamine and trioctylphosphine in the synthesis of copper chalcogenide nanoparticles. *Heliyon* 6, e05130 (2020).

29. Zhang, L., He, R. & Gu, H. C. Oleic acid coating on the monodisperse magnetite nanoparticles. *Appl. Surf. Sci.* 253, 2611–2617 (2006).
30. Insin, N. *et al.* Incorporation of iron oxide nanoparticles and quantum dots into silica microspheres. *ACS Nano* 2, 197–202 (2008).
31. Porta, F., Krpetić, Ž., Prati, L., Gaiassi, A. & Scarì, G. Gold-ligand interaction studies of water-soluble aminoalcohol capped gold nanoparticles by NMR. *Langmuir* 24, 7061–7064 (2008).
32. Fang, R. *et al.* [6,6]-Phenyl-C61-Butyric Acid Methyl Ester/Cerium Oxide Bilayer Structure as Efficient and Stable Electron Transport Layer for Inverted Perovskite Solar Cells. *ACS Nano* 12, 2403–2414 (2018).
33. Doan-Nguyen, V. V. T., Carroll, P. J. & Murray, C. B. Structure determination and modeling of monoclinic trioctylphosphine oxide. *Acta Crystallogr. Sect. C Struct. Chem.* 71, 239–241 (2015).
34. Jin, L. H. *et al.* Evolution of precursor in the epitaxial CeO2 films grown by chemical solution deposition. *J. Eur. Ceram. Soc.* 35, 927–934 (2014).
35. Kumar, S. & Ojha, A. K. Ni, Co and Ni-Co codoping induced modification in shape, optical band gap and enhanced photocatalytic activity of CeO2 nanostructures for photodegradation of methylene blue dye under visible light irradiation. *RSC Adv.* 6, 8651–8660 (2016).
36. Ye, J. *et al.* Doped Bilayer Tin(IV) Oxide Electron Transport Layer for High Open-Circuit Voltage Planar Perovskite Solar Cells with Reduced Hysteresis. *Small* 17, 1–9 (2021).
37. Chen, Q. *et al.* Controllable self-induced passivation of hybrid lead iodide perovskites toward high performance solar cells. *Nano Lett.* 14, 4158–4163 (2014).
38. Servaites, J. D., Ratner, M. A. & Marks, T. J. Organic solar cells: A new look at traditional models. *Energy Environ. Sci.* 4, 4410–4422 (2011).
39. Shi, J. J. *et al.* S-shaped current-voltage characteristics in perovskite solar cell. *Wuli Xuebao/Acta Phys. Sin.* 64, (2015).
40. Xu, L. *et al.* Inverted perovskite solar cells employing doped NiO hole transport layers: A review. *Nano Energy* 63, 103860 (2019).
41. Guerrero, A., Juarez-Perez, E. J., Bisquert, J., Mora-Sero, I. & Garcia-Belmonte, G. Electrical field profile and doping in planar lead halide perovskite solar cells. *Appl. Phys. Lett.* 105, 1–5 (2014).

42. Laban, W. A. & Etgar, L. Depleted hole conductor-free lead halide iodide heterojunction solar cells. *Energy Environ. Sci.* 6, 3249–3253 (2013).

43. Yang, G. *et al.* Interface engineering in planar perovskite solar cells: Energy level alignment, perovskite morphology control and high performance achievement. *J. Mater. Chem. A* 5, 1658–1666 (2017).

44. Natu, G. *et al.* Valence band-edge engineering of nickel oxide nanoparticles via cobalt doping for application in p-type dye-sensitized solar cells. *ACS Appl. Mater. Interfaces* 4, 5922–5929 (2012).

45. Ye, J., Li, Y., Medjahed, A. A., Pouget, S., Aldakov, D., Liu, Y., & Reiss, P. (2021). Doped Bilayer Tin (IV) Oxide Electron Transport Layer for High Open‐Circuit Voltage Planar Perovskite Solar Cells with Reduced Hysteresis. Small, 17(5), 2005671.

Conclusion

The experimental chapters presented in this thesis each offer their own conclusions. The significance of the obtained results as well as their potential importance for the PV scientific community are examined in further detail here.

First, we optimized the precursor composition for the preparation of the perovskite layer used in p-i-n PSCs comprising a Cu-doped NiO HTL prepared by a standard sol-gel method. Excess PbI_2 and MACl were introduced as additives, which led to a significant improvement in the photovoltaic conversion efficiency of the resulting PSCs. Based on these findings, we developed in the following a facile strategy for the passivation of the NiO HTL using the bifunctional molecule DMAP to improve the quality of the interface with the perovskite layer. By creating chemical interactions, this bifunctional molecule can cross-link the Cu:NiO HTL with the triple cationic perovskite (CsFAMA) layer. Improved perovskite crystallization and thin film morphology, as well as better solar cell stability, are all benefits of these interactions. As a result, this research adds to our understanding of how to increase the photovoltaic efficiency and stability of perovskite solar cells by modifying the surface of the HTL NiO, and we expect that similar approaches can be applied to other inorganic hole transport materials.

In the following, we explored two novel approaches aiming at the preparation of high-quality metal-doped NiO HTLs. The first one was based on electrostatic spray deposition (ESD), a technique that is well-known to yield metal oxide thin films of precisely controlled thickness and composition, high conformity even on rugous substrates, and density/absence of pinholes. Cu:NiO films with improved electrical conductivity and smoother surface morphology could be produced using ESD than with the sol-gel method. Moreover, the dopant Cu can be distributed more homogeneously within the NiO film when the layer is electrostatically deposited. PSCs using ESD Cu:NiO HTLs have shown a better PCE, lower hysteresis, improved environmental stability, and greater repeatability, which demonstrates the potential of the ESD method for this domain. Furthermore, electrostatic spray deposition techniques can solve the challenge of preparing homogeneous large-area HTLs with high-quality morphological, optical, and electrical characteristics, which is of high interest for the industrialization and commercialization of PSCs. However, we note that the use of ESD methods implies the very careful selection of the precursors, as their poor solubility in solvents

appropriate for the process could otherwise cause problems such as non-uniformity of the coating.

In a second approach, we focused on the preparation of NiO nanoparticles in order to expand the applicability of NiO hole transport materials, as the ESD process requires high temperatures, incompatible with, for example, flexible substrates. Through the rational use of different organic ligands, we optimized the preparation of sub-10-nm NiO nanoparticles without agglomeration and excellent dispersibility in polar solvents, such as isopropanol. Dense NiO films showing very low surface roughness and controlled thickness were successfully deposited on ITO-coated glass substrates at low temperatures. Unfortunately, the low-temperature annealed HTLs based on NiO nanoparticles exhibited poor electrical conductivity, which led to comparably low power conversion efficiencies in the corresponding PSCs. This shortcoming can likely be overcome in future works by identifying a more suitable surface coating of the NiO nanoparticles in replacement of presently used acetylacetone. Finally, we deposited NiO NPs *on the surface* of the perovskite layer, which enabled the preparation of perovskite solar cells exclusively using inorganic charge carrier transport layers; in the present case, commercial SnO_2 nanoparticles have been used for the preparation of the ETL. We showed that the presence of NiO NPs imparts enhanced "water resistance" to the underlying perovskite layer, which suggests that improved moisture stability can be expected in PSCs using NiO-covered active layers. Further improvement of the device performance of these PSCs requires additional optimizations, which could not be achieved in this thesis due to time constraints. We note that applications of the developed NiO nanoparticles can be expected in the field of perovskite solar cells but also other fields, such as photocatalysis. The same applies to the NiO thin films based on sol-gel and ESD methods: they could be applied as electron-blocking layers underneath thick mesoporous NiO layers in photoelectrodes used in photocatalytic applications.

Summarizing, the key results presented in this thesis contribute to shaping future research directions towards the development of advanced perovskite solar cell architectures. Metal oxides appear to be prime candidates for charge transport layers imparting enhanced environmental and operational stability to PSCs. While for the n-type materials an established choice of candidates exists (TiO_2, SnO_2, ZnO, etc.), the development of p-type materials lags behind, and compounds like spiro-OMeTAD or PTAA are still widely applied despite their obvious drawbacks. NiO is one of the most promising candidates for use as the HTL in PSCs, and our results demonstrate the advantages and shortcomings of three different approaches for the preparation of NiO thin films. They also open up new perspectives for PSCs using all-inorganic charge

transport layers enabling cost reduction and improved stability.

Conclusion

Les chapitres expérimentaux présentés dans cette thèse proposent chacun leurs propres conclusions. La signification des résultats obtenus ainsi que leur importance potentielle pour la communauté scientifique PV sont examinées plus en détail ici.

Tout d'abord, nous avons optimisé la composition de précurseur pour la préparation de la couche de pérovskite utilisée dans les PSC p-i-n comprenant un HTL NiO dopé Cu préparé par une méthode sol-gel standard. Des excès de PbI_2 et MACl ont été introduits en tant qu'additifs, ce qui a conduit à une amélioration significative de l'efficacité de conversion photovoltaïque des PSC résultants. Sur la base de ces résultats, nous avons développé dans ce qui suit une stratégie facile pour la passivation du NiO HTL en utilisant la molécule bifonctionnelle DMAP pour améliorer la qualité de l'interface avec la couche de pérovskite. En créant des interactions chimiques, cette molécule bifonctionnelle peut réticuler le Cu:NiO HTL avec la couche de pérovskite triple cationique (CsFAMA). L'amélioration de la cristallisation de la pérovskite et de la morphologie des couches minces, ainsi qu'une meilleure stabilité des cellules solaires, sont tous des avantages de ces interactions. En conséquence, cette recherche ajoute à notre compréhension de la façon d'augmenter l'efficacité et la stabilité photovoltaïques des cellules solaires à pérovskite en modifiant la surface du HTL NiO, et nous nous attendons à ce que des approches similaires puissent être appliquées à d'autres matériaux de transport de trous inorganiques.

Dans ce qui suit, nous avons exploré deux nouvelles approches visant à la préparation de HTL NiO dopés aux métaux de haute qualité. Le premier était basé sur le dépôt par pulvérisation électrostatique (ESD), une technique bien connue pour produire des films minces d'oxyde métallique d'épaisseur et de composition contrôlées avec précision, de conformité élevée même sur des substrats rugueux et de densité/absence de trous d'épingle. Des films Cu:NiO avec une conductivité électrique améliorée et une morphologie de surface plus lisse pourraient être produits en utilisant l'ESD qu'avec la méthode sol-gel. De plus, le dopant Cu peut être réparti de manière plus homogène au sein du film NiO lorsque la couche est déposée électrostatiquement. Les PSC utilisant les ESD Cu:NiO HTL ont montré un meilleur PCE, une hystérésis plus faible, une stabilité environnementale améliorée et une plus grande répétabilité, ce qui démontre le potentiel de la méthode ESD pour ce domaine. De plus, les techniques de dépôt par pulvérisation électrostatique peuvent résoudre le défi de préparer des HTL homogènes de grande surface avec des caractéristiques morphologiques, optiques et

électriques de haute qualité, ce qui est d'un grand intérêt pour l'industrialisation et la commercialisation des PSC. Cependant, nous notons que l'utilisation des méthodes ESD implique une sélection très minutieuse des précurseurs, car leur faible solubilité dans les solvants appropriés pour le procédé pourrait sinon causer des problèmes tels que la non-uniformité du revêtement.

Dans une deuxième approche, nous nous sommes concentrés sur la préparation de nanoparticules NiO afin d'étendre l'applicabilité des matériaux de transport de trous NiO, car le processus ESD nécessite des températures élevées, incompatibles avec, par exemple, des substrats flexibles. Grâce à l'utilisation rationnelle de différents ligands organiques, nous avons optimisé la préparation de nanoparticules de NiO inférieures à 10 nm sans agglomération et une excellente dispersibilité dans les solvants polaires, tels que l'isopropanol. Des films NiO denses présentant une très faible rugosité de surface et une épaisseur contrôlée ont été déposés avec succès sur des substrats de verre recouverts d'ITO à basse température. Malheureusement, les HTL recuits à basse température basés sur des nanoparticules de NiO présentaient une faible conductivité électrique, ce qui a conduit à des rendements de conversion de puissance comparables dans les PSC correspondants. Cette lacune peut probablement être surmontée dans les travaux futurs en identifiant un revêtement de surface plus approprié des nanoparticules de NiO en remplacement de l'acétylacétone actuellement utilisée. Enfin, nous avons déposé des NiO NPs à la surface de la couche de pérovskite, ce qui a permis la préparation de cellules solaires à pérovskite utilisant exclusivement des couches de transport de porteurs de charge inorganiques ; dans le cas présent, des nanoparticules de SnO_2 commerciales ont été utilisées pour la préparation de l'ETL. Nous avons montré que la présence de NiO NP confère une meilleure « résistance à l'eau » à la couche de pérovskite sous-jacente, ce qui suggère qu'une meilleure stabilité à l'humidité peut être attendue dans les PSC utilisant des couches actives recouvertes de NiO. Une amélioration supplémentaire des performances des dispositifs de ces PSC nécessite des optimisations supplémentaires, qui n'ont pas pu être réalisées dans cette thèse en raison de contraintes de temps. Nous notons que des applications des nanoparticules NiO développées peuvent être attendues dans le domaine des cellules solaires à pérovskite mais aussi dans d'autres domaines, comme la photocatalyse. Il en va de même pour les couches minces de NiO basées sur les méthodes sol-gel et ESD : elles pourraient être appliquées en tant que couches bloquant les électrons sous des couches épaisses de NiO mésoporeuses dans les photoélectrodes utilisées dans les applications photocatalytiques.

En résumé, les principaux résultats présentés dans cette thèse contribuent à façonner les futures directions de recherche vers le développement d'architectures avancées de cellules solaires à pérovskite. Les oxydes

métalliques semblent être des candidats de choix pour les couches de transport de charges conférant une stabilité environnementale et opérationnelle améliorée aux PSC. Alors que pour les matériaux de type n, il existe un choix établi de candidats (TiO_2, SnO_2, ZnO, etc.), le développement des matériaux de type p est à la traîne et des composés comme le spiro-OMeTAD ou le PTAA sont encore largement appliqués malgré leurs inconvénients évidents. . NiO est l'un des candidats les plus prometteurs pour une utilisation comme HTL dans les PSC, et nos résultats démontrent les avantages et les inconvénients de trois approches différentes pour la préparation de films minces NiO. Ils ouvrent également de nouvelles perspectives pour les PSC utilisant des couches de transport de charges entièrement inorganiques permettant une réduction des coûts et une meilleure stabilité.

Cellules solaires p-i-n à base de pérovskites halogénées

Cette thèse concerne le développement de la couche de transport pour les charges positives (trous) utilisée dans des cellules solaires à base de pérovskites halogénées. Le matériau étudié pour cette application est l'oxyde de nickel (NiO). Trois voies différentes ont été explorées dans le but d'optimiser la cristallinité, la morphologie et les propriétés de transport des couches minces de NiO et d'étudier l'influence sur les performances des cellules solaires. Tout d'abord la composition de la couche pérovskite a été optimisée afin de maximiser les performances. Par la suite, nous nous sommes intéressés à la passivation de la couche de transport de trous (NiO) pour améliorer l'interface avec la couche de pérovskite. L'introduction de la 4-diméthylaminopyridine pour passiver le NiO n'a non seulement amélioré fortement le facteur de remplissage (*fill factor*) de la cellule solaire et par conséquent son rendement, mais également la stabilité sous atmosphère humide. Une nouvelle méthode de dépôt pour la couche conducteur de trous NiO est présentée par pulvérisation électrostatique (*electrospray deposition*, ESD). Cette méthode apporte une meilleure morphologie de surface et des couches NiO plus denses que la méthode conventionnelle de dépôt par enduction centrifuge (*spin-coating*). De plus, l'ESD permet d'introduire une quantité précise de dopants dans le NiO, comme par exemple le cuivre ou le lithium. En faisant varier les paramètres tels que la température et le temps de dépôt, nous avons obtenu des films minces de Cu:NiO denses et uniformes. Leur utilisation dans des cellules solaires pérovskite a permis d'améliorer efficacement les performances (rendement proche de 18%). Dans la dernière partie nous développons une nouvelle méthode de synthèse de nanoparticules de NiO. Ces particules d'une taille <10 nm sont synthétisées par voie chimique en solvant organique. L'optimisation de la synthèse a permis de contrôler précisément la taille et la phase cristalline des nanoparticules. Nous démontrons également que les nanoparticules de NiO présentent un potentiel pour des cellules solaires pérovskite entièrement inorganique, en utilisant comme couche de transport d'électrons le SnO_2.

Stable p-i-n solar cells using metal halide perovskites

This thesis concerns the development of the hole transport layer used in halide perovskite solar cells. The material studied for this application is nickel oxide (NiO). Three different routes have been explored in order to optimize the crystallinity, morphology and transport properties of NiO thin films and to study the influence on the performance of solar cells. First, the composition of the perovskite layer was optimized to maximize the performance. Then, we focused on the passivation of the hole transport layer (NiO) to improve the interface with the perovskite layer. The introduction of 4-dimethylaminopyridine to passivate the NiO not only greatly improved the fill factor of the solar cell and therefore its performance, but also the stability under humid atmosphere. A new deposition method for the NiO hole transport layer is presented by electrospray deposition (ESD). This method provides better surface morphology and denser NiO layers than the conventional spin-coating method. In addition, ESD allows the introduction of a precise amount of dopants into the NiO, such as copper or lithium. By varying parameters such as temperature and deposition time, we obtained dense and uniform Cu:NiO thin films. Their use in perovskite solar cells allowed to improve efficiently the performances (efficiency close to 18%). In the last part we develop a new method for the synthesis of NiO nanoparticles. These particles with a size <10 nm are synthesized via a chemical route in organic solvent. By optimizing the synthesis, the size and crystalline phase of the nanoparticles are precisely controlled. Finally, we demonstrate that NiO nanoparticles have a high potential for all-inorganic perovskite solar cells using SnO_2 as the electron transport layer.